EUROPEAN SPACE AGENCY CONTRACT REPORT

The work described in this report was done under ESA contract. Responsibility for the contents resides with the author or organisation that prepared it.

Radiation Testing of CCD and APS Imaging Devices

ESTEC Contract Reference: CCN No. 2 to contract 14028/99/NL/MM

Sira Electro-Optics Limited Reference: 239.DO.53 issue 2

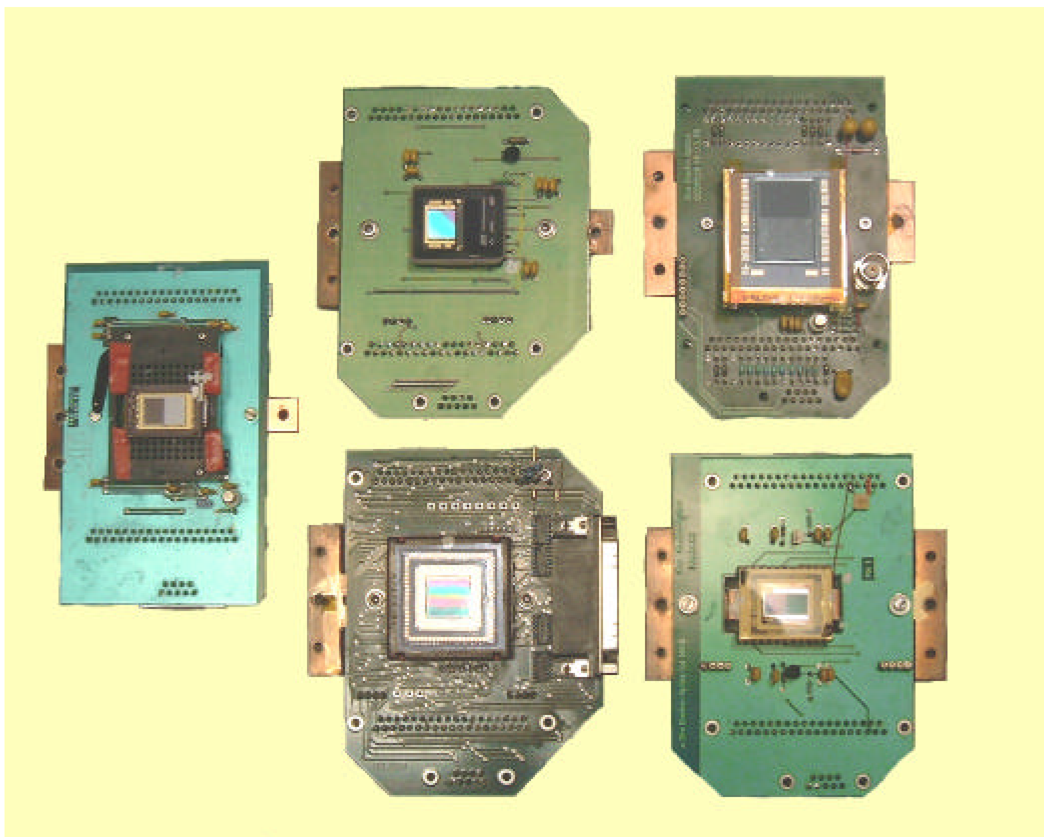

Sira Electro-Optics Limited, South Hill
Chislehurst, Kent, BR7 5EH, England

Telephone: +44 (0) 20 8467 2636
Fax: +44 (0) 20 8468 1771
Email: info@siraeo.co.uk
Website: www.siraeo.co.uk
Registered in England No 2248869

EUROPEAN SPACE AGENCY CONTRACT REPORT

The work described in this report was done under ESA contract. Responsibility for the contents resides with the author or organisation that prepared it.

Final Report
Radiation Testing of CCD and APS Imaging Devices

ESTEC Contract Reference: CCN No. 2 to contract 14028/99/NL/MM
Sira Electro-Optics Limited Reference: 239.DO.53 issue 2

Prepared for ESA, ESTEC

Prepared by G R Hopkinson, Sira Electro-Optics Limited

ESA Study Manager: Ali Mohammadzadeh, ESTEC, TOS-QCA

Authorised by:

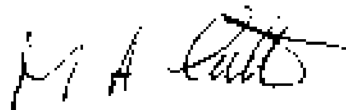

DR M A CUTTER
BUSINESS MANAGER

Date: 17 June 2003

Copyright © Sira Ltd 2003

CONTENTS

Section	Page
LIST OF ACRONYMS	7
SUMMARY	9
1. INTRODUCTION AND SCOPE	15
1.1 Reference Documemts	16
2. TEST OBJECTS	17
2.1 e2v CCDs	17
2.2 Atmel CCDs	18
2.3 STAR-250 CMOS Active Pixel Sensor	19
2.4 IRIS2 CMOS Active Pixel Sensor	20
3. TEST EQUIPMENT	22
3.1 CCD and APS Characterization	22
3.2 APS Irradiation board	23
4. IRRADIATIONS	25
4.1 Cobalt60 irradiations	26
4.2 60 MeV Proton Irradiations	26
4.3 10 MeV Proton Irradiations	27
4.4 Heavy Ion Tests	27
5. RESULTS OF CCD TESTING	29
5.1 Measurements of Conversion Gain	29
5.2 Measurements of Flatband Voltage Shift	31

5.3 Measurements of Linearity and Full Well Capacity **34**

5.4 Measurements of Responsivity/PRNU **37**

5.5 Measurements of Dark Signal **42**
5.5.1 CCD55 Devices 42
5.5.2 CCD57 Devices 47
5.5.3 TH7890M Devices 55
5.5.4 TH7863D Devices 60

5.6 Investigation of Random Telegraph Signal (RTS) behaviour **63**

5.7 Measurments of Charge Transfer Inefficiency (CTI) **73**
5.7.1 Measurements of CTI using First Pixel Response (FPR) 73
5.7.2 CTI Annealing 88
5.7.3 Comparison of CTI Values 91
5.7.4 Measurements of Trap Emission Time Using FPR 92

5.8 Measurements of Output Drain Current **96**

6. RESULTS OF STAR-250 AND IRIS-2 TESTING **97**

6.1 Measurements of Conversion Gain **97**

6.2 Measurements of Image Lag **98**
6.2.1 Tradeoffs Involved in Reducing VPIX voltage 100

6.3 Measurements of Flatband Voltage Shift **104**

6.4 Measurements of Power Consumption **105**

6.5 Measurements of Linearity and Full Well Capacity **106**

6.6 Measurements of Responsivity/PRNU **107**
6.6.1 Initial Measurements on the 5.3 Mrad Irradiated Device 107
6.6.2 Measurements After Cobalt60 Irradiation at ESTEC 107
6.6.3 Responsivity Measurements on Proton Irradiated Devices 108
6.6.4 PRNU Measurements on Proton Irradiated Devices 111

6.7 Measurements of on-chip ADC Performance **115**

6.8 Measurements of Dark Signal **117**
6.8.1 Thermal Dark Current 117
6.8.2 Fixed Pattern Noise 120

6.9 Investigation of Random Telegraph Signal (RTS) Behaviour **123**

6.10 Results of Heavy Ion Testing **126**
6.10.1 STAR-250 Summary 127
6.10.2 IRIS-2 Summary 128
6.10.3 Elantec EL7457C Devices 129

LIST OF ACRONYMS

ADC	Analogue to Digital Converter
ADU	ADC Unit or Analgue to Digital Unit
AIMO	Advanced Inverted Mode Operation
APS	Active Pixel Sensor
DC	Direct Current
DUT	Device Under Test
CCD	Charge Coupled Device
CDS	Correlated Double Sampling
CMOS	Complementary Metal Oxide Silicon
CTE	Charge Transfer Efficiency
CTI	Charge Transfer Inefficiency
DNL	Differential Nonlinearity
DSNU	Dark Signal Nonuniformity
ESA	European Space Agency
FPGA	Field Programmable Gate Array
FPR	First Pixel Response
HCTI	Horizontal Charge Transfer Inefficiency
LED	Light Emitting Diode
MTF	Modulation transfer Function
PRNU	Photo-Response Nonuniformity
ROI	Region Of Interest
RTS	Random Telegraph Signal
SEL	Single Event Latchup
VCTI	Vertical Charge Transfer Inefficiency

SUMMARY

The work described in this report is concerned with the radiation testing of charge-coupled devices (CCDs) and CMOS active pixel sensors (APSs). It is the final deliverable for CCN 2 to ESA contract 14028/99/NL/MM. The main contract involved the upgrading (new video board, framegrabber and software) of the CCD test system previously supplied to ESA. The present work was performed both to test the operation of the upgraded test system and to provide radiation data on imaging devices of interest for space applications.

The devices tested were:

- CCD57-10 (512 x 512 pixels) and CCD55-20 (770 x 572 pixels) frame transfer CCDs from e2v Technologies, Chelmsford, UK (formerly Marconi Applied Technologies)
- TH7863D (384 x 288 pixels) and TH7890M (512 x 512 pixels) frame transfer CCDs from Atmel, Grenoble, France
- STAR-250 CMOS active pixel sensors (custom designed for ESTEC by FillFactory, Belgium), formerly called the OISL sensor
- IRIS2 CMOS active pixel sensors from FillFactory (for heavy ion testing only).

In addition a CMOS CCD driver chip (Elantec EL7457C) was tested for single event latch up in connection with the ALADIN instrument on ADM-AEOLUS.

CCD samples were available from ESA as part of its manufacturer capability approval programme and APS samples as part of Fillfactory device development contracts to ESA. In the case of the e2v CCD57-10, additional samples were procured as part of this contract in order to have enough samples for both cobalt60 and proton irradiations.

The CCDs were irradiated with either cobalt60 gamma rays or protons of energy 9.5 and 60 MeV. The STAR-250 APS devices were given cobalt60 or 9.5 MeV protons. Two devices were tested for single event effects by irradiating with heavy ions. The two IRIS-2 samples were only given a heavy ion test for single event latch-up (SEL).

The work included the design of 'personality' boards for each device to be tested as well as a dedicated 'APS irradiation bias' board which was used during the cobalt60 and heavy ion irradiations of the active pixel sensors.

For some measurements, special techniques had to be developed (or existing ones refined) in order to measure important parameters. This was the case for measurements of charge transfer inefficiency (CTI) and random telegraph signals (RTS) for CCDs and single event effects for the APS devices. In addition, the variation of dark current and image lag with photodiode bias and the changes in photo-responsivity were new effects which had to be investigated for the STAR-250.

It was found that the newly constructed tested equipment functioned well thoughout the tests and the upgrade to the framegrabber and software considerably improved the ease of use of the system.

Measurements of CCD conversion gain (in ADC units, or ADU/electron) were carried out using a Cadmium109 X-ray source. These were for calibration purposes and the results were in line with the manufacturer's data sheet values. X-ray measurements were also made for the STAR-250 APS and it was at this time that it was realized that the standard APS bias voltages resulted in an image lag effect (particularly important for small signal transient events) and a large reduction in the measured conversion gain. The study of this effect and its elimination (through choice of appropriate operating bias) formed a significant part of the study, as will be discussed below. A by-product of this work was the realization that the proton-induced dark current spikes could also be greatly reduced.

Flatband voltage shifts for the CCDs were much as expected from previous studies, though perhaps slightly higher (being ~ 0.15 V/krad(Si) for biased devices, rather than the 0.1 V/krad(Si) previously found). For unbiased devices the shift was about a factor 4 or 5 less. These values were measured by monitoring the effect on surface dark current and the point at which the surface goes into inversion. The Atmel devices (TH7890M and TH7863D) were found to operate satisfactorally thoughout the tests with the datasheet bias voltages. This is probably because these were selected by the manufacturer, taking into account the margin needed for a shift in flatband voltage. However the e2v devices needed changes to the operating bias after irradiation (in particular the readout register clocks needed to be shifted about 2 V). Since failure to do this resulted in complete loss of output signal it is recommended that CCD operating biases are chosen carefully for flight instruments.

No significant changes in CCD linearity/full well capacity, responsivity or photo-response nonuniformity (PRNU) were observed. This agrees with the results of previous invstigations. As noticed before, there is often a differnece in full well capacity between using spot rather than uniform illumination.

Low surface dark currents were achieved for the inverted mode devices (CCD55 and TH7890M) and the surface dark current was also low for the CCD57-10 even though this did not operate in inverted mode (giving a biased cobalt60 damage of 0.03 nA/cm^2/krad(Si) at 20ºC). However the CCD55 and CCD57 showed significant dark charge at the edge of the CCD. This arises both from the metallized storeshield and dark reference regions and also from regions outside the active area.

Results for proton-induced bulk dark current and dark current spikes were essentially as found previously. A major goal of the study was to measure displacement damage for both 9.5 and 60 MeV radiation and the following values were measured for the damage constant ratio:

	Ratio of dark current damage at 9.5 MeV and 60 MeV
CCD55-20	1.7±0.3
CCD57-10	1.7±0.3
TH7890M	1.9±0.3

The values of the damage constants for 9.5 MeV protons were:

	Damage constant at 9.5 MeV nA/cm^2/krad at 20ºC
CCD55-20	0.13±0.02
CCD57-10	0.03±0.005
TH7890M	0.063±0.01

After scaling for the volume of the active region the values above are roughly in line with the universal damage constant suggested by Srour and Lo (IEEE Trans. Nucl. Sci., vol. 47, pp. 2451-2459, 2000).

Note that masking of the 9.5 and 60 MeV fluence regions was acieved using plates of 1.5 mm thick aluminium and 8 mm thick steel, respectively. It was found that the boundaries of the 60 MeV region were blurred by proton scattering and the production of secondary protons and neutrons. This reduces the area of the fluence region that is useful for measurements. The areas achieved in this study were about the smallest that are practical.

Another important goal was to measure annealing behaviour. It was found that annealing of displacement damage induced dark current was significant, but only for temperatures above 110ºC. This stongly indicates that the divacancy is not the only defect responsible for bulk dark current – or else that the divacancies show unusual annealing behaviour.

Random telegraph signals were also studied and plots of RMS value versus average signal for particular pixels (measured over several thousand time samples) were found to be useful to identify RTS pixels. Although an in-depth study could not be performed, the findings reinforced previous studies and the present state of knowledge can be summarized as follows:

- RTS effects are seen in all proton irradiated CCDs and APSs over a range of proton energies (at least 1.5 to 60 MeV).
- In CCDs, the probability for an RTS defect in a pixel is ~ 0.000016 per incident 10 MeV proton and seems to scale with NIEL (though it is not clear whether the elastic NIEL or the total NIEL gives the best fit). Thus, with 20 μm x 20 μm pixels and a fluence of 10^{10} 10 MeV p/cm^2 , ~40% of pixels will show RTS effects. In the STAR-250 the occurrence probability was much lower because of the small area of the photodiodes.
- There is a wide range of switching amplitudes, but in a CCD they are typically 500 to 20,000 electrons/pixel/s at 5ºC. Most large fluctuations occur for pixels with a high pedestal level, but not always – some large dark current spikes do not show RTS effects. The amplitudes decrease with cooling as expected (activation energy ~ 0.6 eV).
- There is also a wide range in time constants – near room temperature they range from seconds to hours (i.e. 4 orders of magnitude), but are mostly of order several minutes.
- The time constants for existing in the high and low dark current states are usually roughly comparable but not always – some pixels show ‘spiking’ - that is, short excursions to either the low or high state.
- The time constants increase as the device is cooled. In CCDs the activation energy is typically 0.9 to 1.6 eV. The fact that some defects switch very fast at room temperature means that RTS effects can still be seen (with time constants of several hours) even at -40ºC.

Measurements of vertical CTI were made for the CCD57, TH7890M and TH7863D devices as a function of signal background and temperature and a substantial database of values was created. The CCD55 was not measured as it had an advanced inverted mode architecture and could not be clocked in the backwards direction (which is needed for first pixel response measurements). Measurenets were also made at the top, centre and botom of frame transfer images so as to estimate the effect of the line move time (at the top of an image all the line moves are fast and at the bottom, half are fast, frame transfer, moves and half are slow, readout, moves). In general the vertical CTI behaviour was as expected, though there was a small but significant dependence of the CTI on temperature in the regime around -30ºC which

was unexpected (since ‘worst case’ CTI was measured – for which all traps are kept empty prior to readout and so there should be little dependence on emission time).

Measurements were also made of emission time constant and the values agreed well with existing data. The decrease in CTI at low temperatures (when the long time constant traps are kept filled) was also seen. The data for the faster traps was best fitted with a multi-trap model as seen previously.

Measurements for the 10 and 60 MeV regions indicated a damage constant ratio of 2.4 for all devices and temperatures. This is slightly but significantly higher than the dark current damage constant ratio discussed above. This indicates a difference in the inventory of the defects responsible. Measurements at different temperatures did not show any large changes in the damage ratio, nor where there any large changes after annealing. However the absolute CTI value did decrease on annealing, particularly after the 150ºC bake. In fact the behaviour with annealing was very similar to that observed for the bulk dark current.

There was a small, but probably significant, difference in the relative concentration of the dominant (long time constant) trap. For the CCD57, 93% of traps had the longer time constant. For the TH7890M, ~ 72% had the longer time constant. Hence there appears to be a difference in trap concentration ratios for the two types of CCD. The trap time constants themseves were not found to vary with proton energy.

For the STAR-250 APS it was discovered that reducing the VPIX voltage (below 4 V) allowed the reset transistor to remain in strong inversion throughout the pixel reset process and so eliminated lag effects. If the VPIX bias was reduced further (below 3V) then dark current spikes were reduced (presumably because the diode bias and so the electric field, where reduced). A side effect was a lowering in full well capacity and gain and greater departures from linearity. However it is expected that some applications would benefit from the near-elimination of dark current spikes.

No significant change in threshold voltages, power consumption or fixed pattern noise were seen. However the responsivity was reduced by a factor 2 after ~ 100 krad(Si) both for cobalt60 gammas and 9.5 MeV protons. The change was wavelength independent and did not anneal (neither after several months storage at room temperature, nor after a bake for 3 days at 83ºC). The PRNU was also seen to increase as the responsivity decreased.

Small increases in surface dark current were observed after cobalt60 irradiation. These were nonuniform over the array, the centre of the image being most affected and the corners the least. There was no significant annealing except that the dark current for the unbiased device (which had previously been lower) increased after several months storage to end up comparable with the values for biased devices. Proton damage produced dark current spikes of large amplitude (but relatively few in number compared with a CCD). These could be reduced by decreasing the VPIX voltage as discussed above. This reduction also essentially eliminated RTS behavior.

During the heavy ion testing no latch up or unusual SEU behaviour was seen in the STAR-250 up to the maximum LET of LET of 68 MeV/mg/cm^2. An increase in ADC noise was seen however, but this is not unexpected. The IRIS-2 device was seen to show excessive currents at 8.27 MeV/mg/cm^2 and above, though the currents were sometimes small, indicating a ‘mini-latch’ effect. As the device was statically biased and was not used for imaging during the heavy ion tests, it is not known if the device would remain functional during these ‘mini-latch’ events.

The Elantec EL7457C 40 MHz CMOS Driver is an ultra-high speed, non-inverting quad CMOS driver. It is capable of running at clock rates up to 40MHz and features 2A peak drive capability and a nominal on-resistance of 3 . The EL7457C is used for driving highly capacitive loads, such as storage and vertical clocks in CCD applications. It is also well suited to automated test equipment (ATE), pin driving, level-shifting and clock-driving applications. No latch up was seen in either device at the maximum LET used of 34 MeV/mg/cm^2 after a total fluence on each device of 1.0 10^6 ions/cm^2. In view of the negligibly small flux of cosmic ray ions in the space environment having LET greater than this value and the small area of the die (~ 4 mm^2) the device can be considered to be immune to latch up.

Because the EL7457C is a commercial-off-the-shelf (COTS) device, it is recommended to perform further heavy ion testing (probably to higher LET) as part of Lot Acceptance Tests on potential flight batches.

Recommendations for use of CCDs and APSs in space

1. Operating biases for e2v CCDs need to be chosen carefully for flight instruments in order to allow for effects of flatband voltage shift on the output stage. These effects are likely to be important for total dose > 5 krad(Si). At higher dose the effect on inversion point may become important.
2. With the e2v CCD55 and CCD57 the dark charge generated at the edges of the CCD needs to be taken into account.
3. RTS effects have to be taken into account whenever dark signal nonuniformity is significant for an application.
4. RTS effects can occur in video chain electronics (affecting every pixel) as well as the CCD. Hence either the signals have to be referred to the overscanned pixel value or the video chain has to be characterized for RTS effects.
5. For the STAR-250 APS it is likely that a reduced VPIX voltage will be needed for most applications. The chosen value depends on a trade-off of linearity/full well and gain versus reduction in dark current spikes.
6. Reduction in responsivity and increase in PRNU have to be considered for the APS
7. In future heavy ion testing of APS it would be useful to perform an imaging test to check if the device is functional during ‘mini-latch’ events.

1. INTRODUCTION AND SCOPE

This report is concerned with the radiation testing of charge-coupled devices (CCDs) and CMOS active pixel sensors (APSs). It is the final deliverable for CCN 2 to ESA contract 14028/99/NL/MM. The main contract involved the upgrading (new video board, framegrabber and software) of the CCD test system previously supplied to ESA. The present work was performed both to test the operation of the upgraded test system and to provide radiation data on imaging devices of interest for space applications.

The devices tested were:

- CCD57-10 (512 x 512 pixels) and CCD55-20 (770 x 572 pixels) frame transfer CCDs from e2v Technologies, Chelmsford, UK (formerly Marconi Applied Technologies)
- TH7863D (384 x 288 pixels) and TH7890M (512 x 512 pixels) frame transfer CCDs from Atmel, Grenoble, France
- STAR-250 CMOS active pixel sensors (custom designed for ESTEC by FillFactory, Belgium), formerly called the OISL sensor
- IRIS2 CMOS active pixel sensors from FillFactory (for heavy ion testing only).

In addition a CMOS CCD driver chip (Elantec EL7457C) was tested for single event latch up in connection with the ALADIN instrument on ADM-AEOLUS.

CCD samples were available from ESA as part of its manufacturer capability approval programme and APS samples as part of Fillfactory device development contracts to ESA. In the case of the e2v CCD57-10, additional samples were procured as part of this contract in order to have enough samples for both cobalt60 and proton irradiations.

The CCDs were irradiated with either cobalt60 gamma rays or protons of energy 9.5 and 60 MeV. The STAR-250 APS devices were given cobalt60 or 9.5 MeV protons. Two devices were tested for single event effects by irradiating with heavy ions. The two IRIS-2 samples were only given a heavy ion test for single event latch-up (SEL).

The work included the design of 'personality' boards for each device to be tested as well as a dedicated 'APS irradiiation bias' board which was used during the cobalt60 and heavy ion irradiations of the active pixel sensors.

For some measurements, special techniques had to be developed (or existing ones refined) in order to measure important parameters. This was the case for measurements of charge transfer inefficiency (CTI) and random telegraph signals (RTS) for CCDs and single event effects for the APS devices. In addition, the variation of dark current and image lag with photodiode bias and the changes in photo-responsivity were new effects which had to be investigated for the STAR-250.

1.1 REFERENCE DOCUMEMTS

[1] Final Report on ESA Contract CCN3 to 12227/96/NL/SB, ‘Radiation Testing of 2-D Imaging Detectors and ADCs for Attitude Sensors’, June 2000.

[2] Final Report on ESA Contract Rider 1 to 9557/91/NL/LC(SC), ‘CCD Radiation Damage Study’, April 1995.

[3] I. H. Hopkins and G. R. Hopkinson, “Random telegraph signals from proton-irradiated CCDs”, IEEE Trans. on Nucl. Sci., vol. 40, no. 6, pp. 1567 -1574, Dec. 1993.

[4] J. Bogaerts. B. Dierickx, and G. Mertens, “Random telegraph signals in a radiation-hardened CMOS active pixel sensor”, IEEE Trans. on Nucl. Sci., vol. 49, no. 1, pp 249-257, Feb. 2002.

[5] J. R. Srour and D. H. Lo, "Universal damage factor for radiation-induced dark current in silicon devices", IEEE Trans. on Nucl. Sci., vol. 47, no. 6, pp 2451-2459, Dec. 2000.

[6] A. Akkerman, J. Barak, M. B. Chadwick, J. Levinson, M. Murat and Y. Lifshitz, "updated NIEL calculations for estimating the damage induced by particles and gamma rays in Si and GaAs", Radiation Physics and Chemistry, vol. 62, pp. 301-310, 2001.

[7] J. Bogaerts. B. Dierickx, G. Mertens and D. Uwaerts, “Total dose and displacement damage effects in a hardened CMOS APS”, IEEE Trans. Electron Devices vol. 50, no. 1, pp 84-90, Jan. 2003.

[8] J. Bogaerts, ‘Total dose irradiation test report’, WP 3.3 of contract 13716/NL/FM(SC), Feb1, 2001.

2. TEST OBJECTS

2.1 E2V CCDS

Both the e2v CCD57-10 and CCD55-20 devices operate in frame transfer mode and have 3-phase electrodes. The devices were selected from those made for ESA's Capability Evaluation Programme. Three of each type were made available directly from that program and a further 2-off CCD57-10 devices were purchased from e2v (selected from excess devices made for the programme).

All the devices were fitted with a temporary window, which was removed for proton irradiation (and then re-fitted afterwards). They all had an aluminium store shield deposited over the storage region.

The CCD57-10s (type number CCD57-10-4-B19) have 512 x 512 image region pixels with pixel size 13 µm x 13 µm and a standard electrode structure (non-IMO). This means that the image and store sections can be clocked in both the forward and backwards directions. Other features are:

- front illuminated
- dump gate
- antibloomed
- split readout register. The two halves of the CCD can be readout through separate amplifiers

The device type numbers and allocations were as follows:

CCD57-10 e2v serial number (batch - wafer- die)	Sira number	Allocation
9311-12-18	1	10 and 60 MeV protons
9311-12-12	2	10 and 60 MeV protons
9311-09-09	3	Cobalt60, biased
9311-17-01	4	Cobalt60, unbiased + biased
9311-12-14	5	10 MeV protons

The CCD57-10s were operated with a line move time of 4 µs and a pixel time of 1 µs.

The CCD55-20 (type CCD55-20-4-B18) has 730 x 576 image region pixels with pixel size 22.5 µm x 22.5 µm and an electrode structure for advanced inverted mode operation (AIMO). This means that the image and store sections can only be clocked in the forward direction. In this case there is a single readout register (and amplifier).

Other features are:

- back illuminated
- non-antibloomed
- dump gate

The device type numbers and allocations were as follows:

CCD55-20 e2v serial number (batch - wafer- die)	Sira number	Allocation
9402-13-11	1	Cobalt60, biased
9402-13-09	2	Destroyed in transit to PSI
9402-13-10	3	10 and 60 MeV protons

The CCD55-20s were operated with a line move time of 12 µs and a pixel time of 1 µs.

2.2 ATMEL CCDS

Both the Atmel TH7863D and TH7890M devices operate in frame transfer mode and have 4-phase image and storage region electrodes (2-phase for the readout register). They have a single output amplifier and no dump gate. The image and storage regions can be clocked in either direction. The devices were non-antibloomed. The devices were selected from those made for ESA's Capability Evaluation Programme. Three TH7863Ds and six TH7890Ms were provided.

All the TH7863D devices and two of the TH7890s were fitted with a temporary window which was removed for proton irradiation. The windows on the other TH7890M devices were removed mechanically and re-attached with tape to form a temporary window.

The TH7863Ds have a metallized storeshield deposited on the storage region. The TH7890Ms had an external metal store shield which was glued above the CCD as part of the package. However a technique has been developed so that this shield could be removed for proton irradiation (being replaced for characterisation with a taped window).

The TH7863Ds have 288 x 384 image region pixels with pixel size 23 µm x 23 µm without a supplementary buried channel. The CCDs had a standard electrode structure (non-MPP).

Two of the three devices are marked on the underside with a code 9814. The CCDs were hand marked in pencil on the underside with chip identification numbers. The three identification numbers were 2, 3 and 5.

The TH7890M has 512 x 512 image region pixels with pixel size 17 µm x 17 µm without a supplementary buried channel. The CCDs have an electrode structure for MPP mode (equivalent to IMO mode for e2v devices). Figure 2-1 is a photograph of the device (taken from the Atmel datasheet).

The two devices with a temporary store shield were hand marked in pencil on the underside with numbers 09 and 10 but were otherwise unmarked. The four devices with a glued window had a code 0026 and a part number TH7890MVRRUB on the window and a chip identification number. The four identification numbers were 9, 11, 24 and 29.

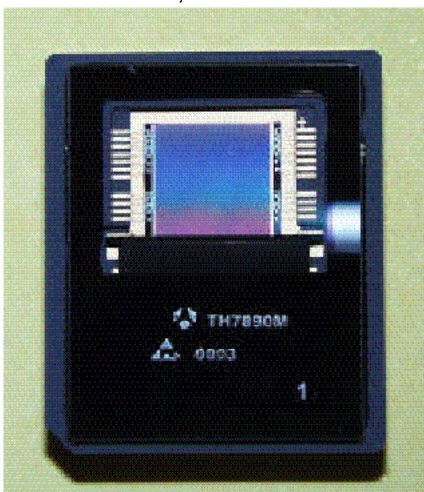

Figure 2-1 Photograph of the TH7890M

As with the e2v CCD57-10, the TH7863D and TH7890Ms were operated with a line move time of 4 µs and a pixel time of 1 µs.

The device type numbers and allocations were as follows:

TH7863D Atmel number	Sira number	Allocation
2	1	Cobalt60, biased
5	2	Cobalt60, un-biased
3	3	10 MeV protons

TH7890M Atmel number	Sira number	Allocation
	1	10 and 60 MeV protons
29	2	10 and 60 MeV protons
9	4	Cobalt60, biased
11	5	Cobalt60, biased
24	3	10 MeV protons
	6	10 MeV protons

2.3 STAR-250 CMOS ACTIVE PIXEL SENSOR

The STAR-250 APS chip from FillFactory, Belgium is a radiation-tolerant version of the ASCoSS sensor. Special features are:

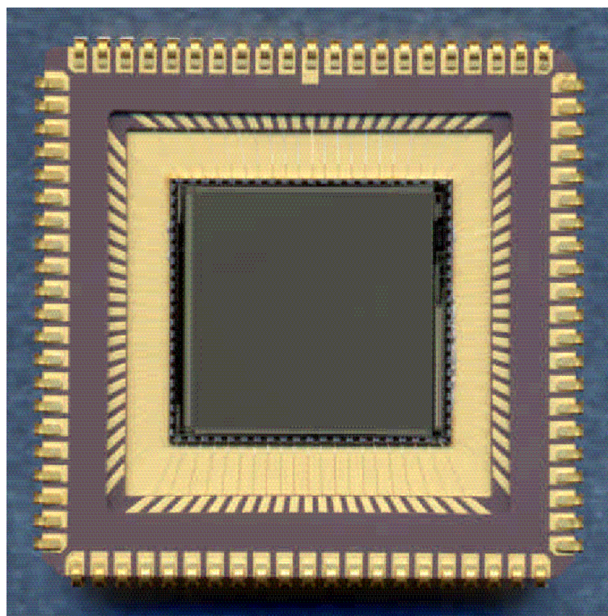

- Integrating APS
- 0.5 µm CMOS technology
- 512 by 512 pixels on 25 µm pitch
- 4 diodes per pixel for improved MTF & PRNU
- Radiation tolerant design
- On-chip double sampling circuit to cancel Fixed Pattern Noise
- Electronic shutter (ability to have short integration times, in multiples of the line readout time)
- Pixel rate up to 5 MHz.
- Region of Interest (ROI) windowing through pre-settable start point of read-out
- Switchable gains for the output amplifier (nominally x1, x2, x4, x8)
- On-chip 10-bit ADC
- Power consumption < 350 mW
- Ceramic JLCC-84 package

Figure 2-2 photograph of the STAR-250 APS device (from the data sheet).

9 devices were available. The glued windows could be removed mechanically and re-attached with tape for temporary use. The devices were hand marked in pencil on the underside with identification numbers; 1, 2, 7, 8, 12, 13, 14, T5 and T9.

The devices were operated at 5 MHz rate pixel rate (the fastest possible with the internal ADC).

The device type numbers and allocations were as follows:

STAR-250, Fillfactory number	Sira number	Allocation
12	1	Cobalt60, biased
8	2	Cobalt60, biased
1	3	Cobalt60, biased
13	4	Cobalt60, un-biased
T5	5	10 MeV protons
14	6	10 MeV protons
2	7	Heavy ion
T9	8	Heavy ion
7	9	spare

2.4 IRIS2 CMOS ACTIVE PIXEL SENSOR

The IRIS2 device from FillFactory, Belgium is a complete 'camera-on-a chip' and requires only a 5V power supply and master clock for operation. Figure 2-3 shows a block diagram of the device. It is produced using the same design rules as the earlier ASCoSS sensor and so was not expected to be particularly radiation tolerant.

The device has 640 x 480 pixels on a 14 µm pitch. The maximum pixel rate is 3.125 MHz. The IRIS2 accepts user commands via either one of two serial command inputs: one interface is asynchronous and compatible with the RS-232/RS-422 standard. The other serial command input is synchronous (data bits and bit clock separated) and complies with PacketWire (see IRIS2 data sheet for further details and references).

The 8-bit image data from the internal flash ADC (and also housekeeping data) are output using one of three output interfaces. There are two serial output interfaces, one asynchronous, the other synchronous and there is one synchronous 8-bit parallel output interface. Both synchronous outputs are compatible with PacketWire; the parallel output is compatible with the PRDC Rice data compressor and with the TEMIC 62700-series of FIFOs .

Additionally, a frame-grabber style digital output can be selected. This features a parallel image data output and frame, line and pixel sync signals.

There is also a buffered analogue output for connection to an external video chain.

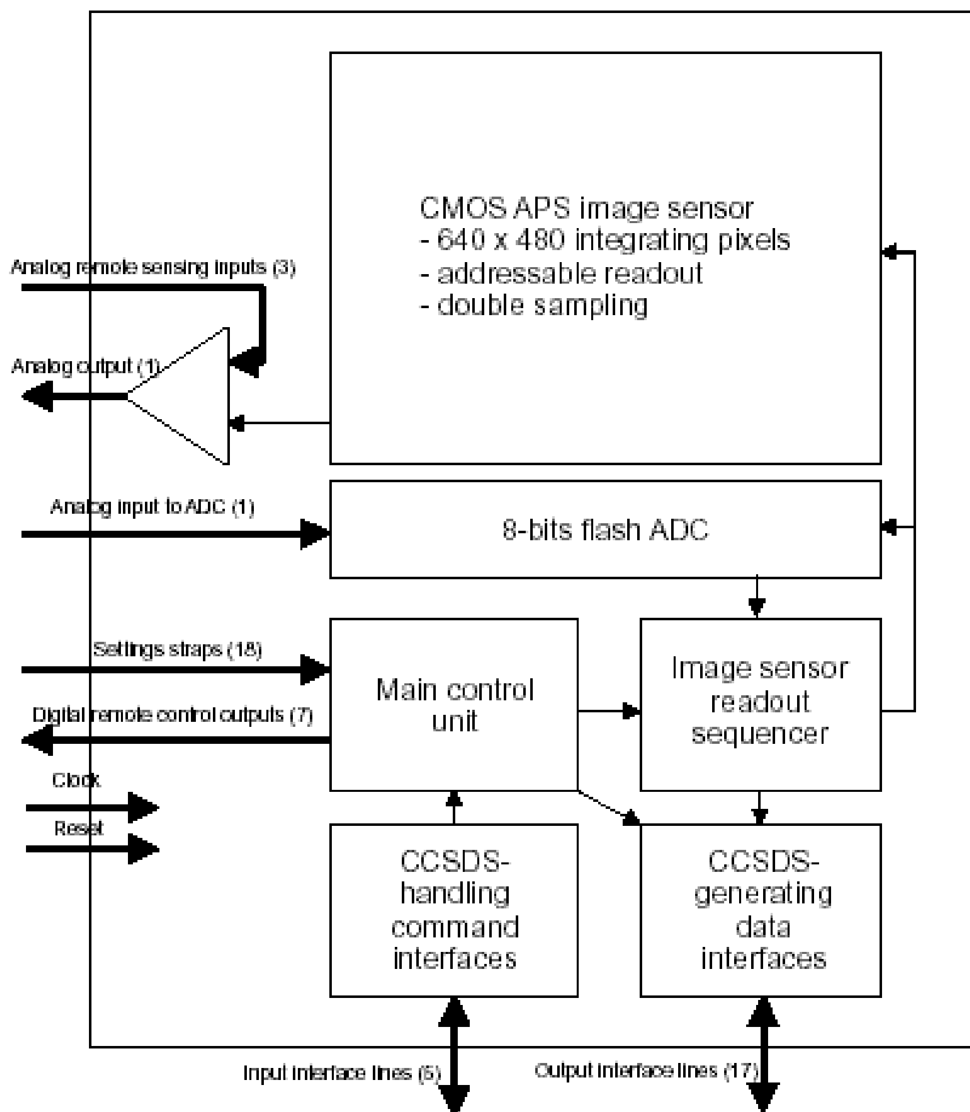

Figure 2-3 Block diagram of the IRIS2 APS

Three devices were available for testing. The glued windows were removed mechanically and re-attached with tape for temporary use. The devices were hand marked in pencil on the underside with identification numbers : 106V, 115V and 101V. The 106V and 115V devices were heavy ion tested for latch-up only and 101V kept as an un-irradiated spare.

3. TEST EQUIPMENT

3.1 CCD AND APS CHARACTERIZATION

Figure 3-1 shows a block diagram of the device characterisation system used for detailed device testing before and after proton and cobalt60 irradiation. This is based around the Sira Universal Camera, which is a programmable bias/clock generator, which has been used in several previous evaluations. The video board has been recently upgraded for ESA to include two video channels each with a choice of 14- or 16-bit ADC and a choice of integrating or clamp-and-sample correlated double sampling (CDS). The minimum pixel rate was 1 MHz and so only the clamp-and-sample CDS was used.

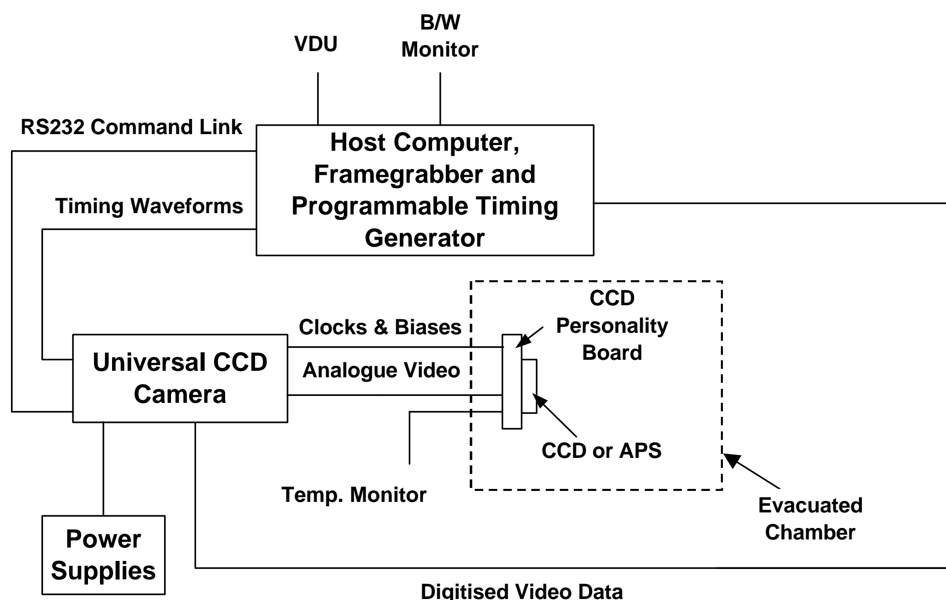

Figure 3-1 Block diagram of sensor characterisation system

The data acquisition system was also upgraded and now includes a 16-bit Phoenix framegrabber (from Datacell, UK) and ImagePro Plus image analysis software (callable from Agilent Vee Pro software for general instrument control and writing of automated test sequences). Image Pro plus macro scripts were written for tasks such as image averaging, dumping statistics of areas of interest to file, capturing of image sequences and RTS data collection. Vee Pro functions were written for linearity testing and measurement of CTI (and trap emission times) and dark current versus substrate voltage. Only for one test, the measurement of APS on-chip ADC differential nonlinearity, was the 'old' Imaging Technology VS100 12-bit framegrabber used.

Each of the devices to be tested (CCD55-20, CCD57-10, TH7863D, TH7890 or STAR-250 APS) was mounted on a dedicated personality board and copper heatsink. This could be mounted either directly to the universal camera electronics (for ‘uncontrolled' room temperature testing) or inside an evacuated Oxford Instrument MM1815 LN2 dewar for cold testing (and at room temperature when temperature control was needed). The heatsink on the personality card was not connected directly to the LN2 tank but was held a few cm away by aluminium spacer rods. A heater on the heatsink was connected to a Melcor MTCA series temperature

controller. This arrangement allowed control of the CCD temperature to ~ ±0.1°C over the range -120 to 30°C.

For the STAR-250 APS, either the analogue output was connected to the universal camera video board (as in the CCD case) or the framegrabber cable was connected directly to a connector on the daughter board which outputs the digitised data from the on-chip ADC, together with frame, line and pixel syncs which are generated by the programmable timing generator. (An external 5V, 0.5A supply was used to power the line drivers for the cable.) In the on-chip ADC configuration the daughter board could not be placed in the evacuated chamber, but this mode was only needed for on-chip ADC testing which was done at room temperature. **Note: for APS testing, the universal camera video board has to be configured by shorting the input AC coupling capacitors (links are available on the board).**

During cobalt60 irradiations the CCD daughter boards were used for individual irradiations of biased devices (only one of each device type needed to be irradiated). In this case a long ribbon cable was used to connect the daughter board to the universal camera. For proton irradiations the CCDs were unbiased and mounted on a shorted pcb.

3.2 APS IRRADIATION BOARD

The APS irradiation board (figure 3-2) was designed to bias the STAR-250 and IRIS2 devices during heavy ion testing (individual devices) and for simultaneous cobalt60 testing of up to 6 biased STAR-250 devices.

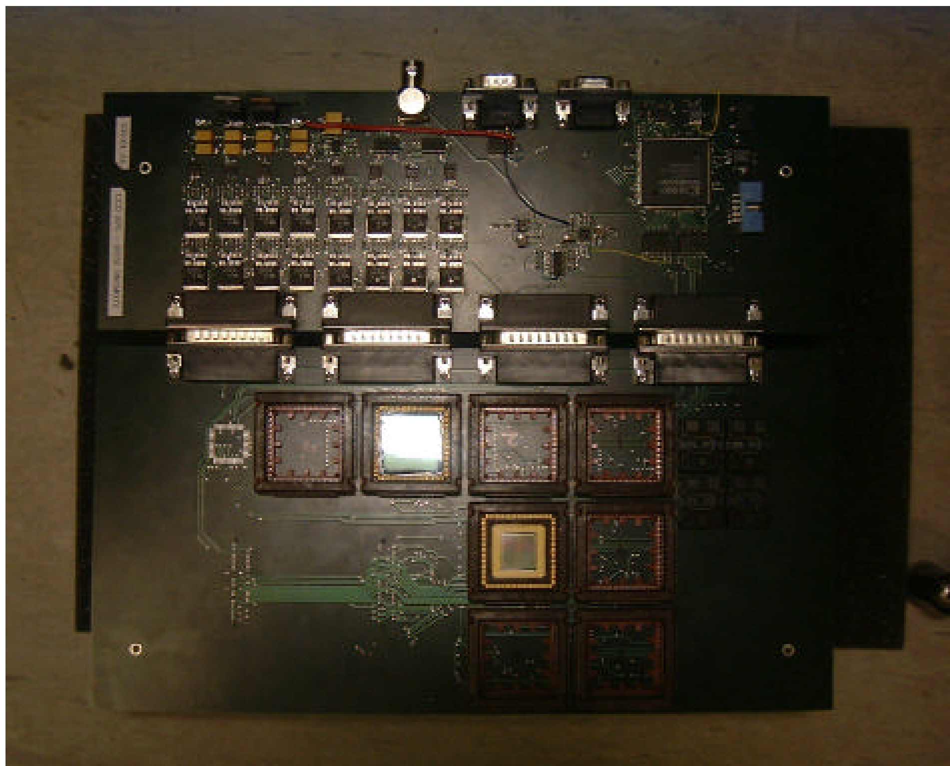

Figure 3-2 Photograph of APS irradiation board

The power supplies to each device could be separately switched on and off via commands from a host PC (relayed via an RS232 link). This enabled some devices to be unbiased for cobalt60 irradiation (but switched on for monitoring of supply currents) and individual device power-on during heavy ion irradiation. The supply currents to the devices were limited by series resistors. The supply voltage to a device was continuously monitored during heavy ion irradiation so that if the current increased due to latch-up (and the supply voltage dropped) then this could be detected. When latch up was detected the power was automatically cycled and the running total of power cycle events and the voltages and currents were dumped to a file. Monitoring of voltages and currents was also performed during cobalt60 irradiation and data dumped automatically to a file at a user-defined sampling interval. Two sequences were used: one kept all 6 STAR-250 devices biased and monitored and one only monitored 4 STAR-250 devices, leaving the other 2 unbiased. Note that there are 2 supplies for each STAR-250, one for the sensor and one for the on-chip ADC. In this way any latch-up in the two parts of the device could be separately detected.

The APS devices were clocked at a frame rate of approximately 50Hz in full frame (non-windowed) mode with DC bias levels as specified in the manufacturer's data sheet.

There were also sockets to enable latch-up and cobalt60 testing of Elantec EL7457C quad CCD driver chips for ESA's Aladin programme (not part of this study).

For heavy ion testing all the devices to be tested (2 x STAR-250 and 2 x IRIS2) were positioned in a horizontal row along the centre of the board and to position the beam over individual devices.

The irradiation board was made in three parts:

- the device board, which has sockets for the devices under test,
- an interface board with a Xilinx Spartan chip for generating the APS clocking waveforms, for handling the RS232 link with the host PC and for multiplexing and monitoring of video outputs and power supply currents. This board was connected to the device board via 50cm ribbon cables (so that the interface board could be shielded from cobalt60 radiation).
- small 'piggy back' board, used only during heavy ion testing, which had a second Xilinx Spartan FPGA to perform histogramming of the Star-250 on-chip ADC data.

There was a facility to switch any one of the STAR-250 APS outputs to a BNC video output connector. The video waveform was mixed with a line sync. so as to form a waveform which gave an image on a TV monitor (which could be recorded on a VCR). This allowed monitoring of functional interrupts in the sensor shift registers. The on-chip ADC was not connected to the video output but instead to a programmable voltage input (from a 16-bit DAC). This allowed monitoring of single event effects in the ADC for a constant input voltage. It was expected that heavy ions would simply produce a widened output histogram due to transient 'noise' but, in case large bit errors were produced, there was the facility to record a separate histogram for those events which were a set threshold away from the main peak (with a power cycle for 'lingering errors', i.e. if there were 10 consecutive readings displaced from the main peak).

4. IRRADIATIONS

The irradiations are summarized in table 4-1 and the dose/fluence levels in table 4-2. Further details are given below. Figure 4.1-1 shows the proposed masking configurations. In all cases the dosimetry was carried out by the staff of the irradiation facility and is believed to be accurate to ±5%.

Table 4-1 Chip allocations

	CCD55-20	**CCD57-10**	**TH7863D**	**TH7890M**	**STAR-250 APS**	**IRIS2 APS**
Number available	**2 (1 was damaged and not used)**	**5**	**3**	**6**	**9**	**3**
Cobalt60, biased	1	1	1	1	3	
Cobalt60, un-biased		1	1	1	1	
10 MeV proton		1	1	2	2	
10/60 MeV proton	1	2		2		
Heavy ion					2	2
Control (in-irradiated)	0	0	0	0	1	1

Table 4-1 dose/fluence levels

	CCD55-20	**CCD57-10**	**TH7863D**	**TH7890M**	**STAR-250 APS**
Cobalt60, biased	17.9 krad(Si) one step	18.1 krad(Si) one step	17.9 krad(Si) one step	11.6 krad(Si) one step	79.2 krad(Si) one step
Cobalt60, un-biased		18.1 krad(Si) plus 17.9 krad(Si) biased	17.9 krad(Si) one step	17.9 krad(Si) one step	79.2 krad(Si)
9.5 MeV proton		0, 1, 3, 10, 20 krad(Si)	0, 3, 10, 20 krad(Si)	0, 1, 3, 10, 20 krad(Si)	0, 1, 10, 100 krad(Si)
9.5/60 MeV proton	0, 10 krad(Si) 10 MeV protons ($1.7\ 10^{10}$ p/cm^2) 60 MeV protons: ($5.9\ 10^{10}$ p/cm^2)	0, 10 krad(Si) 10 MeV protons 60 MeV protons: ($5.9\ 10^{10}$ p/cm^2) =8.1 krad(Si)		0, 10 krad(Si) 10 MeV protons 60 MeV protons: ($5.9\ 10^{10}$ p/cm^2)	

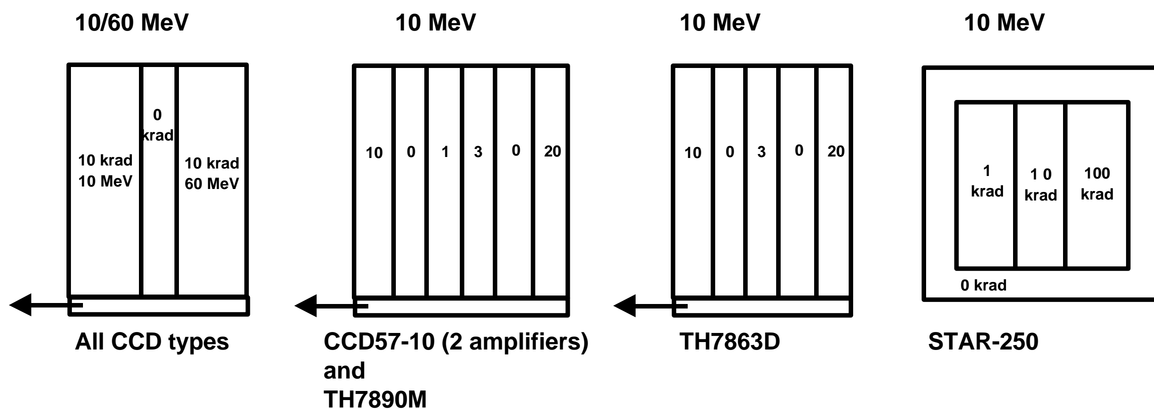

Figure 4.1-1 Masking configurations for proton irradiation.

4.1 COBALT60 IRRADIATIONS

Devices were irradiated with cobalt60 gamma rays at the facility at ESA ESTEC during the period 27-31 May 2002. The dose rate was approximately 1.2 krad/hr and the devices were kept at ambient room temperature. For the Star-250 irradiations the device currents were continually monitored and an image from one device was displayed on a TV screen to check for functionality. The maximum dose on the star-250 devices which could be achieved during the test period was ~ 80 krad(Si), however an additional star-250 device was available to the programme which had previously been irradiated to 5.3 Mrad(Si), with the sensor (but not the ADC) biased. This device was cobalt60 irradiated at room temperature at the J. J. Thomson Irradiation Laboratory of Cranfield University, Shrivenham, UK. The initial dose rate was 20 krad(H_20)/hr (for the first 43.8 hr) increasing to 100 krad(H_20)/hr for the next 45.5 hr and finally 100 krad(H_20)/hr for the final 2.4 hrs – so that the total accumulated dose was 5.3 Mrad(Si). Dosimetry is believed to be accurate to better than 10%. Note that 1 rad(H_20)= 0.896 rad(Si).

4.2 60 MEV PROTON IRRADIATIONS

60 MeV proton irradiations were carried out at PSI, Switzerland during August 2002. It was foreseen to irradiate 2 CCDs of types CCD55-20,CCD57-10 and TH7890M, however one of the CCD55-20 devices was damaged in transit and so was not irradiated. The CCDs were masked by 8 mm bars of stainless steel so that only ~ 1/3 of the CCD columns were irradiated. This left 2/3 free for the subsequent 10 MeV irradiation (see below) thus allowing a comparison of damage for the two proton energies. The CCDs were irradiated unbiased, mounted on a prototype pcb.

It was foreseen to perform the 60 MeV and 10 MeV irradiations to the same displacement damage dose. Taking the latest NIEL values [6], there is a ratio of 3.33 between the NIEL values at the two energies, so to get an equivalent displacement damage dose we have

$$\frac{\text{Fluence of 60 MeV protons}}{\text{Fluence of 10 MeV protons}} = 3.33$$

If we take the older values of Summers et al. (IEEE Transactions on Nuclear Science) then the fluence ratio is 2.24 (a factor 1.5 different). In fact it will be seen that the results suggest that the older NIEL ratio (based on Summers et al.) is more representative for the CCDs tested.

In all the 60 MeV irradiated devices it was found that the shielded region still showed dark current spikes. This is believed to be due to the production of secondary protons and neutrons by interactions of the 60 MeV proton beam with the 8 mm steel shield.

Since only 3 TH7863D devices were available and they have a small area (which is inconvenient for multiple energy irradiations), they were not irradiated at 60 MeV.

4.3 10 MEV PROTON IRRADIATIONS

The '10' MeV proton irradiations were performed at the tandem Van de Graaff accelerator at Ebis Iotron Ltd, Harwell on 9 October 2002. In fact, beam constraints meant that the maximum available energy was 9.51MeV and so the fluence was decreased slightly (for 10 krad(Si) total dose the fluence is 1.7 10^{10}p/cm^2 at 9.51 MeV, compared with 1.8 10^{10} p/cm^2 at 10 MeV). Masking by ~ 1.5 mm aluminium plates was used to achieve several fluence regions on the same device. One device of each of the CCD57, TH7890M and TH7863D was given 9.5 MeV protons to nominally 20, 10, 3, 1 and 0 krad(Si) The 20 and 10 Krad(Si) irradiations were completed successfully but on return to Sira it was found that the fluence for the 3 and 1 krad(Si) irradiations was a factor 10 too low (as estimated from measurements of the average bulk dark signal). The reason for the discrepancy 3krad and 1 krad irradiations giving much lower damage than expected – The test records for the irradiations were re-checked but no discrepancy was found. Hence the reason for the factor 10 is not known at the present time. In the following the affected fluence regions will be described as ~0.1 and ~0.3 krad(Si).

As with the 60 MeV irradiations, the CCDs were irradiated unbiased at room temperature and mounted in shorting connectors. The fluence levels were originally chosen to allow a 1 krad(Si) level for convenient random telegraph signal (RTS) measurements on the larger devices and also fluence levels convenient for CTI measurements (and also representative of a variety of environments). However, as mentioned, above the two lowest 9.5 MeV fluences turned out to be a factor of 10 too low and this had an effect on the RTS measurements.

Similar considerations applied for the STAR-250 except that the device was known to be tolerant to a higher total dose. The APS was masked so that the periphery (including ADC, shift registers and column amplifiers) was shielded and received no irradiation. This was to avoid partial (or stepped) irradiation of the ADC or control circuitry, which might cause subtle effects due to variations in flatband shift. The centre part of the APS was masked to achieve several 1, 10 and 100 krad(Si) fluence regions (1.7 10^9, 1.7 10^{10} and 1.7 10^{11} p/cm^2).

4.4 HEAVY ION TESTS

Heavy ion testing of the CMOS APS devices was performed at the heavy ion facility at Louvain-La-Neuve, Belgium on 21 November 2002. As described in section 3.2, a special irradiation board was constructed to allow biasing of APS devices during heavy ion irradiation and automatic logging of latch-up events, plus monitoring of single event interrupts in the sensor.

The devices were mounted on the centre line of the irradiation board and operated in a dynamic bias condition. During the test the supply voltages and currents were monitored using a Keithley Model 2000 DMM. The voltage supplies have current limiting resistors. The current limit was set to 200mA (the value could be changed by varying the resistance value). If the current increased and the voltage supply dropped and fell below a user-defined threshold then a latch-up event was be flagged and the power cycled (with immediate logging of voltage and current).

5. RESULTS OF CCD TESTING

5.1 MEASUREMENTS OF CONVERSION GAIN

The conversion gain is the calibration factor between CCD signal in electrons and the measured signal in ADC units (ADU). It was measured by exposing the CCDs to soft X-rays from a Cd^{109} radioactive source. This decays to ^{47}Ag giving characteristic X-ray emissions as follows:

$K\alpha$ average energy 22.08 keV
$K\beta$ average energy 25.19 keV

If we assume an electron hole pair is, on average, created for each 3.65 eV energy deposited then the $K\alpha$ and $K\beta$ peaks correspond to signals of 6050 and 6900 electrons, respectively. The value of 3.65 eV changes only slightly with temperature so, even though the CCD was often cooled to reduce dark current non-uniformity, this has a negligible effect on the results.

The electrons/ADU calibrations are given in table 5.1-1 below for the 16-bit ADC operated at 1 MHz pixel rate at the highest gain setting. These values were used throught to convert from ADC units to electrons. In general, values were obtained before and after irradiation. However, after irradiation it was necessary in some cases to adjust the operating voltages in order to accommodate the flatband voltage shift and still obtain acceptable images (see next section). This sometimes led to a decrease in conversion gain.

Table 5.1-1 Values of convertion gain (electrons/ADU, 16 bit, gain 3, 1 MHz pixel rate)

CCD Type	CCD N0.	Comment	Pre-rad electrons/ADU	Post-Rad electrons/ADU
CCD57	1	9.5/60 MeV protons	0.51	0.57
	2	9.5/60 MeV protons	0.51	0.59
	3	Cobalt60 biased	0.51	0.67
	4	Cobalt60 unbiased/biased	0.51	0.71
	5	9.5 MeV protons	0.51	0.67
CCD55	1	Cobalt60, biased	3.00	4.14
	2	Damaged in transit	Not measured	Not measured
	3	9.5/60 MeV protons	2.98	3.90
TH7890M	1	9.5/60 MeV protons	0.63	0.70
	2	9.5/60 MeV protons	0.63	0.66
	4	Cobalt60 biased	0.64	Not measured
	5	Cobalt60 unbiased	0.64	0.66
	3	9.5 MeV protons	Not measured	0.70
	6	9.5 MeV protons	Not measured	0.76
TH7863D	1	Cobalt60 biased	1.53	Not measured
	2	Cobalt60 unbiased	1.51	1.51
	3	9.5 MeV protons	Not measured	1.42

The most convenient way to measure the conversion gain was found to be to record a sequence of, say, 50 X-ray images in frame transfer mode, subtract the dark charge background (if necessary) and then to run an Image Pro Plus macro which searched for events above a defined threshold. Data from these events (and surrounding pixels) was then dumped to file. A plot of the signal (ADU) against event position (column number) is what is often termed a 'stacked line trace' and can be used to pick out by eye the maximum X-ray signals which correspond to single pixel X-ray events (which are not distorted by charge spreading by diffusion to adjacent pixels). A typical plot is shown in figure 5.1-1.

Knowing the electronics gain in V/ADU allows an estimate of the charge to voltage conversion factor.

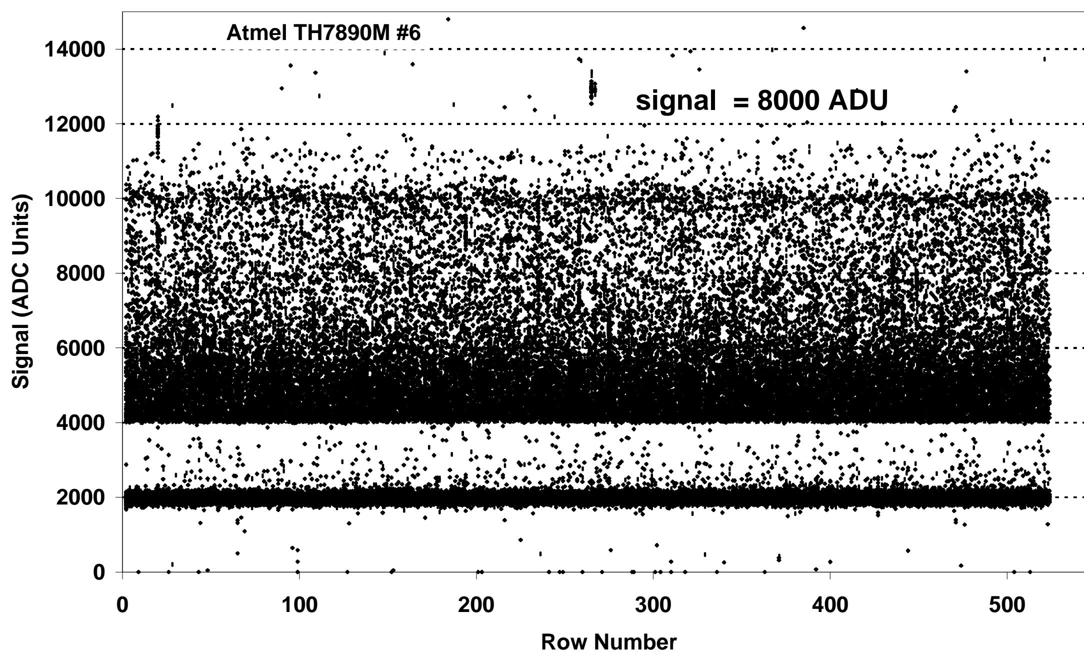

Figure 5.1-1 'Stacked line trace' for Cd^{109} illumination of an Atmel TH890M device after 9.5 MeV proton irradiation, central (unirradiated) part of image.

5.2 MEASUREMENTS OF FLATBAND VOLTAGE SHIFT

Ionization damage causes a build up of charge in the dielectric layer and an increase in the concentration of interface traps. Both effects lead to a change in the effective voltages applied to the CCD. An important parameter is ϕ_{cho}, the channel potential at zero gate voltage. This is around 10 or 11 V for e2v and Atmel CCDs but ***increases*** with total dose. The most important consideration is that charge can be transferred to and readout from the output amplifier. Figure 5.2-1 shows the readout structure of a typical CCD with a single stage amplifier.

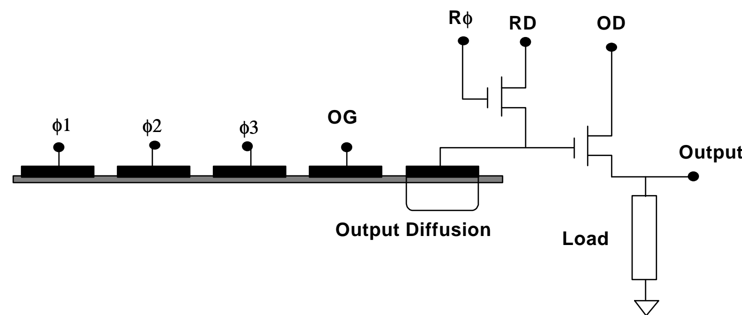

Figure 5.2-1 Readout structure of a typical CCD with a single stage amplifier

There are several 'rules' that must be obeyed for successful readout:

1. The channel potential under the output gate (OG) must be higher than that under the last clocked electrode at its low level, for example:

   $$VOG > \phi R_3(low) + 2\ V$$

2. VRD must be high enough that the output diffusion can accommodate the peak signal swing, for example:

   $$VRD > VOG + \phi_{cho} + V_{signal} + 1\ V$$

3. The reset pulse 'on' level, Rϕ(high) must form a channel of sufficient conductance to reset the output diffusion in a reasonable time, for example:

   $$R\phi(high) > VRD - \phi_{cho} + V_{on}$$

4. The reset pulse 'off' level, Rϕ(low) must be low enough to ensure that charge does not spill into the reset drain, for example:

   $$R\phi(low) < VRD - \phi_{cho} - V_{signal} - 1\ V$$

5. For highest gain (and lowest noise), VOD should be ~ ϕ_{cho} higher than the gate voltage on the output amplifier - and hence VRD, for example:

   $$VOD \sim VRD + \phi_{cho}$$

For pre-rad testing, all the CCDs were operated with manufacturer's 'datasheet' voltages. It was found that the Atmel CCDs did not require voltage adjustments in order to remain operational after irradiation since there was enough voltage margin. With the e2v CCDs it was found that the CCDs were not operational after irradiation and gave a 'blank' image. It was found necessary to reduce the clock low voltages and sometimes VOG by 1 to 2.5 V (depending on the irradiation dose) in order to regain an imaging capability. This is consistent with rule 4 above. Note that with the camera electronics it was not possible to increase VOD since it was already set to its maximum voltage of 30 V and this is probably the reason for the

reduced conversion gain values in table 5.1-1 (the camera electronics could not give a VOD voltage greater than 30 V). The changes needed to maintain device operation are given below:

- CCD57 after cobalt60 irradiation
  - Clock low voltages (I,S and R) changed from 0 V to –2.0 V
  - VOG changed from 3V to 1V
- CCD55 after cobalt60 irradiation (17.9 krad, biased)
  - Clock low voltages (I,S and R) changed from 0 V to –2.5 V
  - VOG changed from 3V to 1V
  - VRD chnged from 17 V to 18 V
- CCD55 after 10 krad 60 MeV protons
  - Clock low voltages (I,S and R) changed from 0 V to –1.0 V

Assuming that a satisfactory image can be obtained at reasonable gain, the only remaining effect of a flatband voltage shift is a change in the voltage at which surface inversion occurs. This 'inversion voltage' is the value of the clock low voltage (relative to substrate) at which the surface dark current starts to decrease rapidly. The shift in inversion voltage is a good measure of the shift in flatband voltage for the CCD. It was measured by plotting dark current versus either image area clock low voltage (for the Atmel CCDs, substrate fixed at 0V) or against substrate voltage (for the e2v CCDs, with clock voltages fixed). Figure 5.2-2 shows typical plots. Values for the flatband voltage shift are summarized in table 5.2-1. Values were not obtained for the TH7863D device since this could not be operated with other than standard (non-inverted) clocks and so an inversion point could not be determined. **Measurements made ~ 6 months after irradiation were the same as the immediate 'post-rad' results – so the effect of annealing was negligible.**

Table 5.2-1 Flatband voltage shift measurements (obtained from shift in inversion point)

CCD Type	CCD No.	Comment	Total Dose krad(Si)	Voltage shift	V /krad(Si)
CCD57	1	9.5/60 MeV protons	8.1 (60 MeV) 10 (10 MeV)	0.35 (60MeV) 0.25 (10MeV)	0.04 0.025
	2	9.5/60 MeV protons	10	-	-
	3	Cobalt60 biased	18.1	2.75	0.152
	4	Cobalt60 unbiased/biased	18.1 (unbiased) + 17.9 (biased)	3.2	0.027 unbiased
	5	9.5 MeV protons (unbiased)	10 20	0.22 0.46	0.022 0.023
CCD55	1	Cobalt60, biased	17.9	2.47 V	0.138
	3	9.5/60 MeV protons	8.1 (60 MeV) 10 (10 MeV)	0.3 V (60 MeV) 0.1 V (10 meV)	0.037 0.01
TH7890M	1	9.5/60 MeV protons	10	Not measured	-
	2	9.5/60 MeV protons	10	Not measured	-
	4	Cobalt60 biased	11.6	1.7	0.147
	5	Cobalt60 unbiased	17.9	0.60	0.033
	3	9.5 MeV protons	10	Not measured	-
	6	9.5 MeV protons	10/20 krad	0.2/0.42	0.021
TH7863D	1	Cobalt60 biased	17.9	Not measured	-
	2	Cobalt60 unbiased	17.9	Not measured	-
	3	9.5 MeV protons	10	Not measured	-

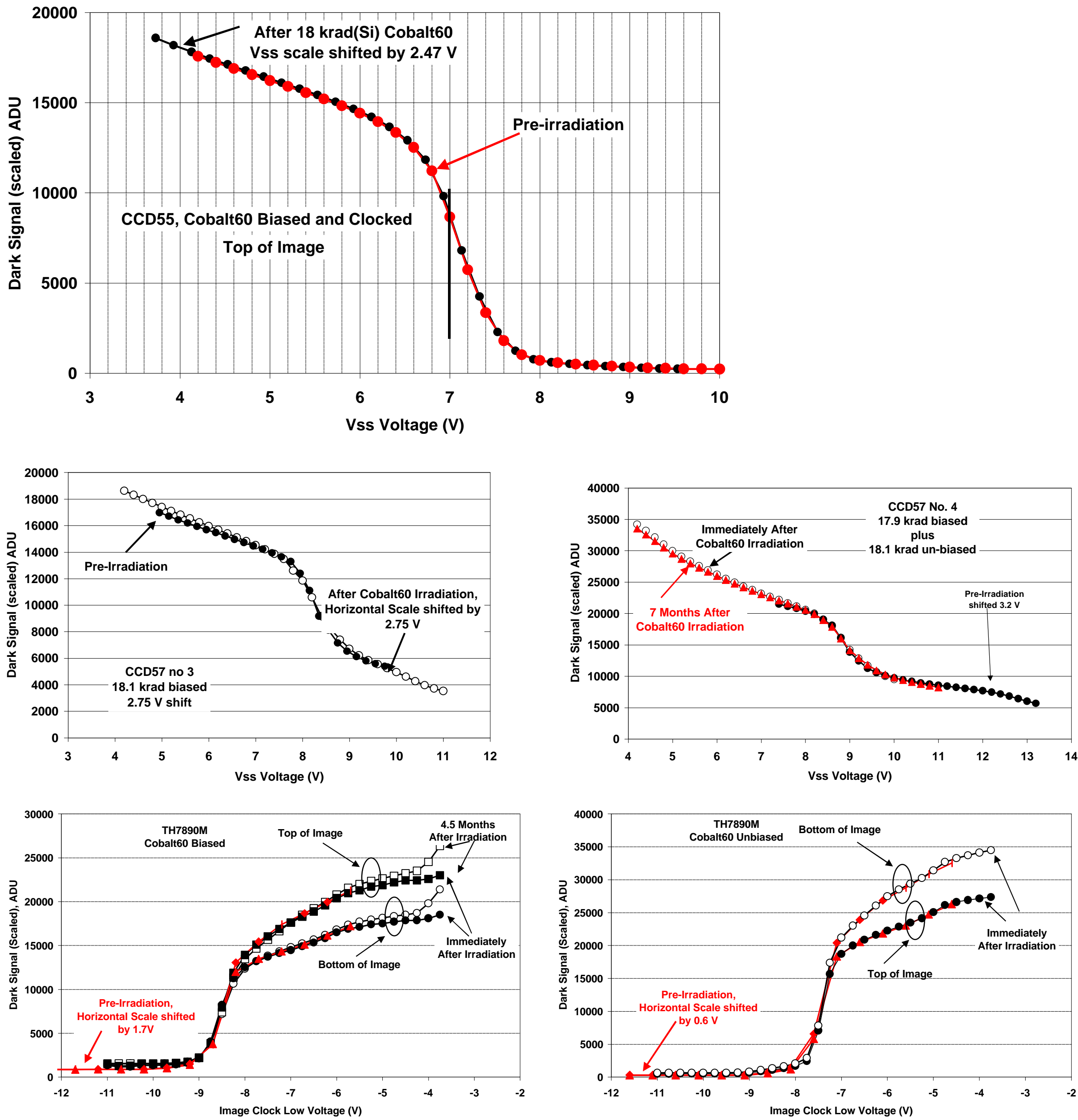

Figure 5.2-2 Plots of dark current versus substrate(Vss) voltage (e2v CCDs) or versus image clock low (TH7890M)

5.3 MEASUREMENTS OF LINEARITY AND FULL WELL CAPACITY

Linearity and full well capacity were measured by applying constant illumination and varying the integration time. An Agillent Vee routine was written to load the timing generator, snap an image and dump the average of three user-defined areas of interest to file. Usually a near-uniform illumination was used but in some cases a spot illumination was also employed. The method of illumination can influence the full well capacity, with spot illumination generally giving a lower value (because surface traps are not kept filled and charge transfer degrades quicker).

Note that the plots do not always pass through the origin. This is because of dark signal which is generated in the storage region during readout (which is not counted as part of the exposure time).

Particularly for the CCD55-20, which is a large device and so a large electrode cvapacitance, it was found that the clock drivers in the present camera electronics did not have enough drive current to give the expected full well capacity for the centre of the image area unless the substrate voltage was reduced (this decreases the capacitance). Figure 5.3-1 shows plots at Vss = 4 V for a proton irradiated device. It is seen that the radiation had no significant effect on the full well capacity. It can also be seen that the full well for uniform illumination is much higher than for spot illumination, as was seen in previous investigations [2]. For spot illumination the full well capacity is ~ 4.6 x 10^5 electrons, which is about 80% of the value from previous investigations [2] on non inverted mode devices. This 80% reduction is in line with expectations for advanced inverted mode CCDs.

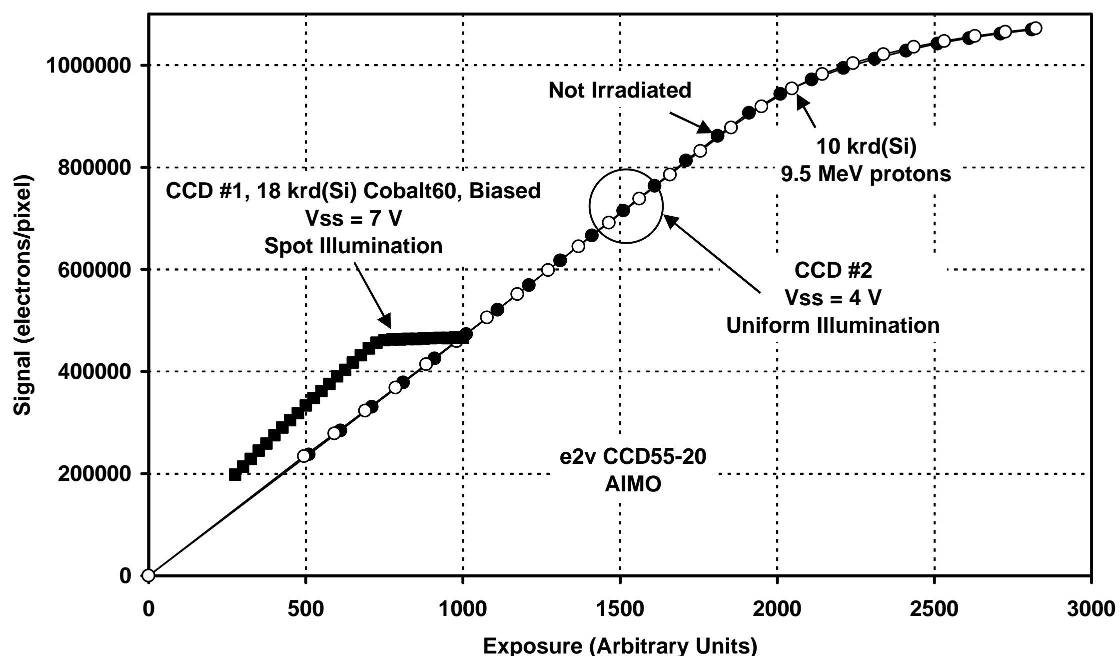

Figure 5.3-1 Linearity plots for CCD55-20 devices

Figure 5.3-2 shows linearity plots for CCD57-10 devices. These were antibloomed devices and it was found that the choice of the antiblooming drain voltage affected the full well capacity (as might be expected). The standard operating voltage is Vabd = 19 V but on some devices this could be decreased to 18V to give a higher saturation level, although with other CCD57-10s this affected the image quality (giving vertical streaks in the image at high signal level). The figure shows plots for two positions in the image for each device and these are seen to give slightly different full well capacities. This is probably due to inadequate drive current in the camera electronics , as discussed above. As for the CCD55-20s, it can be seen that irradiation had little effect on the full well capacity (differences are comparable with the variation over an image).

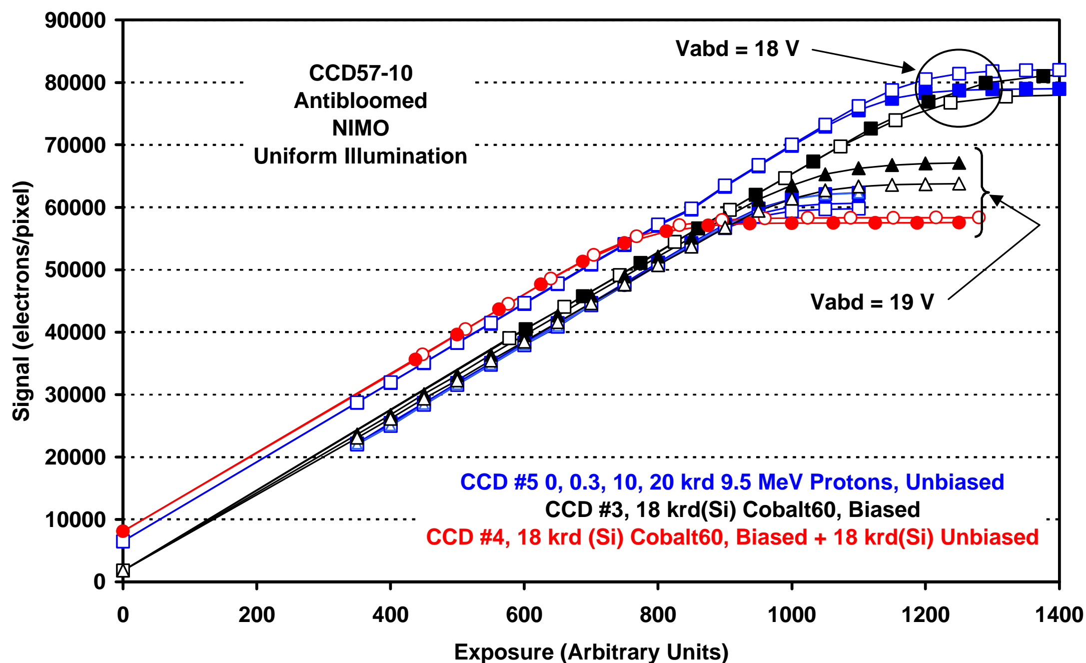

Figure 5.3-2 Linearity plots for CCD57-10 devices

Linearity plots for TH7890M devices are shown in figure 5.3-3 for spot illumination. It is seen that there is no significant change with irradiation. Uniform illumination gave a full well capacity that was higher than the range of the 16-bit ADC, even at the lowest gain.

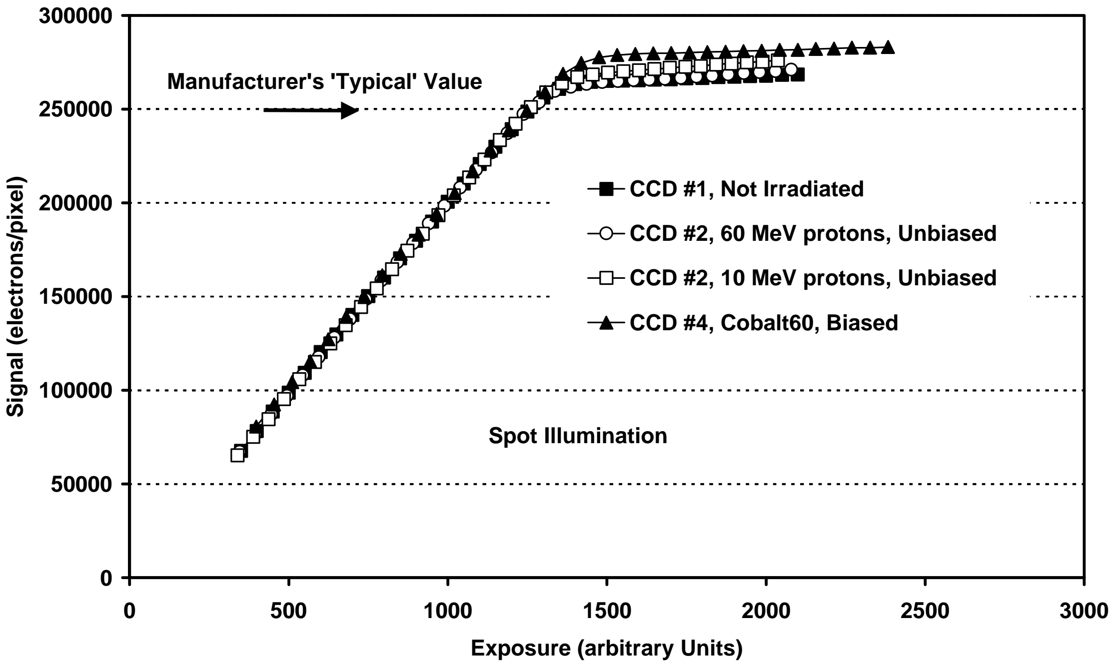

Figure 5.3-3 Linearity plots for TH7890M devices.

For the TH7863D devices (figurte 5.3-4), uniform illumination gave a full well capacity that was higher than the range of the 16-bit ADC, even at the lowest gain, both before and after irradiation. Measurements with spot illumination were not performed, however values are available from previous investigations [2]).

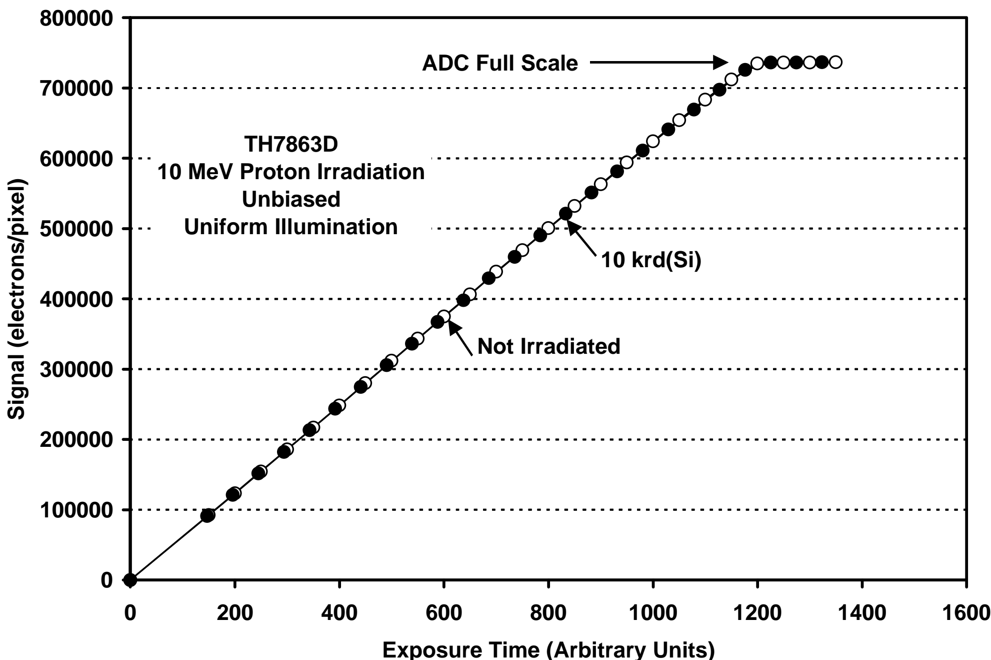

Figure 5.3-4 Linearity plots for TH7863D devices, uniform illumination.

5.4 MEASUREMENTS OF RESPONSIVITY/PRNU

CCDs were illuminated with near flat field illumination from a tungsten lamp under three conditions:

- No filter, broad band illumination
- Green (540 nm, 10 nm bandwidth) filter
- Red (610 nm, 10 nm bandwidth) filter

Changes in responsivity are best assessed with the proton irradiated devices since both irradiated and un-irradiated regions can be measured at the same time. Horizontal profiles across the CCD (averaged over ~ 200 lines) are shown in figures 5.4-1 to 5.4-4 for 10 MeV proton irradiated devices. Discontinuities can be seen at the fluence region boundaries but these are ~ 1% or less (0/20 krad(Si) boundary) and are in any case probably due to CTE effects rather than responsivity changes (the discontinuities are seen to be worse at the bottom of the image).

It is concluded that CCD responsivity is not significantly affected by radiation damage at the level of interest studied here.

Figures 5.4-5 to 5.4-8 show PRNU plots for the same devices (plus, in some cases, cobalt60 irradiated devices). Several features can be noted:

- PRNU is not significantly affected by the radiation damage
- PRNU is worst for the small pixel device (CCD57-10) as expected
- PRNU is worst in the green, as expected since it is then affected by non-uniformities in the electrode structure

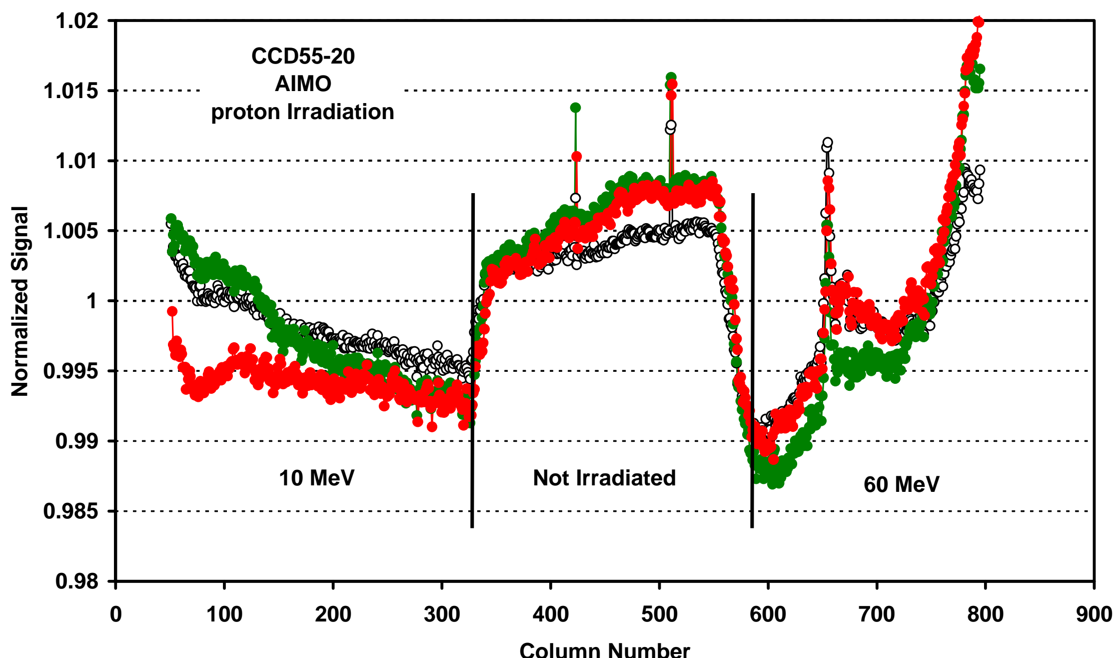

Figure 5.4-1 Thick horizontal profiles for a CCD55-20 device after (unbiased) proton irradiation. The colours indicate the filter used for near-flat field illumination

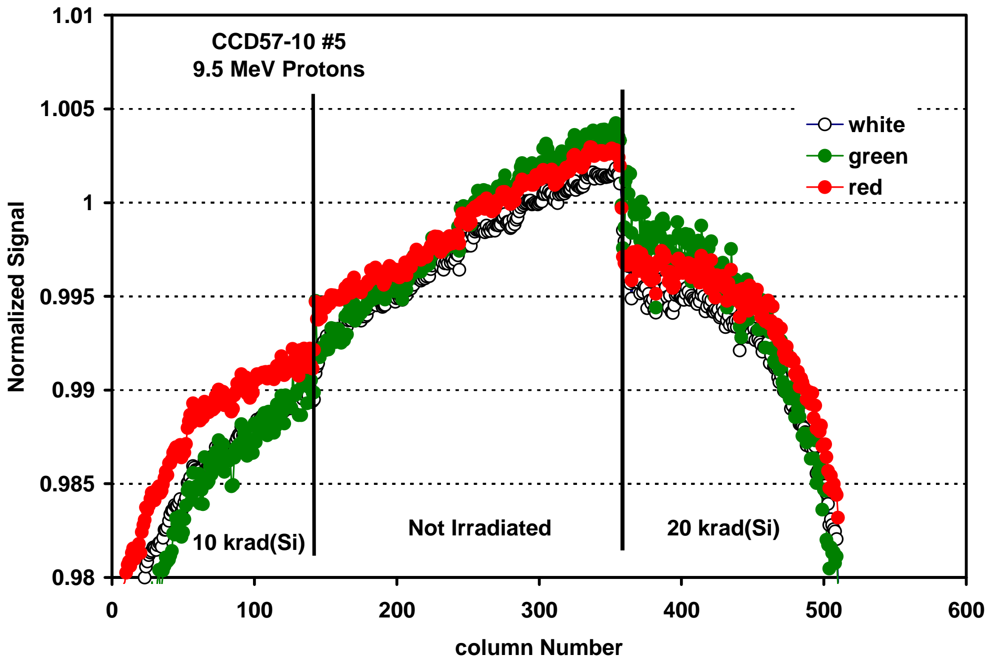

Figure 5.4-2 Thick horizontal profiles for a CCD57-19device after (unbiased) proton irradiation. The colours indicate the filter used for near-flat field illumination

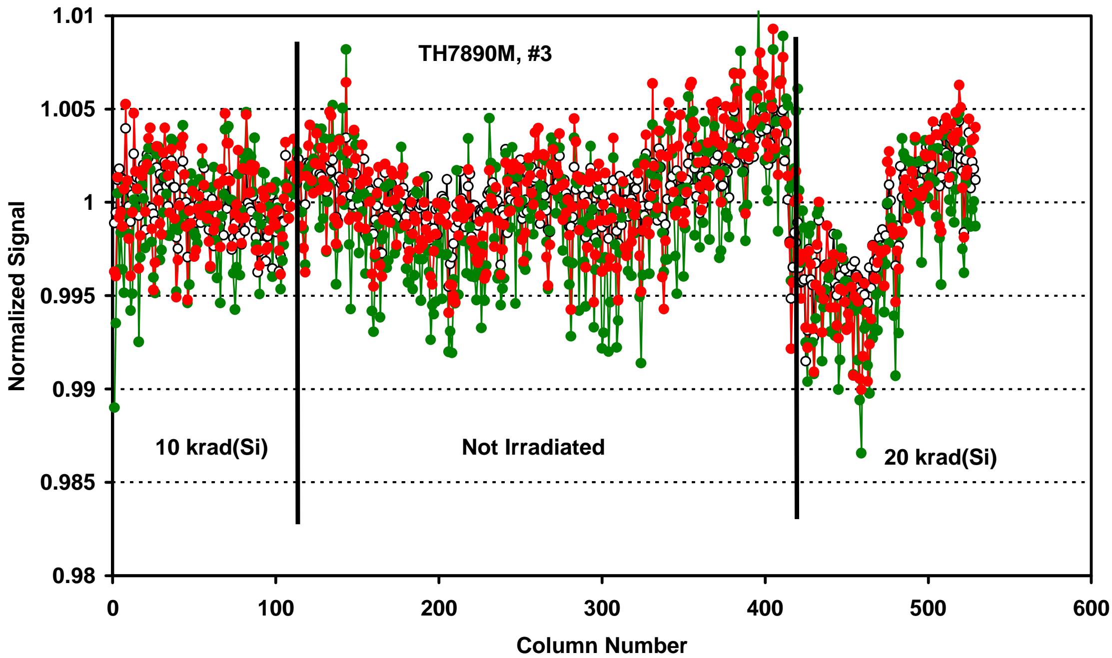

Figure 5.4-3 Thick horizontal profiles for a TH7890M device after (unbiased) proton irradiation. The colours indicate the filter used for near-flat field illumination

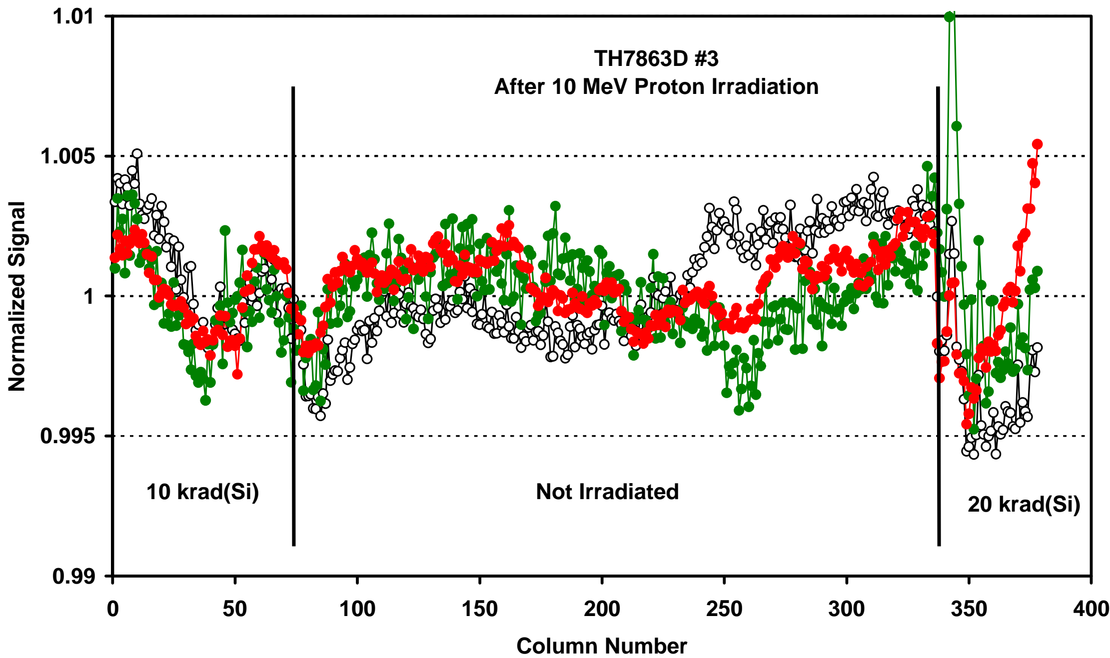

Figure 5.4-4 Thick horizontal profiles for a TH7863D device after (unbiased) proton irradiation. The colours indicate the filter used for near-flat field illumination

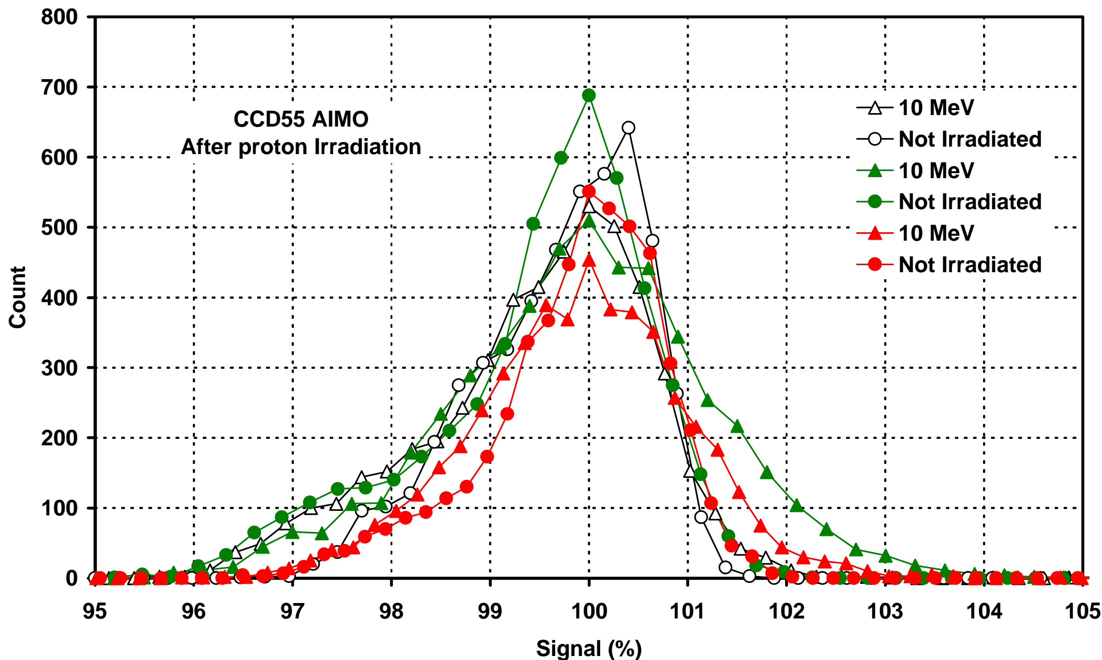

Figure 5.4-5 PRNU results for a CCD55-20 device after (unbiased) proton irradiation. The colours indicate the filter used for near-flat field illumination

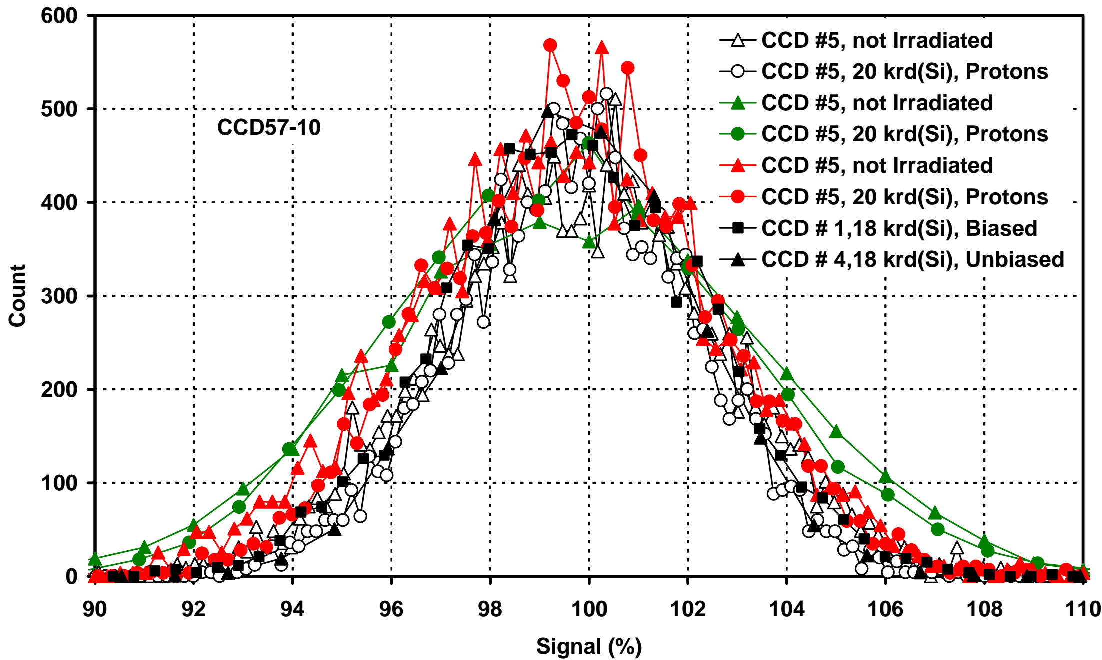

Figure 5.4-6 PRNU results for a CCD57-10 device after (unbiased) proton irradiation. The colours indicate the filter used for near-flat field illumination

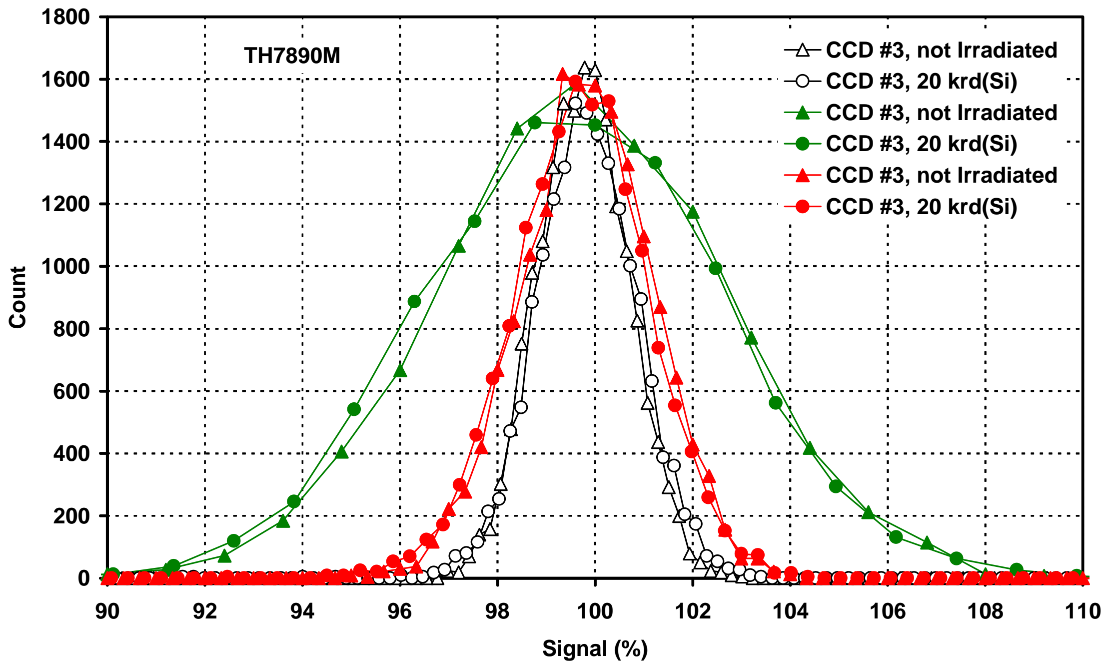

Figure 5.4-7 PRNU results for a TH7890M device after (unbiased) proton irradiation. The colours indicate the filter used for near-flat field illumination

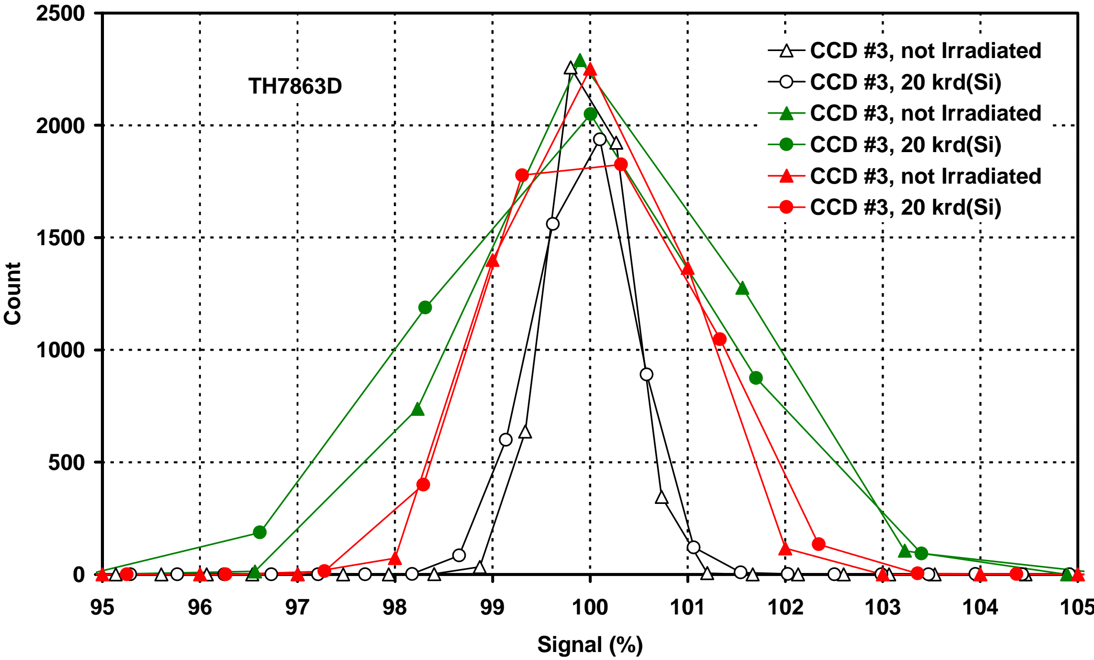

Figure 5.4-8 PRNU results for a TH7863D device after (unbiased) proton irradiation. The colours indicate the filter used for near-flat field illumination

5.5 MEASUREMENTS OF DARK SIGNAL

Measurements were made for each device in darkness from files which were the average of 16 images.

5.5.1 CCD55 Devices

Two devices were available. One (#1) was cobalt60 irradiated to 17.9 krad(Si) and the other (#2) was irradiated with 10 and 60 MeV protons.

Since these are AIMO devices, the surface dark current is suppressed and the effect of cobalt60 irradiation was small for most of the image area. However figure 5.5.1-1 shows that there is a significant dark curent component from the edge of the chip. This seems to come from two components:

- A component coming from the extreme right and left edges of the CCD. This is also seen in CCD57 devices (section 5.5.2) and is believed to be due either to dark current generated in the region outside the active area (where there is a thick field oxide) or to diffusion of a chemical species (e.g. hydrogen) from the field oxide – and subsequent de-passivation of the CCD front surface and increase in interface traps.
- A component associated with the metallized dark reference regions on the back side of the CCD (the side which is optically illuminated) – the dark image has features which line up with the metallizations, though there is some additional spreading inwards (towards the centre of the CCD).

Note that the image has some spots and vertical dark lines – these are due to cosmetic image defects (some overflowed) present when the CCD was delivered.

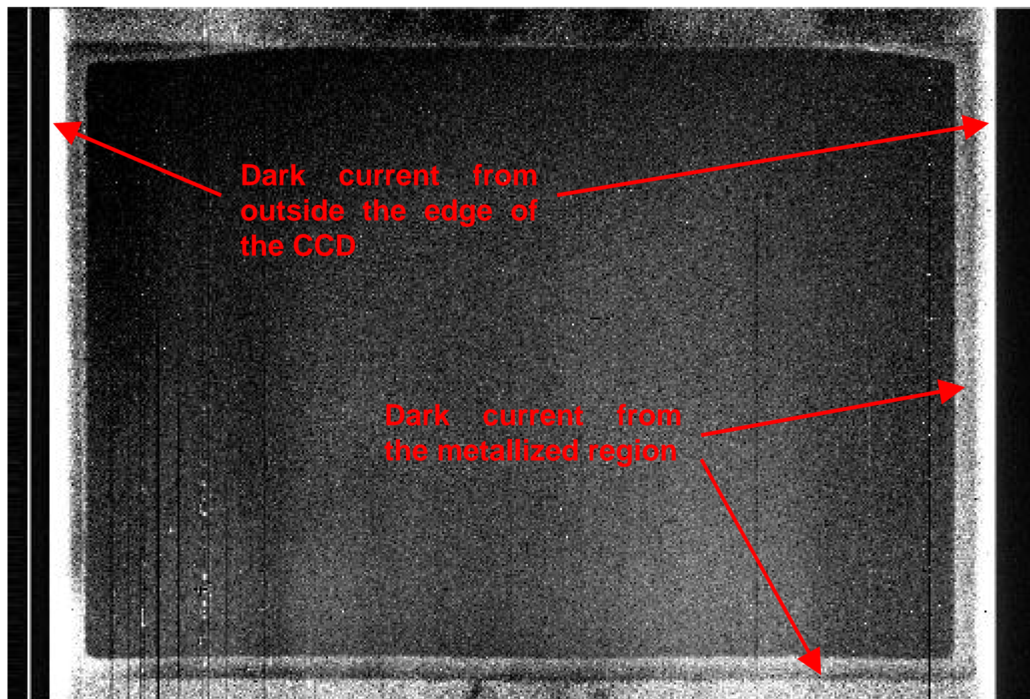

Figure 5.5.1-1 Dark image obtained at 27.6ºC in frame transfer mode for CCD55 #1, 6 months after cobalt60 irradiation to 17.9 krad(Si)

Figure 5.5.1-2 shows a thick horizontal profile (average of 450 rows) across the centre of the figure. It is seen that the dark current at the CCD edges is large. Note that the temperature of the pre-irradiation dark image was not measured accurately and is uncertain to ±1ºC so there is a corresponding uncertainty in the increase in dark current.

Since the image was obtained in frame transfer mode the dark current in figure 5.5.1-2 is the average of both storage and image region components. Vertical profiles show that these are approximately the same (dark current at the top of an image is half that at the bottom with a roughly linear slope in between, hence the image and storage region components are equal). This was the case for the main part of the image as well as the edge components (these had a linear dark slope also). **Note that in figure 5.5.1-2 the dark current is expressed for image region pixels/s and a component will need to be added for the storage region dark current when making predictions.**

The dark signal in the main image area part of figure 5.5.1-1 is slightly uneven – perhaps due to variations in the inversion point.

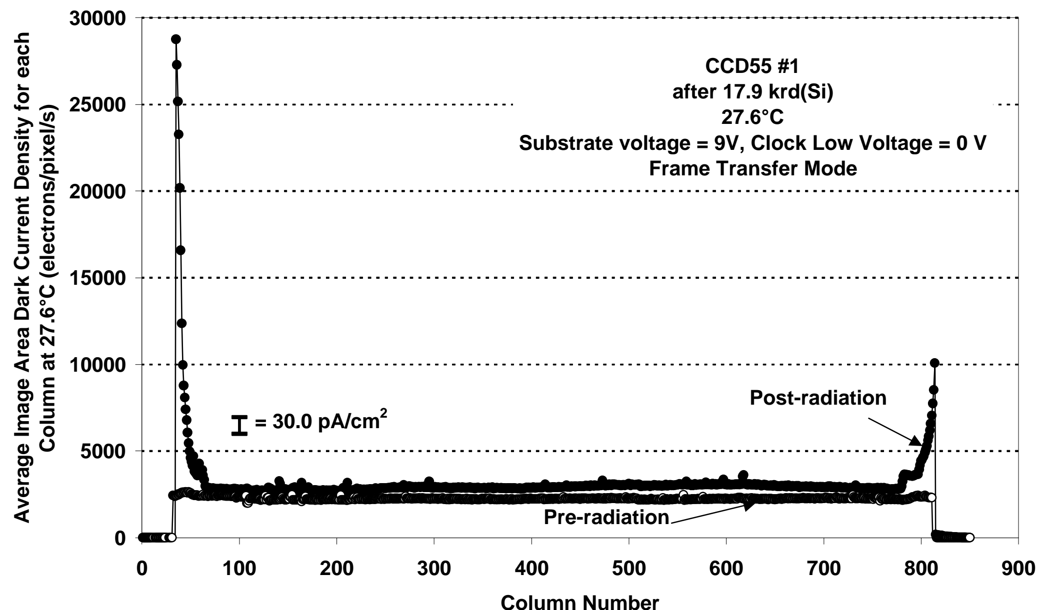

Figure 5.5.1-2 Thick horizontal profile (average of 450 rows) across the centre of the image in figure 5.5.1-1, pre-existing cosmetic white defects have been removed.

Figure 5.5.1-3 shows a dark image for the proton irradiated device. The left side was irradiated with 10 MeV protons (1.7 10^{10} p/cm^2 equivalent to 10 krad) and the right with 60 MeV protons(5.9 10^{10} p/cm^2 equivalent to 8.1 krad). The centre was shielded so that it was not irradiated though, as mentioned in section 4, it received a flux of secondary protons and neutrons during the 60 MeV irradiation. The white column down the centre and the bright white spots are pre-existing cosmetic defects. The image does not show the large dark current at the extreme edge, but only the component, which seems to be associated with the metallization – though the extreme edge component can be seen at low Vss.

Figure 5.5.1-4 shows a horizontal profile (averaged over 450 rows). It can be seen that the 60 MeV irradiation resulted in a substantial horizontal shading in dark current at the edge of the shielding. The cause of this is unknown but may be due to the nature of the back illuminated device since this effect was not seen in the front illuminated CCD57 and TH7890M devices (though there is always a small ‘bump’ at the shield boundary due to secondary particles.

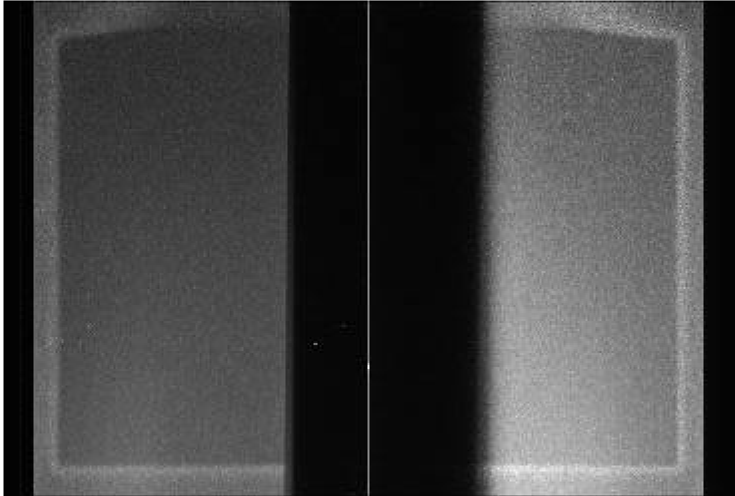

Figure 5.5.1-4 Dark image obtained at 19.9ºC in frame transfer mode for CCD55 #3, after 10 and 60 MeV proton irradiation. The vertical white column was a pre-existing defect.

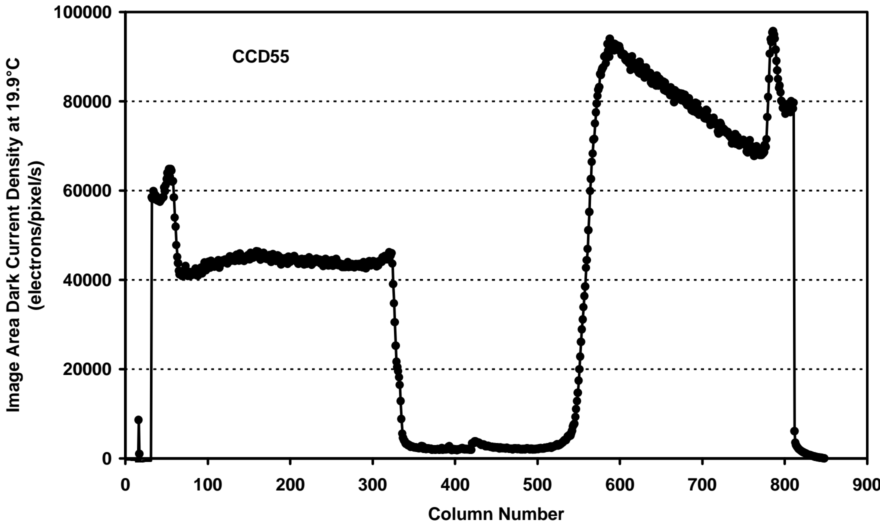

Figure 5.5.1-5 Thick horizontal profile (average of 450 rows) across the centre of the image in figure 5.5.1-4, pre-existing cosmetic white defects have been removed.

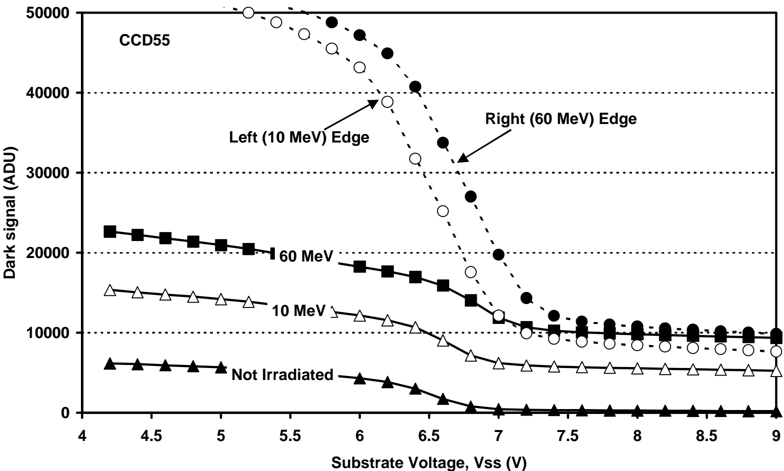

Figure 5.5.1-6 Plots of dark signal versus substrate voltage for CCD55 #3

Additional insight into the nature of the additional edge signal can be gained by investigating the behaviour with substrate voltage and with temperature. Figure 5.5.1-6 shows the variation with Vss. As expected, the 10 MeV and 60 MeV plots are versions of the 0krad curve but offset vertically by a 'constant' level due to bulk displacement damage (bulk dark current does not vary with Vss). The regions at the edge of the chip vary significantly with Vss **– indicating that the edge dark current originates at the CCD surface**. The likely explanation is that hydrogen (or some other chemical species) is released from the back surface metallization and diffuses to the front surface where it increases the density of interface traps. This would explain the diffuse nature of the boundary with the edge region (especially at the corners). Note that other CCD55 devices that have been studied (on other projects) have not shown the edge effect to such a large extent **– hence the effect is probably batch (i.e. process) dependent.**

Figure 5.5.1-7 shows the behaviour with temperature, which, as expected, shows an activation energy of ~ 0.63 eV for all components **– i.e. the edge component is thermal in nature.**

Figure 5.5.1-8 shows dark current histograms at 19.9ºC, after proton irradiation. These have the usual appearance of a main peak and several dark current spikes. The histograms will be broadened due to the nonuniformities in the dark signal but a rough indication of the bulk dark current can be obtained. Note that the above plots all indicate an average vale of 2.0 for the relative signals in the 10 and 60 MeV regions. This allows an estimate of the relative NIEL for average bulk dark current:

CCD55 Relative NIEL for average bulk dark current (10 MeV: 60 MeV protons) = 1.7 ± 0.3

We can also make an estimate of the damage constant:

CCD55 damage constant = 0.13 ± 0.02 nA/cm^2/krad (10MeV protons) at 20ºC
= (3.4 ± 0.7) 10^{5}electrons/cm^3/(MeV/g) at 300K, assuming an active volume of 1500 μm^3 (22.5 μm x 16.5 μm x 4 μm).

These values are slightly higher than expected: ~0.1 nA/cm^2/krad at 20ºC was found in previous Sira studies and Srour [5] gives (1.9 ± 0.6) 10^5 electrons/cm^3/(MeV/g) at 300K, however the present value may include a contribution from ionization damage (the error values quoted above were estimated from measurement and dosimetry errors).

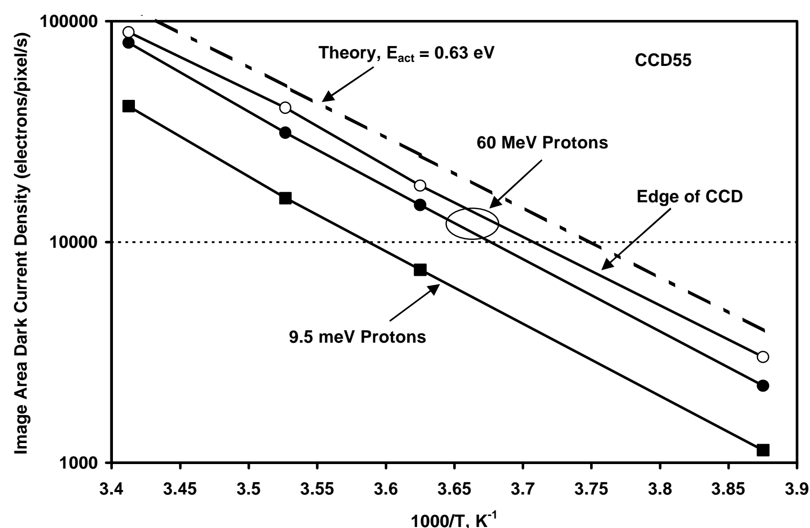

Figure 5.5.1-7 Dark current density versus 1000/T for the 10 MeV and 60 MeV regions and for the right (60 MeV) edge

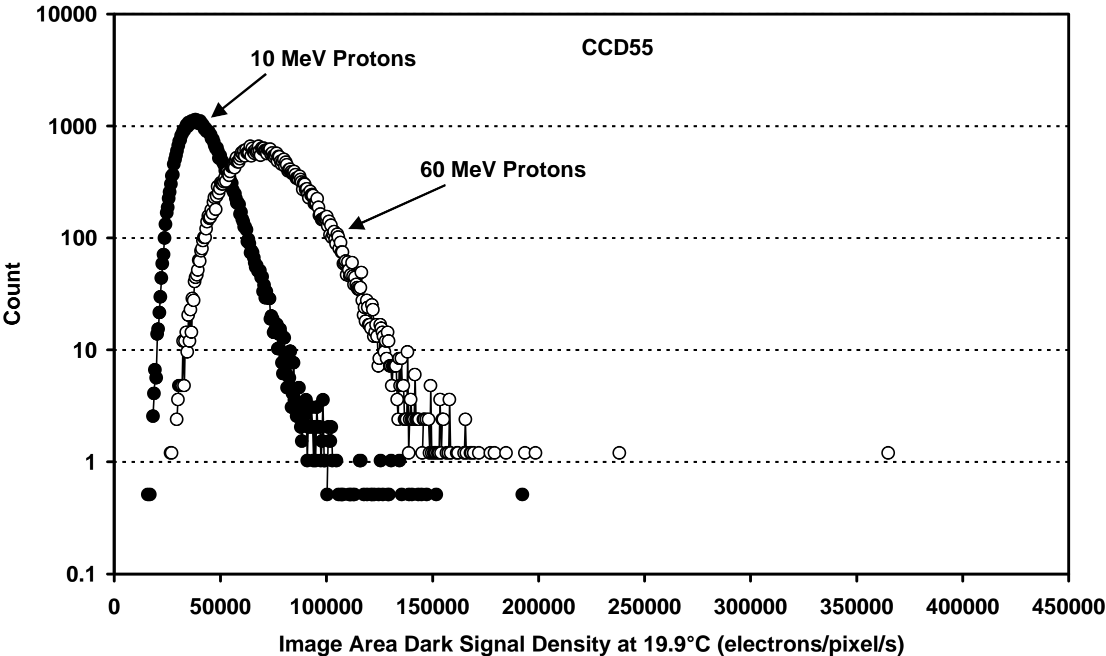

Figure 5.5.1-8 Histograms of the image area dark current density (slope subtracted)

Finally, we show an image obtained in full frame mode. In this the additional dark current from the metallized storage region (and the extreme edge, since Vss is low) can be seen.

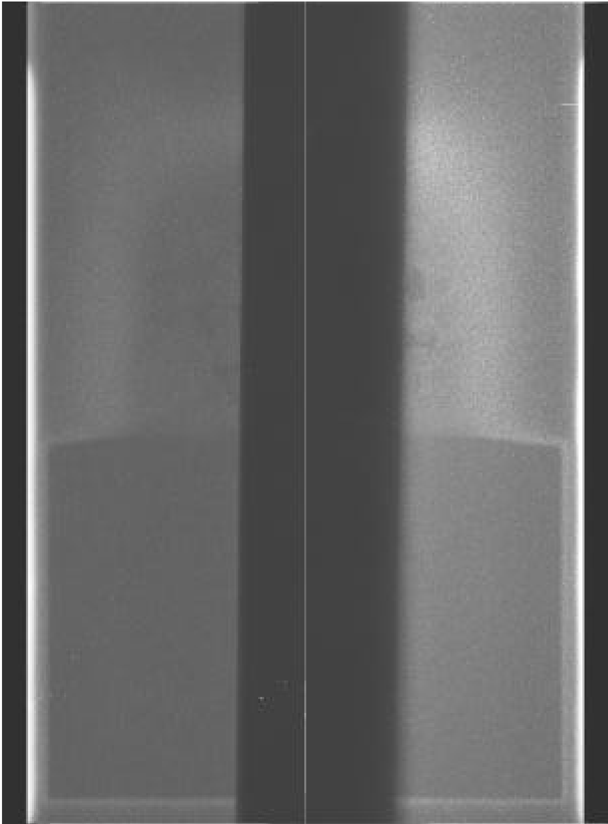

Figure 5.5.1-8 Full frame image from the proton irradiated CCD55 #3, 0.3ºC, 3s integration, Vss = 4.5 V

5.5.2 CCD57 Devices

Unlike the CCD55 devices discussed above, the CCD57s were not inverted mode devices and hence exhibit a large surface dark signal component due to ionization damage. This was reduced as far as possible by integrating under one image clock phase and inverting the others. The variation in dark signal with substrate voltage was shown in figure 5.2-2. The maximum substrate voltages was 9-10 volts (clock low voltages = 0 V). Above this value the vertical charge handling started to degrade.

Figure 5.5.2-1 shows a frame transfer image for CCD57 #3 given a biased cobalt60 irradiation to 18.1 krad(Si). The substrate voltage was 9 V. As with the CCD55, it can be seen that there is an additional component at the extreme left and right edges of the device, though the dark signal from the metallized regions is in this case slightly reduced compared with the main image area. The additional edge component is more pronounced at the bottom of the image because the frame transfer mode gives twice the integration time for the last lines readout. Figures 5.5.2-2 and 5.5.2-3 show thick horizontal and vertical profiles through the image and also for CCD #4 which was given 18 krad both biased and unbiased. For this device the increase in dark signal is higher but this is partly due to the increased flatband voltage shift which takes the device further out of inversion. Probably a better comparison can be made with the CCD #4 image at Vss = 10 V and it can be seen that the increase for the biased and the unbiased devices are comparable (though the unbiased case still probably gives a greater damage).

For a full speed frame transfer image (as in the figures) there is a vertical slope on the dark charge as expected but this is small, presumably because of dynamic dark charge suppression – which happens automatically during readout.

For the image area the increase in dark charge for the biased device is estimated to be given by

CCD 57 (antibloomed version) biased cobalt60 damage = 0.03 nA/cm^2/krad(Si) at 20ºC

This value is significantly lower than previously found for larger pixel devices such as the CCD02 (non-inverted) where ~ 0.5 nA/cm^2/krad(Si) at 20ºC is more typical.

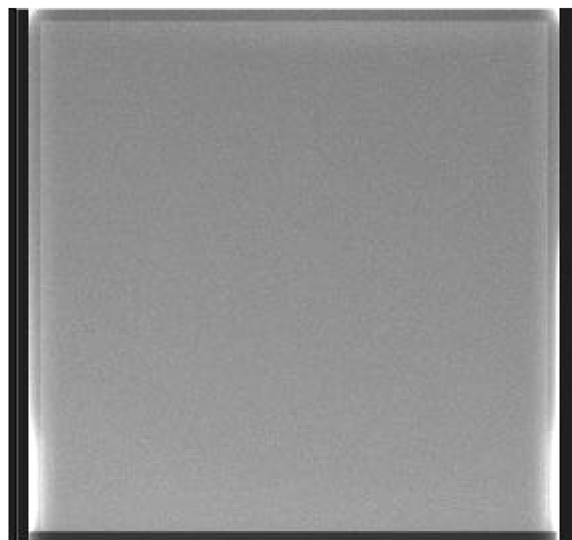

Figure 5.5.2-1 Dark image (full frame, frame time 0.32 s) for 18 krad(Si) irradiated CCD57 #3 at 30ºC

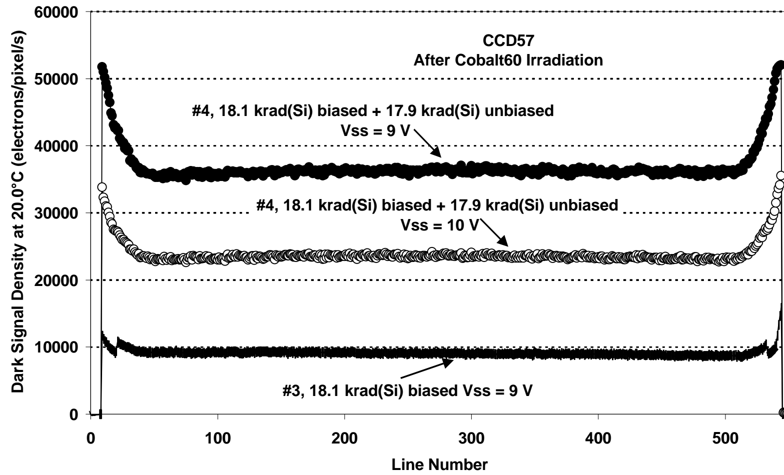

Figure 5.5.2-2 Thick horizontal profiles across dark images for cobalt 60 irradiated CCD57 devices

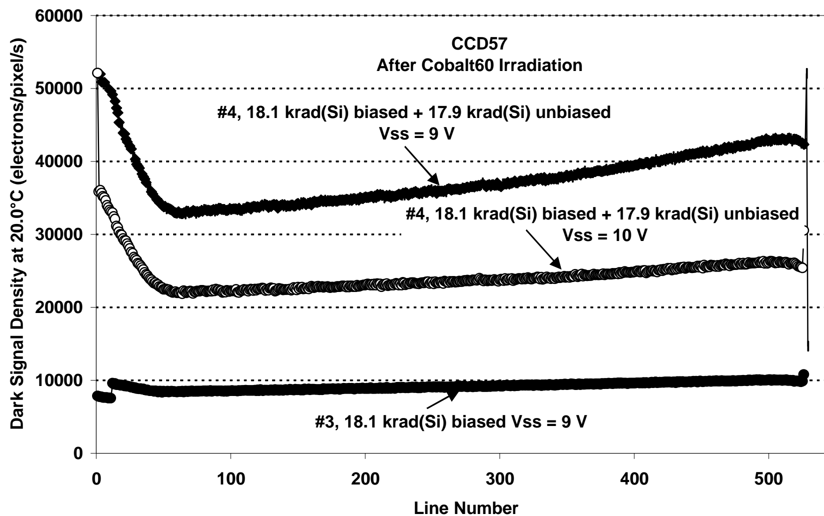

Figure 5.5.2-3 Thick vertical profiles down dark images for cobalt 60 irradiated CCD57 devices

Figure 5.5.2-4 shows an image for CCD #1, which was given both 9.5 and 60 MeV proton irradiation and figure 5.5.2-5 gives a thick horizontal profile. Unlike the CCD55 result, the 60 MeV region is fairly flat (especially bearing in mind that the pixels are nearly a factor 2 smaller). The ratio of the dark current increase for the 9.5 and 60 MeV regions is again (as for the CCD55) = 2.0 (for both devices #1 and #2), so:

CCD57 Relative NIEL for average bulk dark current (10 MeV: 60 MeV protons) = 1.7 ± 0.3

Figure 5.5.2-6 gives a similar horizontal profile for device #5 which was given only 9.5 MeV irradiation (nominally 10 krad, 20 krad and ~ 0.3 krad). The 20 krad region gives twice the damage as at 10 krad - as expected.

Figures 5.5.2-7 and 5.5.2-8 show dark current histograms for the proton irradiated devices with the dark current scaled to its value at 20.5ºC using an activation energy of 0.63 eV. The 10 krad region histograms are very similar. The 5.9 10^{10} p/cm^2 60 MeV histogram is quite similar to the 3.4 10^{10} p/cm^2 9.5 MeV (20krad) histogram which is to be expected since the average bulk

dark current is the same – but at 60 MeV the greater inelastic damage gives a more pronounced tail. Figure 5.5.2.8, which shows the full scale of the dark current damage, indicates significant size of the single pixel dark current spikes (hot pixels) which are relatively enhanced in the –19.6ºC data because of the lowered activation energy due to field enhancement. Figure 5.5.2.9 shows the activation energy as a function of the spike size at 20ºC. As expected there is a trend for the larger spikes to show a lower activation energy (due to field enhancement).

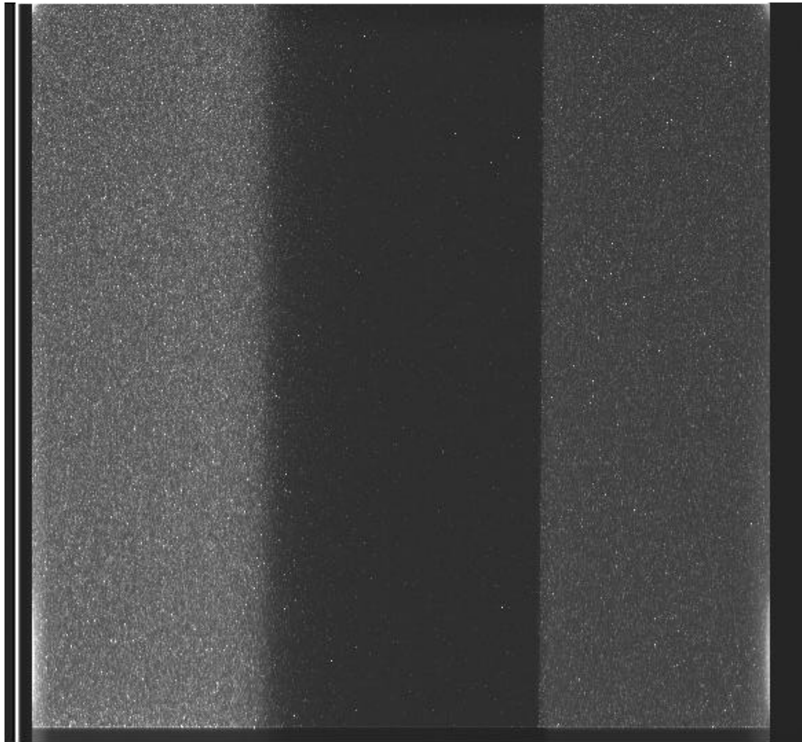

Figure 5.5.2-4 Dark image for 9.5 (right) and 60 MeV (left) irradiated CCD57 #1

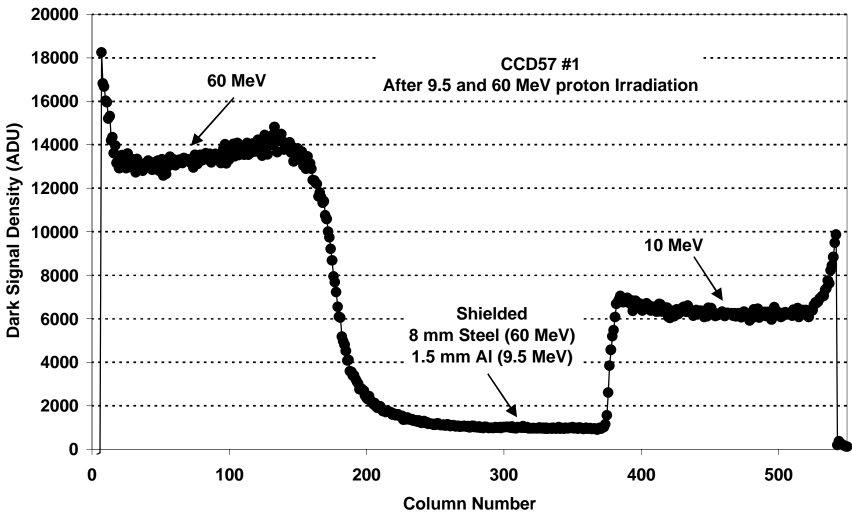

Figure 5.5.2-5 Thick horizontal slice across figure 5.5.2-4

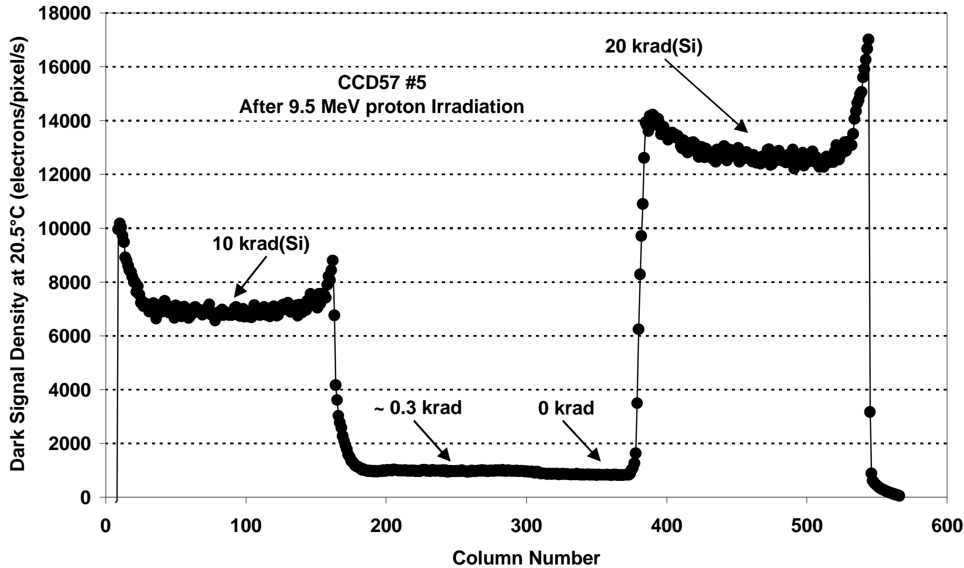

Figure 5.5.2-6 Thick horizontal slice across a dark image for the 9.5 MeV proton irradiated CCD57 #5

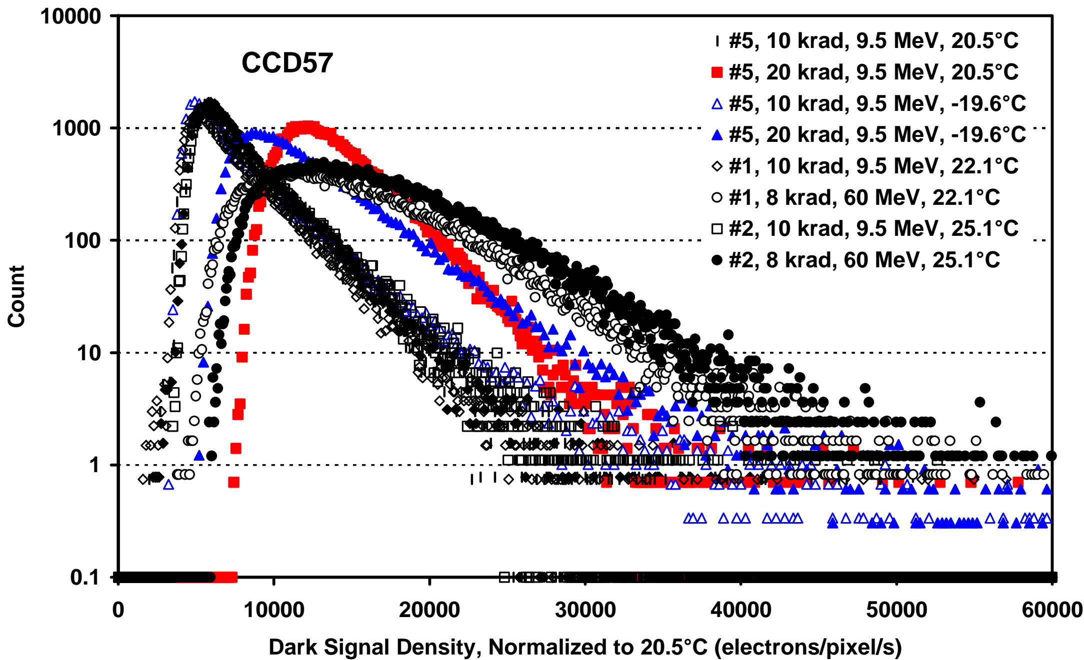

Figure 5.5.2-7 Dark current histograms for proton irradiated CCD57 devices with the dark current scaled to its value at 20.5ºC using an activation energy of 0.63 eV

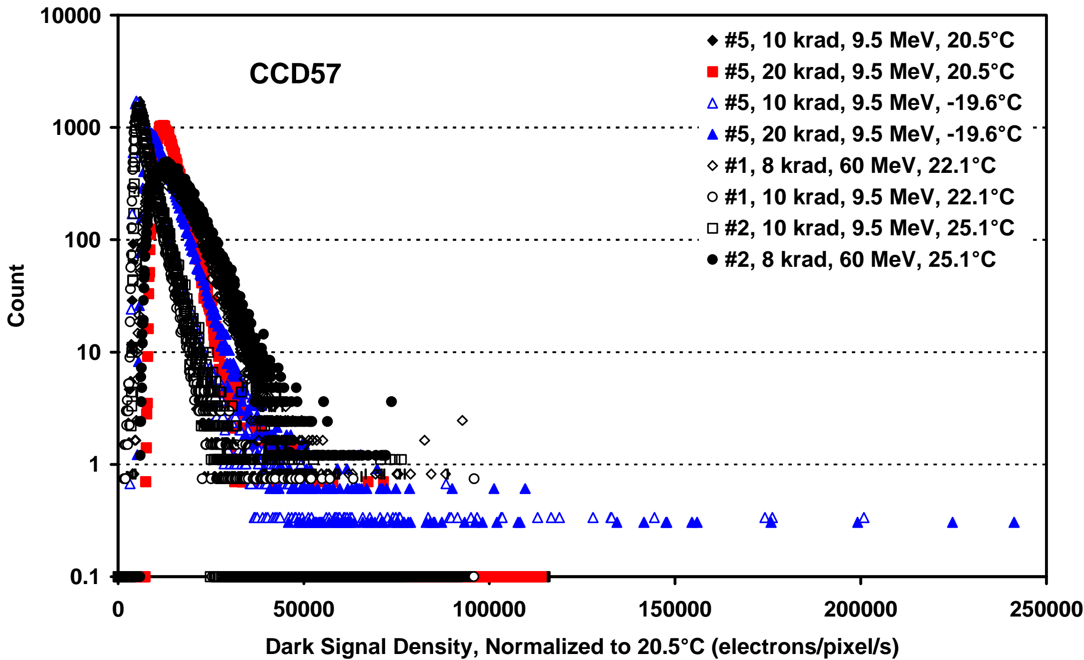

Figure 5.5.2-8 Same as figure 5.5.2-7 but with the horizontal scale reduced to show the full range of the dark current spikes.

From the above data the average damage constant for the 9.5 MeV proton irradiated devices is estimated to be

CCD57 damage constant = 0.063 ± 0.01 nA/cm^2/krad (10MeV protons) at 20ºC = (1.6 ± 0.3) 10^{5}electrons/cm^3/(MeV/g) at 300K, assuming an active volume of 500 μm^3 (13 μm x 9 μm x 4 μm).

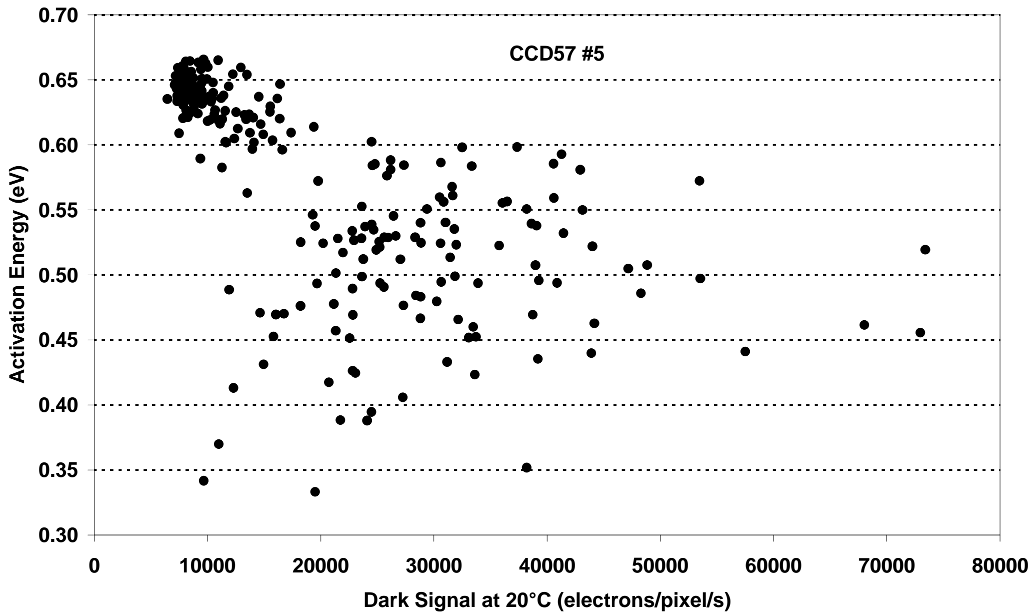

Figure 5.5.2.9 activation energy as a function of the spike size at 20ºC

5.5.2.1 Effect of Annealing

One device (#1) was succesively baked for three days at each of the following temperatures: 83ºC, 110ºC and 150ºC. Figures 5.5.2.1-1 and 5.5.2.1-2 show dark current histograms (showing dark spike reduction) and thick horizontal profiles (average dark signal) which have been scaled so that the plots overlap. It is seen that good scaling can be achieved, implying that annealing is similar at 10 and 60 MeV – apart from after the final annealing stage at 150ºC which shows a proportionaly larger reduction for the 60 MeV region. It is also seen from figure 5.5.2.1-2 that the dark current at the edges of the chip (probably due to the metallized light shield for dark reference pixels) is enhanced by the anneal. This effect is also indicated in the vertical profiles of figure 5.5.2.1-3 where the dark signal for the first few lines is increased (probably due to the effect of the storage region light shield). The scaling factors are shown in figure 5.5.2.1-4.

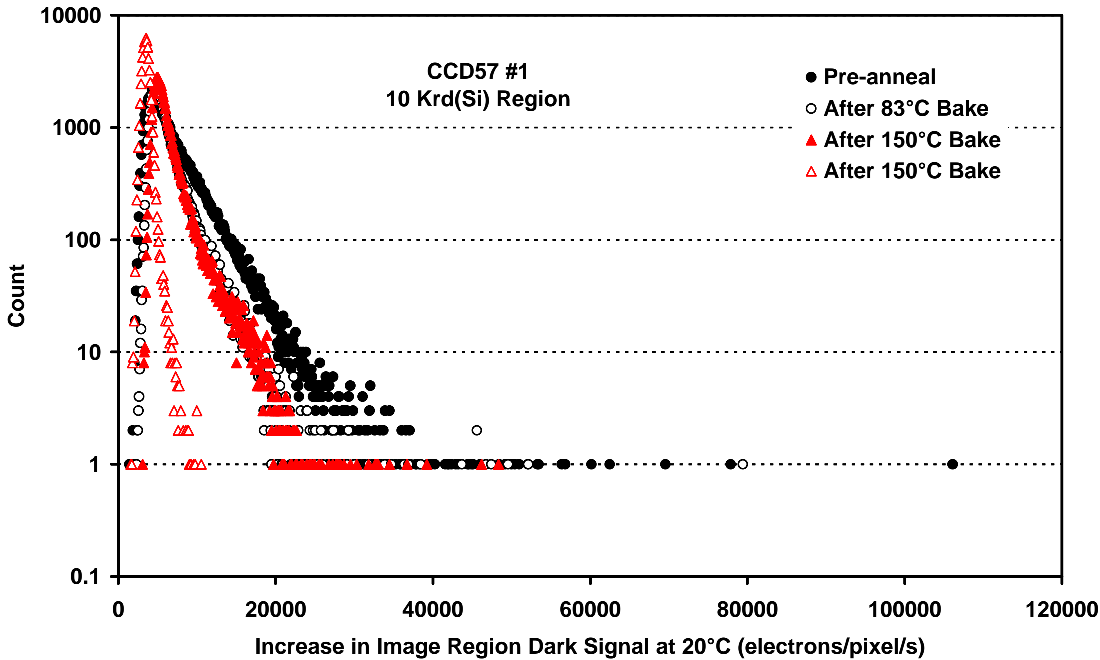

Figure 5.5.2.1-1 Dark current histograms before and after annealing

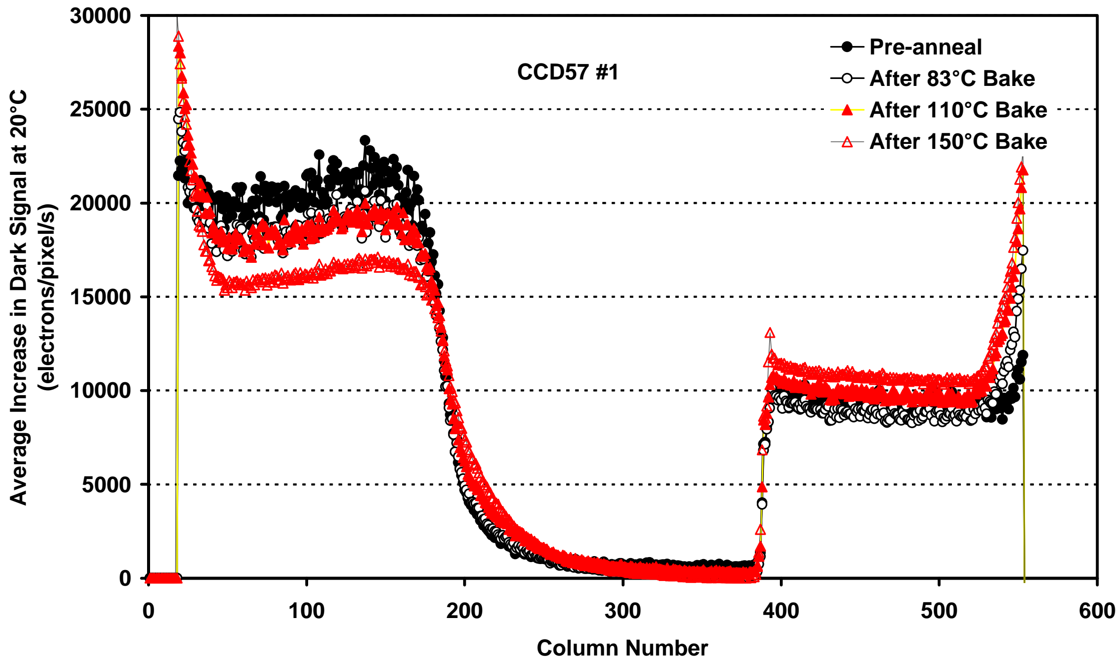

Figure 5.5.2.1-2 Scaled dark current horizontal profiles before and after annealing

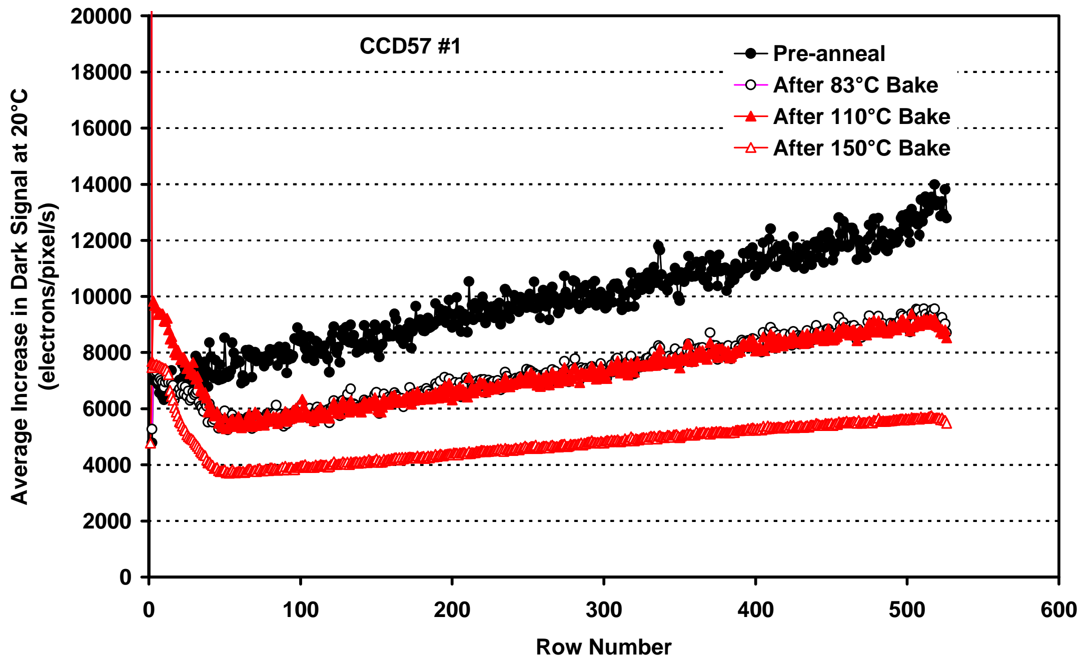

Figure 5.5.2.1-3 Dark current vertical profiles before and after annealing

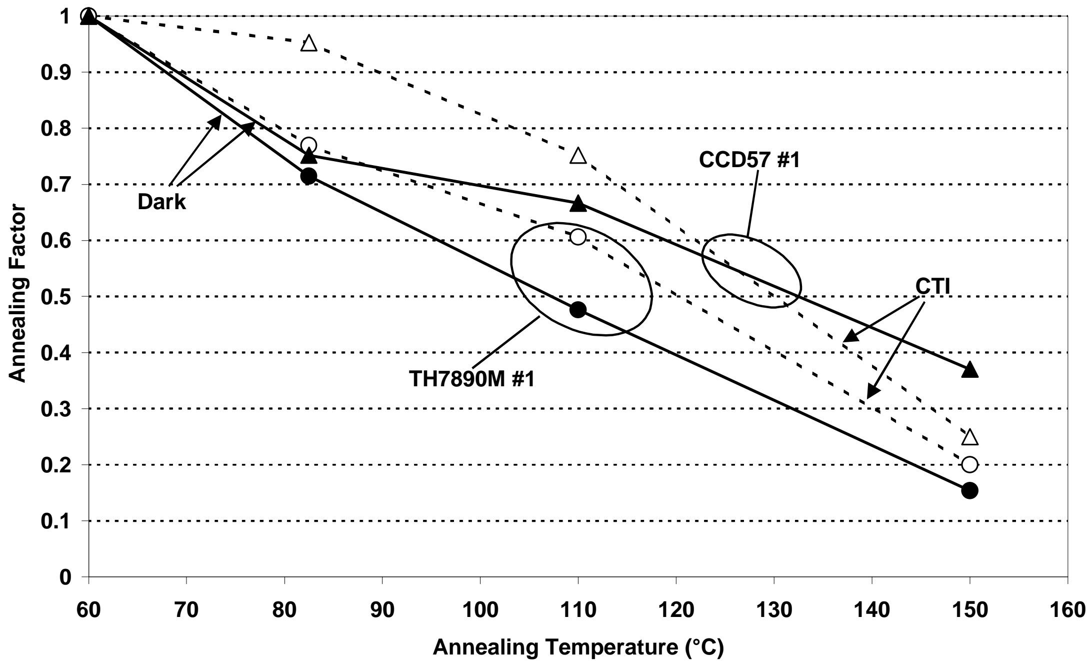

Figure 5.5.2.1-4 Dark current and CTI scaling factors

5.5.3 TH7890M Devices

The TH7890M is an inverted mode (MPP) device and the surface component of the dark current is suppressed. The variation in dark signal with substrate voltage was shown in figure 5.2-2.

Figure 5.5.3-1 shows a frame transfer image for TH7890M #5 given an unbiased cobalt60 irradiation to 17.9 krad(Si). The dark signal is uniform (apart from pre-existing dark current spikes) and the dark current level is approximately the same as obtained pre-radiation (the pre-irradiation temperature was not determined accurately and so the dark current level was only accurate to ~ 30%, being 600 electrons/pixel/s or 33 pA/cm^2 at ~ 28ºC) – i.e the irradiation had no significant effect.

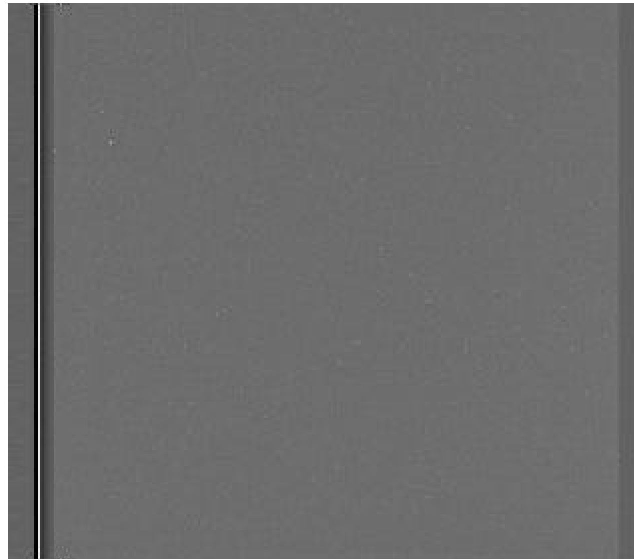

Figure 5.5.3-1 Dark image from CCD #5, after 17.9 krad(Si) cobalt60 (unbiased)

Figure 5.5.3-2 shows a dark image from CCD #1 which was irradiated with both 9.5 and 60 MeV protons and figure 5.5.3-3 displays a horizontal profile average over several hundred rows.

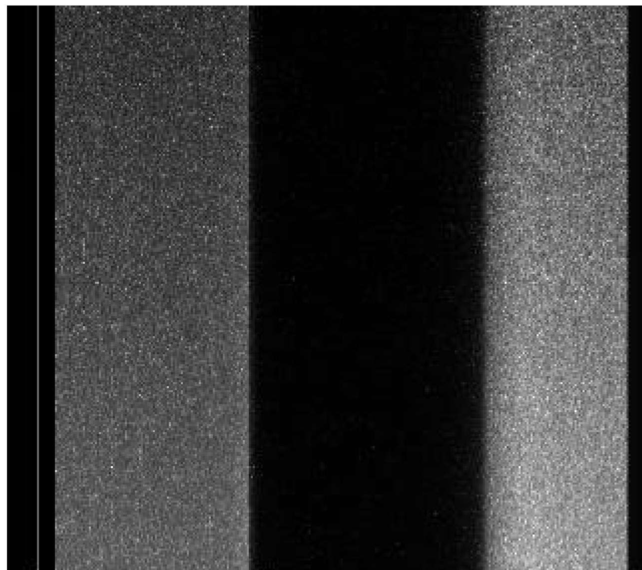

Figure 5.5.3-2 Dark image from CCD #1, irradiated with both 9.5 and 60 MeV protons

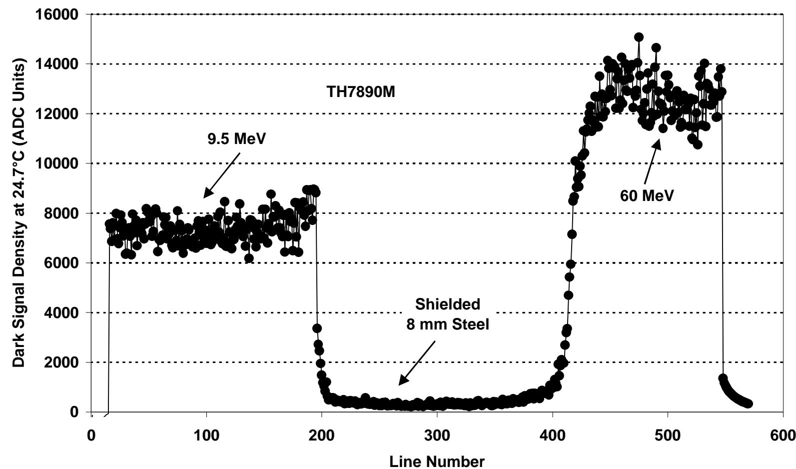

Figure 5.5.3-3 Horizontal profile across figure 5.5.3-2

As with the CCD57 and CCD55 the 60 MeV region has a 'soft' boundary due to proton interactions with the shield material. Figure 5.5.3-4 shows histograms of the image region dark current

The ratio of the dark current increase for the 9.5 and 60 MeV regions is = 1.96 for CCD #1 and 1.69 for CCD #2 (recall that the value was 2.0 for the e2v devices) so:

TH7890M Relative NIEL for average bulk dark current (10 MeV: 60 MeV protons) = 1.9 ± 0.3

Figure 5.5.3-4 gives a similar horizontal profile for device #6 which was given only 9.5 MeV irradiation (nominally 10 krad, 20 krad and ~ 0.3 krad). The 20 krad region gives twice the damage as at 10 krad - as expected.

Figure 5.5.3-5 shows dark current histograms for the proton irradiated devices with the dark current scaled to its value at 20.5ºC using an activation energy of 0.63 eV. The histograms were obtained by subtracting the dark current slope from images such as figure 5.3.3-2. The 10 krad region histograms are very similar. The 5.9 10^{10} p/cm^2 60 MeV histogram is quite similar to the 3.4 10^{10} p/cm^2 9.5 MeV (20krad) histogram which is to be expected since the average bulk dark current is the same – but at 60 MeV the greater inelastic damage gives a more pronounced tail. Note that the dark current spikes (hot pixels) are relatively enhanced in the –19.6ºC data because of the lowered activation energy due to field enhancement. Figure 5.5.3.6 shows the activation energy as a function of the spike size at 20ºC. As expected there is a trend for the larger spikes to show a lower activation energy (due to field enhancement).

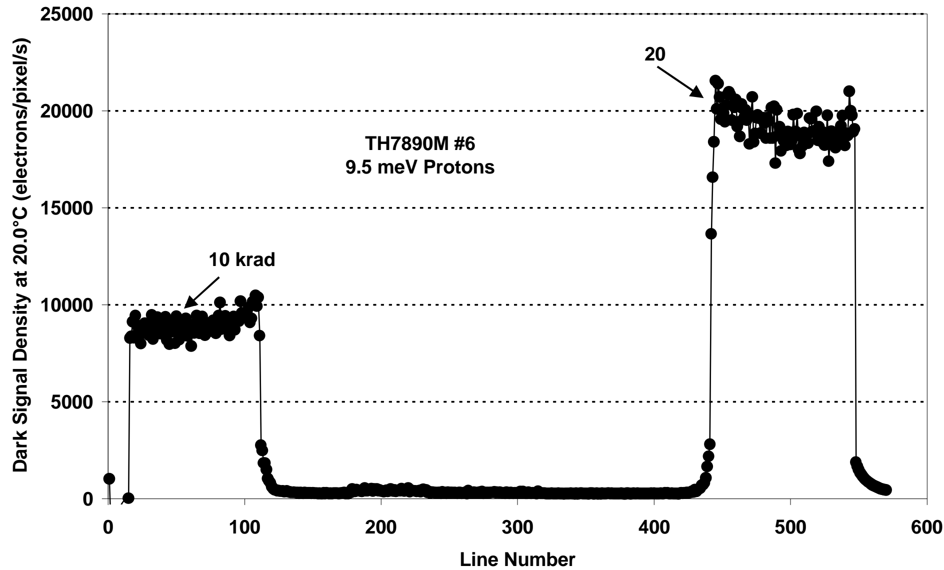

Figure 5.5.3-4 Horizontal profile for device #6, 9.5 MeV irradiation (nominally 10 krad, 20 krad and ~ 0.3 krad).

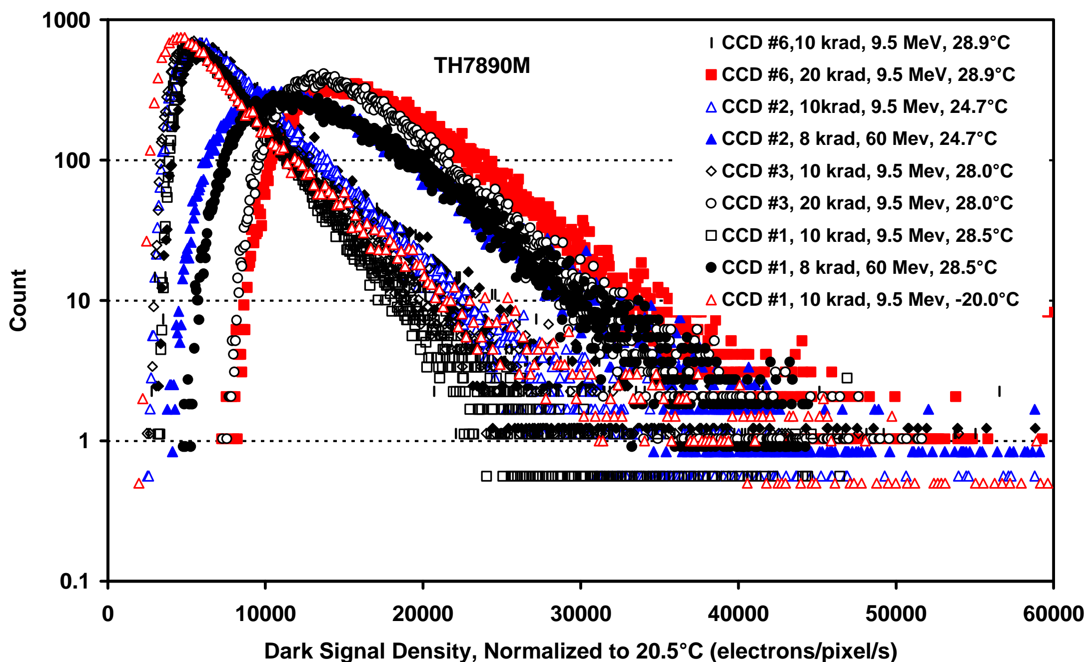

Figure 5.5.3-5 Dark current histograms for the proton irradiated devices with the dark current scaled to its value at 20.5ºC using an activation energy of 0.63 eV

From the above data the average damage constant for the 9.5 MeV proton irradiated devices is estimated to be

CCDTH7890M damage constant = 0.046 ± 0.01 nA/cm^2/krad (10MeV protons) at 20ºC = (1.4 ± 0.3) 10^{5}electrons/cm^3/(MeV/g) at 300K, assuming an active volume of 750 µm^3 (17 µm x 11 µm x 4 µm).

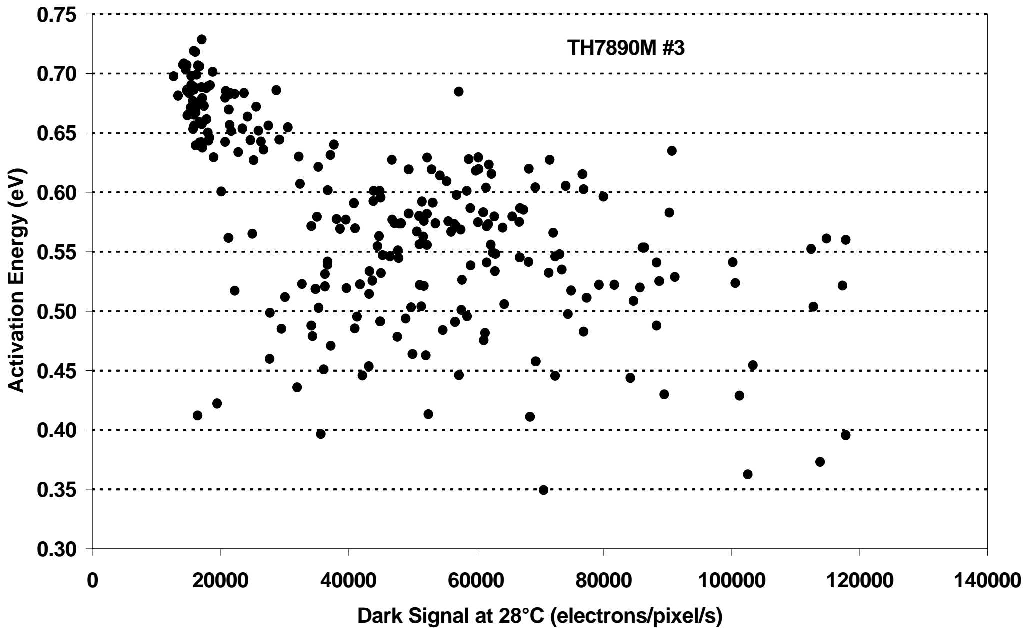

Figure 5.5.3-6 Activation energy as a function of the spike size at 20ºC

5.5.3.1 Effect of Annealing

One device (#1) was succesively baked for three days at each of the following temperatures: 83ºC, 110ºC and 150ºC. Figures 5.5.3.1-1 and 5.5.3.1-2 show dark current histograms (showing dark spike reduction) and thick horizontal profiles (average dark signal) which have been scaled so that the plotts overlap. It is seen that good scaling can be achieved, implying that annealing is similar at 10 and 60 MeV. The scaling factors are shown in figure 5.5.3.1-3.

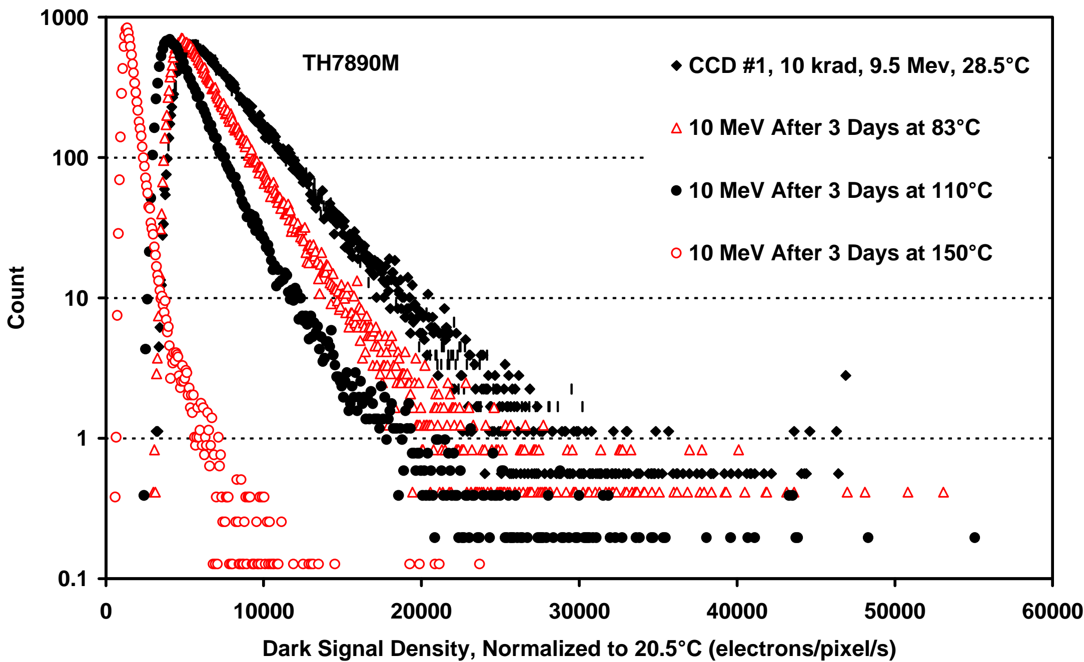

Figure 5.5.3.1-1 Dark current histograms before and after annealing

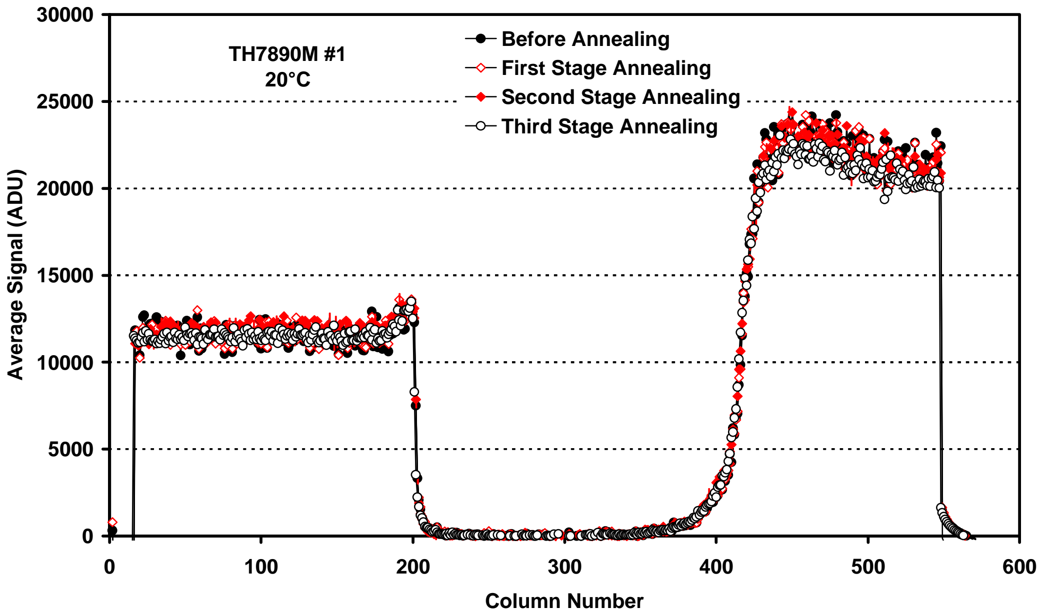

Figure 5.5.3.1-2 Scaled dark current profiles before and after annealing

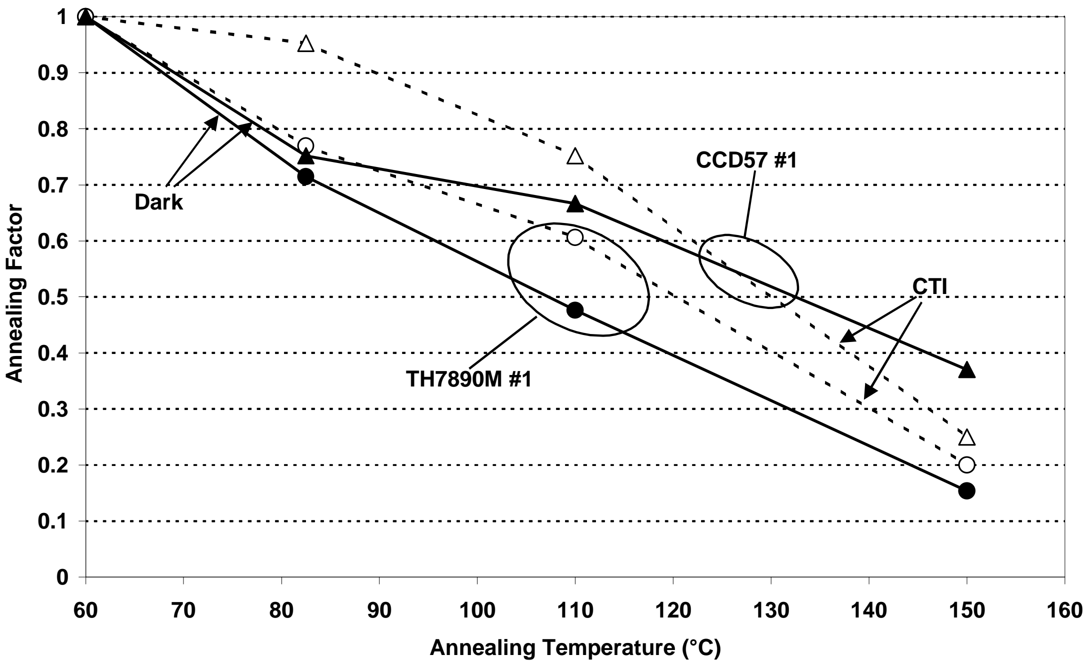

Figure 5.5.3.1-3 Dark current and CTI scaling factors

5.5.4 TH7863D Devices

The TH7863D devices were non-MPP mode with a deposited aluminium store shield. Figure 5.5.4-1 shows the dark image at 24.9ºC from CCD#1 after 17.9 krad(Si) cobalt60 irradiation (frame transfer mode, at minimum integration time = 137.9 ms). The image was taken after 7 months post-irradiation storage at room temperature. There is a large dark current slope arising from dark current generated in the storage region during frame transfer and also some excess charge at the top of the image. This excess charge is caused during frame transfer due to bloom-back of dark charge from the readout register (into the store). The effect was reduced as far as possible by operating the readout register at high speed during frame transfer to clear out the dark charge, but is, in any case, not seen at lower temperatures, when the dark current is reduced.

Note that the dark current for the dark reference region (on the right of the device) is similar to that for the rest of the image.

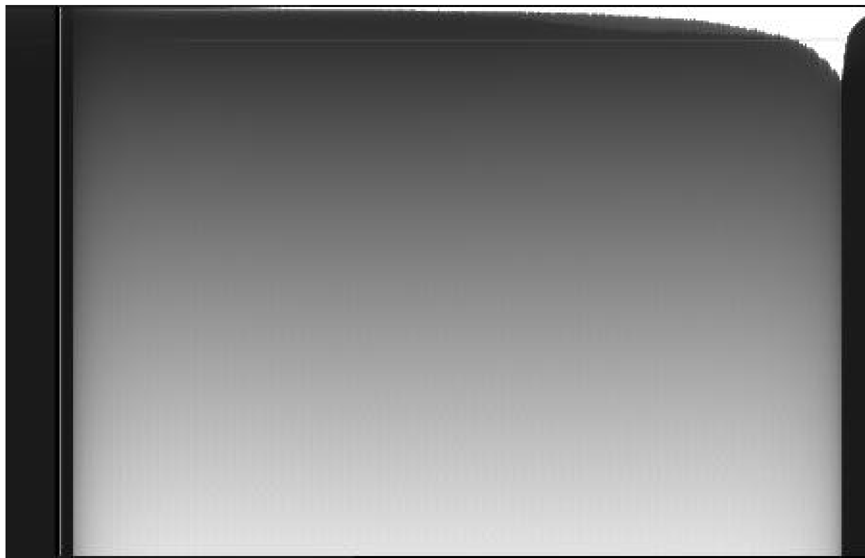

Figure 5.5.4-1 Dark image at 24.9ºC from CCD#1 after 17.9 krad(Si) cobalt60 irradiation

Dark current values for the two cobalt60 irradiated devices are tabulated below. It can be seen that there is a trend for the biased irradiation to give a greater change in dark current and for the radiation-induced storage region dark current to be an order of magnitude greater than that for the image region. Both components tend to show reverse annealing. It is possible that this is not complete even after 7 months (especially for the image region). These findings are in line with previous investigations.

Table 5.5.4-1 Dark current values for 17.9 krad(Si) Cobalt60 irradiated TH7863D devices, in nA/cm2 at 20ºC (calculated assuming an activation energy of 0.63 eV)

Device	Pre-rad	After 4 months storage	Change ($nA/cm^2/krad$) After 7 months	After 7 months storage	Change ($nA/cm^2/krad$) After 7 months
#1, biased image region	1.7	5.7	0.23	9.8	0.46
#2, unbiased image region	1.4	3.2	0.10	4.3	0.16
#1, biased storage region	0.53	83.1	4.6	85.2	4.7
#2, unbiased storage region	0.51	41.7	2.25	38.6	2.1

Figure 5.5.4-2 shows a dark image for the 9.5 MeV proton irradiated device and figure 5.5.4-3 gives a horizontal profile. It can be seen that the dark reference region has a slightly increased dark signal.

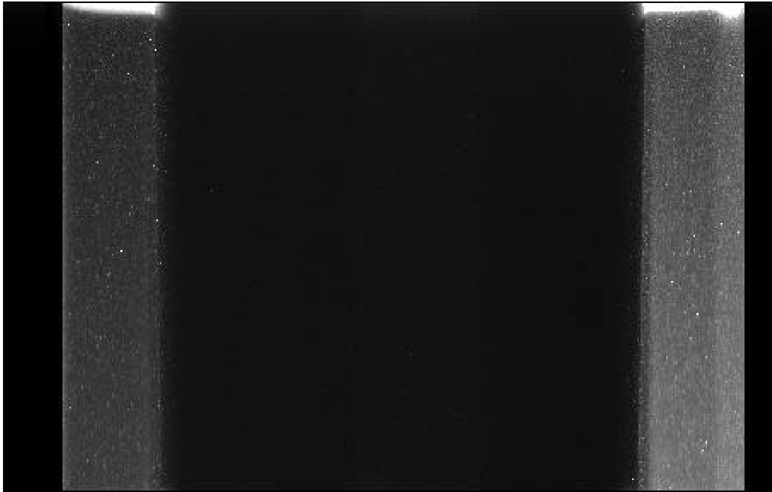

Figure 5.5.4-2 Dark image for CCD #3, 10 krad and 20 krad 9.5 MeV protons, -20.0ºC

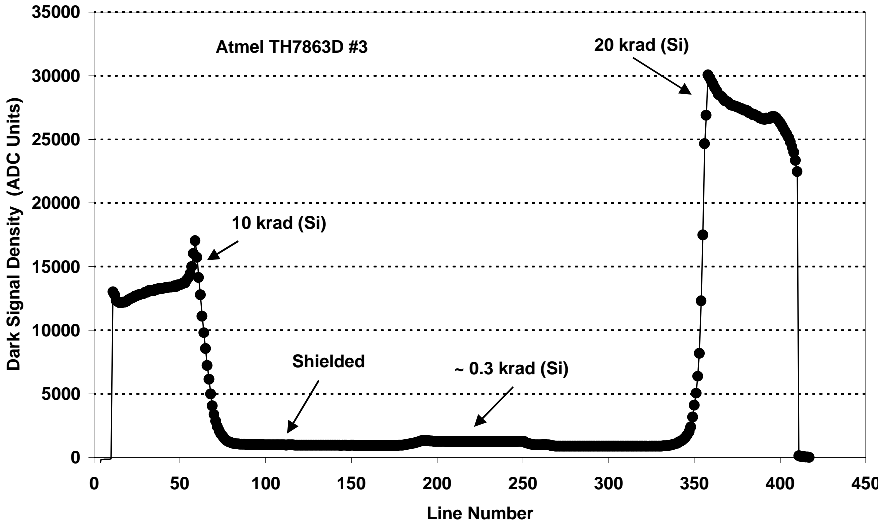

Figure 5.5.4-3 Horizontal profile (averaged over several rows) across figure 5.5.4-2

Figure 5.5.4-4 shows a dark signal histogram for the 10 krad region (the 20 krad region suffers from CTI degradation). Finally figure 5.5.4-5 shows a full frame image – illustrating the increased dark signal from the storage region.

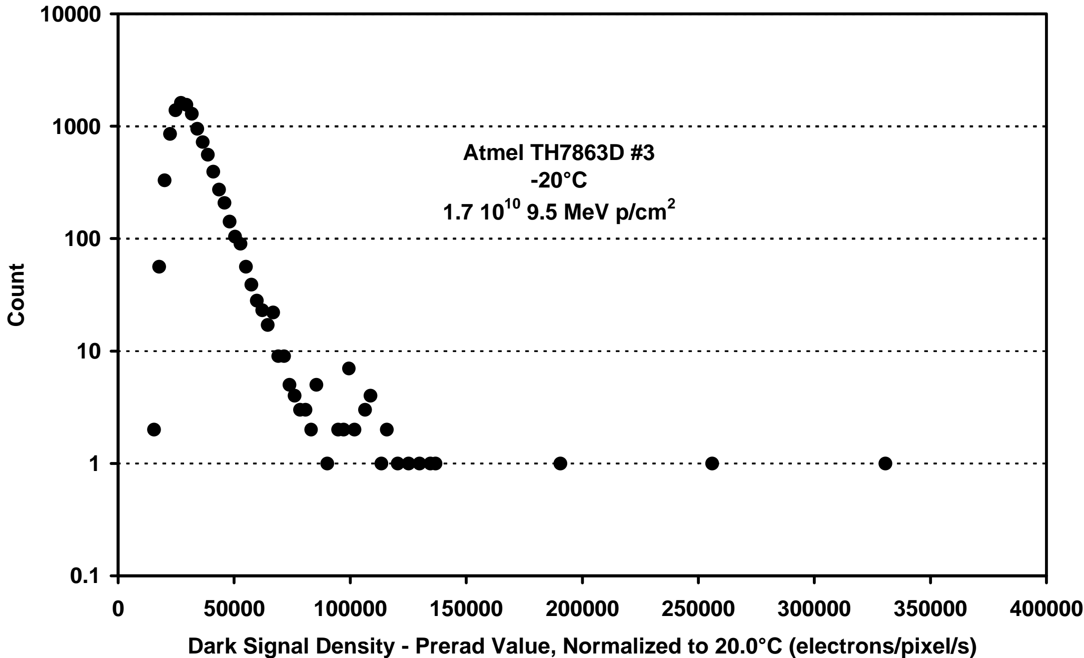

Figure 5.5.4-4 Dark signal histogram for the 10 krad region of CCD #3

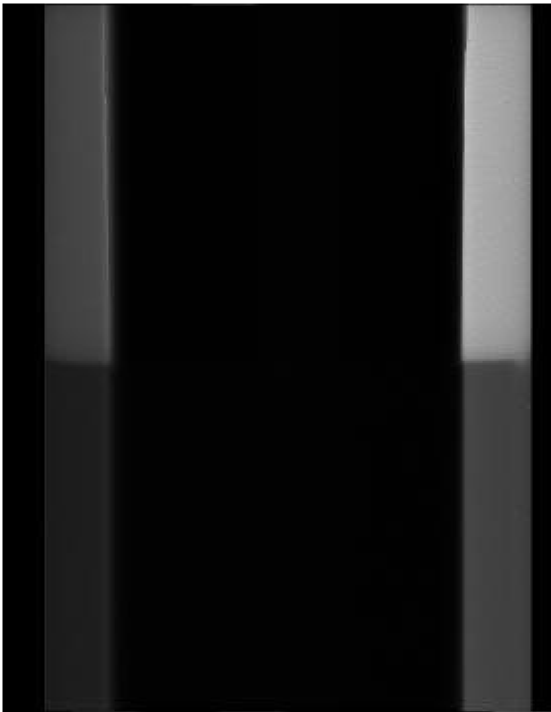

Figure 5.5.4-4 Full frame image for CCD #3 showing increased dark current for the storage region (top of image), 8^{0}C, 500 ms integration time.

5.6 INVESTIGATION OF RANDOM TELEGRAPH SIGNAL (RTS) BEHAVIOUR

The constraints of the study did not allow an exhaustive investigation of random telegraph signal (RTS) effects. Instead, data were collected at several temperatures and used to investigate methodologies for identifying and quantifying RTS behaviour.

Measurements were made on all four CCD types at temperatures in the range –40 to 30ºC. It was found that up to 1,000 pixels could be conveniently tagged using ImagePro Plus and used for data collection. Experimental runs of up to 10,000 samples were made and the results imported to MS Excel™ spreadsheets (though the present test computer is prone to run out of memory for the largest spreadsheets).

For the identification of RTS defects it was found convenient to plot the standard deviation of the signal against the average signal value for each tagged pixel. This we term an 'RTS noise plot'. Figure 5.6-1 shows a typical example. The pixels which are significantly above the noise level (which increases slighlty with signal due to shot noise) are nearly always showing RTS behaviour. Pixels can either be tagged at random (to investigate occurrence probabilities) or specific (e.g. high signal) pixels can be tagged.

In general it was found that the 1.7 10^{10} 9.5 MeV p/cm^2 regions (and the equivalent 60 MeV areas) resulted in nearly all the pixels showing fluctuations – and this fluence is too high to study occurrence probabilities. For this it is better to use the ~ 0.1 and 0.3 krad regions although the dosimetry for these is somewhat uncertain. (1 krad would be ideal but, as mentioned above, there seems to have been an error in the proton irradiation for the low fluence regions and only 0.1 and 0.3 krad was achieved.)

One feature which is generally apparent from the RTS noise plots is that RTS behaviour is not one-to-one correleated with the spike size: some large spikes do not show RTS effects (whereas most do) and some small spikes do show RTS behaviour (though most do not).

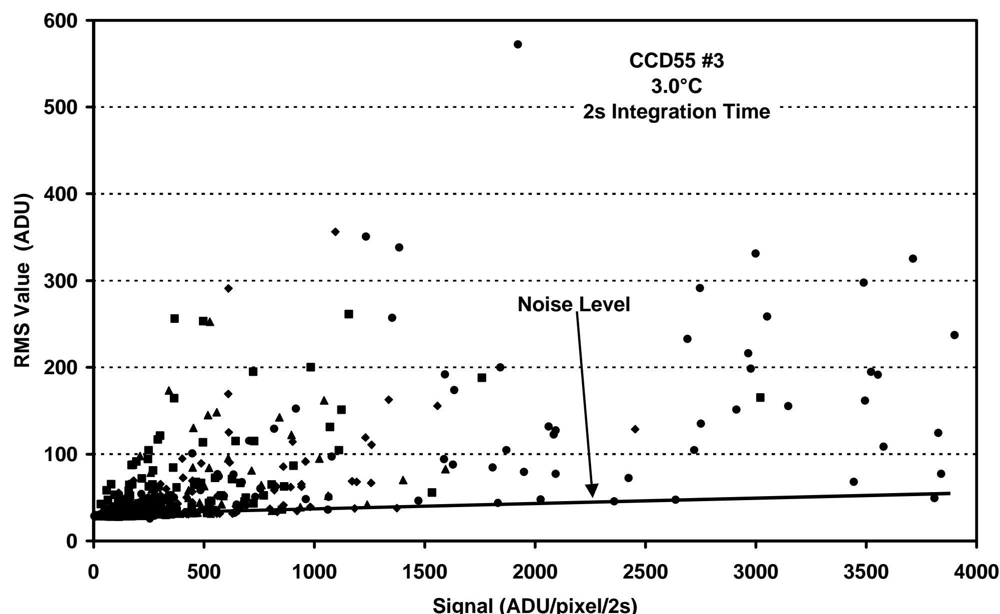

Figure 5.6-1 RTS noise plot for a CCD55 device at 3.0ºC, 2s integration time for four sets of tagged pixels.

Figures 5.6-2 and 5.6-3 show RTS noise plots for the 0.1 and 10 krad(Si) regions of a CCD57-10 device, but the variance is plotted rather than the RMS so as to emphasise the linear increase of the noise baseline (due to Poisson statistics). Figure 5.6-4 shows the same data as 5.6-3 but with an expanded vertical scale – this plot clearly illustrates that nearly all the pixels in the 10 krad region show increased noise due to RTS.

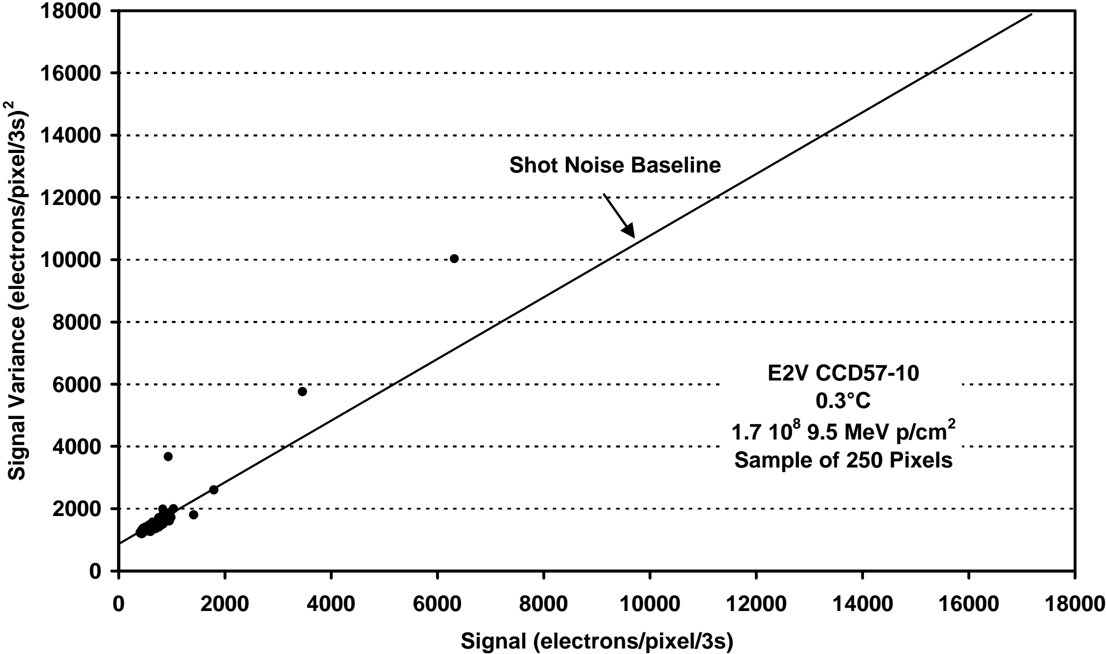

Figure 5.6-2 Variance versus signal plot for random pixels in the ~0.3 krad(Si) region of a CCD57-10 device.

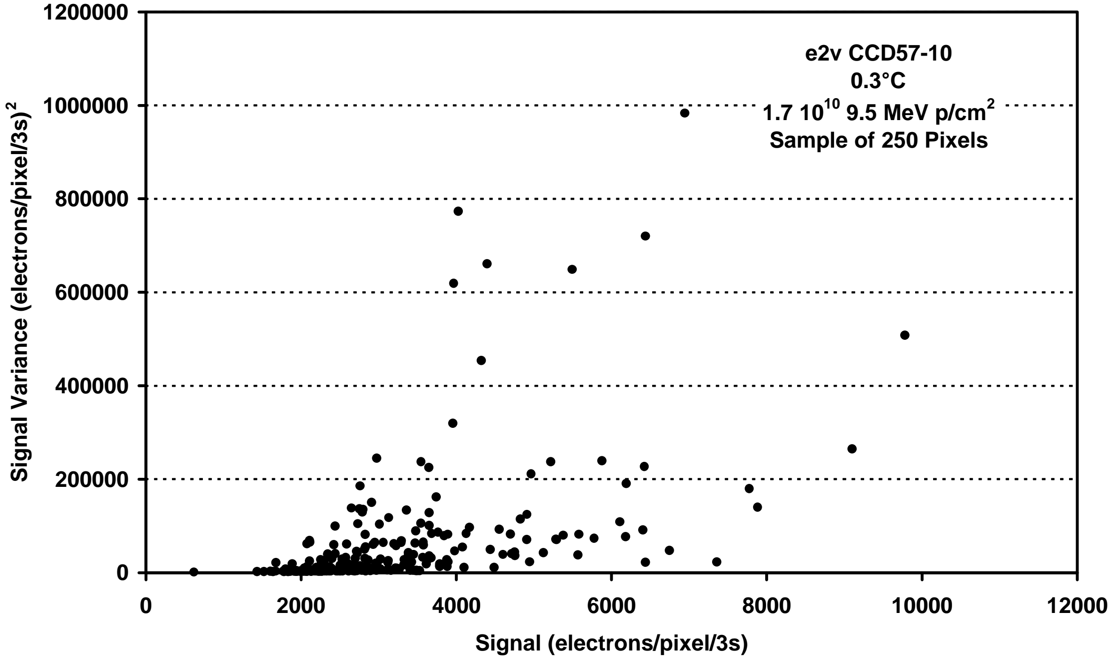

Figure 5.6-3 Variance versus signal plot for random pixels in the 10krad(Si) region of a CCD57-10 device.

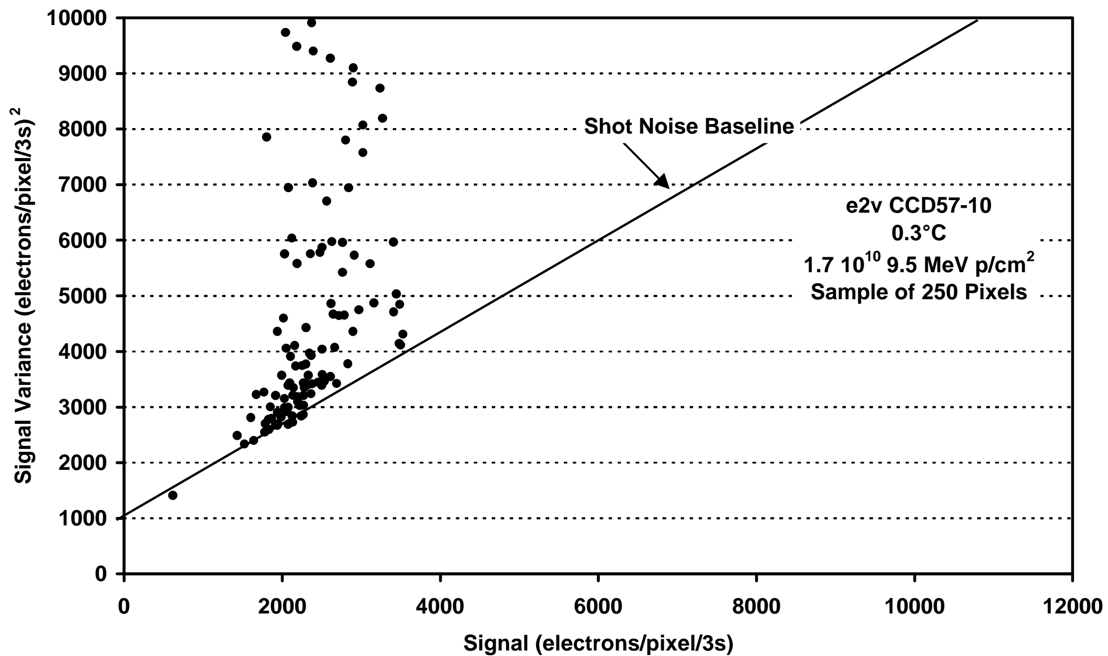

Figure 5.6-4 As figure 5.6-3, but the vertical scale is expanded

The data from RTS noise plots can also be used to investigate the temperature behaviour of RTS amplitudes (since these will be directly related to the RMS noise values). Figure 5.6-5 shows the RMS values (logarithmic scale) versus 1000/T. For the low RMS (non-RTS) pixels the RMS is dominated by the (constant) readout noise and so these pixels do not show a linear trend (the trend that is shown is rather spurious as it is due to the fact that different integration times were used at the different temperatures and the signals are scaled for this to give ADU/pixel/s). It is seen that the amplitudes of the higher noise (RTS) pixels vary with an amplitude activation energy ~ 0.6 eV as expected (though the very largest amplitudes are field enhanced and show a slightly lower activation energy).

At -40ºC the amplitudes are very small (and the time constants are long) but figures 5.6-6 and 5.6-7 show that fluctuations can still be seen in a 13 hour observation period – though probably more would be noticeable if the observations could be extended.

Note that it has not been possible to perform detailed analysis of the time constants as this involves time consuming examination of the behaviour of each individual pixel. However the trends are in line with previous studies:

- at any temperature there is a wide range of time constants – ranging from seconds to hours at room temperature (i.e. 4 orders of magnitude)
- although there is a wide range, most time constants are several minutes at 25ºC and several hours at 10ºC, implying an an activation energy in the range 0.9-1.1 eV

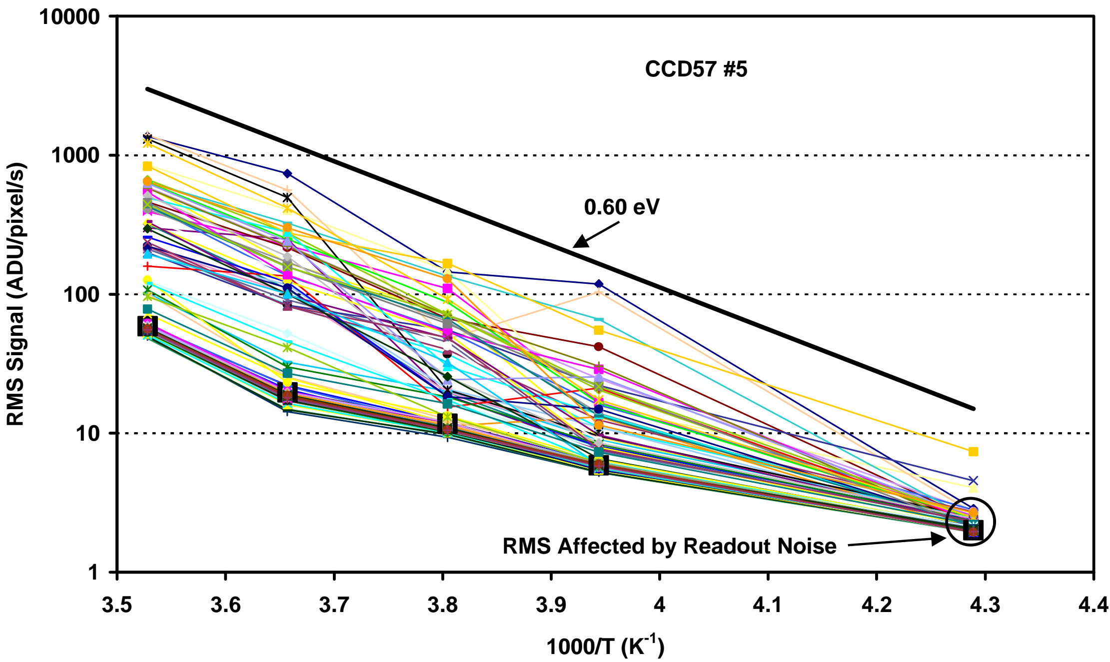

Figure 5.6-5 RMS signal versus 1000/T for the 10 krad(Si) region of a proton irradiated CCD57-10

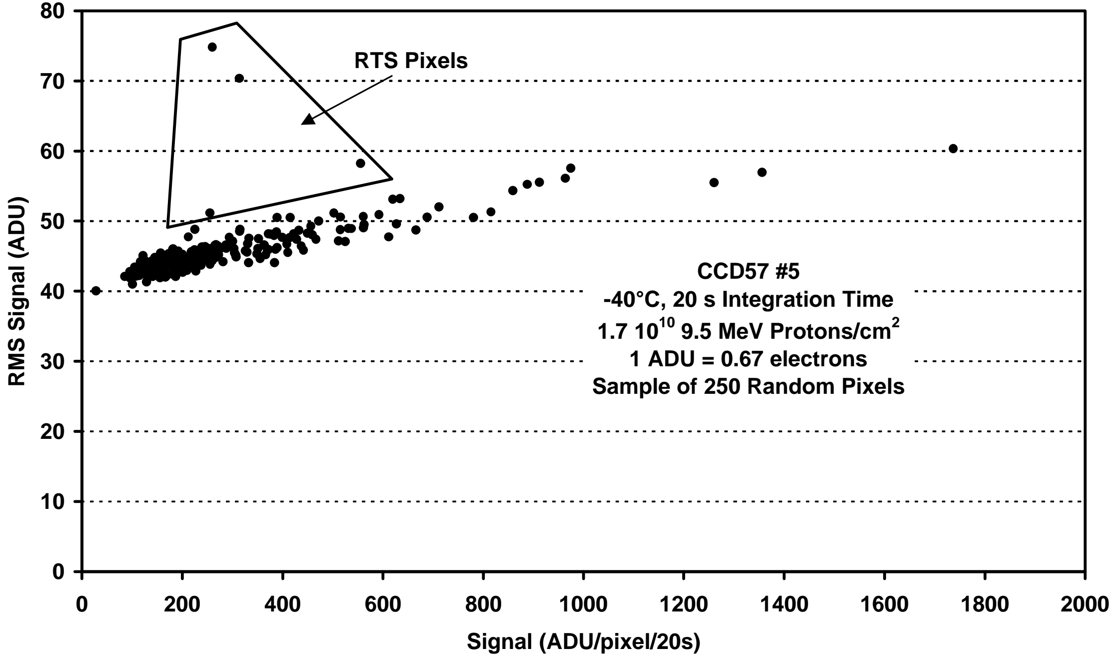

Figure 5.6-6 RTS Noise plot at -40ºC showing that some RTS fluctuations can still be seen during a 13 hour observation even though the amplitudes are small and the time constants long.

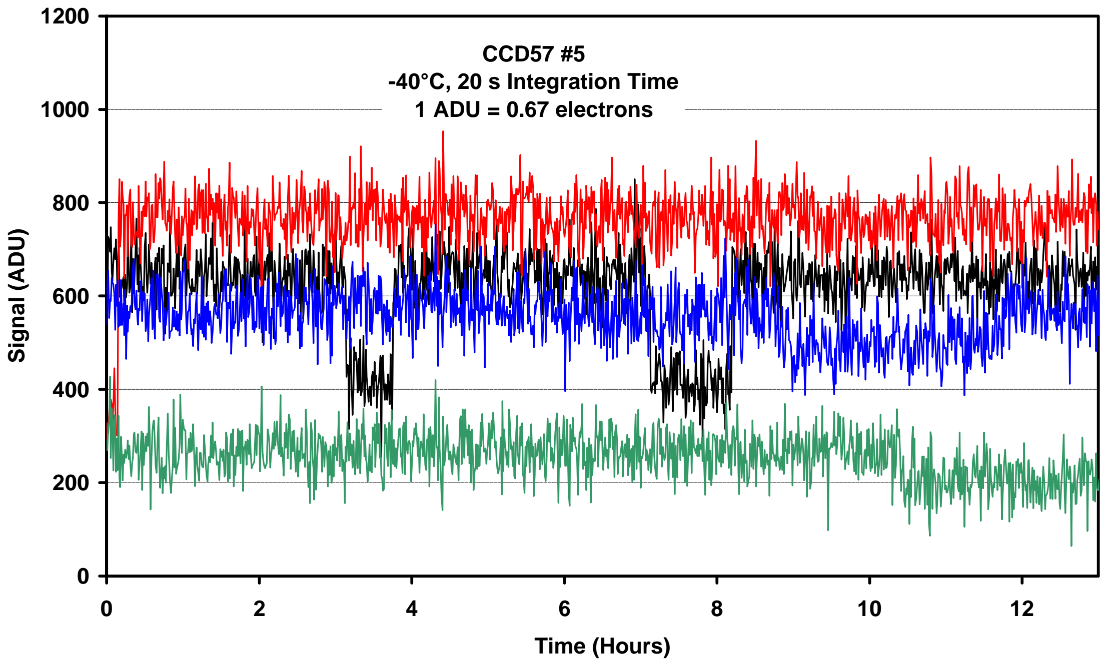

Figure 5.6-7 RTS traces for some of the pixels at -40ºC

Figure 5.6-8 shows more RTS noise data for a fluence of ~5 10^8 9.5 MeV p/cm^2. There are six RTS pixesl, a value in good agreement with the occurrence probability of 0.000016 per proton/pixel originally found.

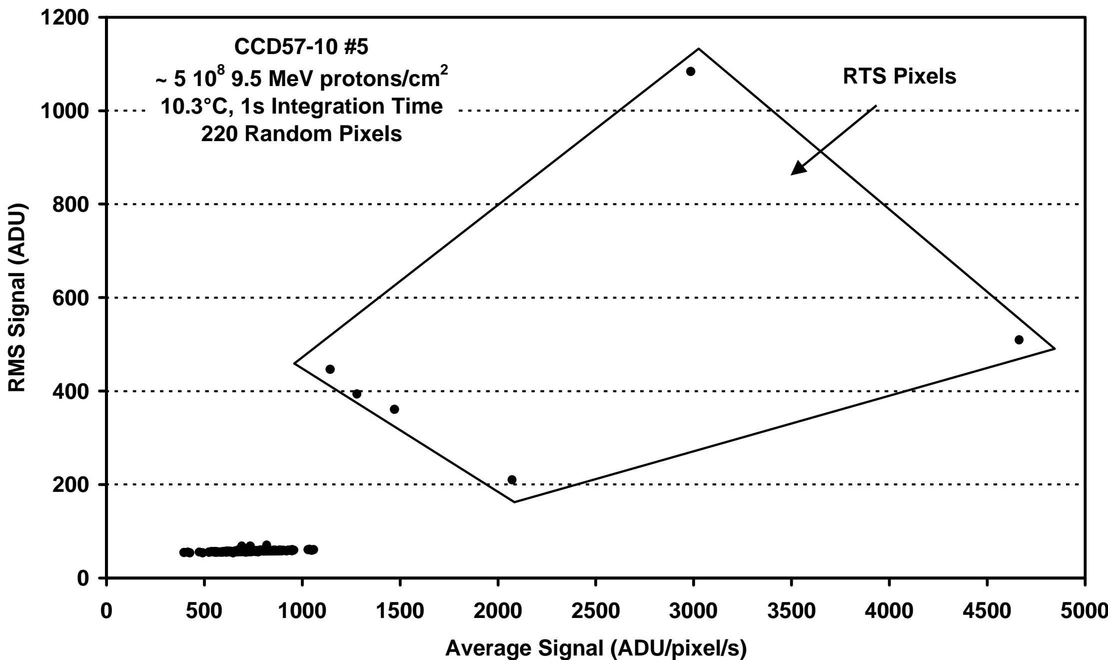

Figure 5.6-8 RTS noise plot for the ~0.3 krad(Si) region of a proton irradiated CCD57-10

Figure 5.6-9 shows the RMS signals for 250 pixels after annealing. It is seen that the RMS does not decrease significantly till after the 150ºC anneal. There are some fluctuations in the RMS values but this is to be exppected since some pixels with long time constants may, or may not show a transition during the period of the observations (which was 10,000 samples). It can be seen that, even after 3 days at 150ºC there are still 3 pixels in the sample which show RTS, but for most the fluctuations have disappeared. After 150ºC, therefore, the noise comes almost entirely from readout and shot noise (on the dark signal). Figure 5.6-10 shows the noise variance versus signal, which indicates a linear behaviour with a slope ~ 0.6 electrons/ADU as expected from the earlier X-ray calibrations of conversion gain (section 5.1).

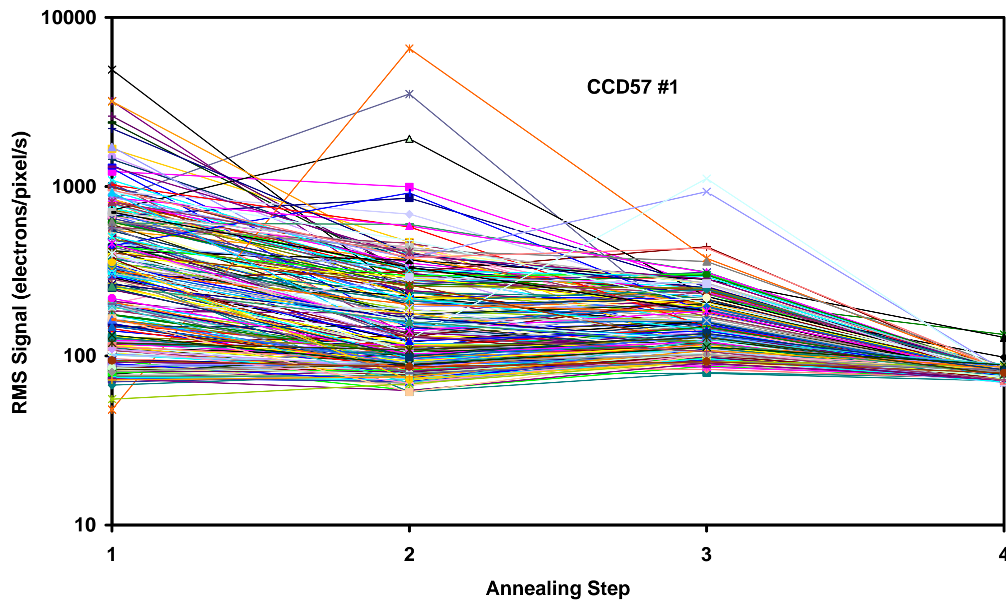

Figure 5.6-9 RMS signal (20ºC, 320 ms integration time) after annealing for the CCD57-10 device. The annealing steps were: 1: pre-annealing, 2: after 3 days at 83ºC, 3: after a further 3 days at 110ºC, 4: after a further 3 days at 150ºC.

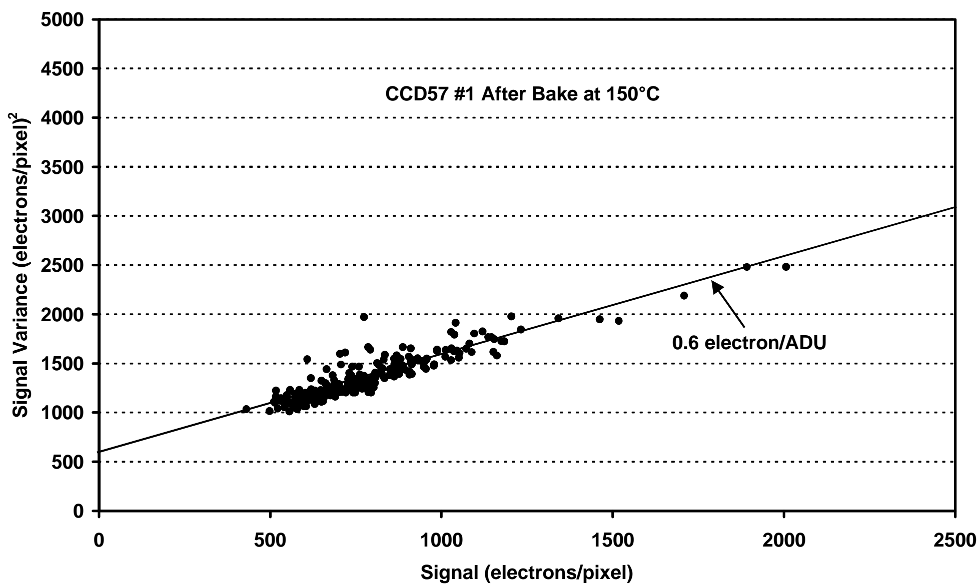

Figure 5.6-10 RMS noise (variance) plot after annealing, nearly all the noise comes from readout and shot noise. The noise variance agrees well with the calibration of electrons/ADU.

Figures 5.6-11 and 5.6-12 show similar RTS noise plots for the ~5 10^8 9.5 MeV p/cm^2 fluence region of a TH7890M device. There are about ~6 RTS pixels in each sample, again agreeing with the value of 0.000016 /proton/pixel. Figure 5.6-13 shows a plot for the 10 krad(Si) region, again showing that in that case most pixels show RTS.

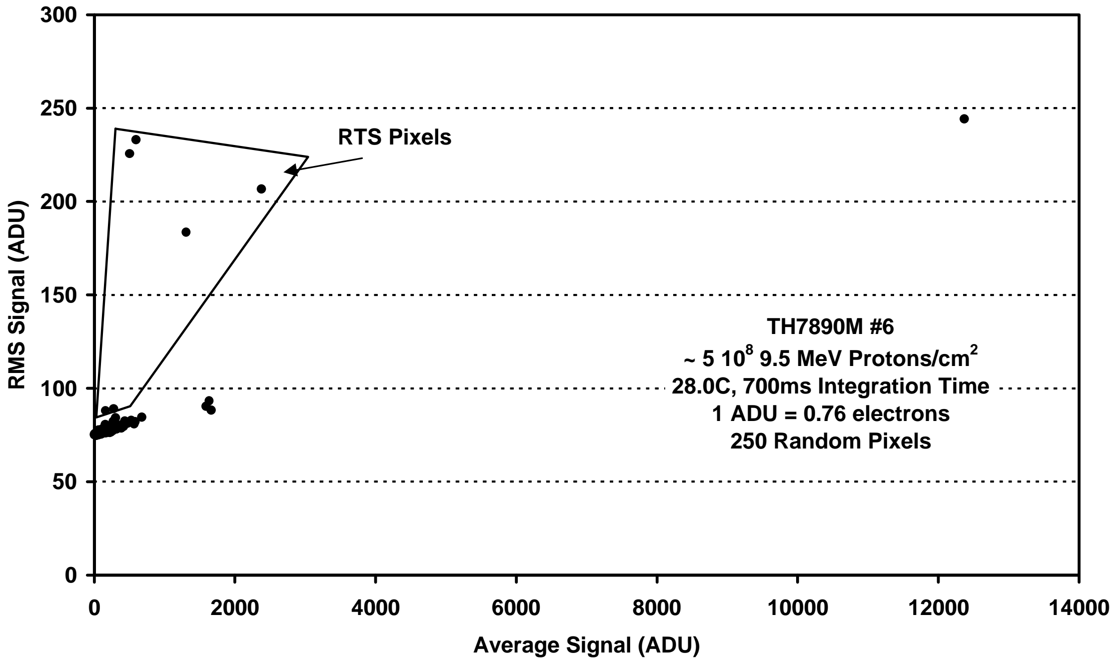

Figure 5.6-11 RTS Noise plot for a TH7890M device

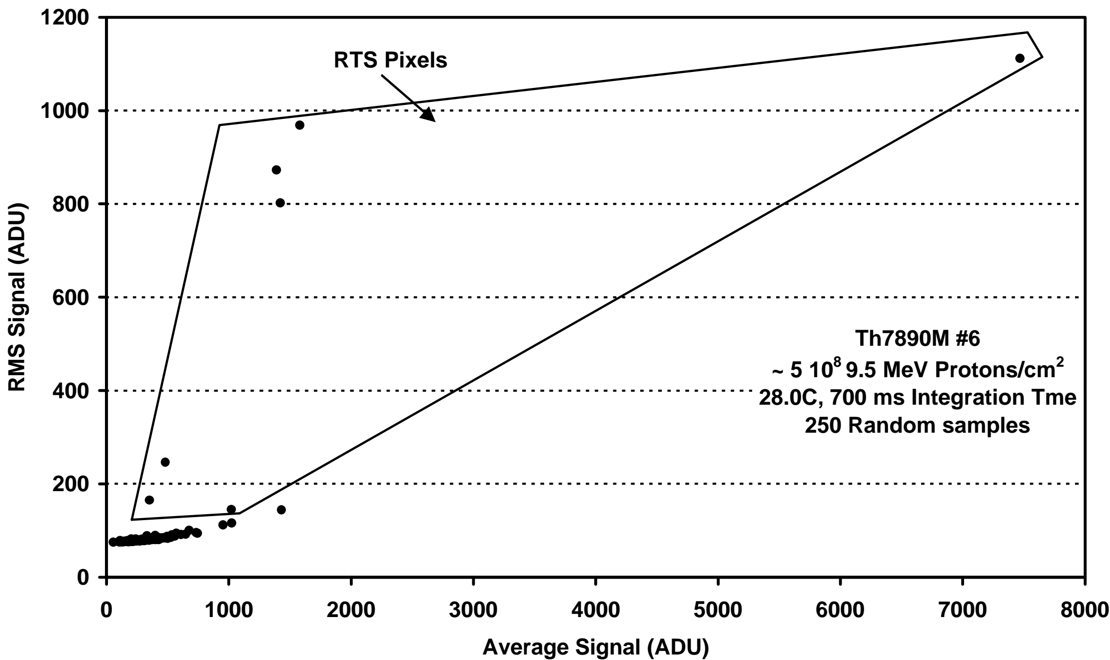

Figure 5.6-12 RTS Noise plot for a TH7890M device

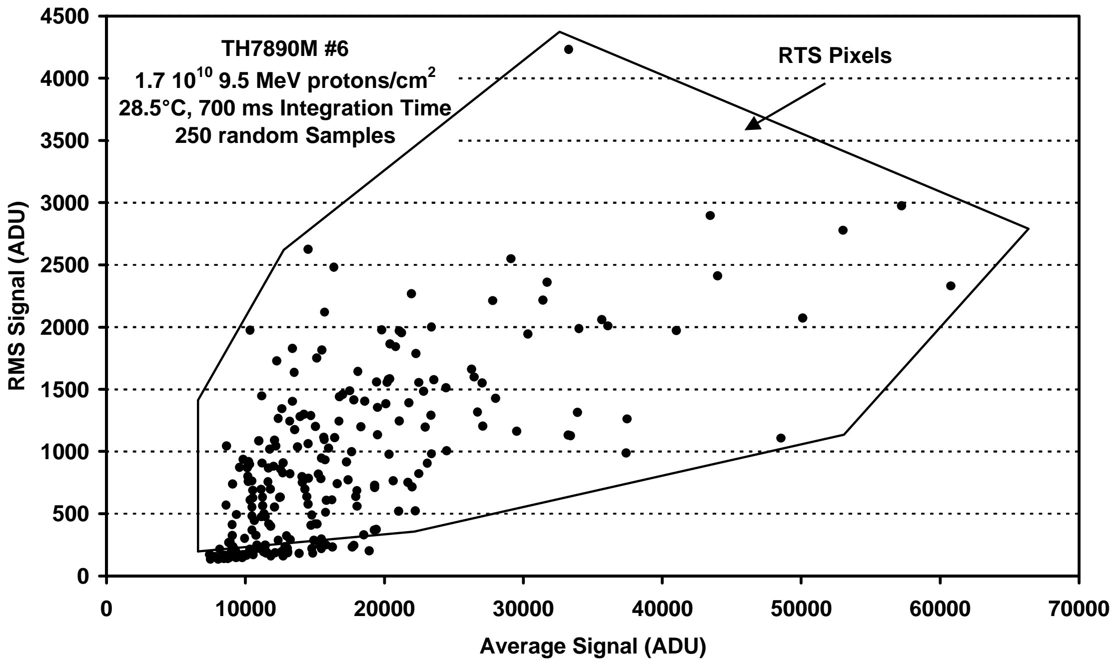

Figure 5.6-13 RTS Noise plot for a TH7890M device

The annealing behaviour for the TH7890M is shown in figure 5.6-14 and , as for the CCD57-10, most of the annealing occurs after the 150ºC stage.

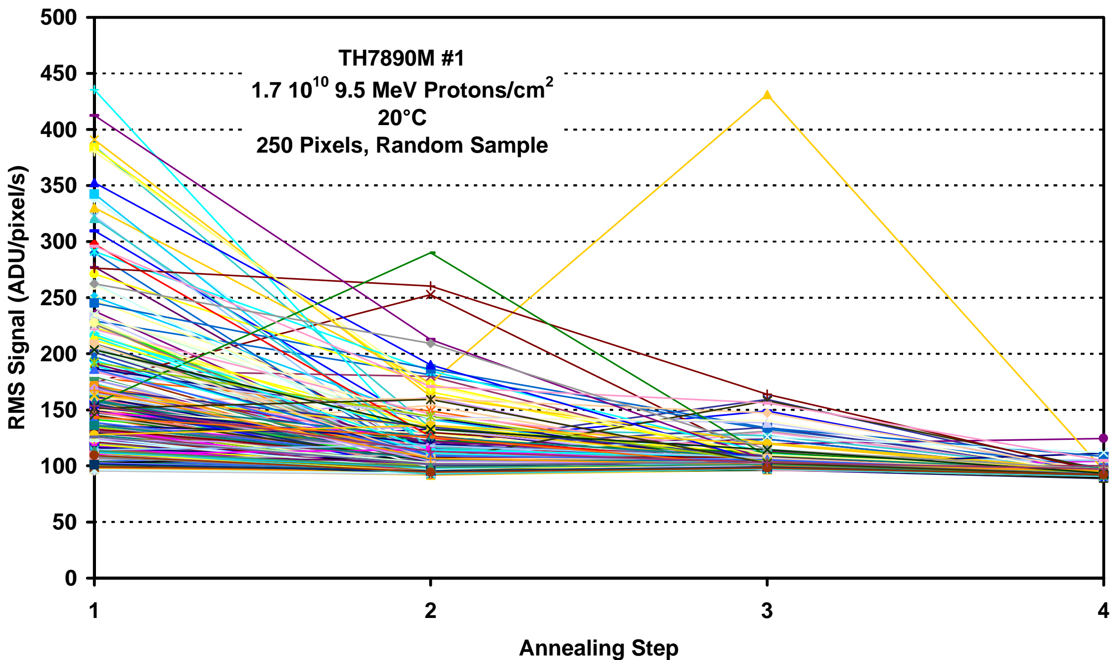

Figure 5.6-14 RMS signal (20ºC, 320 ms integration time) after annealing for the CCD57-10 device. The annealing steps were: 1: pre-annealing, 2: after 3 days at 83ºC, 3: after a further 3 days at 110ºC, 4: after a further 3 days at 150ºC

Figure 5.6-15 shows an RTS noise plot for the TH7863D device at 30ºC.

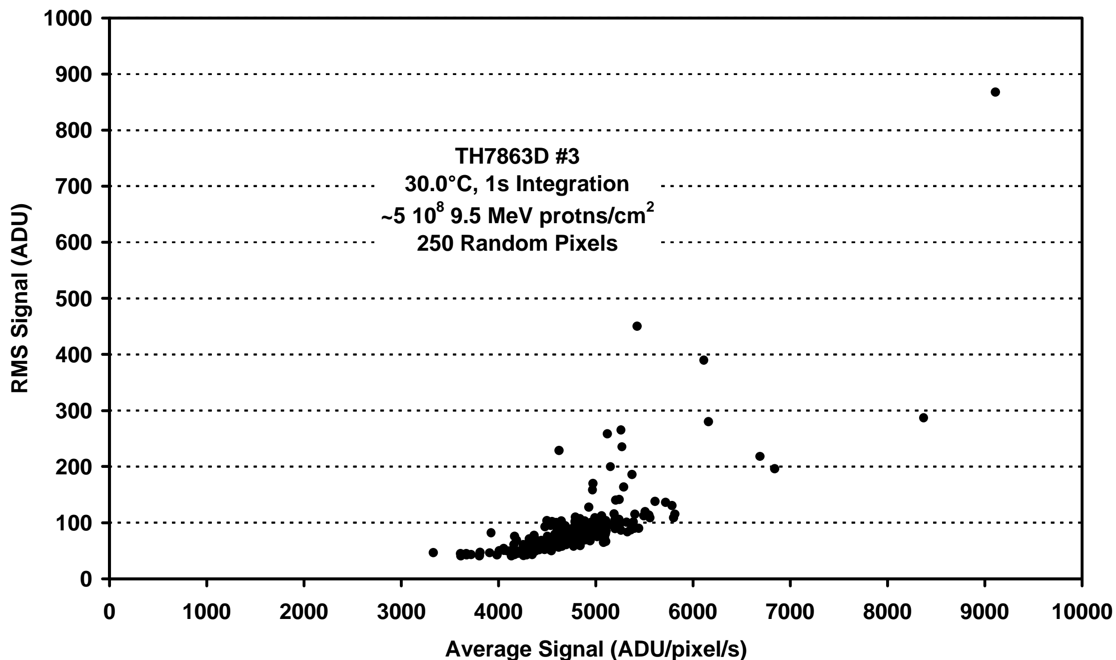

Figure 5.6-15 RTS noise plots for the proton irradiated TH7863D device

In the above experiments data was always obtained from overscanned pixels which have no CCD signal but give the 'electronic' baseline offset for the off-chip video chain and ADC. It was usually found that these values gave a constant level (with readouit noise), but occasionally it was found that switching behaviour could be seen (in which case all the pixels were affected by the same change in offset). To investigate this further some runs were made with the CCD disconnected and again, in some cases fluctuations could be observed. Examples are given in figures 5.6-16 and 5.6-17. Note that this RTS-like behaviour is not due to irradiation (since the video board was not irradiated) but may be due to 'popcorn' or similar noise in one of the amplifiers. This does not seem to have been seen before in CCD systems, but this is probably because it has not been looked for.

The fluctuations were usually quite small (~ 50 ADU or 100 μV) but could be important for critical applications. This illustrates the need to always refer CCD signals to the overscanned pixel level. If this is not possible then applications will need to carefully check for offset fluctuations in the video electronics chain.

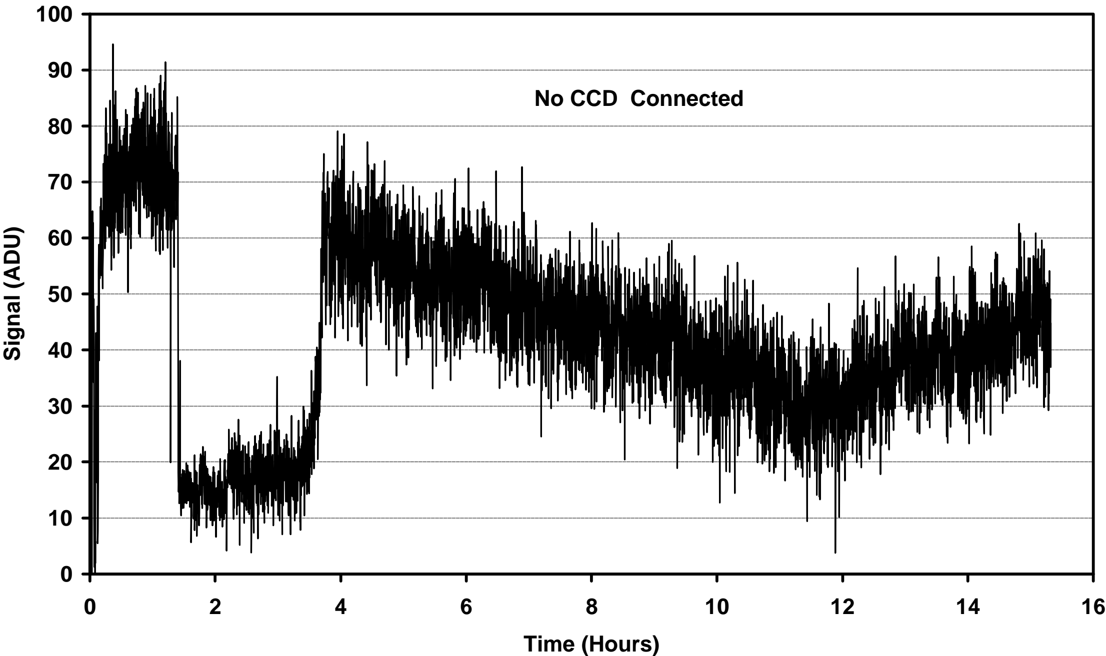

Figure 5.6-16 A signal trace obtained with the CCD disconnected

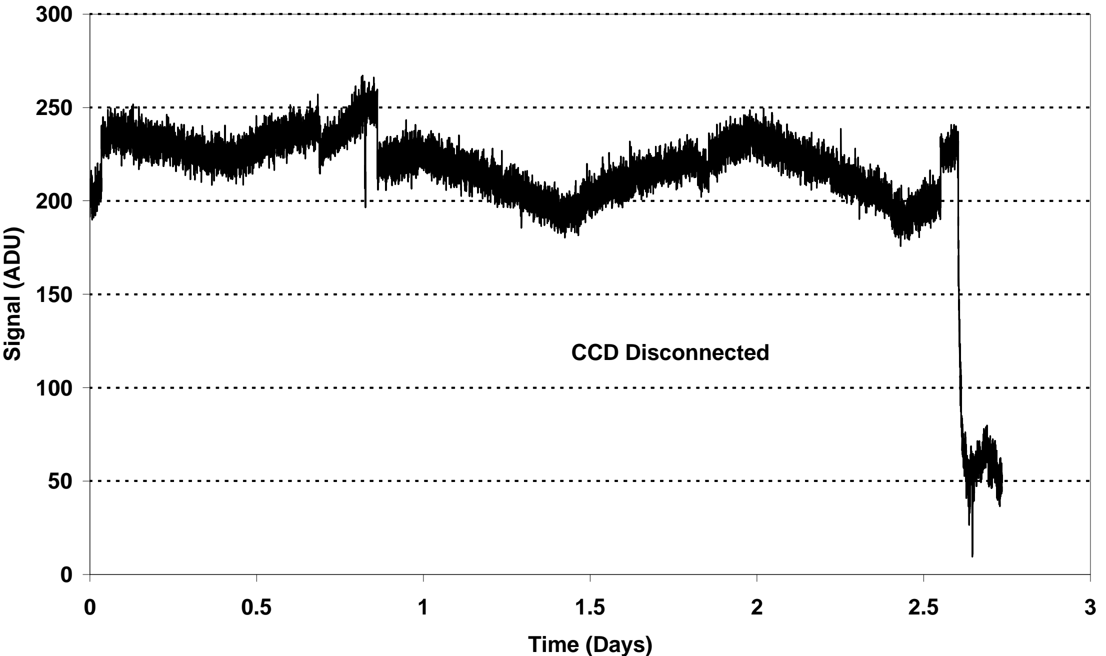

Figure 5.6-17 A signal trace obtained with the CCD disconnected

5.7 MEASURMENTS OF CHARGE TRANSFER INEFFICIENCY (CTI)

5.7.1 Measurements of CTI using First Pixel Response (FPR)

Measurements of the vertical CTI were made using the first pixel response (FPR) method for the CCD57-10, TH7890M and TH7863. The CCD55-20 could not be measured this way because of its AIMO structure which did not allow the image and storage regions to be clocked backwards. Measurements were made for a variety of signals and backgrounds. The clocking sequence was as follows:

- Expose the CCD with flat field illumination from an LED synchronized with the CCD clocking
- Move charge back from the image/storage region boundary to create a 'gap'
- Expose again to create background charge in the gap
- Frame transfer the image into the storage region
- Readout the image

It was usually arranged that the 'gap' was such that the CTI measurement was for a line of pixels at the centre of the image. Hence the number of transfers = number of image/storage region lines (moved at frame transfer rate = 4μs) and half the number at readout rate. With the TH7890M some measurements were also done with the FPR line at the top and bottom of the image (corresponding to nearly all frame transfer line moves and equal numbers of frame transfer and readout line moves, respectively.

It was usually found that the ratio between the CTIs for the 9.5 MeV and 60 MeV regions was 1.47±0.2 in the range –10 to -50ºC. This is not the same value as found for bulk dark current (which was ~ 2.0) suggesting that a different mixture of defects is responsible.

In all cases, the CTI for unirradiated regions was at least an order of magnitude less than for the irradiated regions. Hence it has been considered negligible and has been omitted from the plots in the following sections. For most signal and background conditions the unirradiated CTI was of the order of 10-5. However for small signals and backgrounds the CTI tended to be increased (just as for the irradiated regions). Figure 5.7.1-1 shows some typical results for a CCD57-10 and a TH7890M.

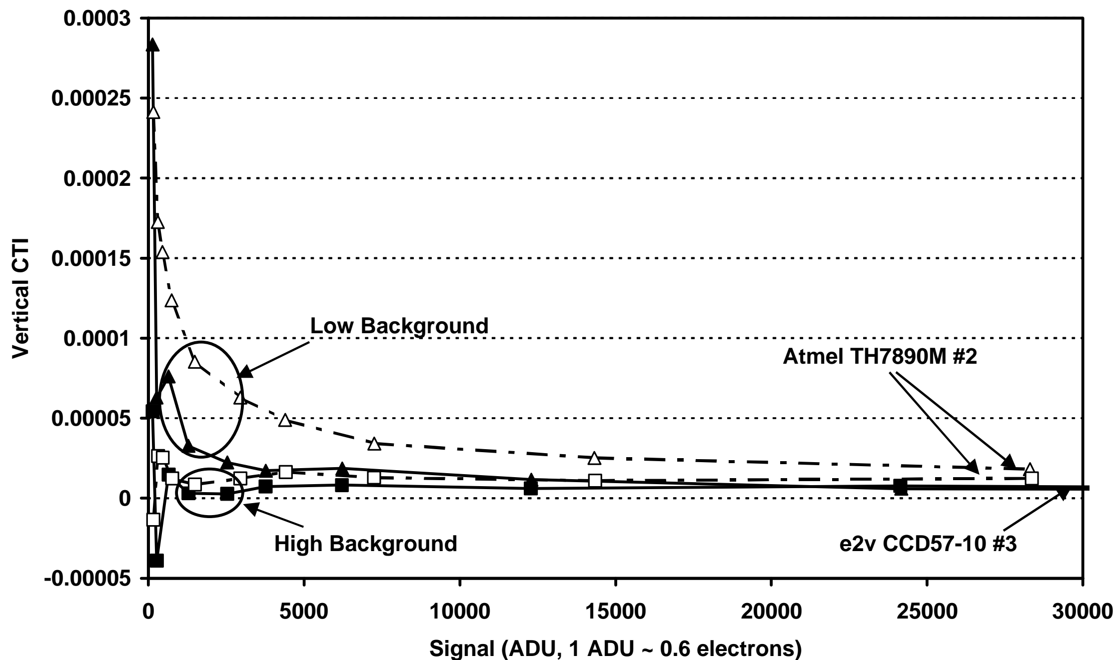

Figure 5.7.1-1 FPR CTI for unirradiated regions of a CCD57-10 and a TH7890M.

5.7.1.1 FPR Measurements on CCD57-10 devices

Vertical CTI data for the centre of CCD57-10 devices at various temperatures are shown in figures 5.7.1.1-1 to 5.7.1.1-3. The values can be scaled so that the CTI plots overlay as shown in figure 5.7.1.1-4. Note that the same scaling factors were used for the three devices #1, #2 and #5. Figure 5.7.1.1-5 shows the scaling factors versus temperature. It is seen that the CTI decreases as the device is cooled, but at the higher temperatures (-20 to -30ºC) the effect is not large.

The above values are for the centre of the image. Figures 5.7.1.1-6 and 5.7.1.1-7 show the way the CTI varies with position in the image – with top of the image (mostly fast frame transfer line moves) giving a lower CTI and the bottom of the image (equal numbers of fast and slow line moves) giving a higher CTI. The data is consistent with a factor ~ 3 difference in CTI between the two types of line moves, which is similar to the findings of previous investigations.

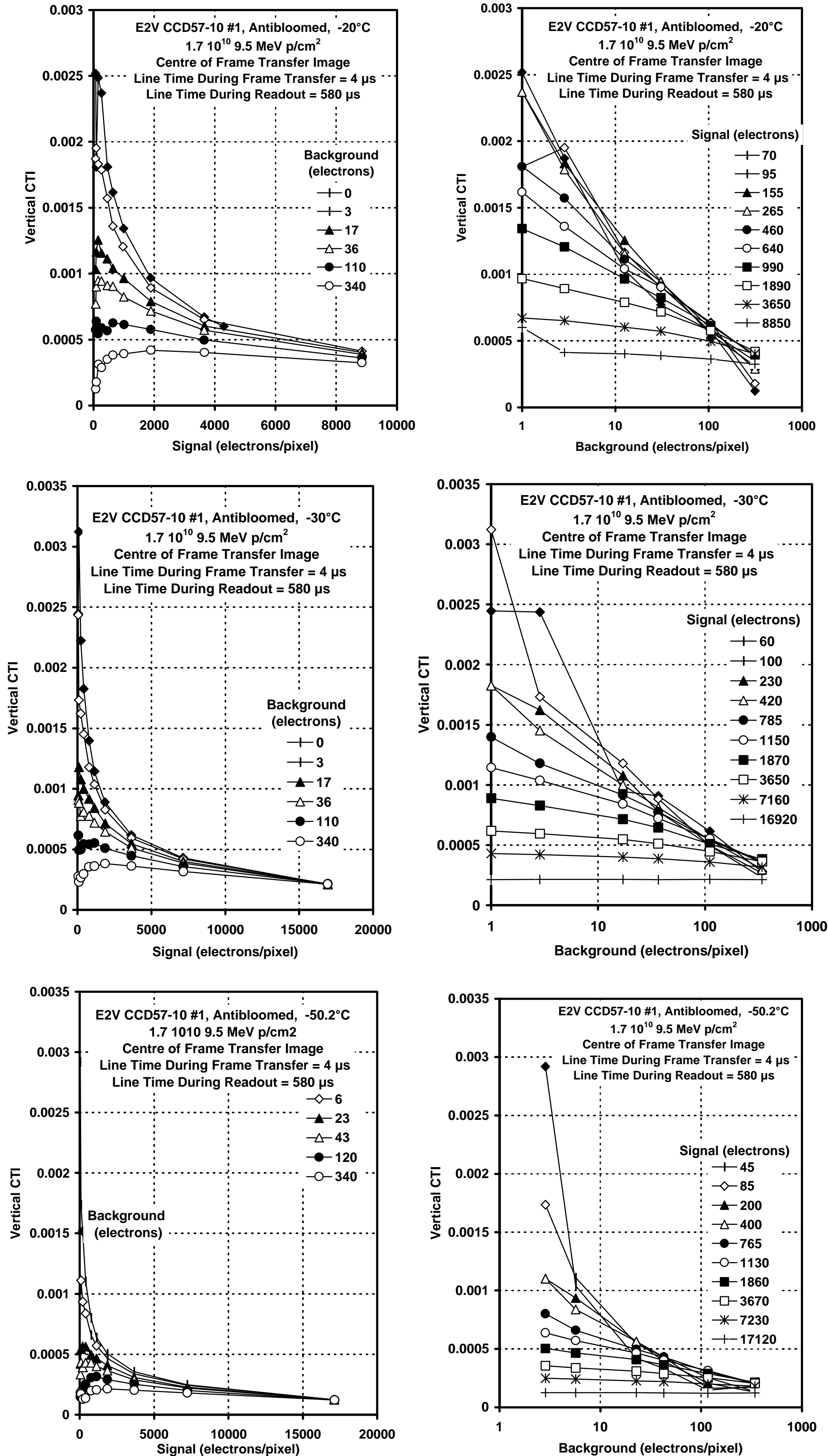

Figure 5.7.1.1-1 FPR CTI for CCD #1, centre of image

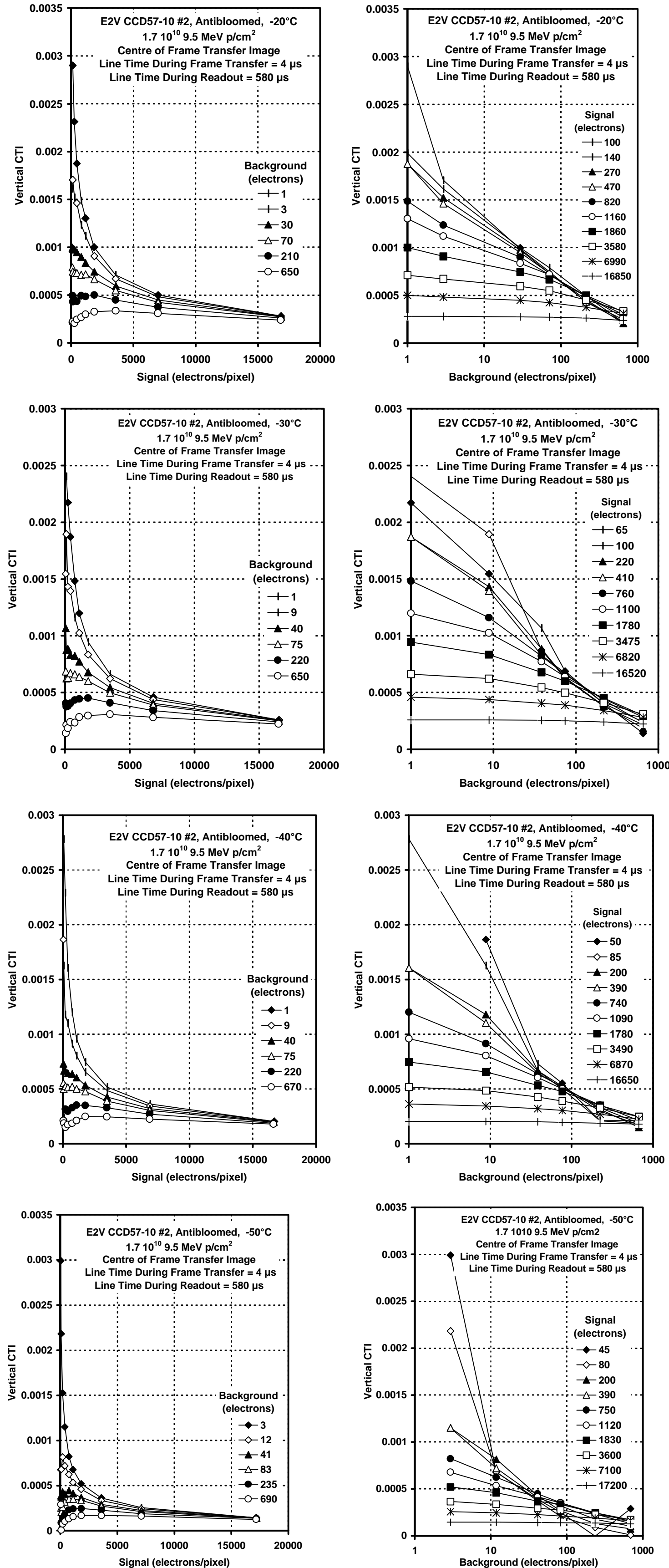

Figure 5.7.1.1-2 FPR CTI for CCD #2, centre of image

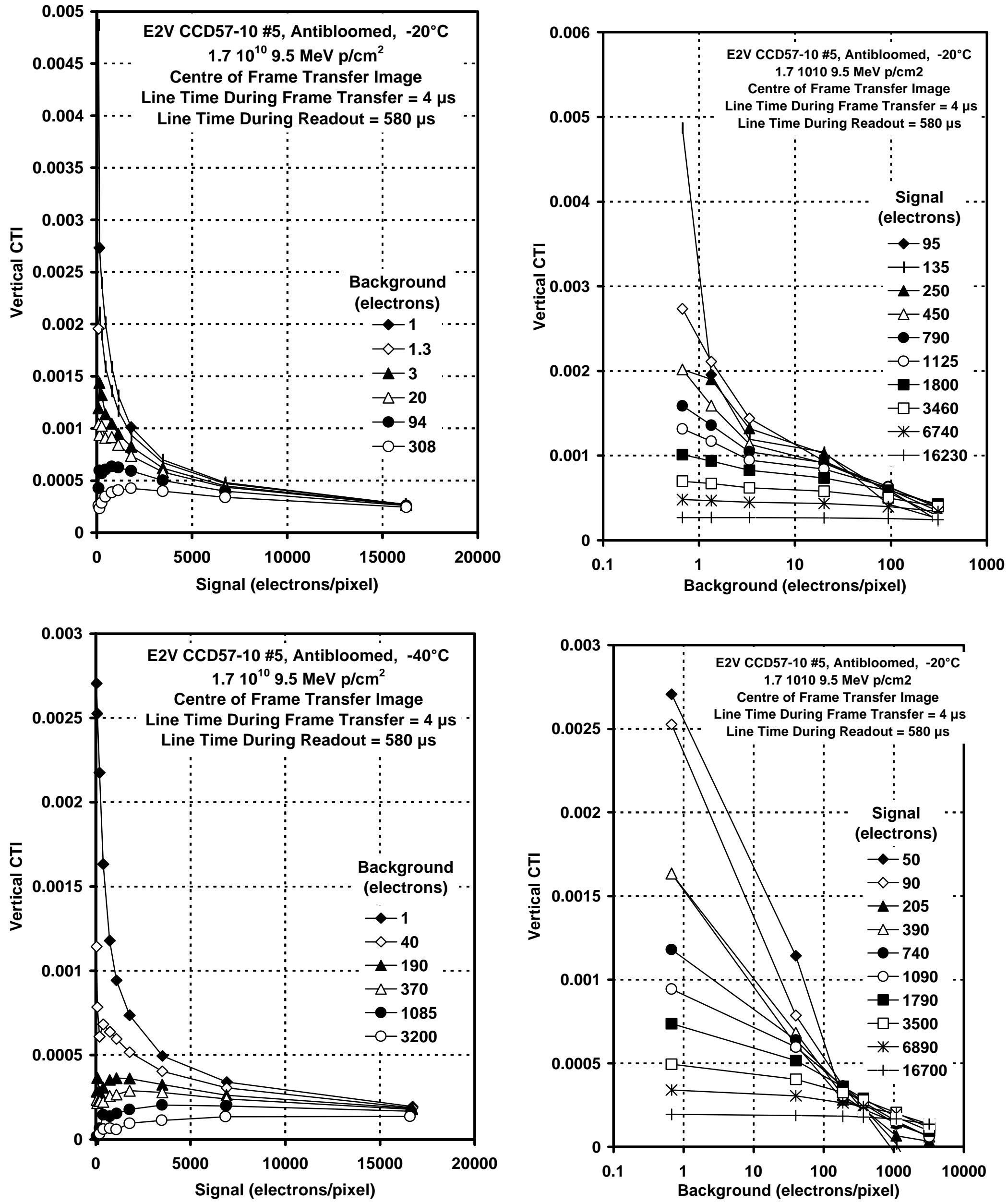

Figure 5.7.1.1-3 FPR CTI for CCD #5, centre of image

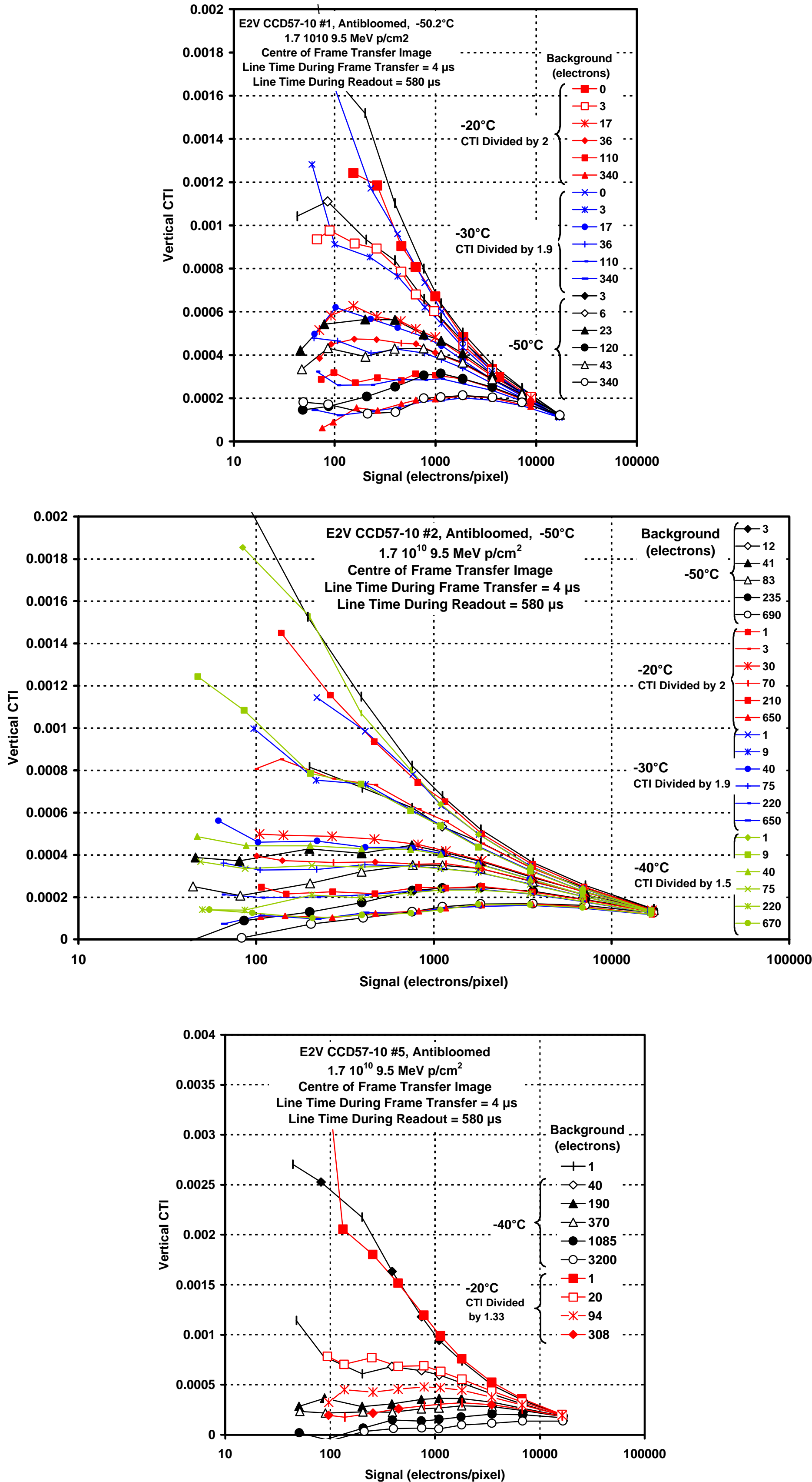

Figure 5.7.1.1-4 FPR CTI values, scaled for temperature, centre of image

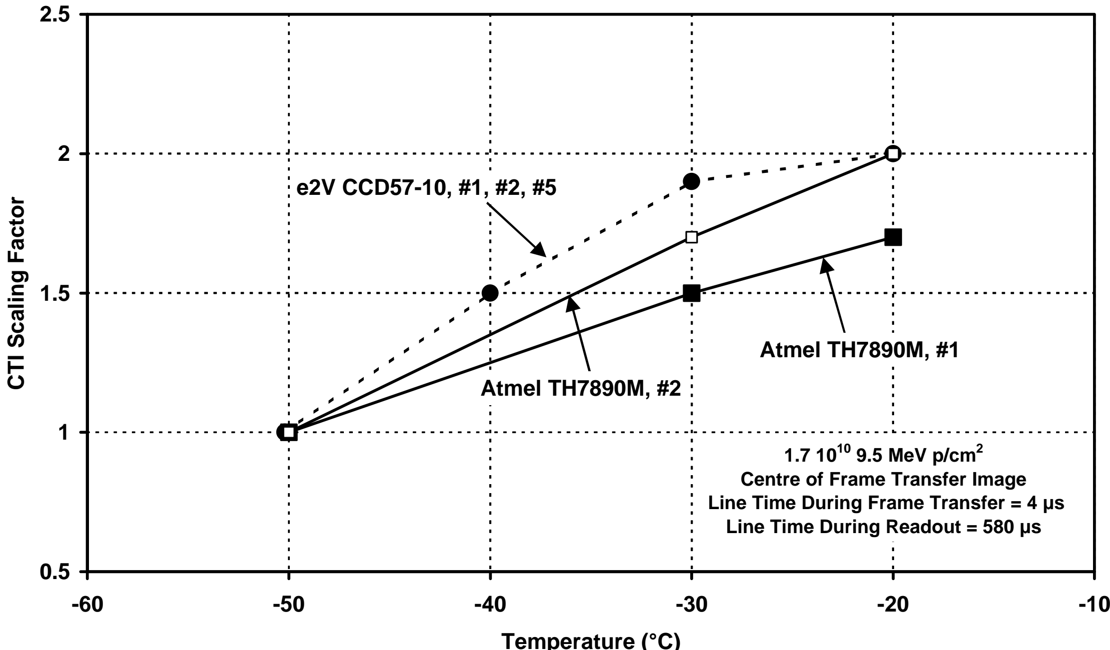

Figure 5.7.1.1-5 FPR CTI scaling factors.

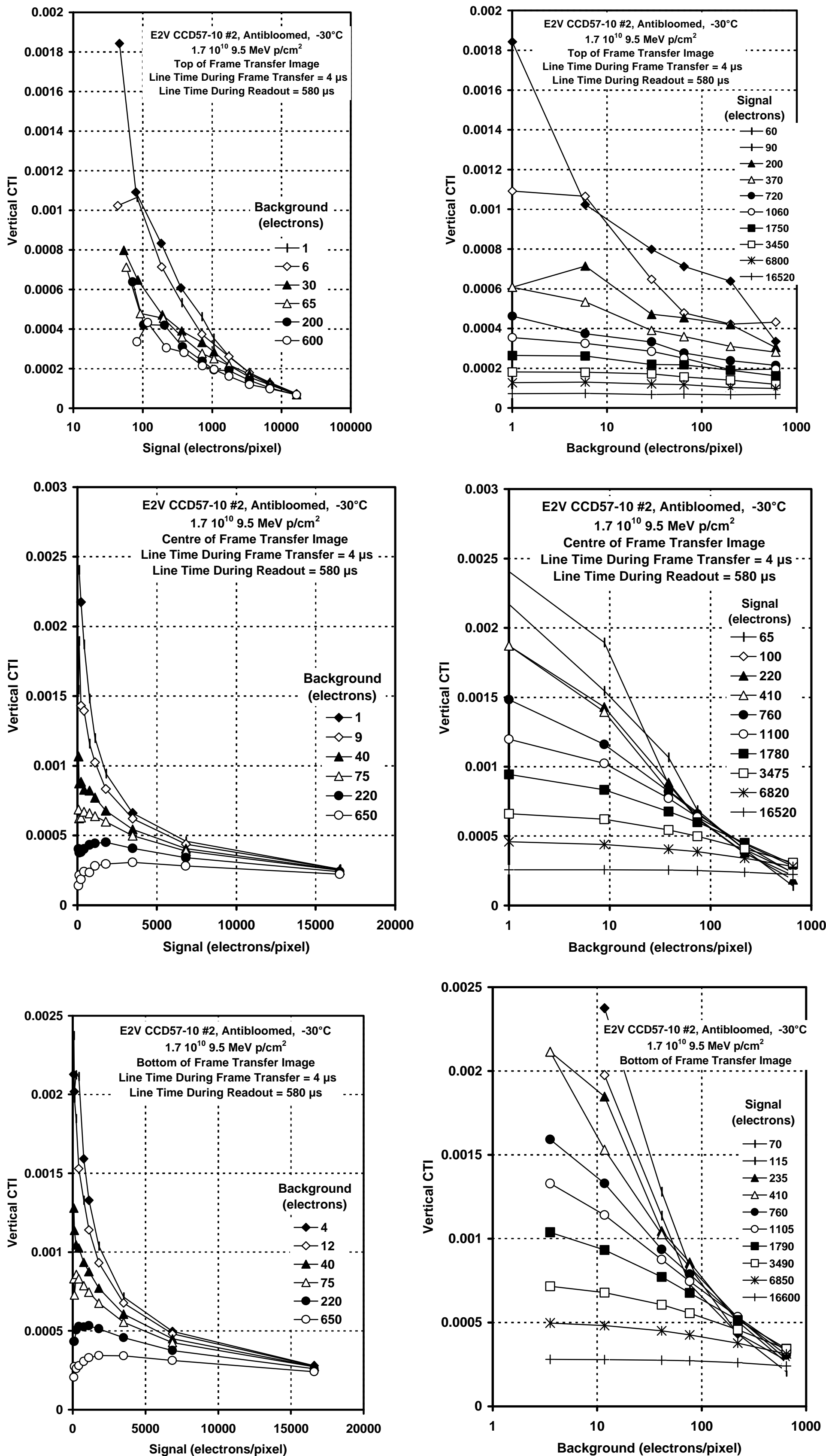

Figure 5.7.1.1-6 FPR CTI, -30°V

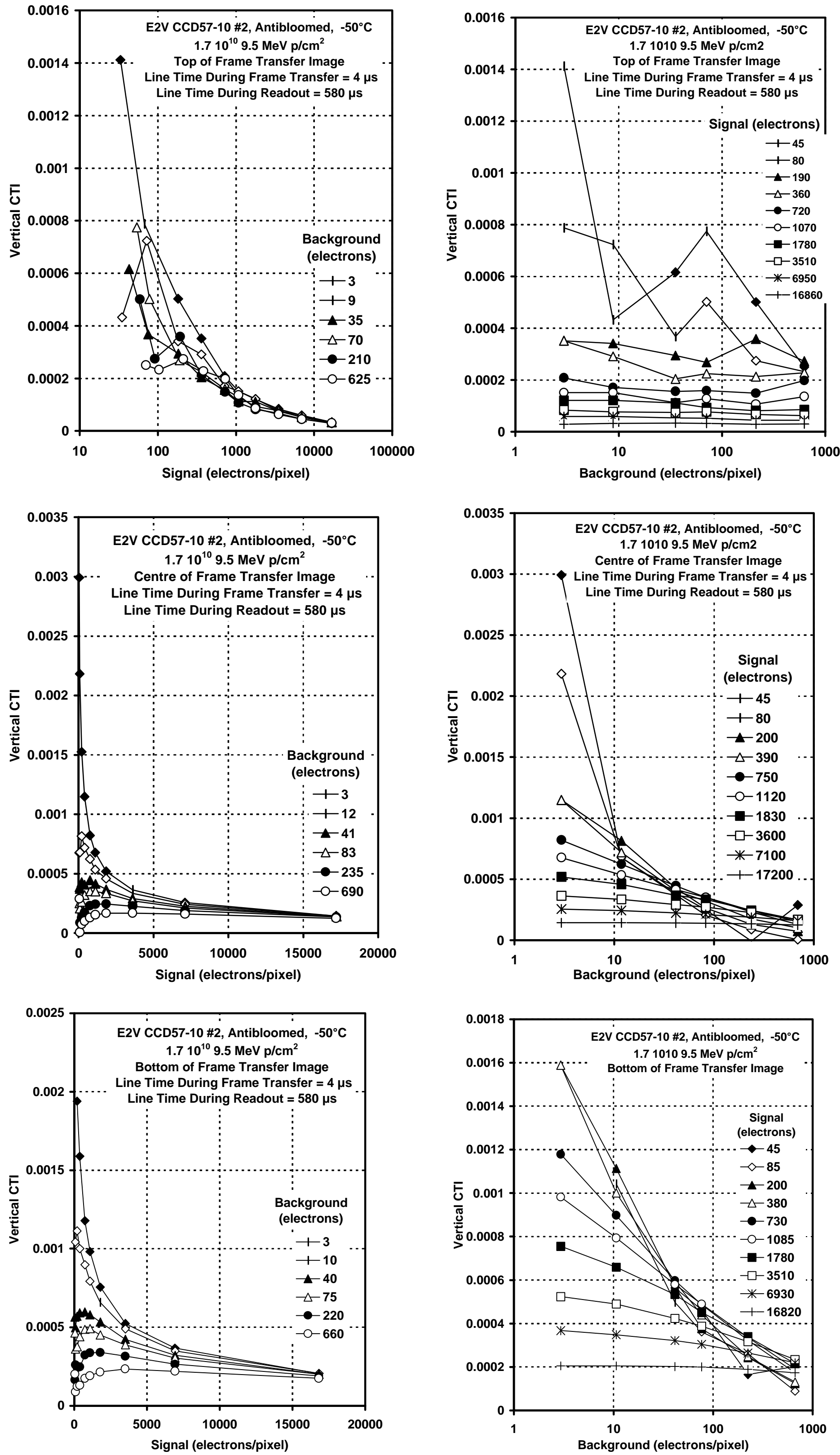

Figure 5.7.1.1-7 FPR CTI, -50ºV

If the CCD is cooled to temperatures around –100ºC the dominant trap can be kept filled and the CTI is reduced (see para 5.7.2). Figure 5.7.1.1-8 shows that the improvement is roughly a factor 6 compared with -50ºC. There is considerable scatter in the plots because of measurement uncertainties but it can be seen that there is little difference in the CTI over the range –95 to -120ºC.

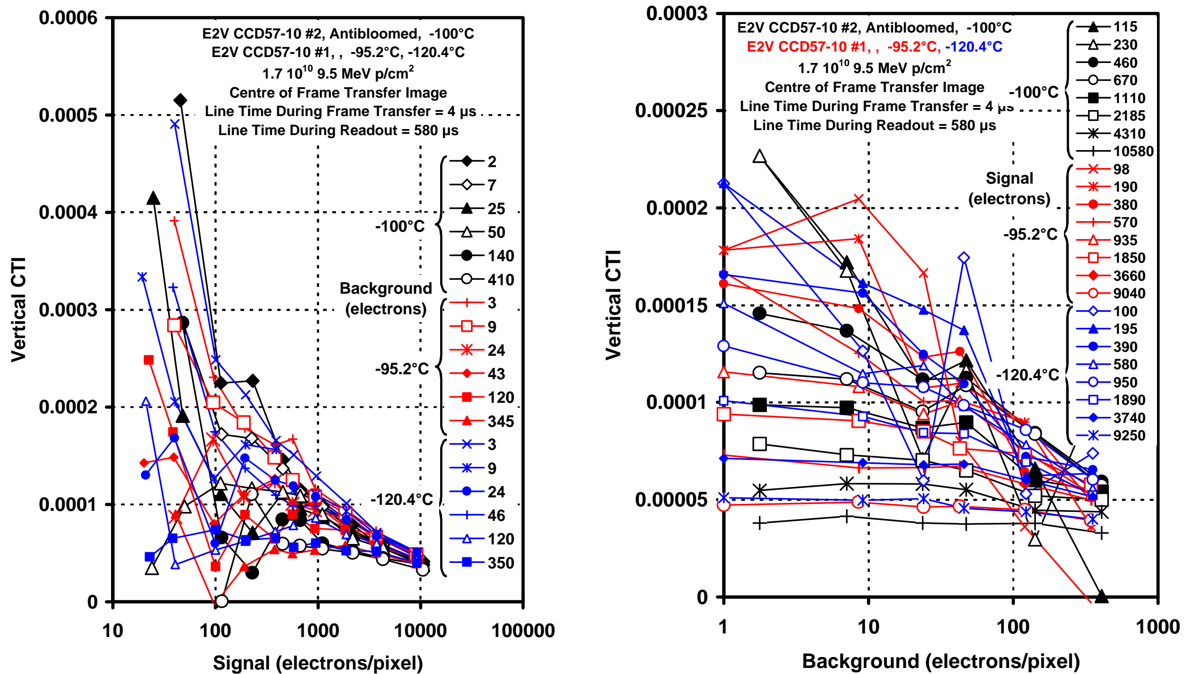

Figure 5.7.1.1-8 Vertical CTI at low temperatures

5.7.1.2 FPR Measurements on TH7890M devices

CTI values at varying signal, background and temperature for the TH7890M devices are given below in figure 5.7.1.2-1 for data taken at the centre of the image. As with the e2v ccd57-10 the vertical CTI reduces with cooling and the plots can be overlayed if the data is appropriately scaled (figure 5.7.1.2-2). The scaling factors are plotted against temperature in figure 5.7.1.1-5, along with the corresponding e2v data. Slightly different scaling factors were needed for the two CCDs that were studied at different temperatures.

Figure 5.7.1.3 shows results at -90ºC and -110ºC. It is seen that the CTI is reduced compared with the -50ºC data. An attempt at scaling the data to compare with -50ºC is shown in figure 5.7.1.4. The scaling is not so good as at the higher temperatures but seems to be still aproximately valid. Figure 5.7.1.2-5 shows the scaling factors as a function of temperature (same as figure 5.7.1.1-5 but extended to lower temperatures).

The above values are for the centre of the image. Figure 5.7.1.2-5 show the way the CTI varies with position in the image – with top of the image (mostly fast frame transfer line moves) giving a lower CTI and the bottom of the image (equal numbers of fast and slow line moves) giving a higher CTI. The data is consistent with a factor ~ 3 difference in CTI between the two types of line moves, which is similar to the findings of previous investigations.

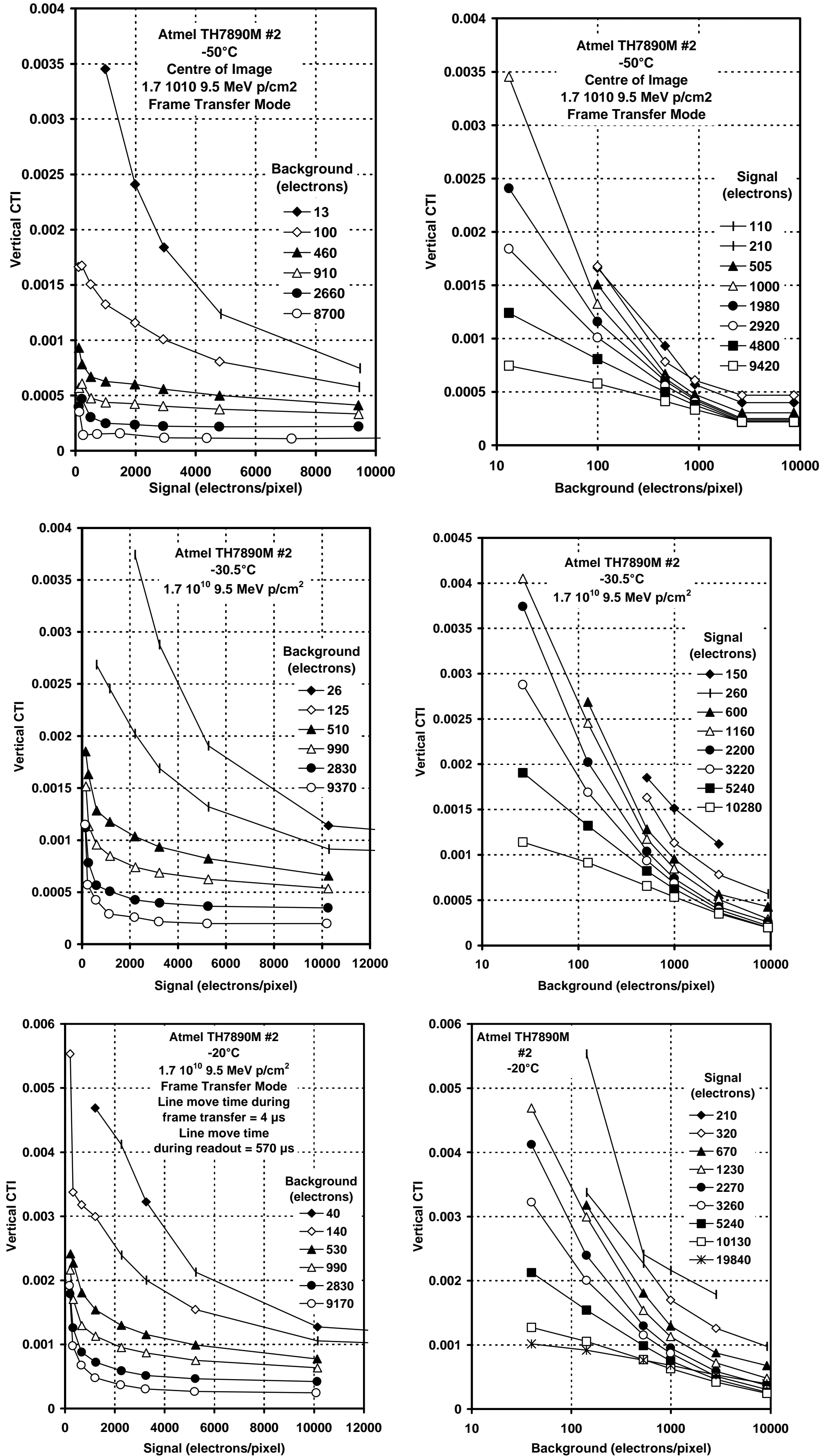

Figure 5.7.1.2-1 FPR CTI for CCD #2, centre of image

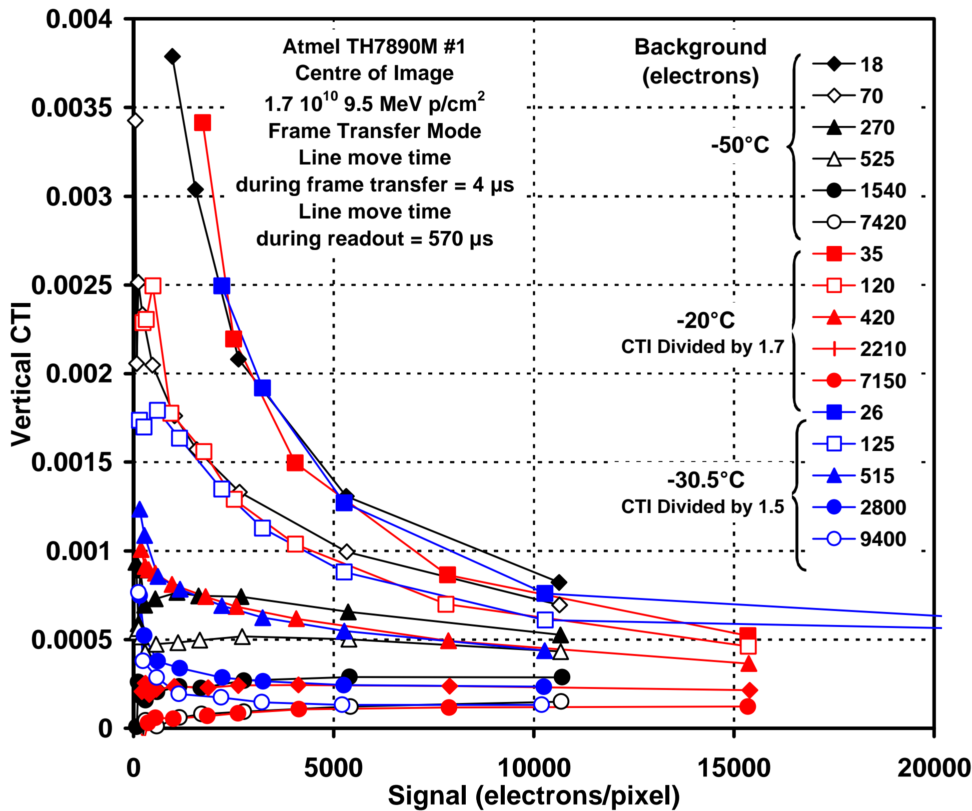

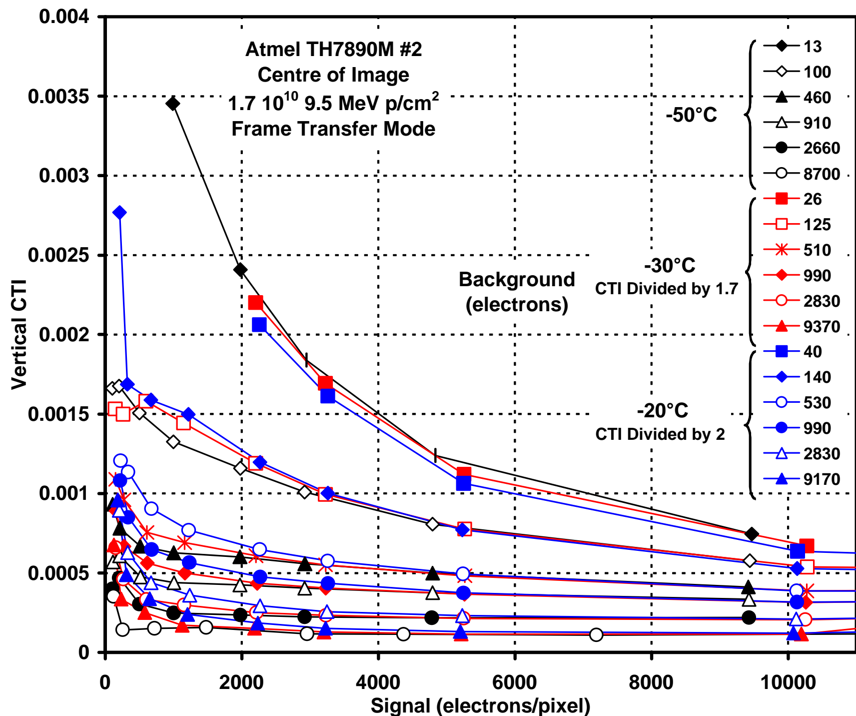

Figure 5.7.1.2-2 Vertical CTI at various temperatures. The CTI has been scaled so that the plots are overlaid

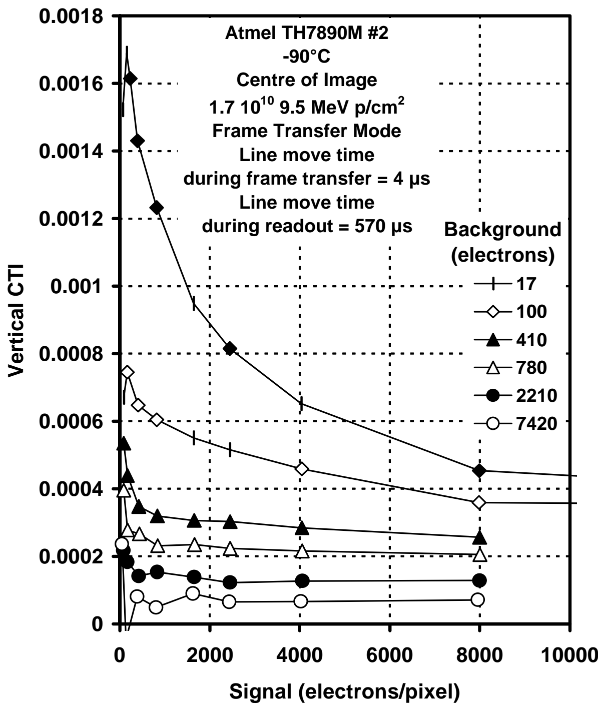

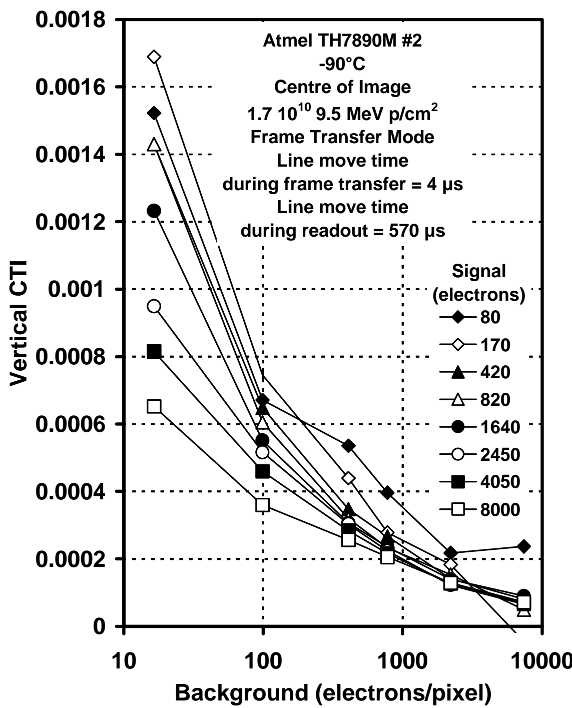

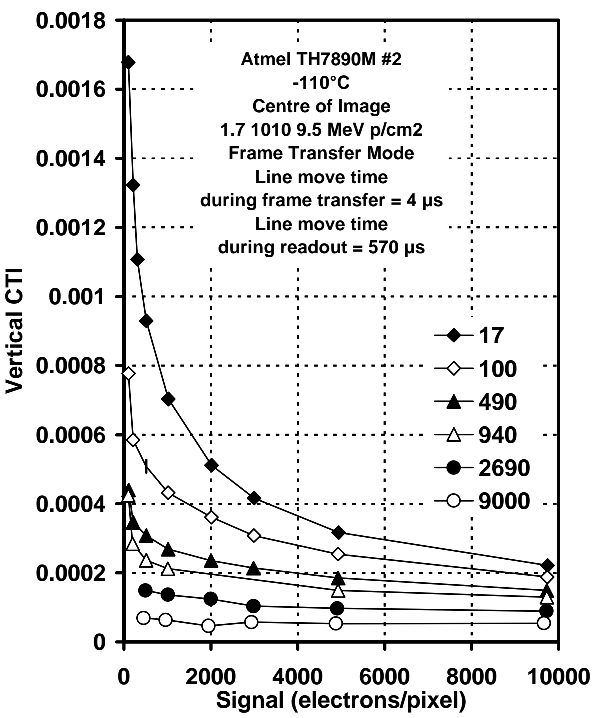

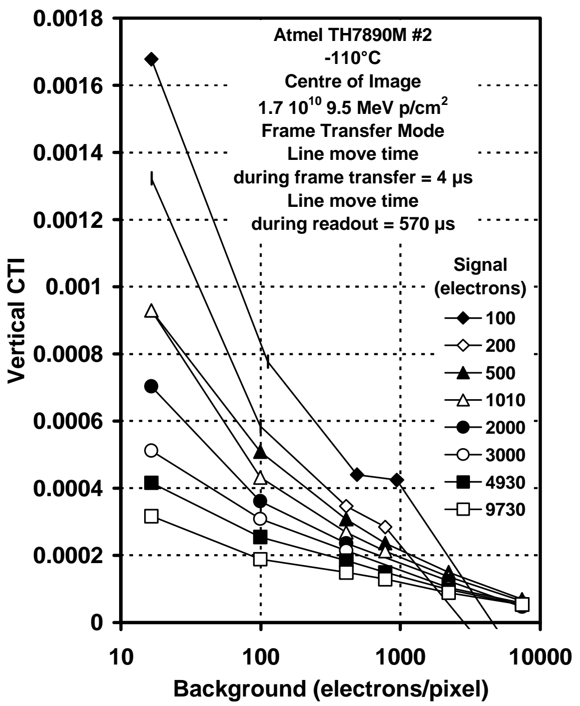

Figure 5.7.1.2-3 vertical CTI data at low temperatures

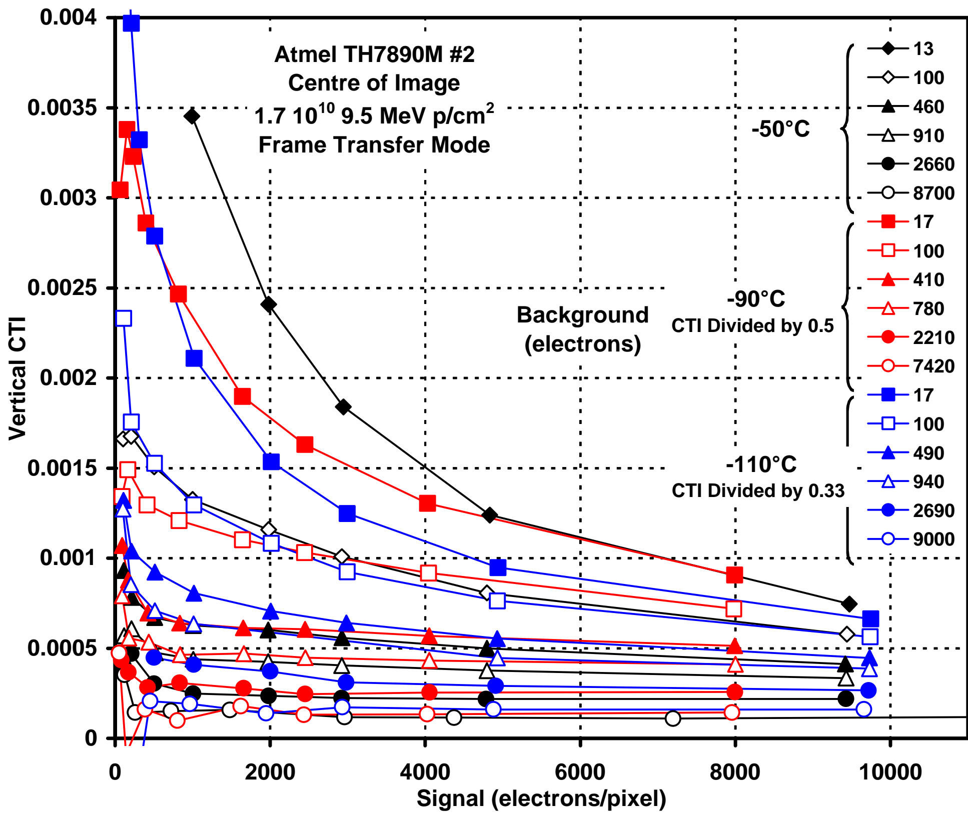

Figure 5.7.1.2-4 Scaled vertical CTI data at low temperatures

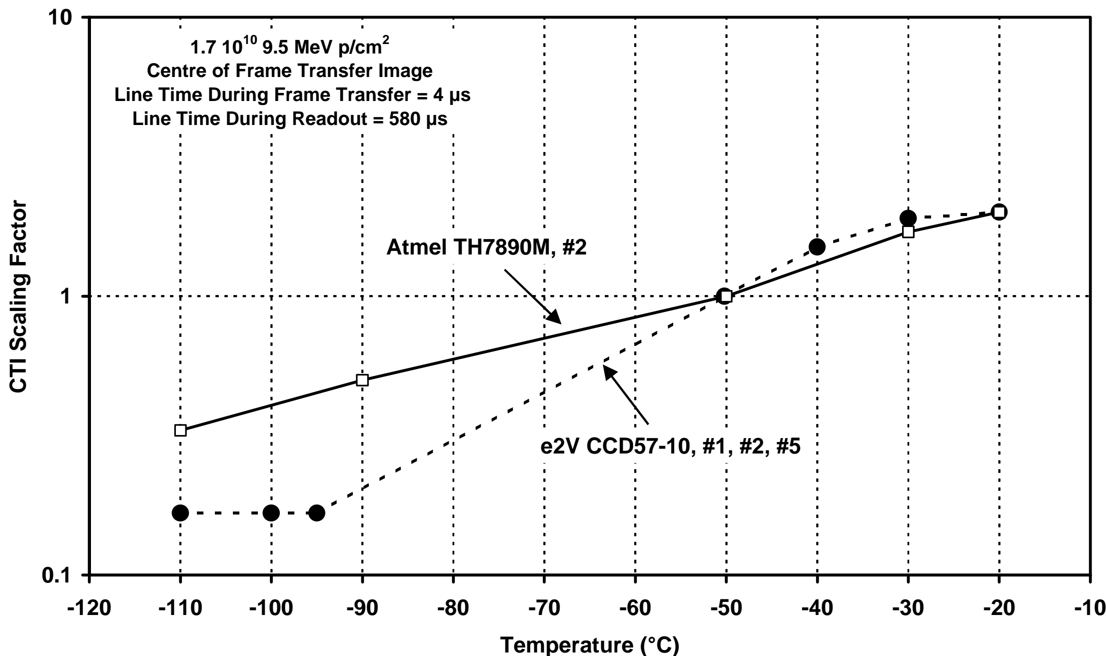

Figure 5.7.1.2-5 CTI scaling factors

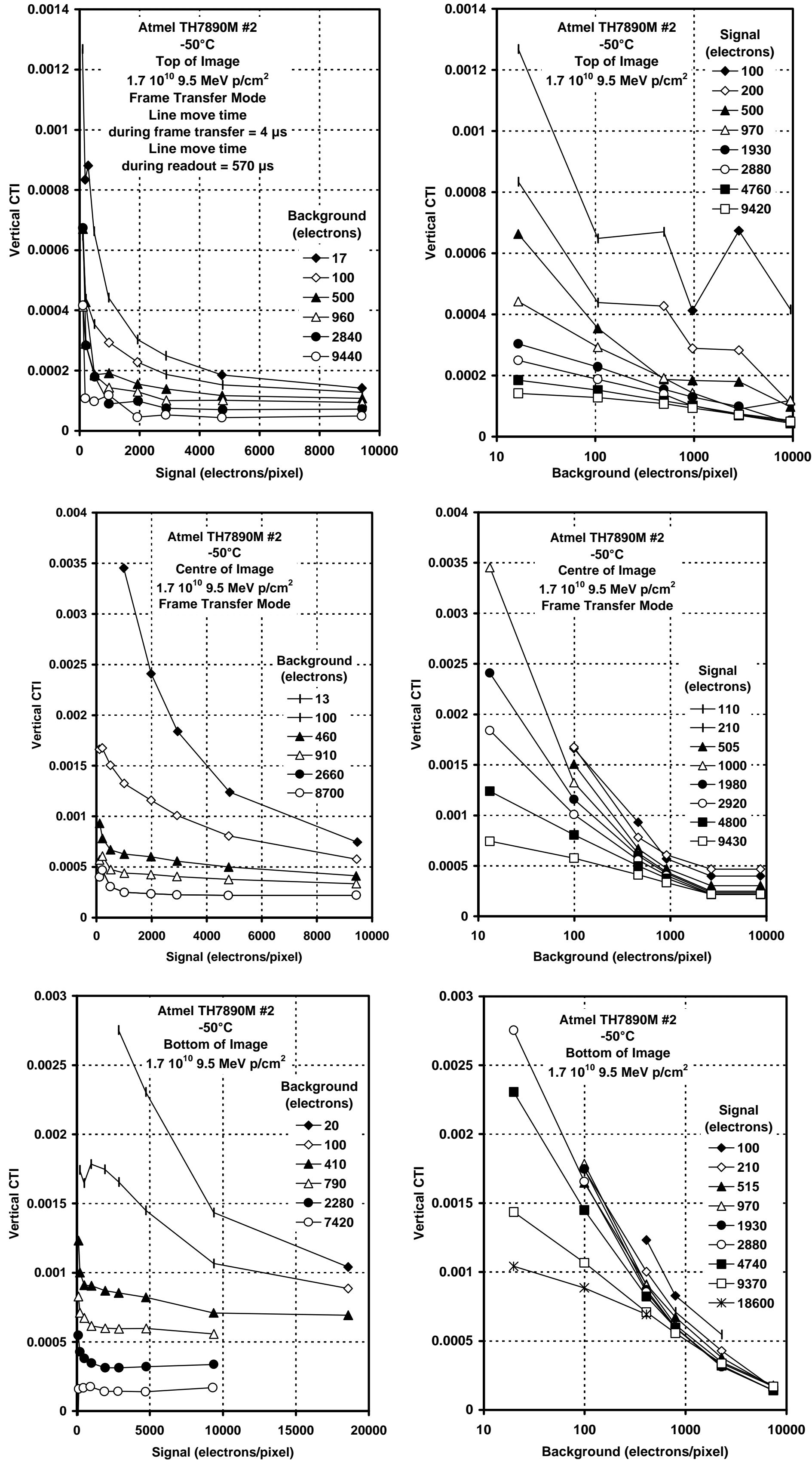

Figure 5.7.1.2-6 CTI values for the top, centre and bottom of the image

5.7.1.3 FPR Measurements on TH7863D devices

Vertical CTI data for the TH7863D device that was proton irradiated is shown below.

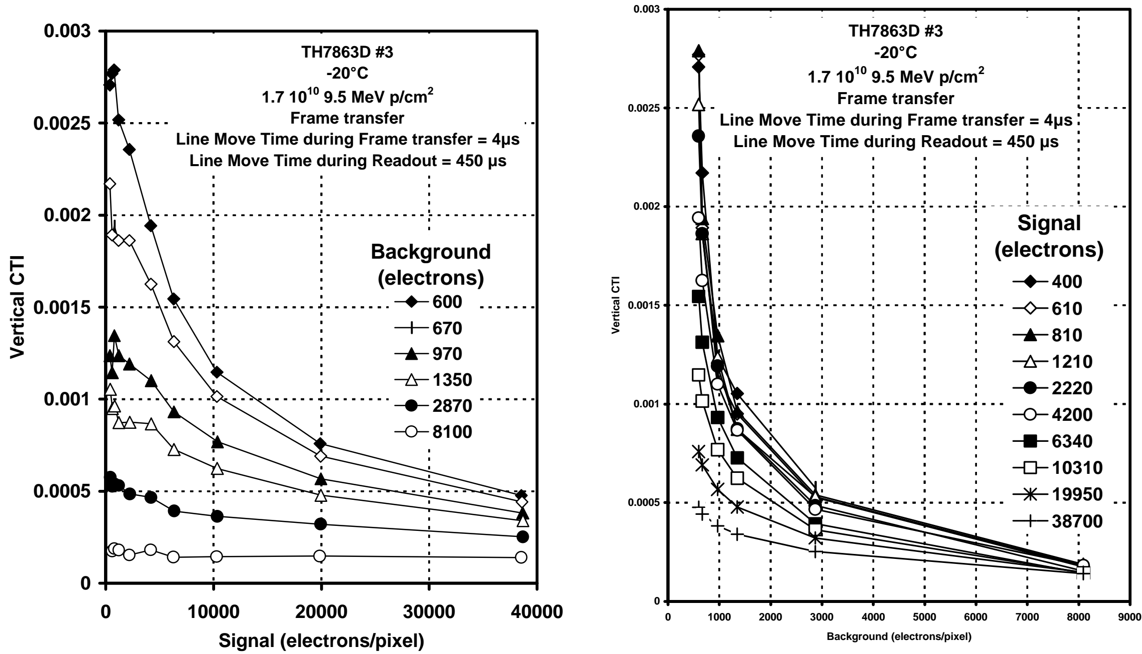

Figure 5.7.1.3 TH7863D FPR CTI data for CCD # 3

5.7.2 CTI Annealing

Vertical CTI FPR measurements were made at –50 and -20ºC before annealing and after 3 days bake, first at 82.5ºC, then at 110ºC and finally at 150ºC. It was found that the CTI was progressively reduced and that the values could be scaled so that the CTI curves accurately overlapped.

5.7.2.1 e2v CCD57-10

Figure 5.7.2.1-1 shows the scaled CTI data before and after baking. The scaling factors are shown, along with the corresponding dark signal annealing factors in figure 5.7.1-2.

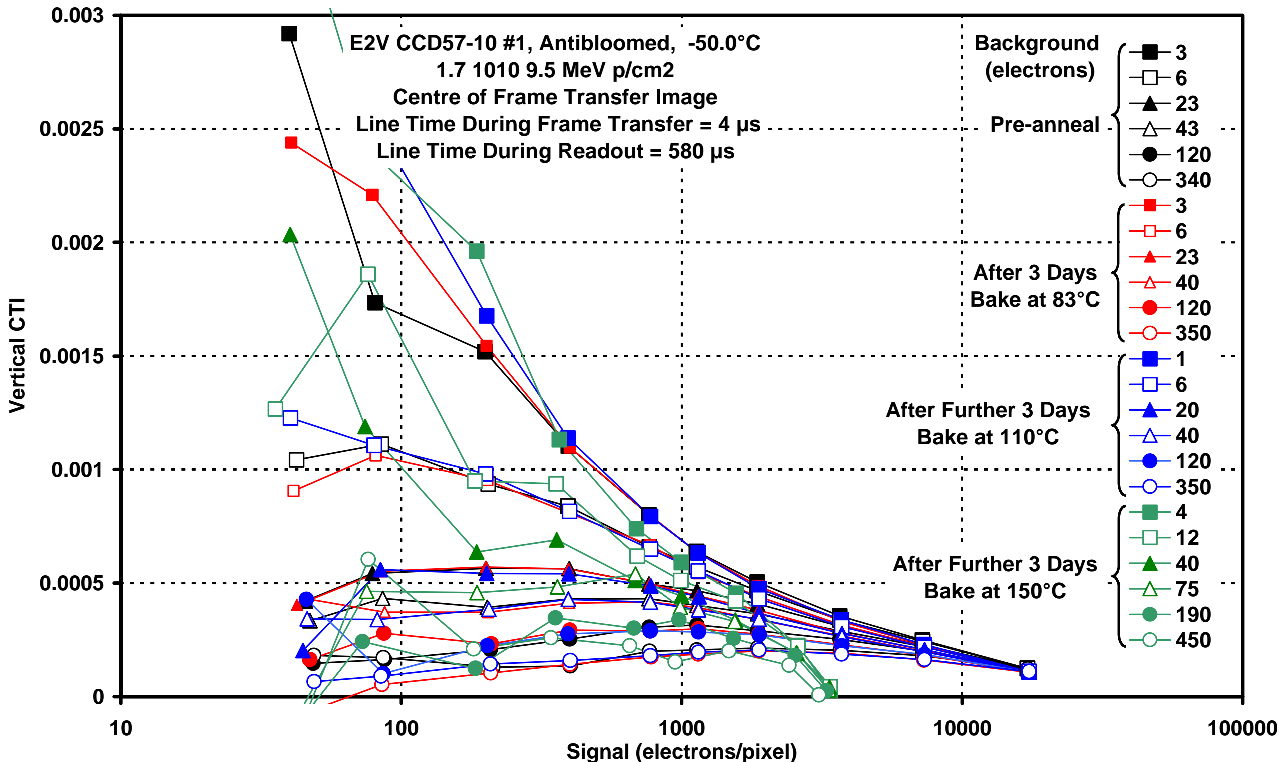

Figure 5.7.2.1-1 Scaled CTI data for the CCD57 before and after annealing.

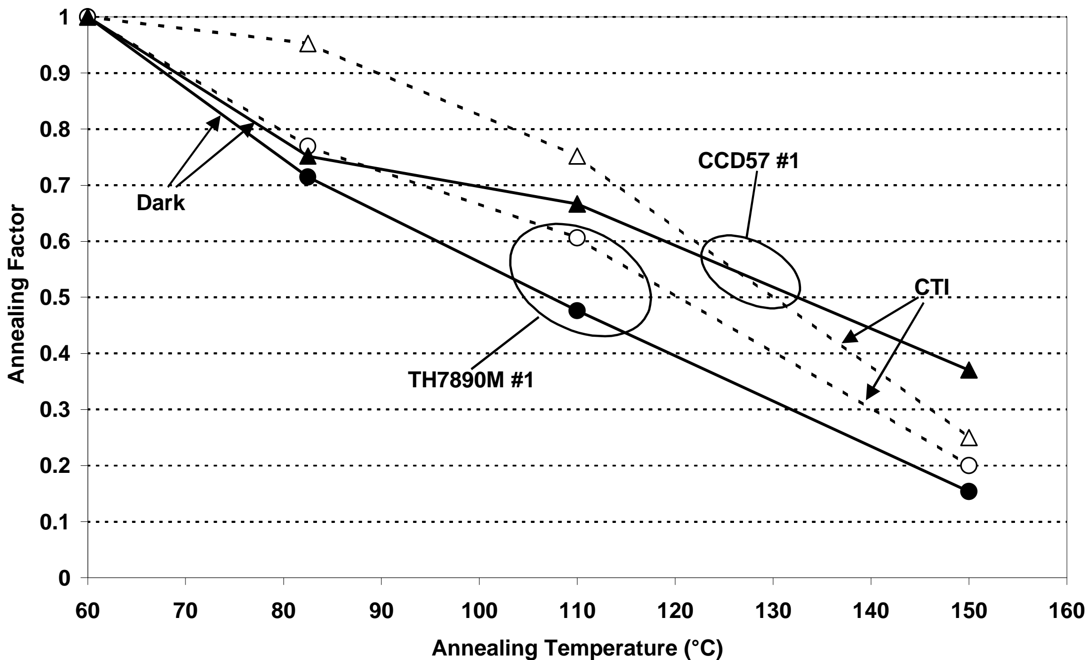

Figure 5.7.2.1-1 Annealing factors for CTI and average dark signal

5.7.2.2 Atmel TH7890M

Figure 5.7.2.2-1 shows the scaled CTI data before and after baking. The scaling factors were shown, along with the corresponding dark signal annealing factors in figure 5.7.1-2.

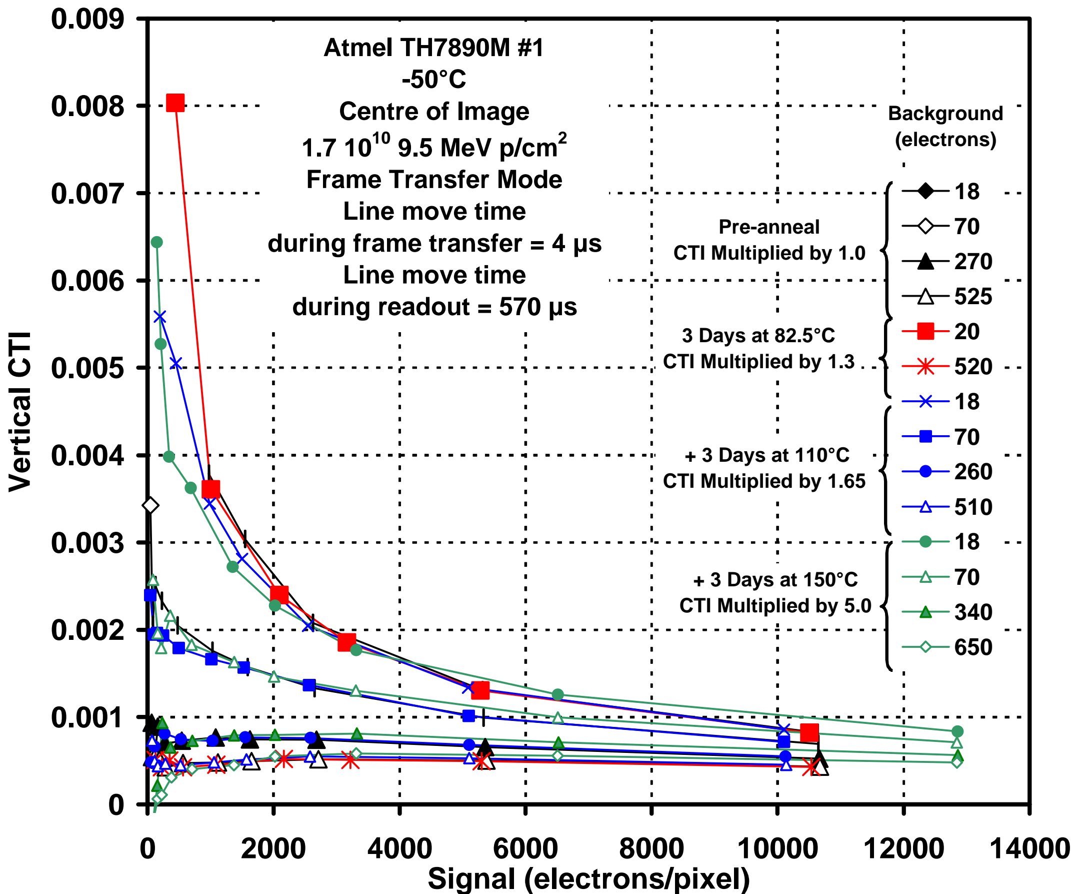

Figure 5.7.2.2-1 Scaled CTI data for the TH7890M before and after annealing.

5.7.3 Comparison of CTI Values

It is rather difficult to compare the vertical CTI values for the three chips because of the differences in the background, signal, temperature and clocking dependencies. Figure 5.7.3-1 shows values at -20ºC (which was a temperature where measurements were available for all three device types). Two sets of plots are shown: at low backgrounds (~30 electrons) and at higher backgrounds (~500 electrons). Note that the TH7863D could only be measured at high backgrounds because of the large surface dark current.

It is seen that the TH7890M and TH7863D are roughly comparable if the TH7890M data is multiplied by 1.7. This factor is in good agreement with the ratio of the pixel size (factor 1.8) – though strictly speaking the width of the channel stops also has to be taken into account.

At low backgrounds the CCD57 data has to be multiplied by 4.5 to be comparable with the TH7890M, but at high background the multiplying factor is 3 (though an exact comparison is not possible because of differences in the background value). This is again reasonable since, although the ratio of pixel areas is 1.7, the CCD57 is an antibloomed device and so has a smaller channel width.

It is concluded that, to a first approximation, the differences in CTI are consistent with the differences in pixel architecture.

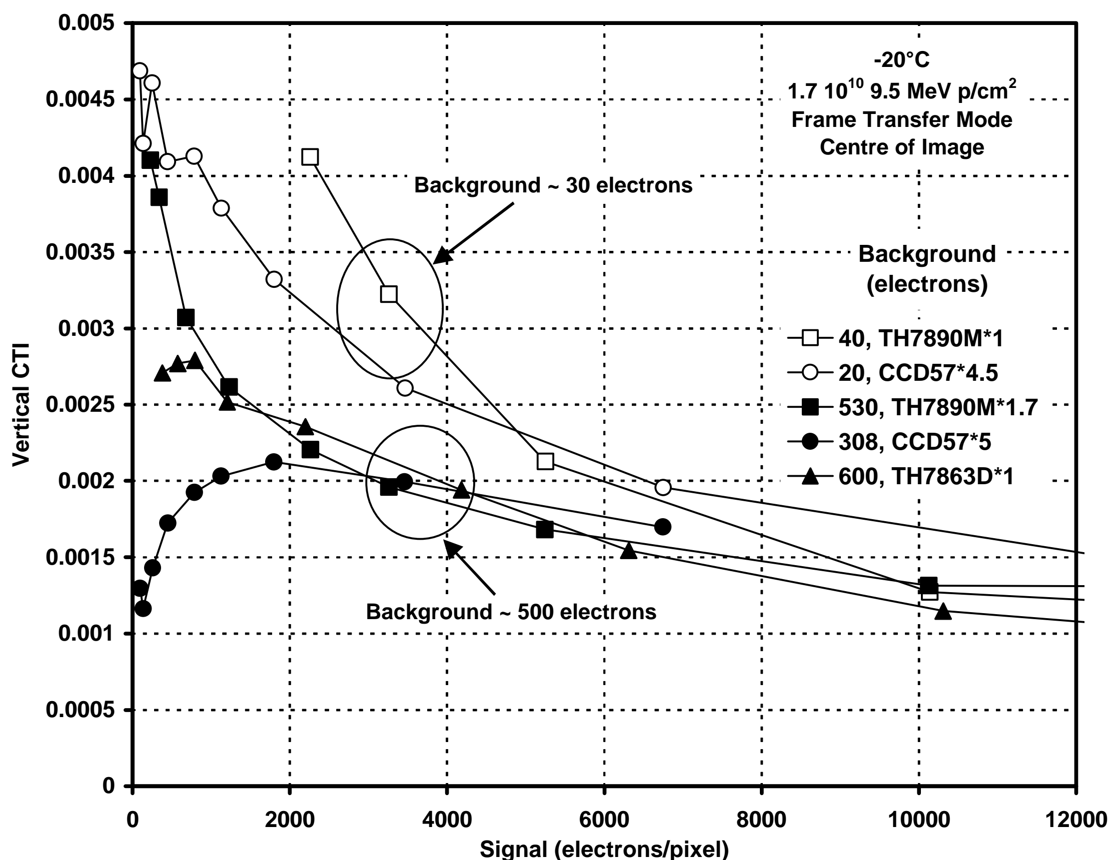

Figure 5.7.3-1 Vertical CTI devices for the CCD57, TH7890M and TH7863D at -20ºC, after scaling of CTI values.

5.7.4 Measurements of Trap Emission Time Using FPR

Trap emission times were measured using the FPR technique and varying the 'gap' between the pre-injected and the signal charge. This was done for the CCD57-10 and TH7890M devices.

All the measurments could be fitted with a long time constant and a very short one (the starting value of VCTI plot). For the CCD57, 93% of traps had the longer time constant (both the devices measured, CCDs 1 and 2). For the TH7890M, ~ 72% had the longer time constant (77% for CCD #1 and 66% for CCD #2). Hence there appears to be a difference in trap concentration ratios for the two types of CCD. A ratio of ~1.5 was obtained for the CTI values at 9.5 and 60 MeV for all devices, regardless of FPR 'gap' and temperature. The trap time constants themseves were not found to vary with proton energy.

Figures 5.7.4-1 and 5.7.4-2 show results for the CCD57 and figure 5.7.4-3 for the TH7890M. The values obtained for the long time constant trap are shown in figure 5.7.4-4. These values are in very good agreement with previous measurements and give a trap energy level of 0.440 eV. A good candidate for this trap is the E centre but it is possible that a mixture of traps are involved (possibly including the divacancy and other higher order vacancy centres). Measurements of the vertical CTI were also made at temperatures around –90ºC but these seemed to give time constants around 130 ms which is too fast for the E center. Possibly at this temperature there are a mixture of traps that cannot be easily separated using the vertical CTI measurements.

The 3-phase readout register of the CCD57-10 also allowed measurements of trap time constants. This was useful to extend the measurements of the longer time constant trap (and measurements are included in figure 5.7.4-4) and at temperatures around -100ºC to measure the short time constant trap. The low temperature results are shown in figure 5.7.4-5. The emission time of the fast trap is ~ 20 µs, which is consitent with what might be expected for the divacancy (0.23 eV) but the temperature dependence shown in the figure indicates a trap level ~ 0.17 eV or less. This value is more indicative of the A center, but these traps are several orders of magnitude faster so this possibility is ruled out. Again, it is possible (if not likely) that the temeprature variation of the time constant is being distorted by the presence of more than one trap.

Figure 5.7.4.5 also shows results from fitting a multi-trap model to the horizontal CTI data. The fits to the data with this model are just as good (maybe slightly better in some cases) so the fit is plausible. The plot shown gives an activation energy 0.23 eV, which would be consistent with the divacancy. But note that the data alone cannot be used to distinguish the model to be used. It appears that much better quality data (many more data points and repeated measurements) would be needed to determine the traps unambiguously. This could perhaps be achieved but only with an order of magnitude increase in measurement effort.

The trap times (in µs) used in the multi-trap model are listed below, with the traps used in the 0.23 eV plot highlighted in bold. The entries shown '*' are would be too long or to short to measure. The trap concentrations were approximately equal.

	Trap A	**Trap B**	Trap C
-90ºC	*	**4 µs**	20 µs
-100ºC	*	**9 µs**	40 µs
-120ºC	22 µs	**70 µs**	*
-125ºC	30 µs	**110 µs**	*

Note that the CTI values are about an order of magnitude reduced at temperatures around -100ºC (compared with near room temperature), as would be expected from the fact that the long time constant traps are kept filled.

Figure 5.7.4-6 shows trap emission times after annealing. The shapes of the plots for the 9.5 and 60 MeV regions are very similar, indicating that there is little change in the trap concentration ratios.

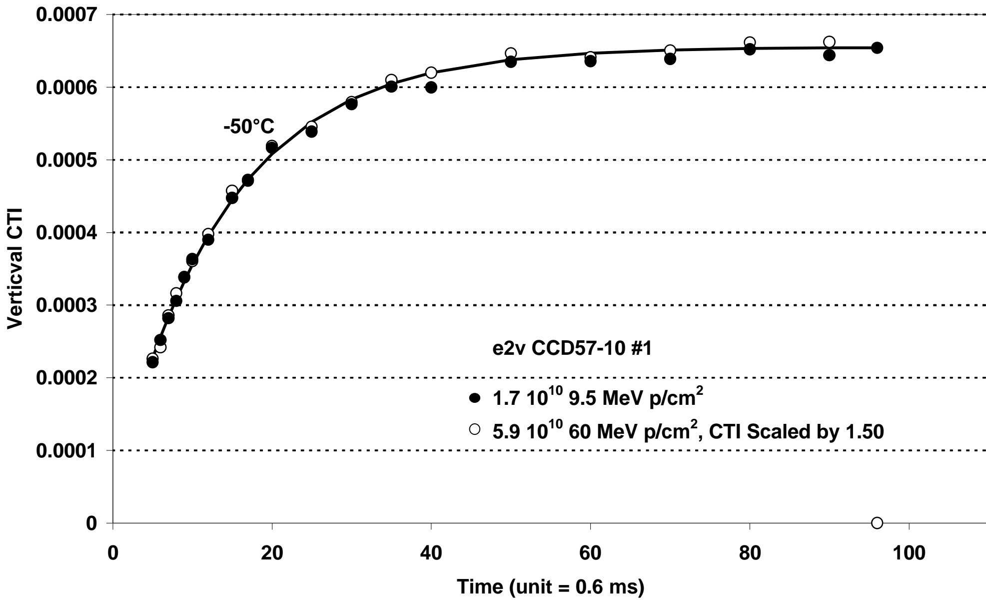

Figure 5.7.4-1 CTI versus FPR 'gap' for the CCD57 #1 .The 60 MeV CTI values have been divided by 1.47 to make the plots coincide. Also shown (thick line) is a theoretical fit assuming a long time constant trap and a very short time constant trap which gives an offset to the CTI values for small gap times.

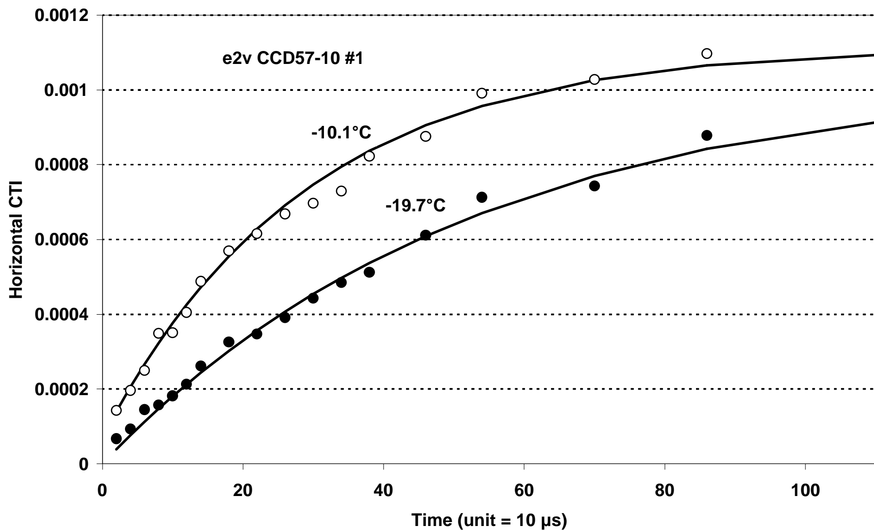

Figure 5.7.4-2 As figure 5.7.2-1 but obtained using horizontal CTI

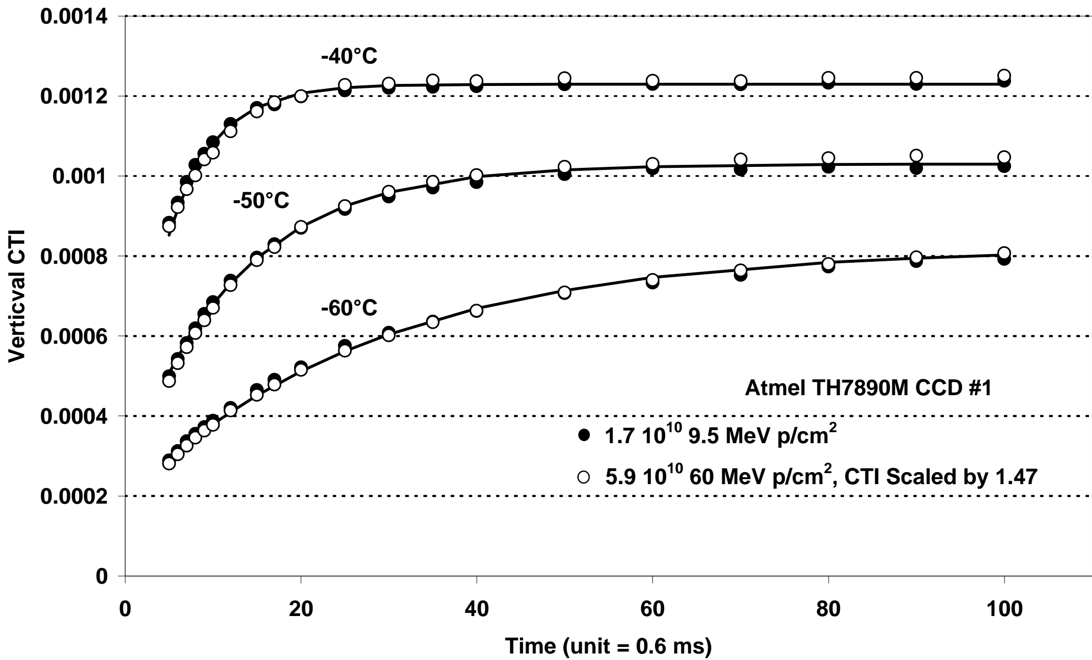

Figure 5.7.4-3 As figure 5.7.4-1 but for the TH7890M (#1)

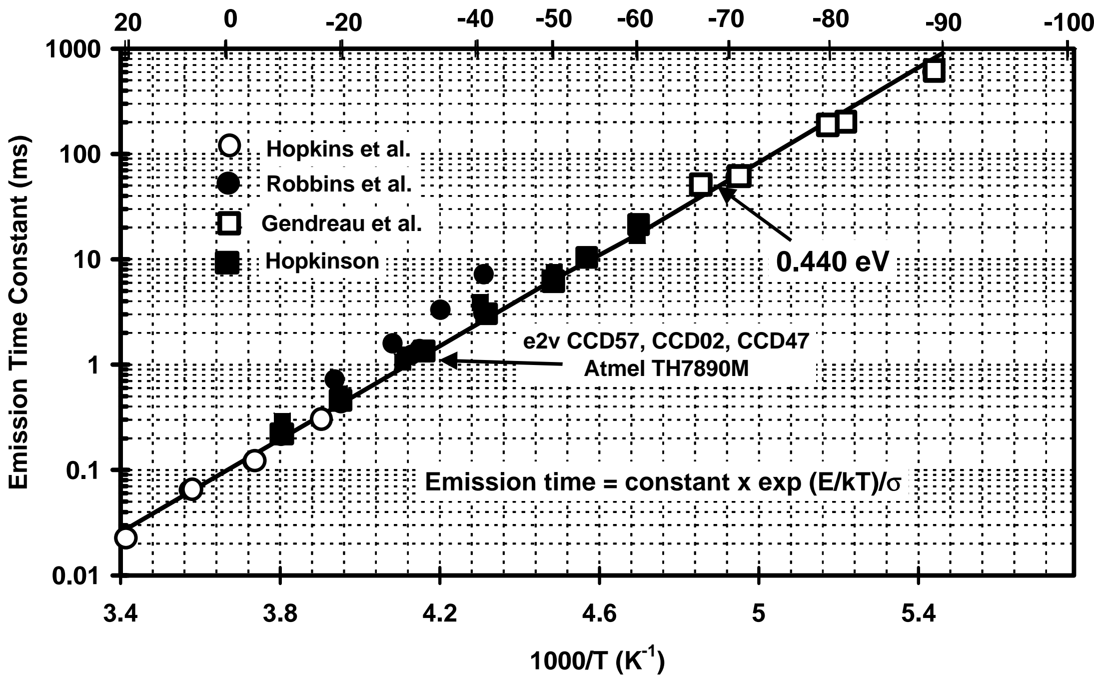

Figure 5.7.4-4 Measuremtnts of trap emission time versus temperature for the longer time constant trap (trap level 0.440 eV)

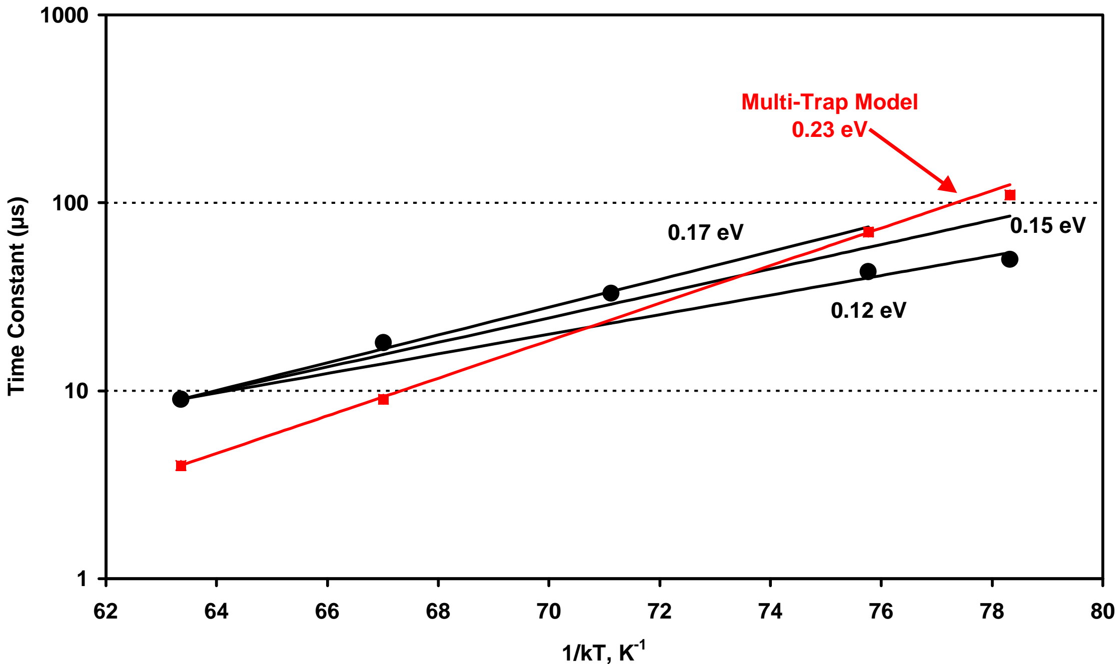

Figure 5.7.4-5 Measurements of fast trap emission time constants at low temperature for the CCD57-10 (# 5) obtained from the horizontal CTI. Also shown in black are predictions based on three notional trap energy levels (note, a single trap level is assumed). In red are shown results from a multi-trap model which is also consistent with the CTI data.

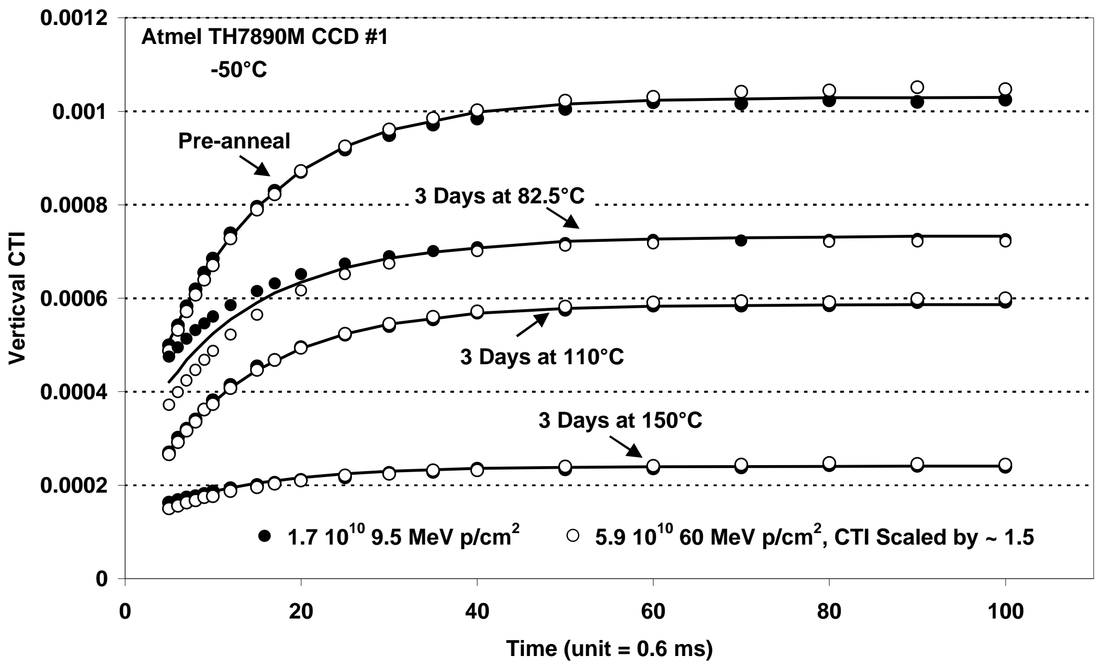

Figure 5.7.4-6 Emission time contants before and after annealing

5.8 MEASUREMENTS OF OUTPUT DRAIN CURRENT

Output drain current (that is, the current to the output amplifier) was measured by monitoring the voltage across a 10R resistor in the Vod supply line. The measured values (predominantly for the cobalt60 irradiated devices) are given in table 5.8-1 below. The current is one of the main contributors to power dissipation (the other being the power dissipated in the clock electrodes – which is proportional to their capacitance and is not expected to vary with radiation).

In the case of the CCD57 there are two CCD amplifiers and the measured current is the sum of the two.

Table 5.8-1 Measurements of CCD output drain current (mA)
(- = not measured)

CCD Type	CCD No.	Comment	Total Dose krad(Si) on O/P amp.	Pre-Irradn (mA)	Post-Irradn (mA)	Change mA/krad
CCD57	1	9.5/60 MeV protons	10	-	-	-
	2	9.5/60 MeV protons	10	-	-	-
	3	Cobalt60 biased	18.1	5.4	5.8	0.023
	4	Cobalt60 unbiased/biased	18.1 (unbiased)+ 17.9 (biased)	5.4	5.8	0.012
	5	9.5 MeV protons (unbiased)	10/ 20	5.4	5.5	0.003
CCD55	1	Cobalt60, biased	17.9	9.1	9.3	0.011
	2	9.5/60 MeV protons	8.1 (60 MeV) 10 (10 MeV)	-	-	-
	3	Damaged in transit	-	-	-	-
TH7890M	1	9.5/60 MeV protons	10		2.9	-
	2	9.5/60 MeV protons	10	-		-
	4	Cobalt60 biased	11.6	2.6	3.0	0.033
	5	Cobalt60 unbiased	17.9	-	3.2	-
	3	9.5 MeV protons	10	-	2.9	-
	6	9.5 MeV protons	10	-		-
						-
TH7863D	1	Cobalt60 biased	17.9	6.4	8.4	0.11
	2	Cobalt60 unbiased	17.9	6.7	7.7	0.05
	3	9.5 MeV protons	10	-	7.0	-

It can be seen that the amplifier current tends to increase with radiation but the changes are small. The largest change is for the TH7863D, which has also been measured in previous studies, with exactly the same results: 0.11 mA/krad (biased) and 0.05 mA/krad (unbiased).

6. RESULTS OF STAR-250 AND IRIS-2 TESTING

6.1 MEASUREMENTS OF CONVERSION GAIN

The conversion gain is the value calibration factor between APS signal in electrons and the measured signal in ADC units (ADU). As with the CCDs, it was to use soft X-rays from a Cd^{109} radioactive source. This decays to ^{47}Ag giving characteristic X-ray emissions as follows:

Kα	average energy 22.08 keV
Kβ	average energy 25.19 keV

If we assume an electron hole pair is, on average, created for each 3.65 eV energy deposited then the Kα and Kβ peaks correspond to signals of 6050 and 6900 electrons, respectively. However for the pre-irradiation measurements it was found that only small sized X-ray events could be detected (a similar situation ocurred for previous measurements on the ASCoSS chip). As an alternative, the full well capacity was measured as 40,000 electrons at gain 0 (16 bit external ADC and x 0.5 gain on the daughter board). This can be combined with the manufacturer's design value of 300,000 electrons to give a conversion gain value of

Conversion gain =0.95 electrons/ADU at gain 3

Since the gain 3 setting gives a gain of 7.9 relative to gain 0.

After the irradiations the transient response was investigated in more detail and it was found that, with normal biasing, the APS suffers from image lag (see section 6.2 for more details). This effect could be eliminated by reducing the VPIX voltage and a Cd^{109} X-ray calibration could then be achieved. However, since the APS photodiodes have a small area, it required a large number of X-ray interactions to produce enough 'single pixel' events to give a good calibration. Hence only one of the proton irradiated devices was measured in this way.

It can be seen from the 'stacked line trace' of figure 6.6-4 that the conversion gain varies with radiation dose. The single pixel events are still rather difficult to identify and so the calibration is rather subjective. The values obtained from the figure are:

APS #5 10 MeV proton irradiated (unbiased), measured 1 month* after irradiation

0 krad region	0.65 electrons/ADU
10 krad region	0.82 electrons/ADU
100 krad region	0.96 electrons/ADU

These values were used throughout to convert from ADC units to electrons. Since the flatband voltage shift was small (see section 6.3), there was no need to adjust the bias voltages after irradiation (other than the vpix change, mentioned above).

6.2 MEASUREMENTS OF IMAGE LAG

It was mentioned in the previous section that early attempts at X-ray gain calibration showed very small X-ray signals. Later investigation revealed that X-ray events could be detected provided there was some background light falling on the detector, but it was noticed that events tended to persist over more than one image, suggesting a lag effect.

The layout of the readout circuit for each pixel is as follows:

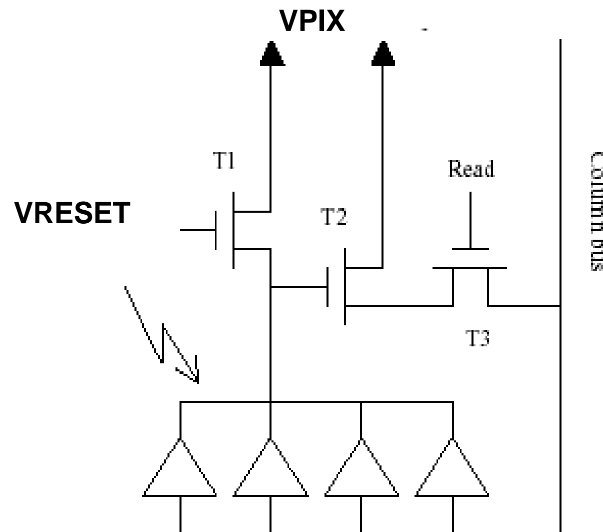

Figure 6.2-1 Block diagram of a pixel

The voltages of importance here are:

- VPIX (drain of reset MOSFET, but also drain of source follower MOSFET)
- VRESET (high level of reset pulse) = VDDA (5V)
- MOSFET threshold voltage, Vth ~ 1V

If VRESET-VPIX > Vth, the reset MOSFET is in its linear regime during reset and acts as an ideal switch.

If VRESET-VPIX < Vth, the reset MOSFET is not in its linear regime during reset, but in weak inversion, thus causing image lag. It behaves as a current source with a long time constant.

The value VRESET-Vth is the highest (starting) voltage on the photodiode. By collection of photo-generated charge or dark current the voltage on the photodiode will gradually drop. The pixel's (highest) output voltage is (VRESET-Vth-Vth) or (VPIX-Vth) whichever is the lower.

The STAR-250 datasheet suggests to have both VPIX and VDDA (=VRESET) = 5.0 V. This implies that the reset transistor will be in weak inversion for small signals. A modification was made to the test electronics to allow VPIX to be varied. It was found that the lag effect was eliminated for VPIX values below 4.0 V as expected (V_{th} is 1 V). This was checked by using an LED flash synchronised to the APS timing, and capturing multiple images.

For VPIX below 4.0 V there was no signal in images other than the one in which the LED flashed. For VPIX = 5.0 V there was a residual image (lag) in each subsequent frame. The

brightness of these residual images was approximately constant, independent of the original signal. This might be expected since the detector only goes 'laggy' when the signal is within 1 V of VRESET. Therefore, they are relatively more important at lower signal levels.

The following values were obtained for the brightness of the LED spots:

LED spot brightness (ADC units, above background, 1 ADC unit ~ 0.6 electrons)

	VPIX = 2.7 V (no lag)	VPIX= 5 V
Signal in main spot (flash)	160,000	160,000
Residual signal in next (2nd) image	0	1,600
Residual signal in 3rd image	0	800
Residual signal in 4th image	0	400
Residual signal in 5th image	0	240
Signal in main spot (flash)	42,000	39,000
Residual signal in next (2nd) image	0	1,700
Residual signal in 3rd image	0	1,000
Residual signal in 4th image	0	450
Residual signal in 5th image	0	300
Signal in main spot (flash)	21,000	15,500
Residual signal in next (2nd) image	0	1,700
Residual signal in 3rd image	0	850
Residual signal in 4th image	0	600
Residual signal in 5th image	0	400
Signal in main spot (flash)	18,000	12,000
Residual signal in next (2nd) image	0	2,000
Residual signal in 3rd image	0	1,000
Residual signal in 4th image	0	500
Residual signal in 5th image	0	250
Signal in main spot (flash)	9,500	4,000
Residual signal in next (2nd) image	0	1,600
Residual signal in 3rd image	0	800
Residual signal in 4th image	0	400
Residual signal in 5th image	0	250
Signal in main spot (flash)	5,200	1,000
Residual signal in next (2nd) image	0	700
Residual signal in 3rd image	0	500
Residual signal in 4th image	0	300
Residual signal in 5th image	0	200

6.2.1 Tradeoffs Involved in Reducing VPIX voltage

Reducing VPIX has some additional effects whose magnitude depends on the size of the change:

- Reduction in full well signal
- Change in gain (charge to voltage conversion factor)
- Reduction in the size of dark charge spikes (hot pixels)

The change in full well signal is small for small changes in VPIX. The change in the brightness of hot pixels (e.g. due to proton damage) is large if VPIX is reduced below about 3.5 V. Hence there is a trade-off between dark current and full well signal.

The change in full well signal for small changes in VPIX is given in figure 6.2-2 below:

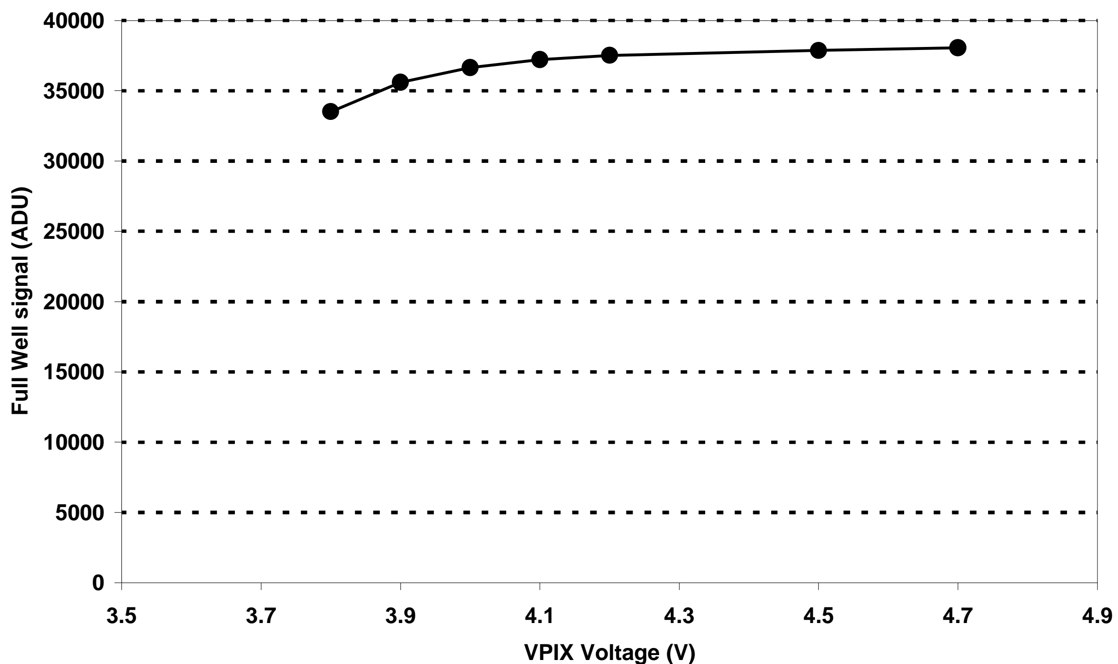

Figure 6.2-2 Full well signal versus VPIX

Small changes in VPIX cause only a minor change in full well voltage, but the effects for larger reductions in VPIX are more pronounced. This is because the maximum voltage that can be output is VPIX-V_{th}, as mentioned above. To illustrate the effects, figure 6.2-3 shows linearity plots at several values of VPIX (obtained by varying the exposure time at constant illumination).

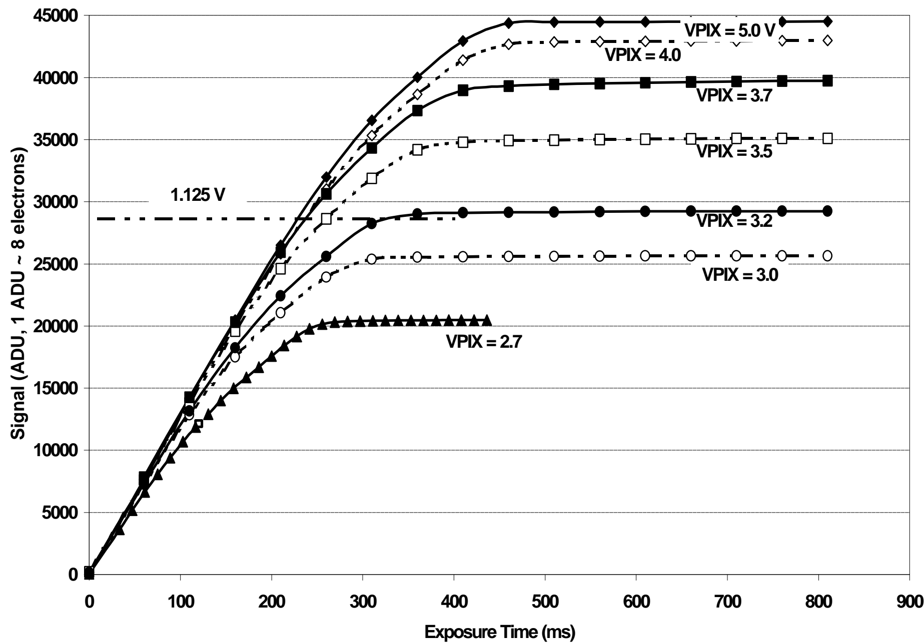

Figure 6.2-3 Linearity plots at several values of VPIX. Also shown is the 1.125 V range of the on-chip ADC

Several things are happening in this figure:

- The full well voltage is decreasing (decrease in full well signal in ADC units)
- The full well charge is decreasing (the exposure time at which saturation is reached decreases)
- The small signal gain (slope of the linearity plot) decreases
- The plots become more non-linear (i.e. curved) at intermediate signal levels

The change in gain is shown below (figure 6.2-4). This data was obtained both by measuring the slope of the linearity plots of figure 6.2-3 (at small signals) and by simply measuring the signal as a function of Vpix. However since the plots become more non-linear at large signals and the non-linearity varies with VPIX, the gain curves also vary with signal level. (The bottom curve, filled triangles, was obtained for a light level just below saturation at VPIX = 2 V).

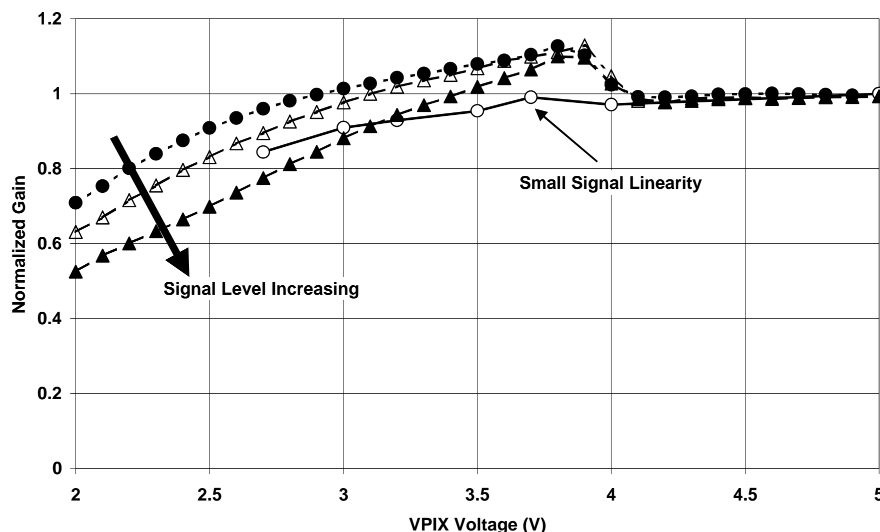

Figure 6.2-4 Normalised gain versus VPIX

Finally, the change in brightness of the brightest dark current spikes, after the APS was irradiated with 100 krad of 10 MeV protons, is also shown:

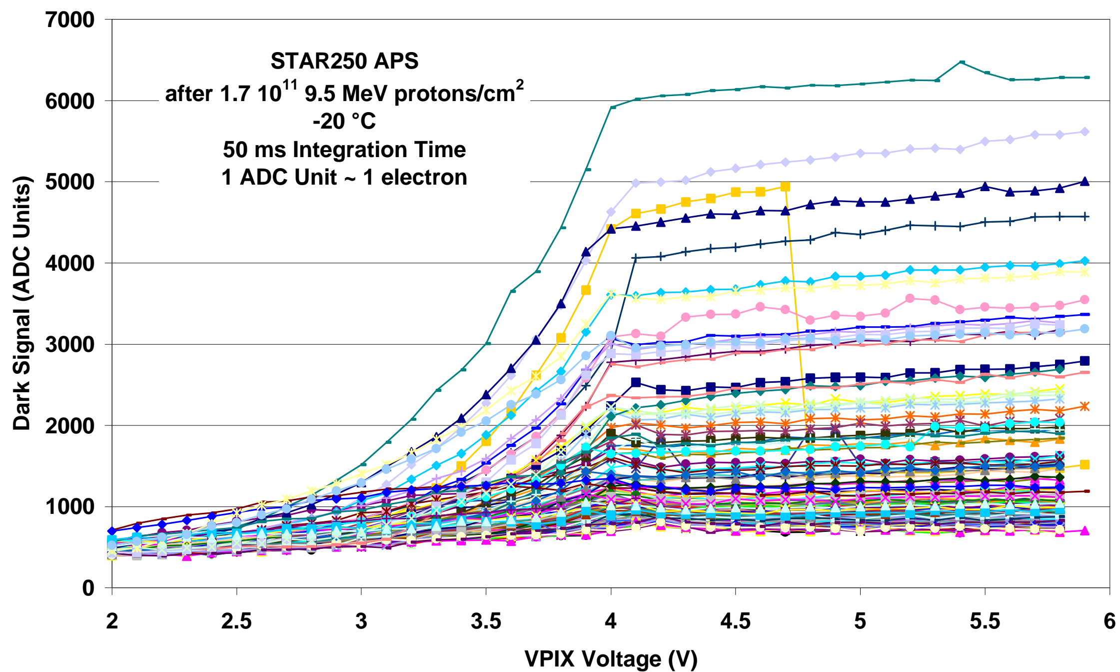

Figure 6.2-5 Dark signal for 100 of the brightest pixels after proton irradiation. Also shown are plots for low dark current pixels so as to indicate the baseline signal level.

Below VPIX = 4.0 there is a substantial decrease in dark current, probably because of a reduction in the electric field within the photodiode. This is discussed further in section 6.8.1. Note that some pixels show erratic dark current switching, this is due to Random Telegraph Signal (RTS) behaviour (section 6.9). Figure 6.2-6 shows histograms at VPIX = 2.7 V and 5.0 V. Most of the pixels have dark currents within the main peak. Only a few (the dark current spikes) show high dark current.

Another effect of improper resetting for high VPIX voltages seems to be that the short integration time mode does not work correctly for small signals. Figure 6.2-7 shows dark images for a proton irradiated device (see section 6.8.1) both for normal (55 ms) exposures and at reduced integration time (10 line moves, i.e. approximately 1 ms exposure). It can be seen that at VPIX = 5 V the difference between the two exposures is very small.

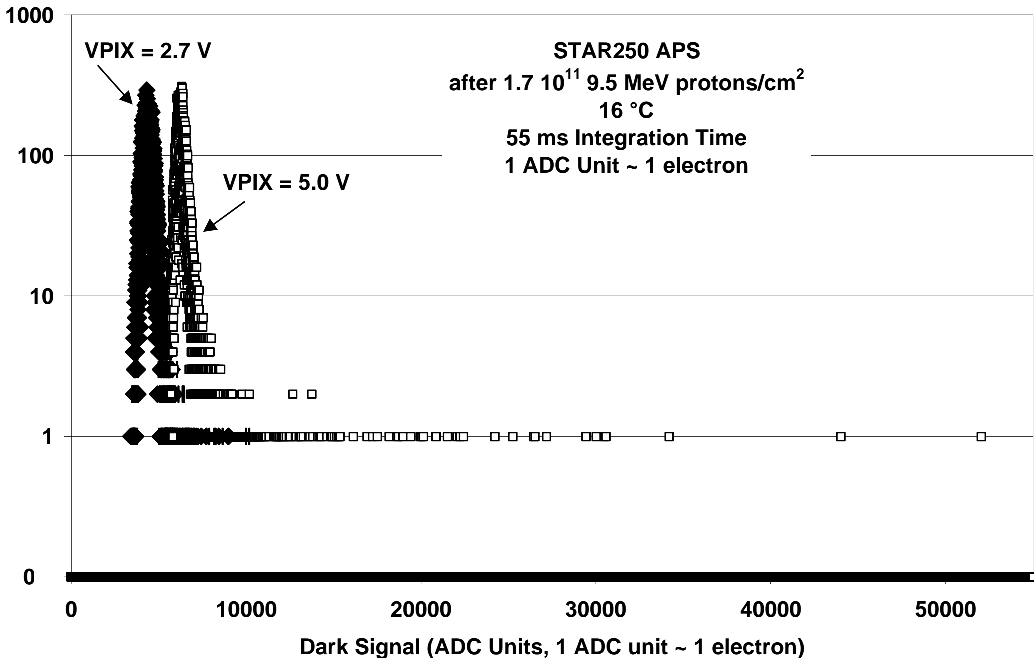

Figure 6.2-6 Dark signal histograms at VPIX = 2.7 V and 5.0 V, fixed pattern noise has not been subtracted.

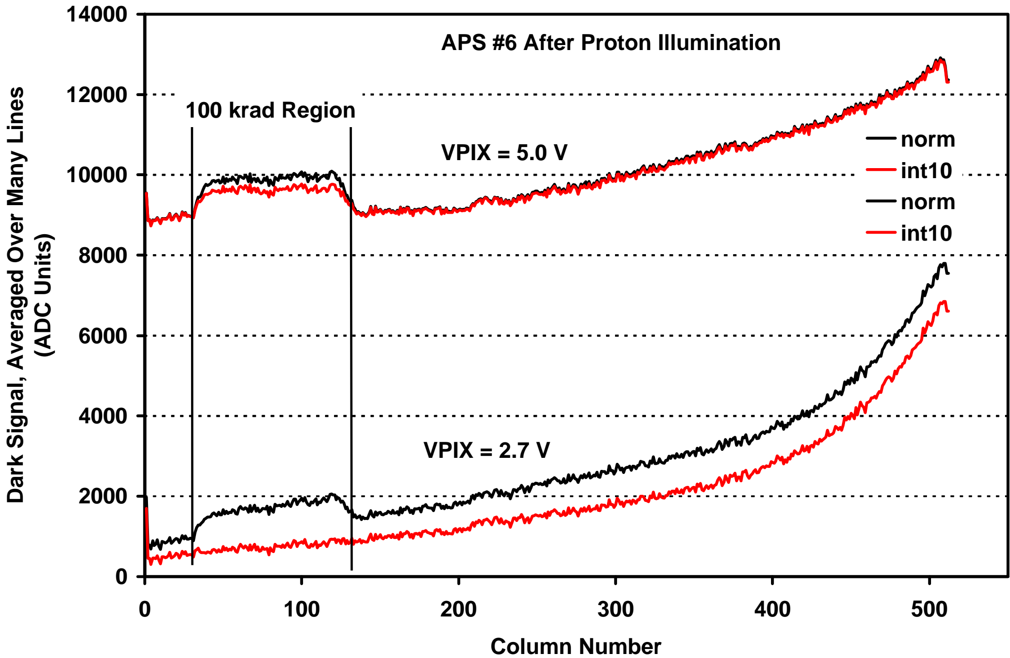

Figure 6.2-7 Dark Images at normal and reduced integration time for two values of VPIX

6.3 MEASUREMENTS OF FLATBAND VOLTAGE SHIFT

Measurements of flatband voltage shift were made by varying the clock voltages under computer control (using an Agilent Vee routine) and observing the appearance of the recorded images. The step size was 0.05 V. For each clock voltage the 'threshold' was taken as the last voltage for which normal operation was achieved. For the devices cobalt60 irradiated to 79 krad(Si) there was no discernible change in threshold voltage. For the device irradiated to 5.3 Mrad the shifts were as shown in figure 6.3-1. In this case it was not possible to make pre-irradiation measurements. Instead the post irradiation values are compared with the average pre-irradiation values for four of the other devices.

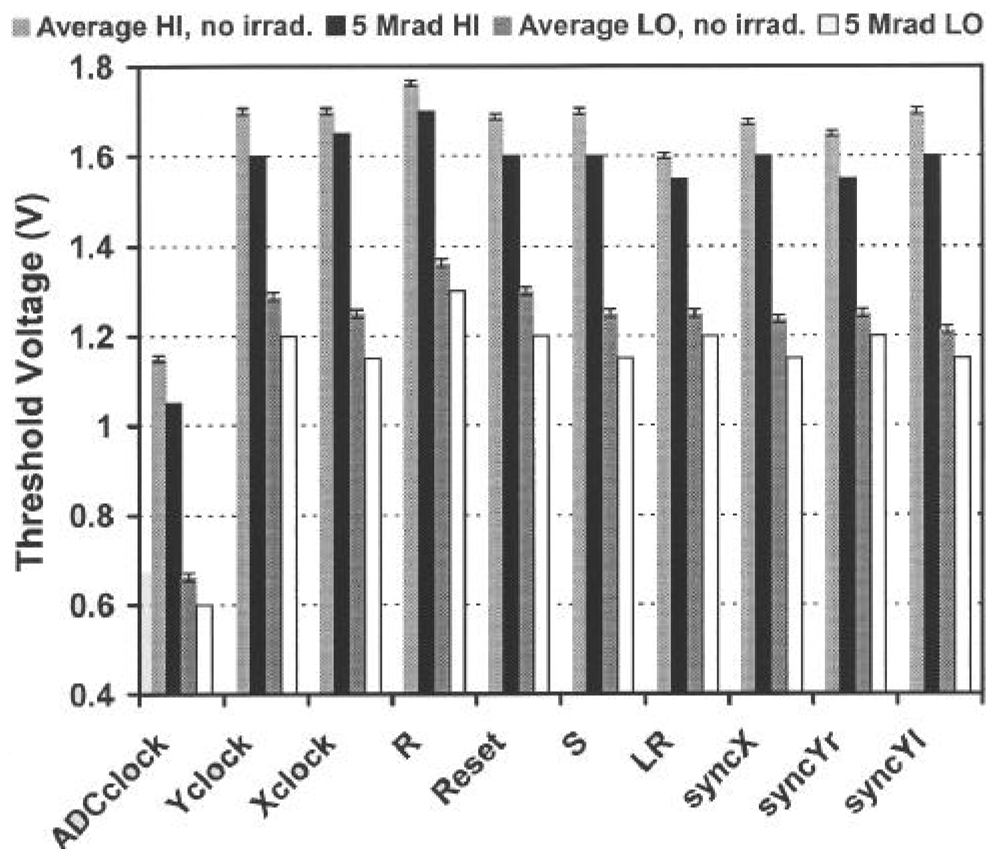

Figure 6.3-1 Clock threshold voltages for un-irradiated (grey) and irradiated (black and white) devices. The error bars show the spread in values for the four un-irradiated sensors

The 5.3 Mrad thresholds are consistently below the unirradiated values with an average difference of 80 mV with a standard deviation of the mean 20 mV. (So the average threshold shift after 5.3 Mrad was 80±20 mV.) Note that a much larger threshold voltage swing could be tolerated before the device fails to operate (typical applied clock swings are 0 to 3.3 V).

6.4 MEASUREMENTS OF POWER CONSUMPTION

Measurements of both the sensor and on-chip ADC currents were made continuosly during the cobalt60 irradiation and during device measurement steps (during and after irradiation). The results are shown in figures 6.4-1 and 6.4-2. There was a very small increase in sensor current for the biased devices which annealed out after irradiation. The changes in ADC current were within the measurement error (the current sometimes changed by ~ 2 mA when the device was re-inserted in its socket). These results show that the design changes implemented by the manufacturer to suppress field oxide leakage were successful.

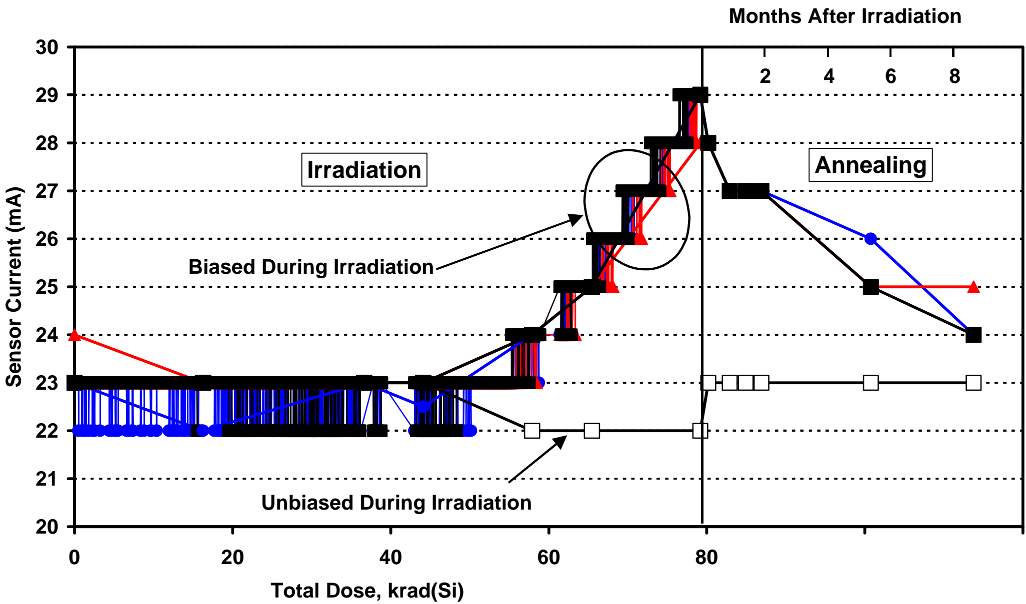

Figures 6.4-1 Sensor current

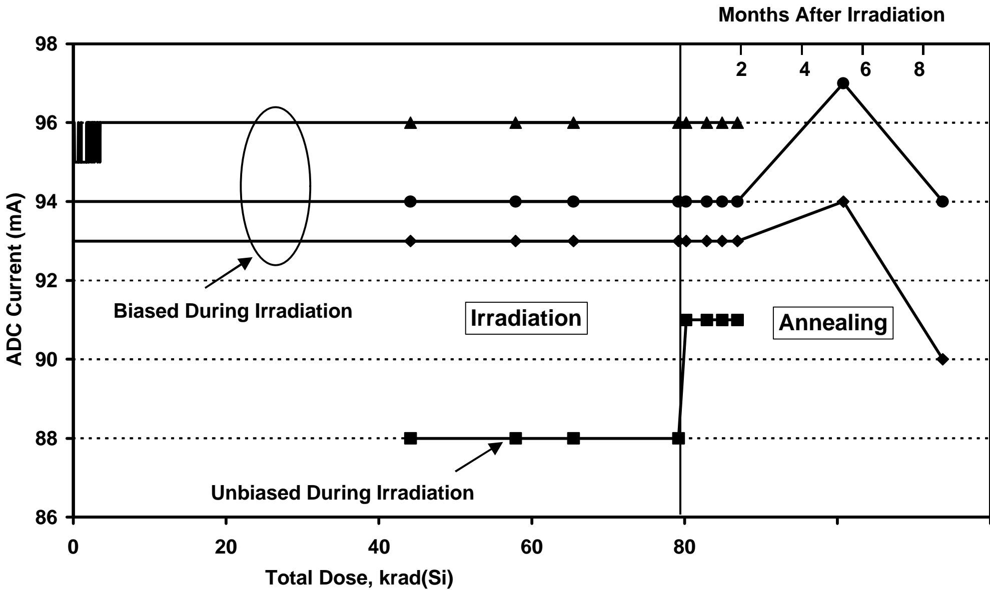

Figures 6.4-2 On-chip ADC current at 5 MHz clock rate

6.5 MEASUREMENTS OF LINEARITY AND FULL WELL CAPACITY

Linearity and full well capacity were measured by varying applying constant illumination and varying the integration time. An Agilent Vee routine was written to load the timing generator, snap an image and dump the average of three user-defined areas of interest to file. A near-uniform illumination was used. No change with radiation was observed as illustrated in figure 6.5-1 below.

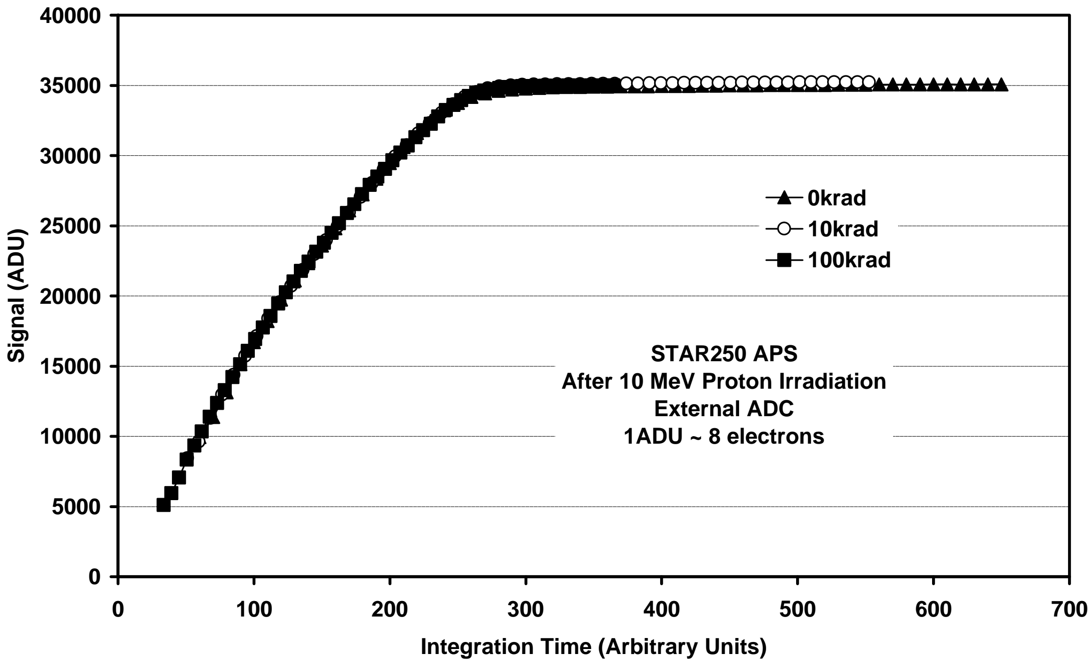

Figure 6.5-1 Linearity plots for a proton irradiated STAR-250 devce.

6.6 MEASUREMENTS OF RESPONSIVITY/PRNU

6.6.1 Initial Measurements on the 5.3 Mrad Irradiated Device

Responsivity values were obtained with a tungsten-halogen lamp calibrated against a UDT S390 radiometer. Measurements were made using narrow (10 nm) interference filters and also for broadband (no filter) illumination. The relative ratios between the 5.3 Mrad device and the means for the 4 unirradiated devices (later irradiated at ESTEC) are given below:

Broadband Illumination (BBI)	0.58
BBI + near IR cutoff filter	0.72
540 nm filter	1.7
650 nm filter	1.5
810 nm filter	1.6

The spread in the average responsivity values for the unirradiated devices (including measurement errors) was ~ ±15% so it is seen that the departures from unity relative responsivity are probably significant. The irradiated APS seems to have decreased responsivity for broadband illumination but increased responsivity in the range 540-810 nm. In fact it will be seen that values obtained with a narrow band filter are unreliable because the spectral response is strongly modulated (presumably by the effects of optical interference in surface layers) and these modulations vary from device to device. However the factor ~2 difference in white light response after 5.3 Mrad(Si) is still valid.

6.6.2 Measurements After Cobalt60 Irradiation at ESTEC

Measurements of responsivity were made prior to irradiation and 3.5 and 8 months afterwards, again using a tungsten-halogen lamp calibrated against a UDT S390 radiometer. Values for the pre/post responsivity ratios are given in the table below for broadband (white) illumination after 3.5 months. The data after 8 months was not significantly different.

Table 6.6-2 Ratio of the post irradiation responsivity (79.2 krad cobalt60) to the pre-irradiation value

Device number	Responsivity ratio Error ~ ± 0.1
1, biased	0.54
2, biased	0.51
3, biased	0.49
4, unbiased	0.42

These results again indicate a large change in responsivity after irradiation.

6.6.3 Responsivity Measurements on Proton Irradiated Devices

Measurements on the proton irradiated devices are useful since it is possible to compare the response of both the irradiated and non irradiated regions at the same time. The two devices were not biased during irradiation but it can be seen from the table above that there is not a large bias dependence – and, if anything, unbiased is the worst case. Figure 6.6-1 shows flat field white light images for the two devices, with dark images (of the same integration time) subtracted

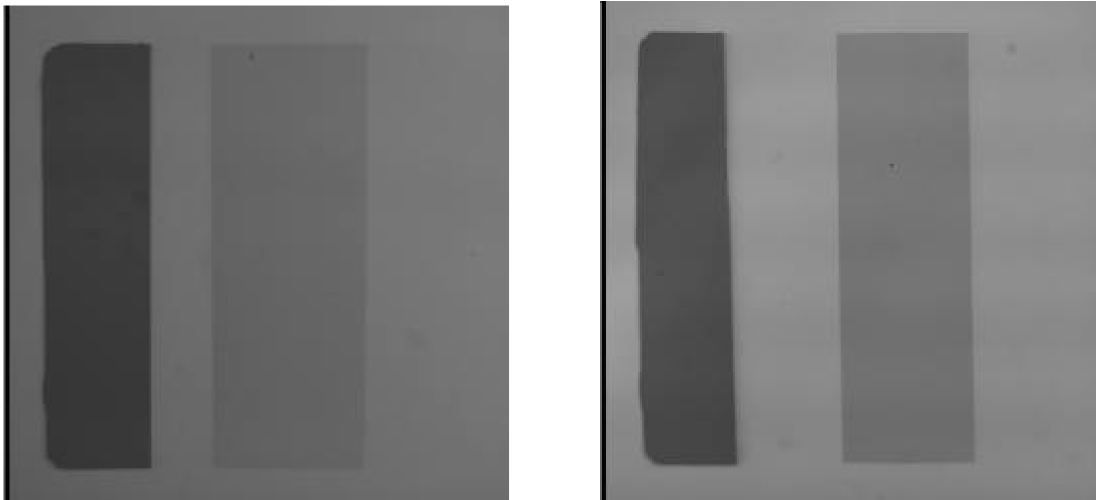

Figure 6.6-1

APS #5, white light flat field image 1 day after 10 MeV proton irradiation

APS #6, white light flat field image 12 days after 10 MeV proton irradiation

The decrease in signal for the irradiated regions (100krad and 10krad) can be clearly seen. The decreased signal for the 1 krad region can also be observed (in the original image) if the contrast is increased. Figure 6.6-2 plots the change in responsivity versus 10 MeV ionising dose (krad) for the two devices. The change after 100 krad is very similar to the values given in table 6.6-1. The plots are nonlinear, indicating a saturation effect at high dose. A saturation effect is also suggested by the fact that the 100 krad value is also similar to the 5.3 Mrad(Si) value given above (0.58). It is seen from figure 6.6-2 that the responsivity was not significantly affected by 4 months storage, unpowered, at room temperature. The data is for VPIX =5V. Also shown is data at VPIX = 2.7 V. The responsivity is essentially the same though the radiation-induced decrease is slightly less, so it is concluded that the choice of VPIX voltage has no significant effect on the responsivity changes. Measurements using narrow band green and red filters again gave essentially the same results, confirming the wavelength independence of the effect. It is also seen that an anneal at 84^{0}C produced only a very small recovery.

Since a similar responsivity change can be seen both with cobalt60 irradiation and with 10 MeV protons, it is likely to be due to total dose. The next question is whether it is due to changes in sensor response (pixel geometry or quantum efficiency) or to an electronic effect (change in gain of the pixel amplifier). Note: only the pixels were proton irradiated and not the peripheral circuitry (column amplifiers and output node). A change in pixel response might be indicated by a change in the responsivity degradation with wavelength. Hence proton-irradiated device #5 was used to obtain a spectral responsivity curve for both the 0 krad and 100 krad regions. The results are shown in figure 6.6-3. It is seen that there is a decrease in response, which is the

same as shown in figure 6.6-2 (0.56 at 100krad) but is **independent of wavelength**. This suggests that the effect is not due to optical effects. To check if the gain of the sensor was changing the same APS was illuminated with CD^{109} X-rays and a 'stacked line trace' of X-ray events was formed. This is shown in figure 6.6-4. It is seen that the gain is indeed reduced in the irradiated regions, though the magnitude of the change is hard to determine since the 'single' pixel X-ray events are not clear (due to the very small area of the photodiodes and consequent large number of partial X-ray events).

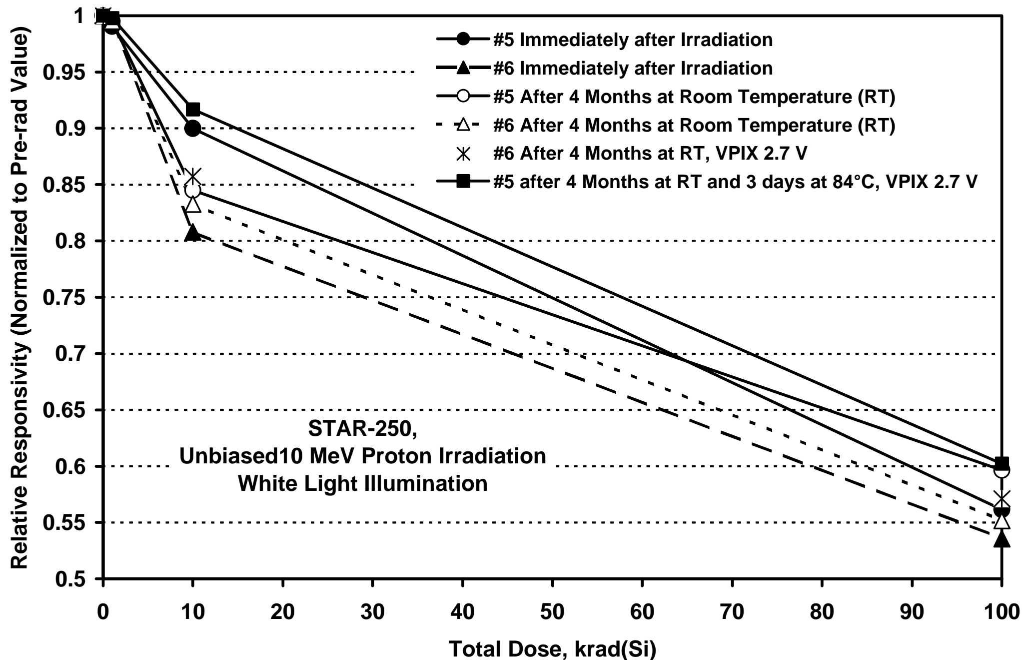

Figure 6.6-2 Change in responsivity versus 10 MeV dose (krad) for the two devices, broadband (white light) illumination

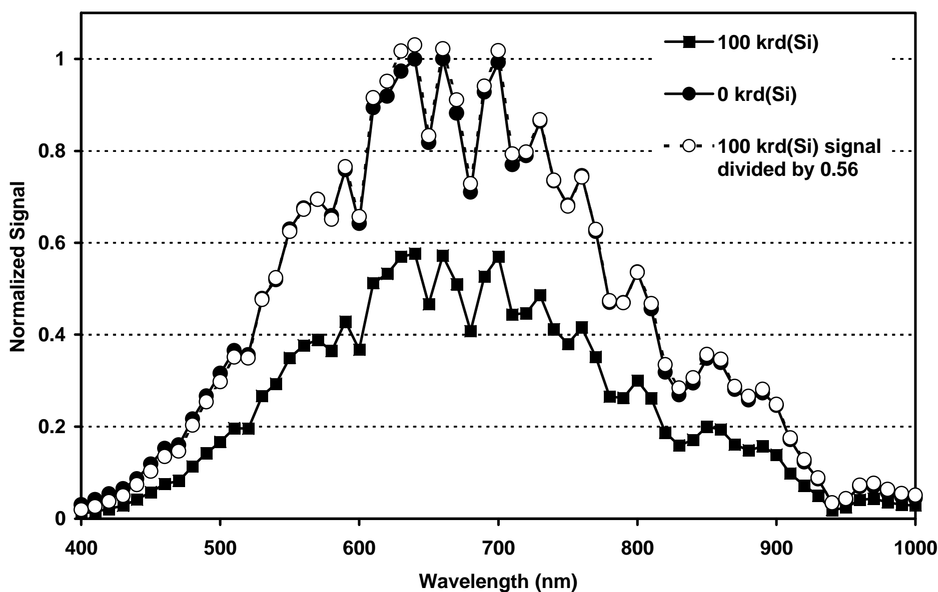

Figure 6.6-3 Spectral response plot for APS #5

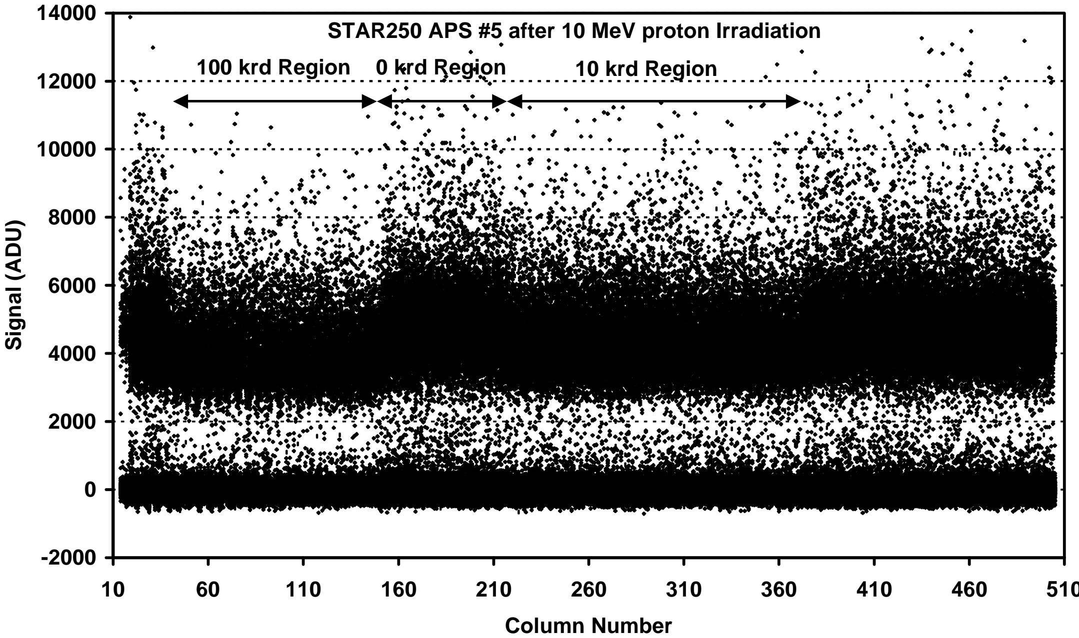

Figure 6.6-4 Stacked line trace of Cd109 X-ray events for APS #5

The basic conclusion is that the responsivity changes are predominantly due to a total dose effect which changes the gain of a pixel.

6.6.4 PRNU Measurements on Proton Irradiated Devices

The proton irradiated devices were also used to investigate changes in PRNU. The PRNU is dominated by 'swirl' patterns in the APS response. The amplitude of the 'ripples' is roughly 2% as shown in the vertical profiles of figure 6.6.4-1.

After irradiation the responsivity was reduced as discussed above. However it is interesting to note that the amplitude of the 'swirl' pattern was not reduced in line with the responsivity. In fact the amplitude did not seem to be reduced at all. Simple addition of an offset value to the irradiated regions gave a flat field 'pattern' which matched across a fluence region boundary. The resulting offseted images are shown in figures 6.6.4-2 to 6.6.4-4. The fluence regions do not have rectangular boundaries and so there are artefacts at the edges of a region, but it can be seen that the swirl patterns match well.

At this point it was checked that the same procedure could not be applied to a scene image – these show a 'real' responsivity change where the image has to be multiplied by a 'responsivity' factor to obtain image matching across a fluence region boundary (see figure 6.6.4-5). This means that the swirl pattern does not decrease in amplitude in an irradiated region, whereas the responsivity does. In other words the small (~2%) signal that is responsible for the PRNU pattern is not affected by the responsivity change which affects the major part of the signal.

After normalization by the reduced signal level (after irradiation) the PRNU will therefore **increase** in proportion to the responsivity decrease – i.e. by a factor ~ 2 after 80 krad(Si).

Further images for a 80 krad(Si) cobalt60 device (#4, biased) are given in figure 6.6.4-6. Both images are dark signal corrected and have essentially the same absolute PRNU (verified by image subtraction but the mean values are different by a factor 2 (the pre-irradiation image is a factor 2 brighter). It is interesting to note that the responsivity after irradiation is not as reduced in the corners of the image as at the centre. This is similar to the effect with dark images where the damage is less in the corners (c.f. the diagonal profiles in figure 6.6.4-7).

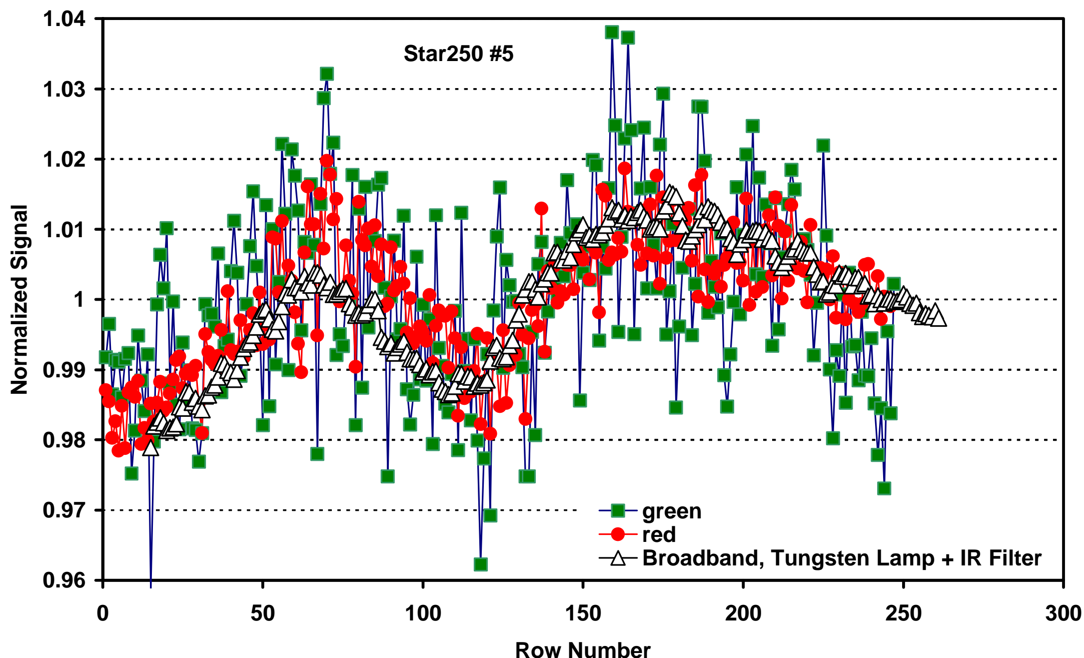

Figure 6.6.4-1 Vertical profiles down flat field images

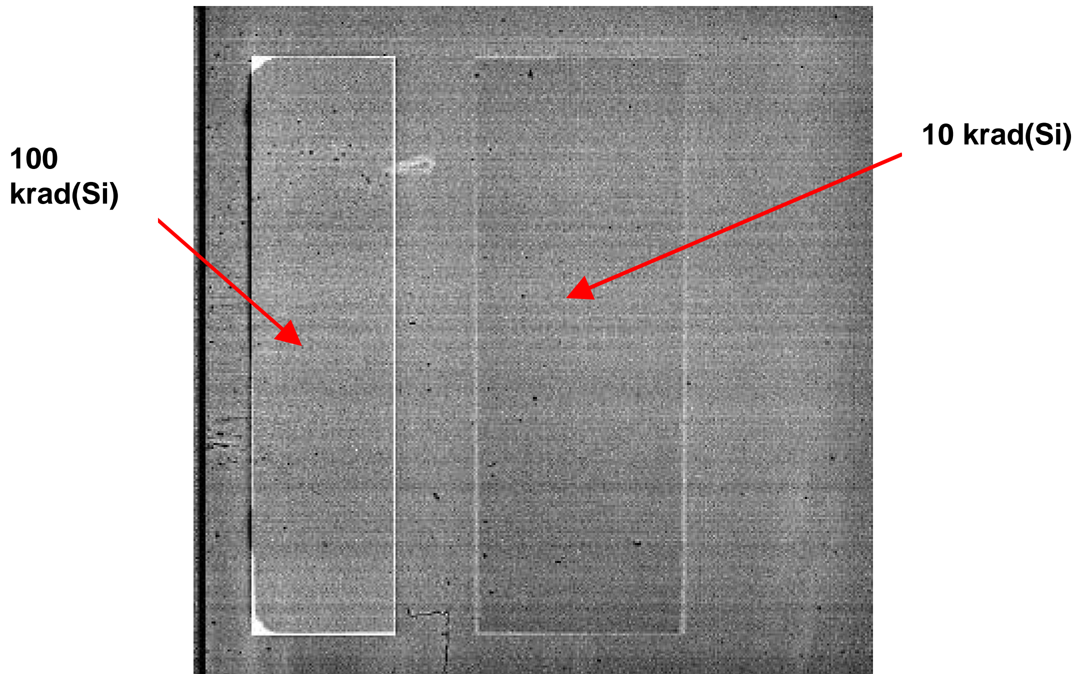

Figure 6.6.4-2 Flat field image for proton irradiated APS #5, with green (540 nm)filter. The 100 krad(SI) region was offset (added to) by 43% of signal and the 10 krad(Si) region by 7.5 %

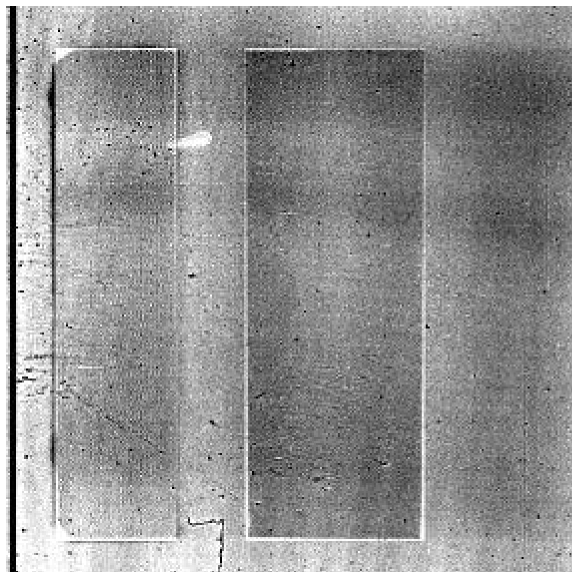

Figure 6.6.4-3 Flat field image for proton irradiated APS #5, with red (650 nm)filter. The 100 krad(SI) region was offset (added to) by 37% of signal and the 10 krad(Si) region by 6.7 %

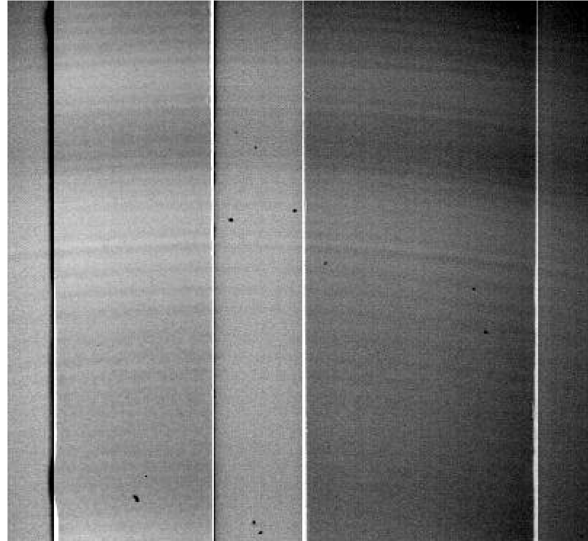

Figure 6.6.4-4 Flat field image for proton irradiated APS #5, with broadband illumination. The 100 krad(SI) region was offset (added to) by 39% of signal and the 10 krad(Si) region by 7.5 %

Figure 6.6.4-5 Scene image for proton irradiated APS #5, with broadband illumination. The 100 krad(SI) region was divided by a factor 0.62.

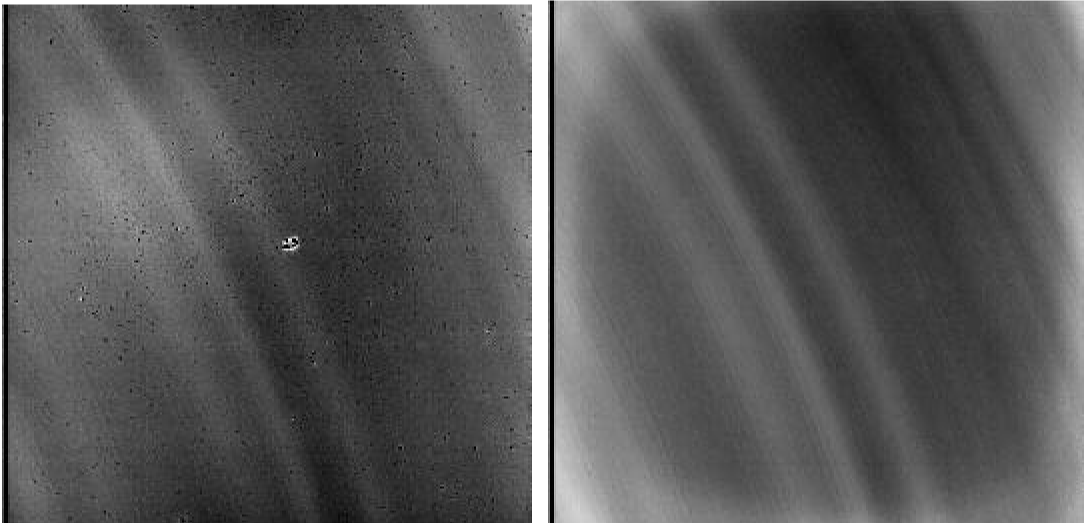

Figure 6.6.4-6 Flat field images (broadband) for cobalt60 irradiated APS #4 before (left) and after irradiation. The light level (and the PRNU) are approximately the same but the average response (signal level) is reduced after irradiation by a factor ~2.

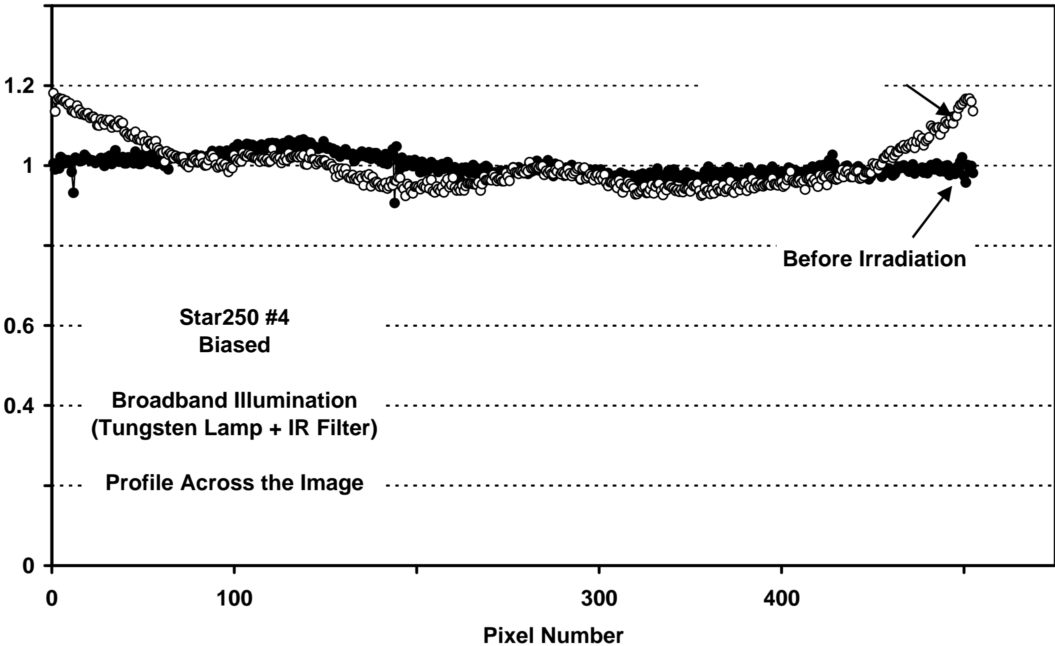

Figure 6.6.4-6 Diagonal profiles across a flat field image from device #4

6.7 MEASUREMENTS OF ON-CHIP ADC PERFORMANCE

The on-chip ADC performance was measured by placing the sensor in darkness and varying the bref voltage linearly between 0.474 and 2.72 V. A line of image data was collected for each bref value so that the resultant image was 1000 lines deep and varied linearly in brightness from top to bottom. Plots of the output of a single column from this image (which are plots of output versus bref) are shown in figure 6.7-1. These plots are for the 4 APS devices that were cobalt 60 irradiated (3 biased, one unbiased) both before and after irradiation (i.e. 8 plots in all). These are very similar apart from two post-biased irradiation plots which are shown in red in the diagram. Note that experiments with an external ADC and varying bref show nonlinearities below bref = 0.4 V (so the black reference input circuit is nonlinear below this bias voltage) but since bref is higher than this in figure 6.7-1 the effect of the bias circuit itself is thought to be small.

The figure indicates a worst case offset change of ±20 ADU after 88 krad(Si).

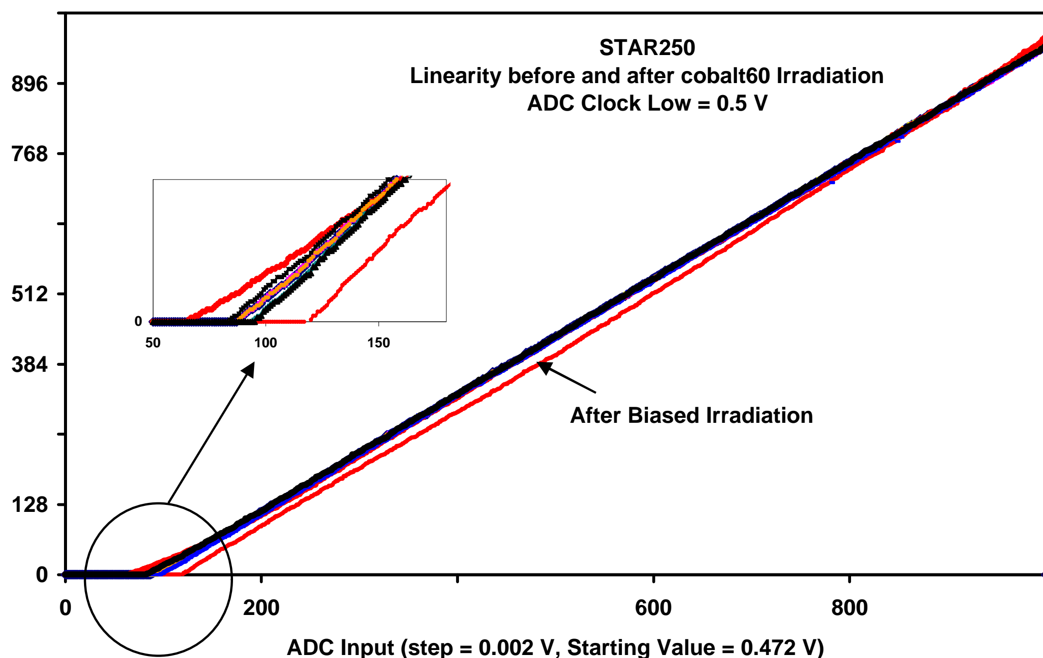

Figure 6.7-1 Linearity plots obtained before and after irradiation by varying the bref bias.

Histograms of the whole image give an estimate of the differential nonlinearity (DNL). This was found to change little with radiation as illustrated by figure 6.7-2. The ADC performance is reasonable and there are no missing codes.

The device which was given 5.3 Mrad(Si) with the ADC unbiased showed a curious effect on the DNL as shown in figure 6.7-3. However a spare device which was not irradiated but was measured several times for checking performance eventually showed ADC errors also. Possibly there is a reliability or handling (e.g. ESD) concern with the on-chip ADC (the 5.3 Mrad device experienced considerable handling as it had to be de-soldered from its camera pcb before characterization).

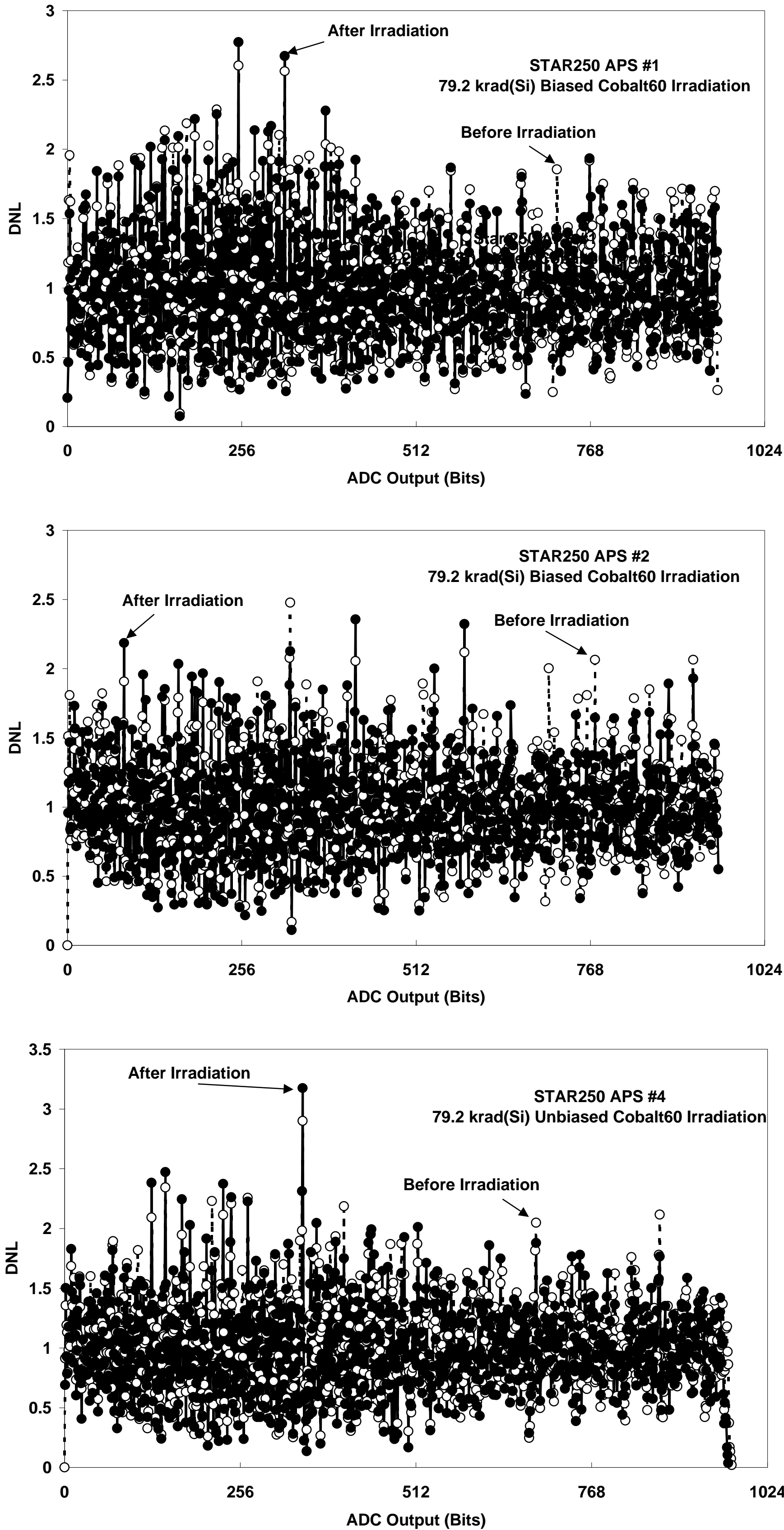

Figure 6.7-2 STAR-250 on-chip ADC differential nonlinearity

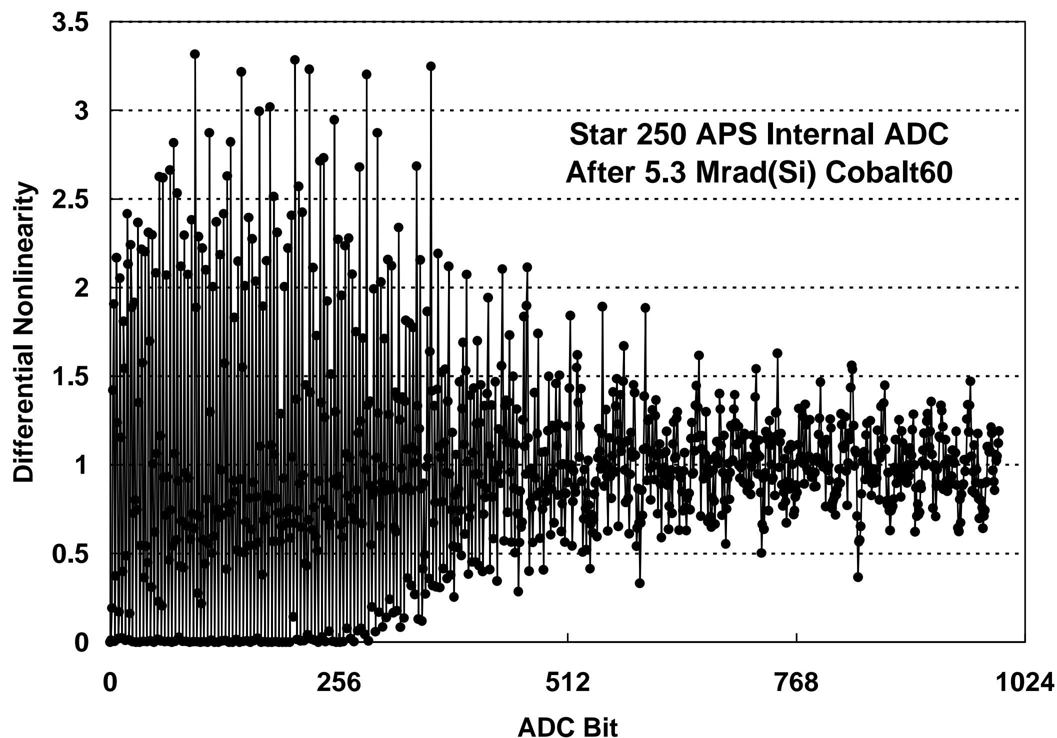

Figure 6.7-3 STAR-250 on-chip ADC differential nonlinearity after 5.3 Mrad(Si)

6.8 MEASUREMENTS OF DARK SIGNAL

6.8.1 Thermal Dark Current

Measurements of the thermal dark signal were made by recording images at various integration times and temperatures (16 frame averages) and subtracting images for short (10 line readout time) integrations to remove the fixed pattern noise. It was found that the dark current was nonuniform, with the centre containing appreciably more signal than the edges. Figure 6.8.1-1 shows an example. Similar images have been obtained by the manufacturer [8]. Presumably the nonuniformity is due to differences in interface trap density, perhaps caused by variations in hydrogen passivation.

Figure 6.8.1-2 shows a summary of the results. The unbiased device initially showed a lower dark current but after 8 months storage at room temperature the dark current was close to that of the biased devices. Most of the measurments were made at VPIX = 5 V but some were made at VPIX = 2.7 V. After correction for the change in gain (roughly a factor 0.8) the dark current was slightly reduced at 2.7 V but VPIX does not have a large effect. The Ionization induced dark currents are quite small indicating the effectiveness of the manufacturer's hardening by design. It is seen that the dark current is thermal in character and, as expected, has an activation energy of 0.65 eV.

Dark current measurements for the proton irradiated devices were given in figures 6.2-6 (fixed pattern noise not subtracted). Ffurther results are given in figures 6.8.1-3 to 6.8.1-5, where the fixed pattern noise (obtained for a short, 10-line integration) has been subtracted Note that this subtraction tends to give too low an average value for high VPIX values because of the lag

effect (see next section). This is the reason why the mean level (and the half width of the peak) are slightly increased at vpix = 2.7 V. The size of the spikes is however significantly reduced. Data were also collected after 3 days bake of device #1, unbiased at 84ºC, but this produced only a very small increase in the dark signal.

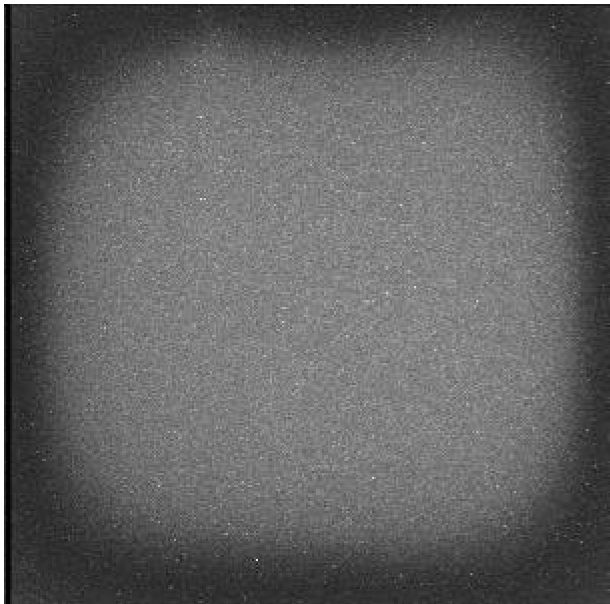

Figure 6.8.1-1 APS Dark image after 80 krad cobalt 60 irradiation

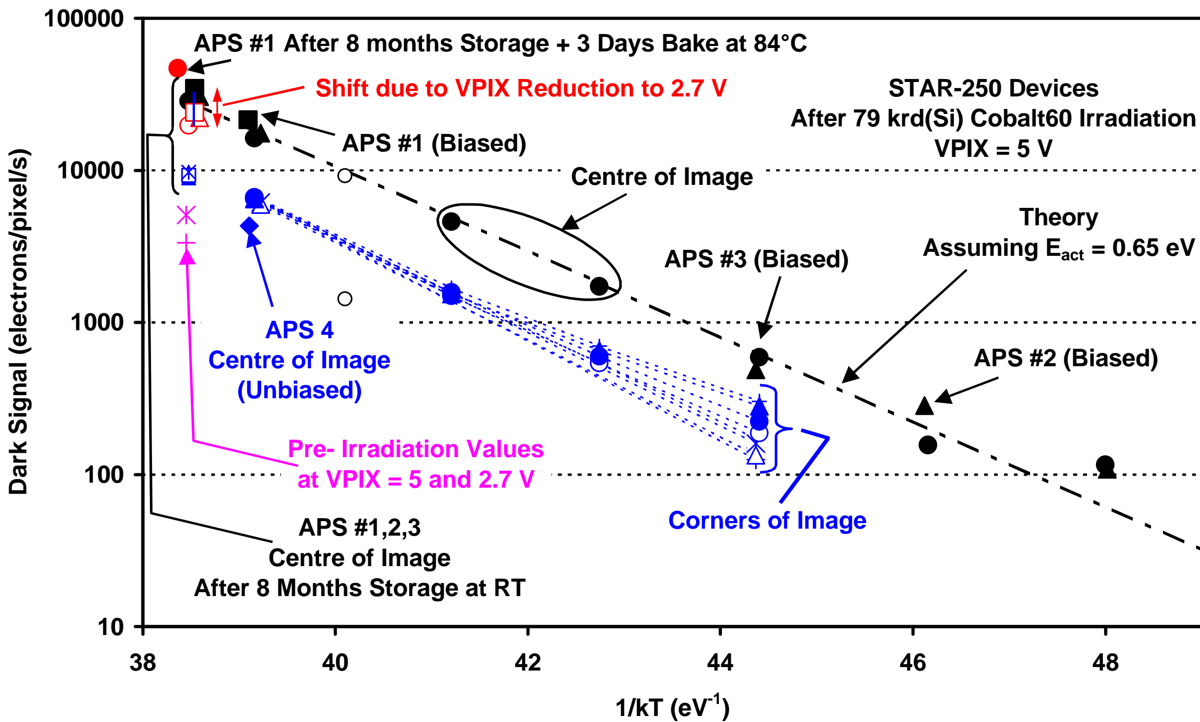

Figure 6.8.1-2 Dark current data for cobalt60 irradiated APS devices.

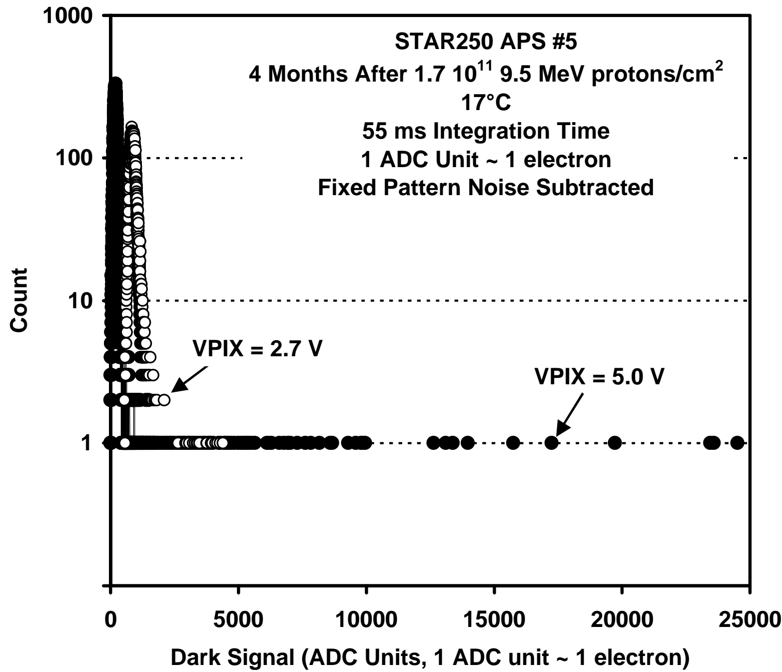

Figure 6.8.1-3 Dark current histograms

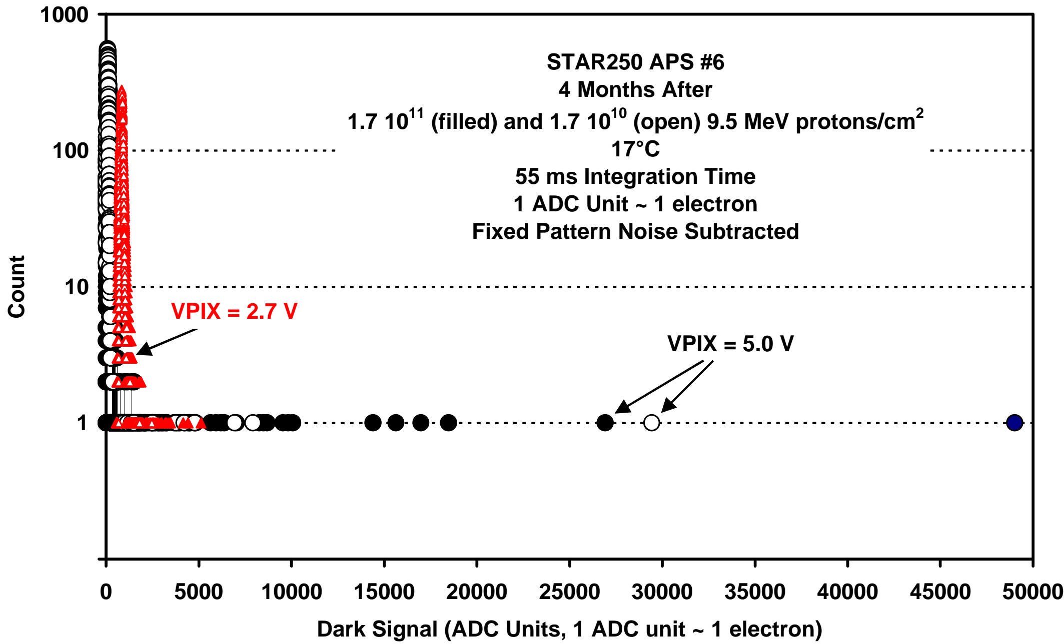

Figure 6.8.1-4 Dark current histograms

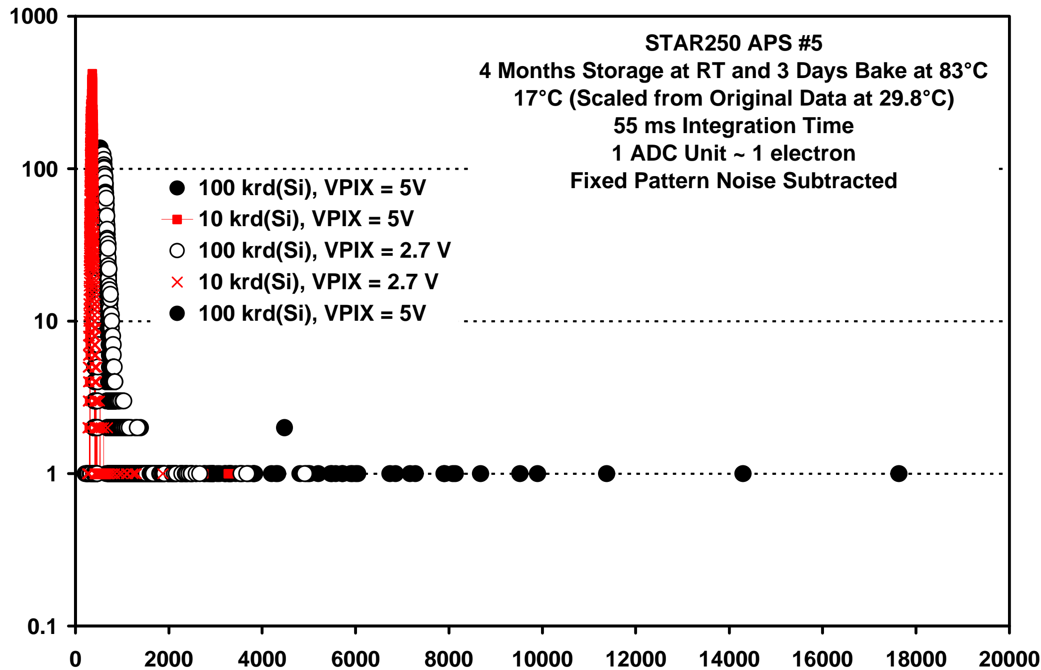

Figure 6.8.1-5 Dark current histograms

6.8.2 Fixed Pattern Noise

Fixed pattern noise is independent of integration time and can be measured on short (10 line readout time) integrations. Results were obtained pre-irradiation (cobalt60) and post-irradiation (8 months after 80 krad(Si)) for the same conditions (black reference voltage, VPIX and external ADC). The fixed pattern noise takes the form of low contrast vertical stripes and a gradual horizontal shading across the image (right hand side being brighter). Figure 6.8.2-1 shows a region on the left side of the chip both pre- and post-irradiation for a typical device (APS #4). It is seen that the pattern of vertical stripes is the same. Figures 6.8.2-2 and 6.8.2-3 show horizontal profiles across devices #1 and #4 averaged over all lines (to remove the effect of dark current spikes, which still show up even on ten line integrations). Averaging over lines (thick profile) is valid since the fixed pattern noise does not vary significantly in the vertical direction.

It is seen that the profiles before and after irradiation are closely matched, with the exception that there is a ‘hump’ in the centre of the image, which matches the profile of the radiation-induced dark current and which still shows in a 10 line integration. This dark current effect will be somewhat pronounced since the images were taken at VPIX = 5V and so short integration mode is not very effective (the VPIX effect was not known about, pre-irradiation), c.f. figure 6.2-7. The other devices behaved in a silmilar manner. **The conclusion is that the 80 krad(si) irradiation did not significantly affect the fixed pattern noise.**

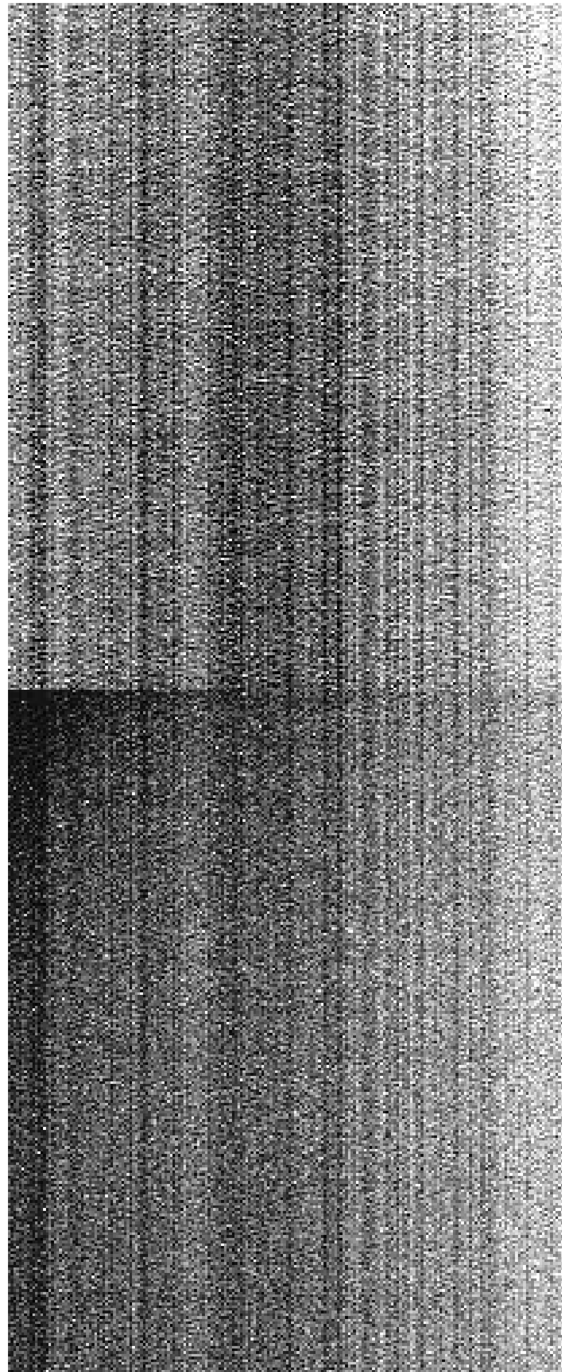

Figure 6.8.2-1 Region on the left side of the chip, both pre- irradiation (top) and post-irradiation (bottom) for a typical device (APS #4)

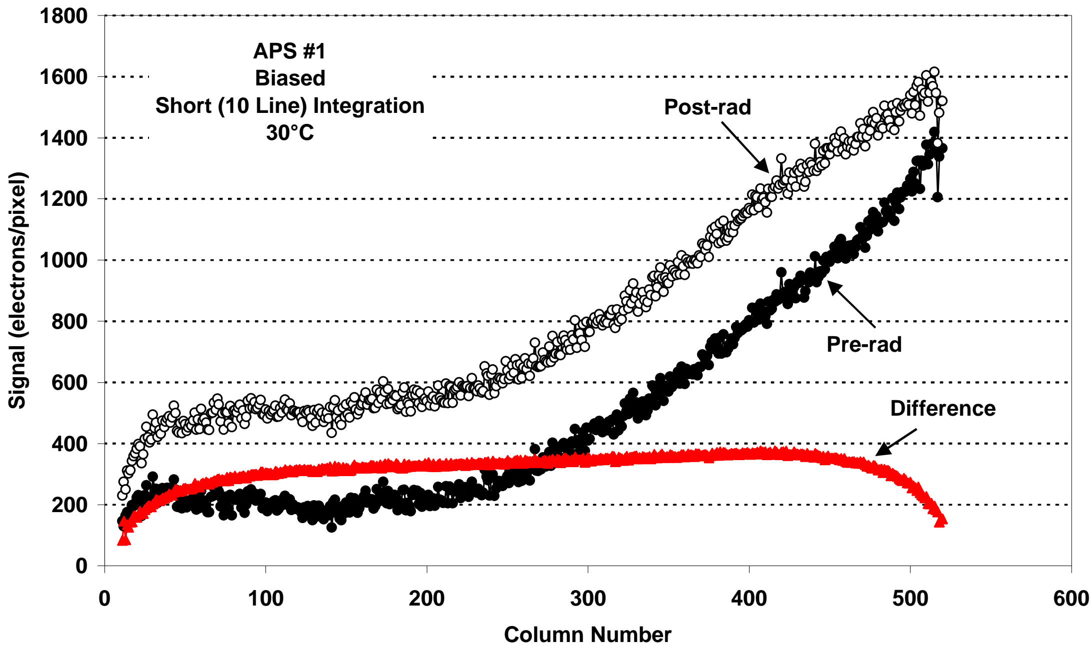

Figure 6.8.2-2 Thick horizontal profiles (averaged over all lines) for APS #1

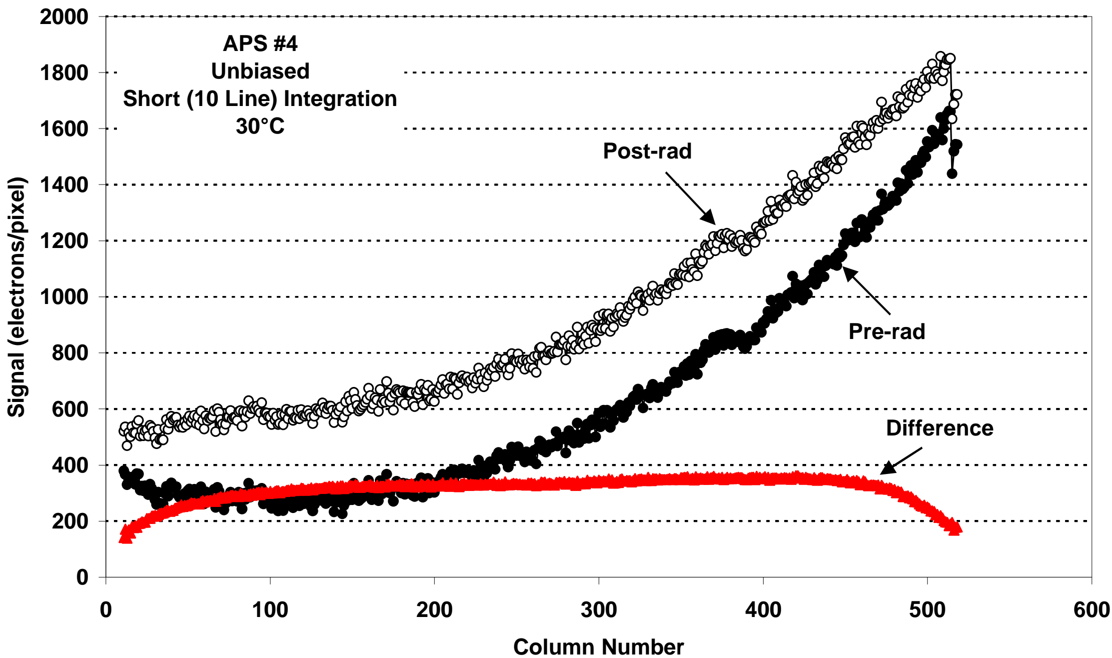

Figure 6.8.2-3 Thick horizontal profiles (averaged over all lines) for APS #4

6.9 INVESTIGATION OF RANDOM TELEGRAPH SIGNAL (RTS) BEHAVIOUR

Measurements were also made of random telegraph signal (RTS) behaviour in the photodiode dark currents. Similar results were found to Bogaerts et al [4] but if the VPIX voltage was reduced to 2.7 V then nearly all the dark current spikes disappeared. Random samples of 250 pixels in the 100 krad(Si) region showed only about 15 low amplitude RTS pixels at VPIX = 2.7 V and in the 10 krad region only the occasional 1 or 2 RTS pixels. However if the highest amplitude spikes were selected for the 100 krad region then roughly half showed RTS behaviour (figure 6.9-1).

Examples of RTS noise plots and traces at -20ºC and 27ºC are given in figures 6.9-2 to 6.9-5. Activation energies for the RMS and average values of each pixel are given in figure 6.9-6. It is seen that the activation energies are 0.6 eV.

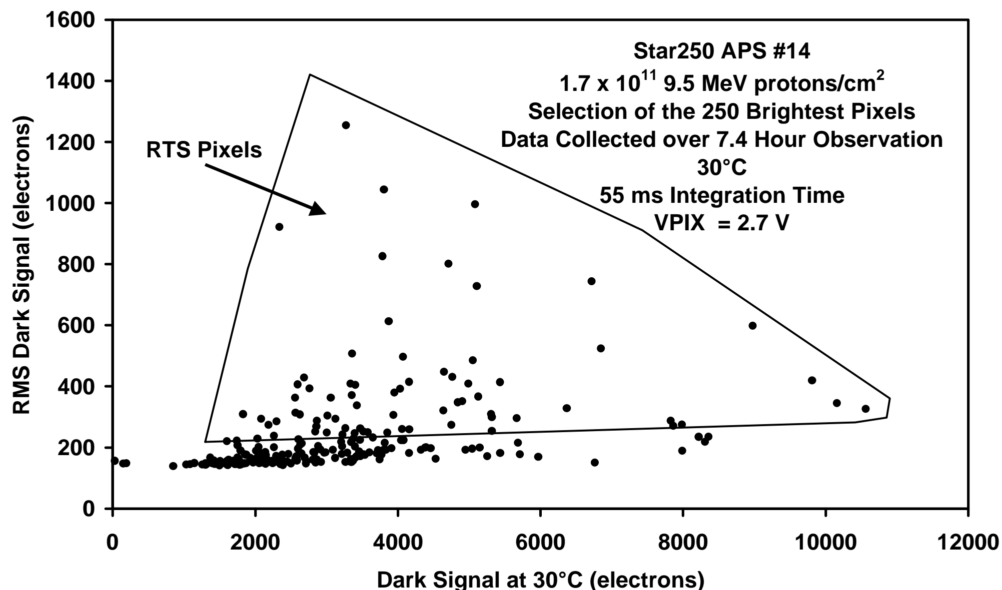

Fig. 6.9-1 RTS pixels can be identified by high RMS values

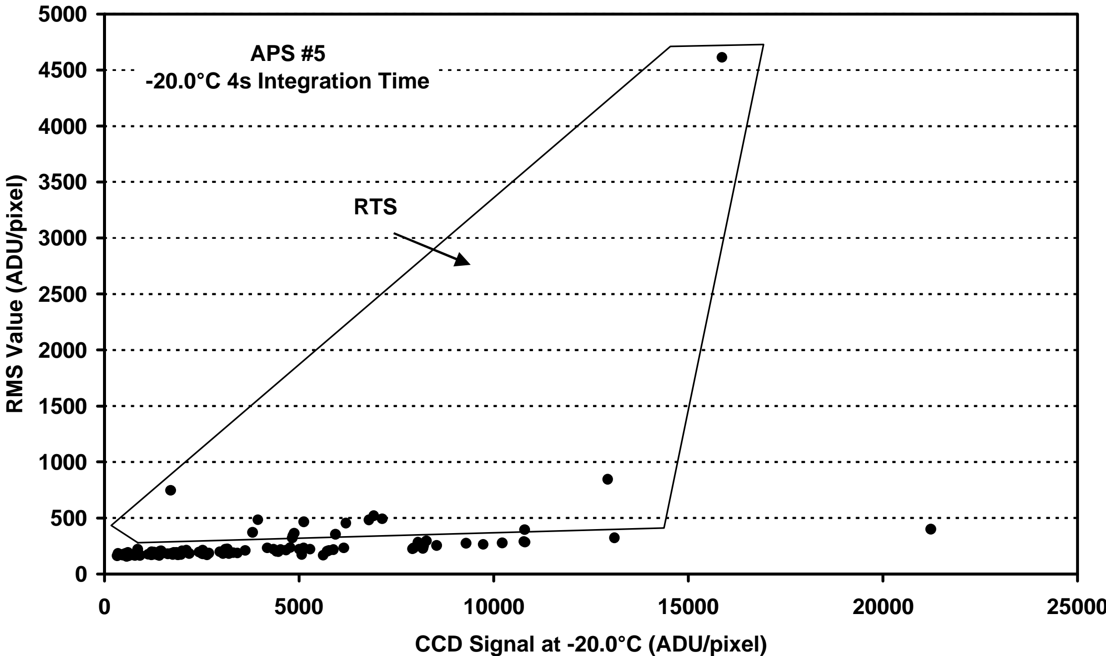

Figure 6.9-2 RTS noise plots for the brightest spikes at -20ºC

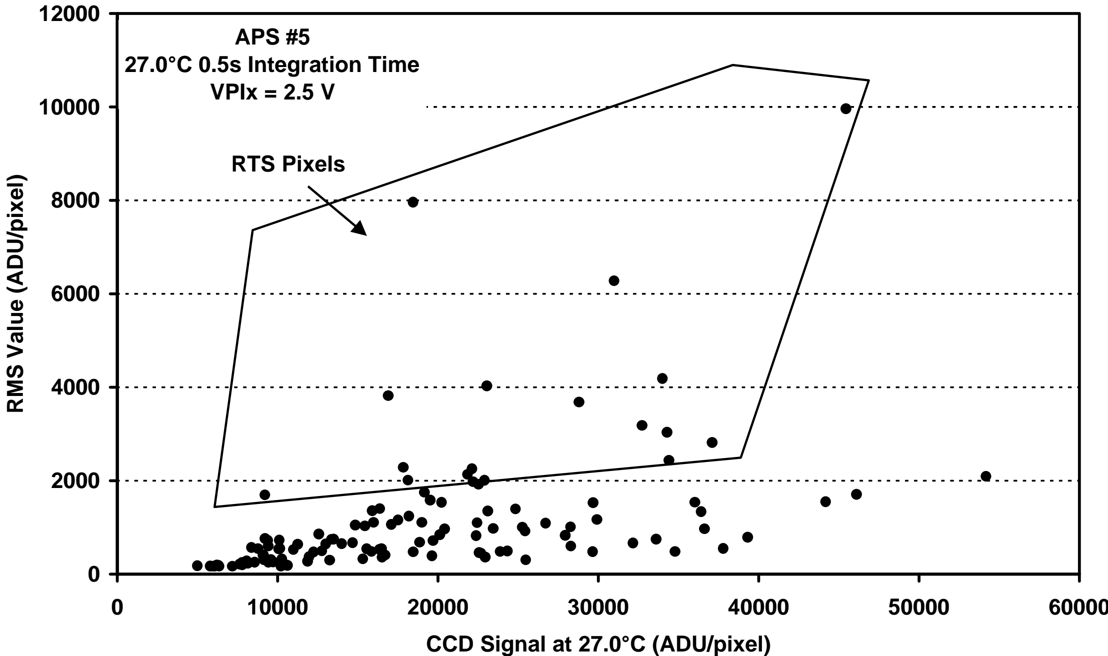

Figure 6.9-3 RTS noise plots for the brightest spikes at 27ºC

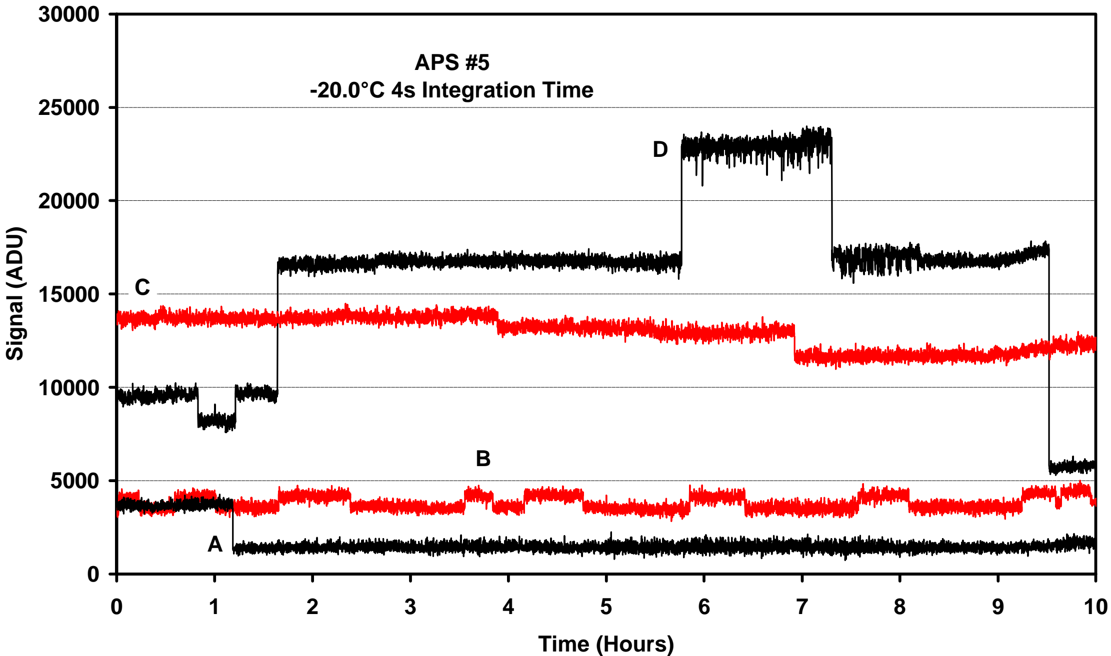

Figure 6.9-4 RTS traces at -20ºC, VPIX = 2.5 V

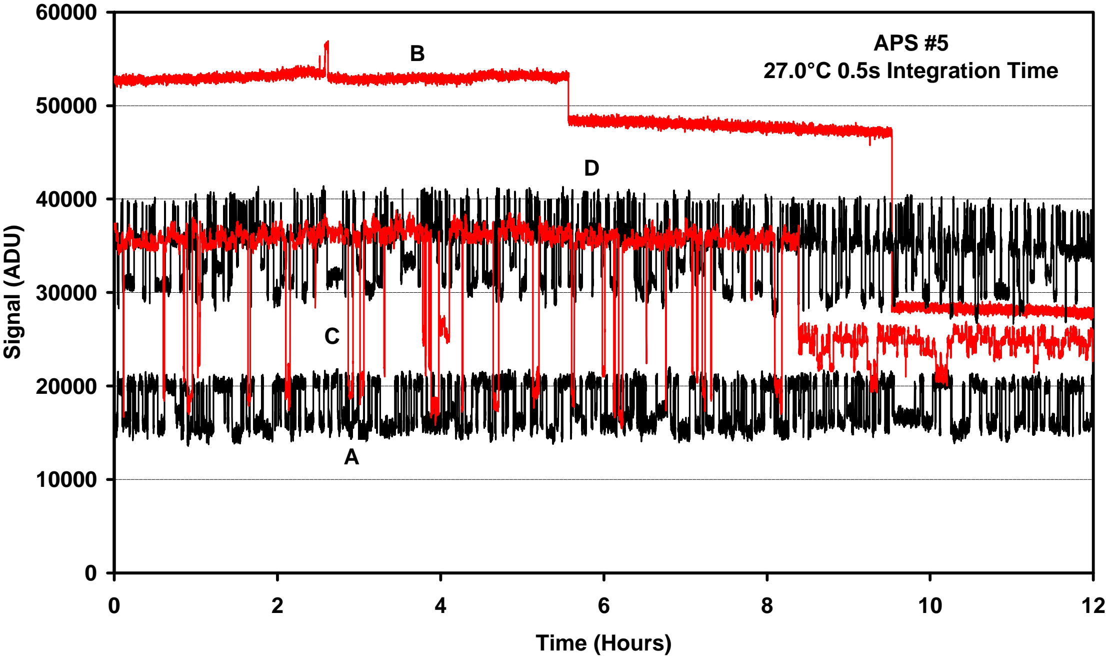

Figure 6.9-5 RTS traces at 27ºC, VPIX = 2.5 V

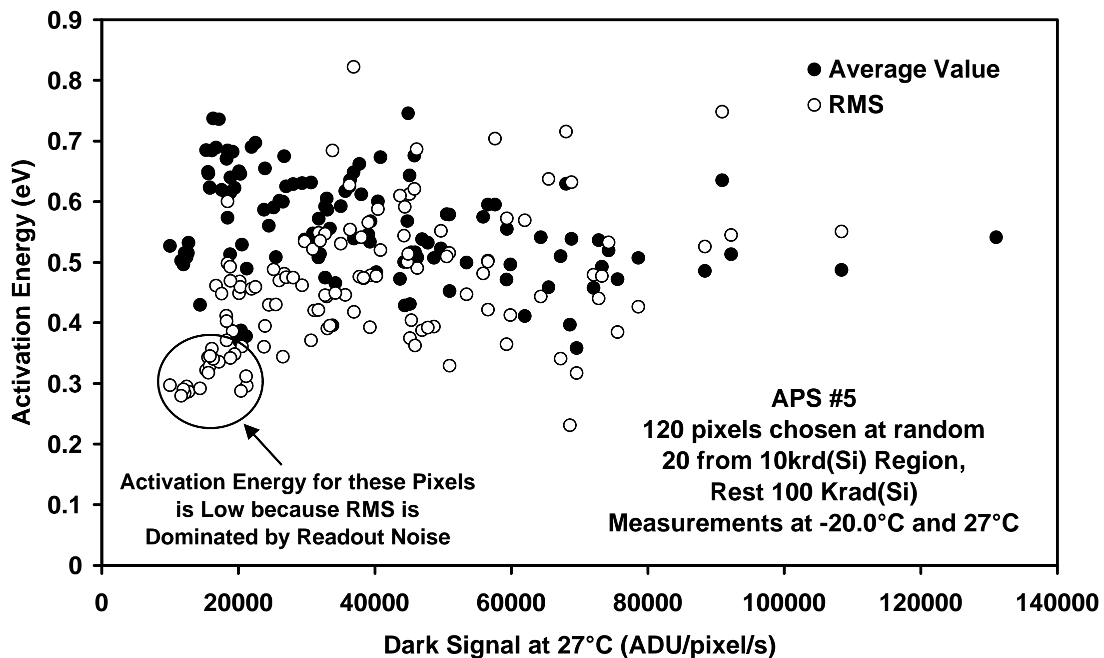

Figure 6.9-6 Activation energies for dark current spikes, VPIX = 2.5 V

6.10 RESULTS OF HEAVY ION TESTING

Heavy ion testing was performed on both the STAR-250 and the IRIS-2 APS as well as Elantec EL7457C CCD clock driver ICs, though only the STAR-250 was tested for single event upsets, the other two devices were tested for single event latch up (SEL) only.

As mentioned in section 3.2, the device currents were continuosly monitored during the test and an event was logged every time the current exceded a (user selectable) threshold value, at which point the power was cycled and the test resumed. For the STAR-250 the analogue output was fed to a TV monitor and video recorder so that a record could be kept of any single event interrupts. In fact none were observed and the images were all of the appearance of figure 6.10-1, that is a dark background with 'white spots' due to the transient signals produced by the ionization of the heavy ions. In fact these transients were a useful real time indicator of the ion flux.

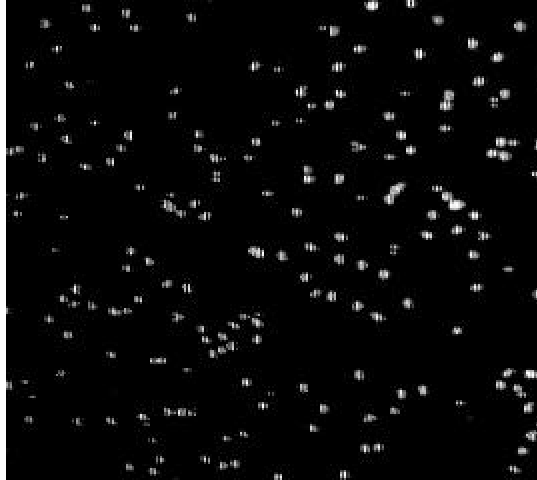

Figure 6.10-1 single video frame obtained during heavy ion irradiation of the STAR-250 APS showing random transient events.

The on-chip ADC of the STAR-250 was not connected to the analogue output of the sensor array, but instead to a DC voltage provided by a DAC. The digitized values were collected by an FPGA on the DUT board and transmitted to the data logging computer. A log was kept of the histogram of ADC values. If a value exceded a user defined value for more than 10 samples then an error would be flagged and the power recycled. This procedure was designed to check for (and correct) any lingering errors (a form of single event functional interrupt). In fact no such events were observed.

6.10.1 STAR-250 Summary

No latch up was observed in either of the two devices tested, up to the maximum LET of 68 MeV/mg/cm^2 (Kr ions at 60º incidence at a fluence on each device of 1 x 10^6 ions/cm^2). In fact here was no increase in current to a measurement accuracy of 0.1mA (measured average values: 23 mA for the sensor and 91 and 95 mA for the ADC at 5 MHz rate). Neither were there any major single event interrupts in either the sensor (monitored via the video waveform) or the ADC. However an increase in noise due to small signal transient events was seen in the ADC data. This is illustrated in figure 6.10-2. The noise spreads over roughly ± 40 ADU (out of a full range of 1024 bits). During the tests several ion LETs were used:

- 14.1 MeV/mg/cm^2 (Ar, 0º incidence)
- 28.2 MeV/mg/cm^2 (Ar, 60º incidence)
- 48 MeV/mg/cm^2 (Kr, 45º incidence)
- 68 MeV/mg/cm^2 (Kr, 60º incidence)

The noise histograms were similar in appearance for all these LETs.

Note that the central portion of the histograms are affected by overflow errors in the data collection system. This probably explains the 'spikey' nature of the histograms.

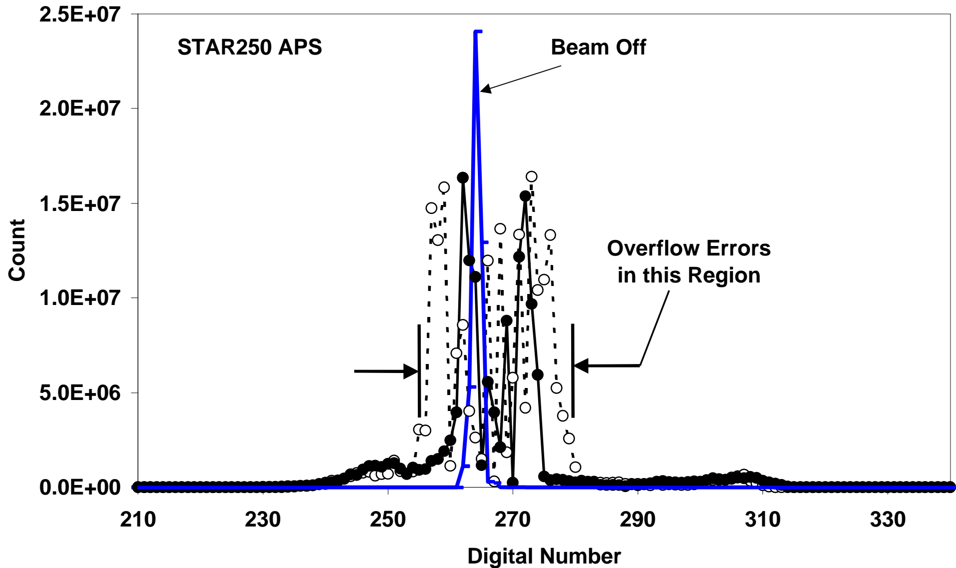

Figure 6.10-2 Histograms of STAR-250 on-chip ADC data during heavy ion testing

6.10.2 IRIS-2 Summary

Two IRIS-2 devices were tested for single event latch-up (SEL). No latch up was seen at 5.85 MeV/mg/cm^2 (Ne, 0º incidence) but SEL was observed at 8.27 MeV/mg/cm^2 (Ne, 45º incidence) and above. The number of SEL events increased with particle LET. It was seen that several of the SEL events gave only a small increase in power supply current – small enough to be non-destructive even if the power was not recycled. It is not known however if the device was still functional during these 'mini-latch' events. A histogram of the SEL currents obtained from all the runs (various LETs) is shown in figure 6.10-3. Most events had a current of 220 mA or greater (the current limiting circuit reduced the voltage to ~ 3.7 V for this current) but latches of ~ 100 mA were also observed. The typical operating current was 43 mA.

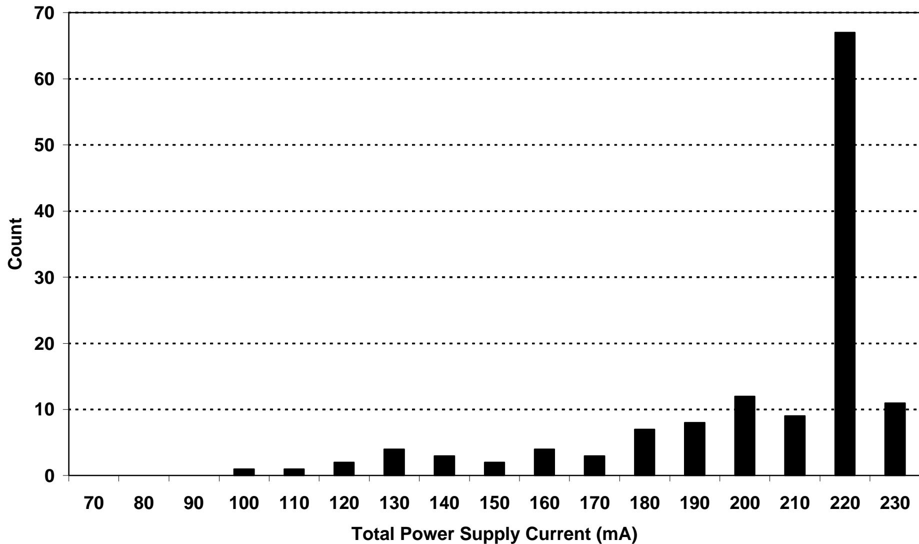

Figure 6.10-3 Histogram of SEL power supply currents for the IRIS-2 devices under heavy ion irradiation

The event rates observed were as follows for the two devices (labelled #1 and #2 in the table):

LET MeV/mg/cm^2	Ion Fluence	Number of events	Average cross section
5.85	3.0 10^6/cm^2 #1 5.0 10^6/cm^2 #2	0	0
8.27	3.5 10^6/cm^2 #1 5.0 10^6/cm^2 #2	16 #1 9 #2	2.9 10^{-6} cm^2
14.1	7.5 10^5/cm^2 #1 6.0 10^6/cm^2 #2	14 #1 88 #2	1.5 10^{-5} cm^2
28.2	~ 10^6/cm^2	Too fast to count	Not measured

6.10.3 Elantec EL7457C Devices

The Elantec EL7457C 40 MHz CMOS Driver is an ultra-high speed, non-inverting quad CMOS driver. It is capable of running at clock rates up to 40MHz and features 2A peak drive capability and a nominal on-resistance of 3 . The EL7457C is used for driving highly capacitive loads, such as storage and vertical clocks in CCD applications. It is also well suited to automated test equipment (ATE), pin driving, level-shifting and clock-driving applications.

Two devices were irradiated with Kr ions at 0° incidence, the effective LET of the ions being 34 MeV/mg/cm^2. The devices had previously been de-lidded by ESTEC and were mounted in zero insertion force (ZIF) sockets on a specially designed test board with current limiting and logging (to PC) of voltages and currents. These were measured with a Keithley 2000 multimeter, connected to the PC via a IEEE 488 interface. The angle of incidence was limited to 0° by the sides of the ZIF sockets (shadowing effect).

During the test the devices were operated with a 5V 12 MHz input clock and 5V bias (so the outputs were switching between 0 V and 5 V.

No latch up was seen on either device at the maximum LET used of 34 MeV/mg/cm^2 after a total fluence on each device of 1.0 10^6 ions/cm^2. In view of the negligibly small flux of cosmic ray ions in the space environment having LET greater than this value and the small area of the die (~ 4 mm^2) the device can be considered to be immune to latch up.

Devices were also cobalt60 irradiated at ESA ESTEC at the same time as the CCDs and STAR-250 APSs. Three sets of four devices were irradiated to 6.3 krad(Si), 18.1 krad(Si) and 27.2 krad(Si). The rising and falling edge delays were similar for all devices and were in the range 18 – 30 ns at all frequencies (in the range 1 to 6 MHz). However the 18 and 27 krad(Si) devices showed oscillatory behaviour at 1 MHz (but not at 2 MHz or above). Hence use at low doses should be acceptable but further testing is recommended for doses above 6 krad(Si)

Because the EL7457C is a commercial-off-the-shelf (COTS) device, it is recommended to perform further cobalt60 and heavy ion testing (probably to higher LET) as part of Lot Acceptance Tests on potential flight batches.